Université de Mons
Faculté Polytechnique

Energy Storage Integration in Market-Based Energy Systems: Advanced Technologies and Decision-Making Models

Hooman Khaloie

Ph.D. Dissertation submitted in partial fulfillment of the requirements to attain the degree of Doctor of Philosophy in Engineering Sciences & Technology

Members of the Examination Jury:

Prof. Zacharie De Grève	Université de Mons, Chairman
Prof. Dirk Van Hertem	KU Leuven, External Member
Prof. Georges Kariniotakis	Mines Paris - PSL, External Member
Prof. Bashir Bakhshideh Zad	Université de Mons, Secretary
Dr. Jean-François Toubeau	Université de Mons, Co-Promoter
Prof. François Vallée	Université de Mons, Promoter

Thursday 15th of January, 2026

"Pressure is a privilege. It means things are expected of you."

Attributed to Billie Jean King

Acknowledgements

This dissertation reflects four years of effort and was shaped not only by my work as a Ph.D. researcher in the Power Systems & Markets Research (PSMR) group at the University of Mons, but also by the support of many people around me. I would like to use this space to express my sincere gratitude to those who stood by me and helped make this work possible.

I would first like to thank my supervisor, Prof. François Vallée, for his mentorship and guidance over the last four years, as well as during the year before my Ph.D. I am grateful for the trust and confidence you placed in my work and for the academic freedom you gave me to grow as both a researcher and a person. The belief you showed in my work shaped my growth far more than any result or publication ever could. Thank you for being such an available and supportive supervisor. Even during busy periods, weekends, and holidays, you always offered kind and constructive feedback. I also feel very fortunate for the many opportunities for self-improvement and international training that you encouraged and supported.

I would also like to extend my gratitude to my co-promoter, Dr. Jean-François Toubeau, for the constructive discussions and thoughtful exchanges we shared over the past years. I truly hope our paths cross again and that we can relive some of those great moments.

Next, I would like to sincerely thank Prof. Giovanni Sansavini and Prof. Hakan Ergun for hosting me during external research stays at ETH Zürich and KU Leuven, respectively. I am grateful for the engaging research discussions, guidance, and the many formal and informal meetings. Special thanks also go to the team members I met during these visits, Andrej, Blazhe, Kaan, and Hatice, for the constructive exchanges and the memorable coffee breaks. I also thank Behnam for the friendly lunch breaks during my time at ETH Zürich.

I genuinely thank the members of the examination committee, Prof. Dirk Van Hertem, Prof. Georges Kariniotakis, Prof. Bashir Bakhshideh Zad, and the chair, Prof. Zacharie De Grève. I am truly honored that you took the time to review this dissertation and share thoughtful and constructive feedback.

I am sincerely grateful for the opportunity to complete this thesis as part of the DISCRETE project, supported by the FPS Economy, SMEs, Self-Employed, and Energy through the Energy Transition Fund.

My thanks go to all current and former GELE members who made my Ph.D. journey so enjoyable. While it is difficult to mention everyone by name, I am grateful to each of you for the engaging discussions, collaborations, coffee chats, and the truly wonderful time we shared. I am especially thankful to Prof. Olivier Deblecker for his managerial support over the past four years. A big thank you as well to the students I was fortunate to supervise during these years, Chloé, Sarah, and William. Thank you for your enthusiasm, effort, and research contributions. I also cannot close this paragraph without thanking my amazing office mates, Jamal and Hossein, for sharing daily life with me throughout these years. Special thanks to Jamal, my dear friend. We met six years ago, and I was incredibly lucky to have you close by through every happy and difficult moment of the past four years. Your desk will always feel next to mine, even when you are not physically there.

Last but not least, I would like to dedicate this thesis to my beloved family. I am deeply grateful to my parents, for their sacrifices and for supporting me at every step of my life. My father has been the kindest teacher I have ever known and my role model, and my mother has been the backbone of our family, whose selflessness and care have shaped me more than I can express.

Just as importantly, my deepest thanks go to my wife, Shima, my best friend and constant companion. Thank you for believing in me ten years ago and for standing by me ever since. I am especially grateful for everything you carried during the past four years so I could pursue this academic journey, even while you faced professional setbacks of your own. Thank you for managing our family so beautifully and for giving me the peace of mind to work late when needed. I dedicate this thesis to you, because your love has been the driving force behind every effort that brought it to completion. No matter what I achieve, you will always remain the most important discovery of my life.

Hooman Khaloie
Mons, Jan. 2026

Abstract

Bulk, or large-scale, energy storage systems are indispensable for future energy networks with very high shares of intermittent renewable generation. The increasing penetration of wind and solar resources requires substantial flexible capacity that can shift energy over many hours or days, hedge against forecast errors, and provide multi-market services. In this context, long-duration energy storage technologies, such as advanced compressed air and liquid air systems, are attracting growing attention and moving toward large-scale demonstration worldwide. Yet, bulk storage investments remain difficult to justify because of high upfront costs and uncertain, market-driven revenue streams, even in net-zero carbon roadmaps for the coming decades. This thesis therefore asks a central question: how can we design operational and market-integration models that enable bulk and long-duration storage assets to make informed, profit-seeking decisions while supporting the secure and cost-efficient operation of future low-carbon power systems?

To address this question, the thesis first establishes physical and methodological foundations for bulk storage operation in market environments. It clarifies the roles and applications of storage across different timescales, presents a technology-oriented view of bulk storage and its interfaces with wholesale electricity markets, and identifies the main products and services relevant for long-duration flexibility. On this basis, the work develops a common mathematical framework based on deterministic and scenario-based stochastic programming, multi-level models, optimality conditions, and mathematical programs with equilibrium constraints. The interaction between optimization and data-driven methods is also examined, thereby laying the foundation for learning-assisted solution approaches that accelerate decision-making.

Within this framework, the thesis first develops a risk-aware market dispatch

model for a grid-scale lithium-ion battery that participates in day-ahead and intraday electricity markets from a non-strategic, price-taking perspective. A risk-neutral bidding formulation serves as a reference and is extended to an operational model with second-order stochastic dominance constraints that control the downside risk of revenues relative to a data-driven benchmark portfolio. Numerical studies under realistic price scenarios show that appropriate risk constraints can substantially reduce regret and improve the reliability of battery revenues, at the cost of a moderate reduction in expected profit.

Motivated by the need for long-duration flexibility and by the potential to exploit cross-vector synergies, the thesis then turns to emerging bulk storage concepts that either couple electricity and gas systems or integrate different storage media. Within this context, it first develops a two-stage stochastic dispatch model for an integrated liquid air energy storage and liquefied natural gas system that co-optimizes electricity generation, liquefaction, regasification, and cold-exergy use across power and gas markets. A probabilistic payback period metric is introduced to assess economic feasibility under uncertainty. Second, the thesis studies the strategic look-ahead operation of a hybrid above-ground compressed air and liquid air storage plant that offers energy in a day-ahead market with network constraints. A bi-level market model is cast as a mixed-integer mathematical program with equilibrium constraints, and a learning-assisted solution approach is proposed to warm-start integer decisions. Case studies on systems of increasing size show how hybridization, forecast horizon, and strategic behavior affect profitability, market prices, and dispatch patterns, and illustrate the value of combining advanced optimization with data-driven techniques for bulk storage operation.

Taken together, the developments and case studies in this thesis demonstrate that risk-aware, multi-market, and learning-assisted models enable bulk and long-duration storage assets to convert their physical flexibility into more predictable and robust revenue streams, while aligning their operation with prevailing market rules and network constraints. Overall, the proposed methodologies provide a coherent toolbox for operators, planners, and investors who seek to integrate large-scale storage into liberalized energy markets, and they contribute to the broader transition toward data-driven, market-aware operation of flexible resources in future net-zero power systems.

Contents

List of acronyms

List of Figures

List of Tables

CHAPTER 1

Introduction

This chapter introduces the motivation, scope, and research questions of the thesis. It links net-zero climate targets, the rise of variable renewable generation, and the resulting need for flexibility with a focus on bulk energy storage as an arbitrage actor in wholesale electricity markets. On this basis, it formulates three research questions on risk-aware dispatch of grid-scale storage, market-based operation, and economic feasibility of advanced bulk facilities, and strategic look-ahead dispatch of hybrid long-duration storage systems supported by learning-based warm-start techniques, and it summarizes the corresponding contributions and structure of the thesis.

1.1. Background and Motivation

The worldwide pursuit of carbon neutrality is one of the defining challenges of this century, driven by the urgent need to reduce the harmful consequences of climate change [1]. Achieving this objective requires balancing the amount of greenhouse gases released into the atmosphere with those that are removed or compensated, thereby bringing the net release to zero [2]. This transformation is fundamental to reducing the risks associated with climate instability and to ensuring the sustainability of ecosystems and human societies. Maintaining global temperature rise within the thresholds established in international agreements, such as the Paris Agreement, is central to this objective [3]. Exceeding these thresholds could produce severe outcomes, including rising seas threatening coastal communities, more intense and frequent extreme weather, and extensive biodiversity loss [4]. The most recent findings of the Intergovernmental Panel on Climate Change (2023) emphasize that global emissions must peak imme-

diately, decline by about 45% relative to 2019 levels before 2030, and reach neutrality by mid-century [5]. Nevertheless, the current trajectory diverges sharply from this requirement. In 2023, worldwide emissions, including land-use change, reached 57.1 gigatonnes of carbon dioxide equivalent ($GtCO_2e$), of which 53 gigatonnes were produced by fossil fuel and industrial activities. This represented a growth of 1.3% to 1.9% compared with 2022, far exceeding the long-term average annual increase of 0.8% recorded between 2010 and 2019. This persistent upward trend demonstrates the growing urgency of a structural transition toward a low-carbon energy system, where both technological and systemic solutions are required to reverse the emission trajectory.

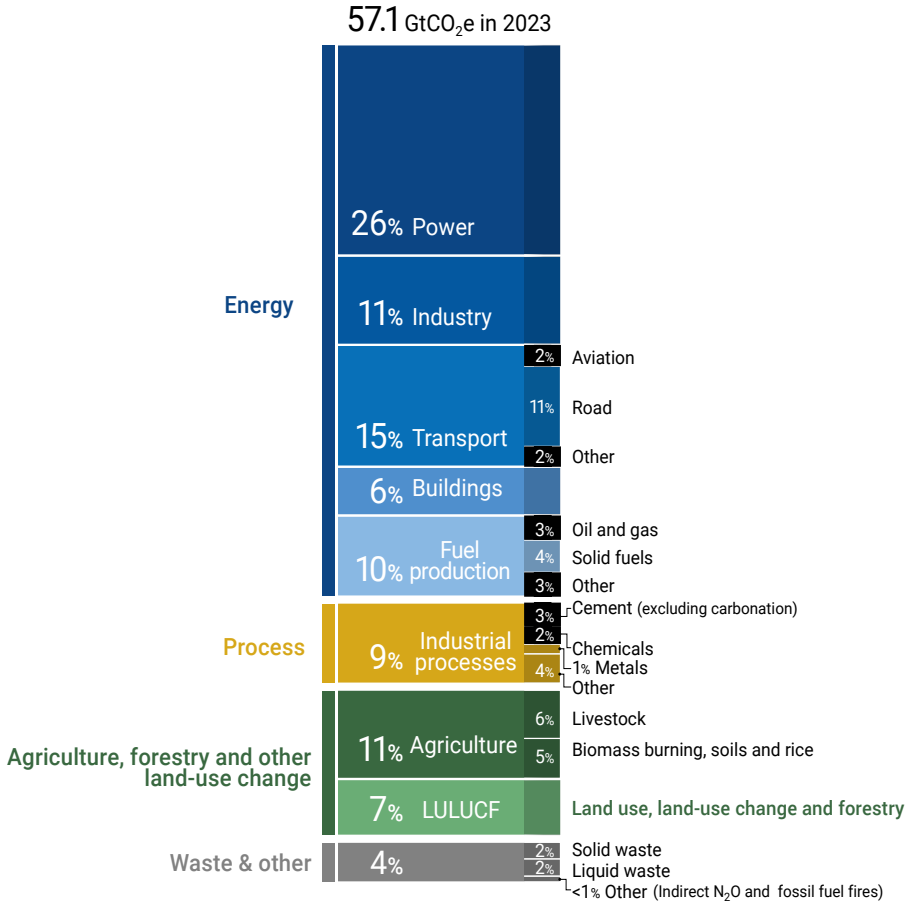

Figure 1.1: The breakdown of total greenhouse gas emissions in 2023.
Note: This chart is taken from [6].

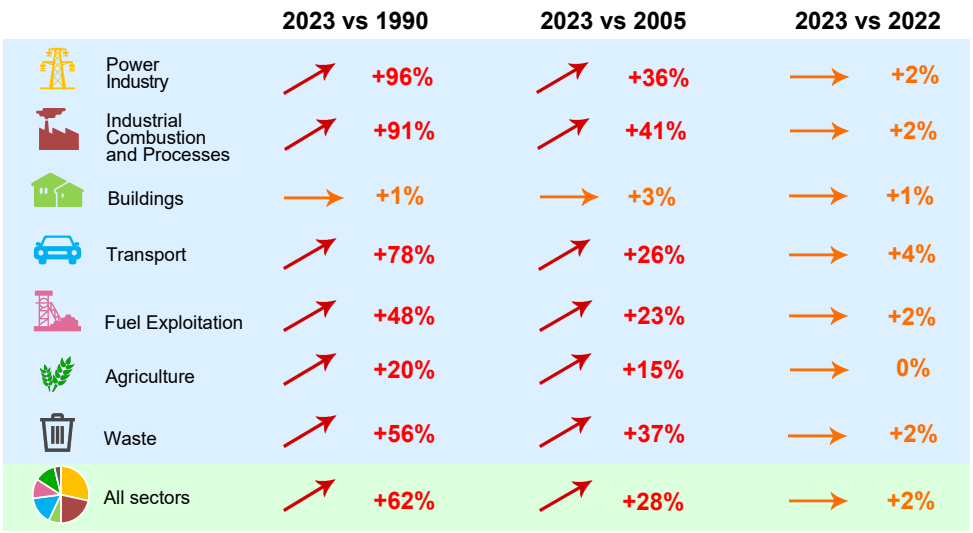

Figure 1.2: Trend of greenhouse gas emissions across major sectors since 1990.
Note: This figure is adapted from [7].

The global emission profile for 2023, presented in Fig. 1.1, highlights the central role of the energy system [6]. Power generation was the largest contributor, accounting for 26% of global emissions, equivalent to 15.1 $GtCO_2e$. Transport followed with 15%, industry with 11%, fuel production with 10%, and buildings with 6%. Outside the energy sector, additional emissions originate from industrial processes, agriculture, land-use change, and waste, which together formed a substantial share of the total. Understanding their evolution over time is essential for assessing progress toward decarbonization. While the 2023 snapshot illustrates the dominance of energy-related emissions, the historical evolution shown in Fig. 1.2 provides essential insight into how these contributions have evolved over time. As indicated in Fig. 1.2, the long-term trajectory reveals a widening gap between observed emissions and trajectories consistent with climate-stabilization pathways [7]. Since 1990, the following sectoral trends can be observed:

- The power sector has been the fastest-growing source, with emissions increasing by 96%.
- Industrial combustion and processes followed closely, rising by 91%.
- Transport emissions expanded by 78%.

- Fuel exploitation grew more moderately, recording a 48% increase.
- Emissions from the building sector remained largely unchanged, with only a 1% increase since 1990.
- On a global scale, total greenhouse gas emissions in 2023 were 62% higher than in 1990, 28% higher than in 2005, and 2% above 2022 levels, as indicated in the lower panel of Fig. 1.2 [7].

Reaching net zero requires a profound transformation of the global energy system. This transformation extends beyond simple energy substitution and demands a fundamental rethinking of how energy is produced, stored, and traded across interconnected sectors. The central difficulty arises from the continued dependence on fossil fuels, which account for the majority of energy-related emissions. Decarbonizing energy supply through large-scale deployment of renewable and sustainable sources is therefore essential to achieving this goal [8]. Such a transformation entails both the reduction of carbon emissions and the restructuring of energy infrastructure, with renewable sources serving as the foundation [9].

Net-zero emissions are achieved when the release of greenhouse gases by human activity is balanced by their removal through natural systems or technological measures [8]. An increasing number of countries, companies, and international organizations have committed to achieving this target by mid-century, with some aiming as early as 2030. This shared commitment reflects the recognition that reducing emissions is essential for limiting global warming and protecting societies and ecosystems. The importance of net zero reaches beyond the environment: *economically*, it stimulates innovation in green technologies, reduces fossil fuel volatility, and creates new employment opportunities [10]. *Geopolitically*, it reduces pressures linked to energy security. *Socially*, it protects health by reducing pollution and strengthening vulnerable communities against climate impacts. Air pollution from fossil fuel combustion causes respiratory and cardiovascular diseases as well as premature deaths, especially in urban settings. Reducing dependence on fossil fuels therefore delivers immediate public-health benefits, promotes cleaner urban environments, and supports long-term sustainability [11]. Together, the environmental, economic, and social benefits make net-zero emissions central to shaping a just and sustainable global future.

As stated earlier, the move toward net-zero emissions depends heavily on

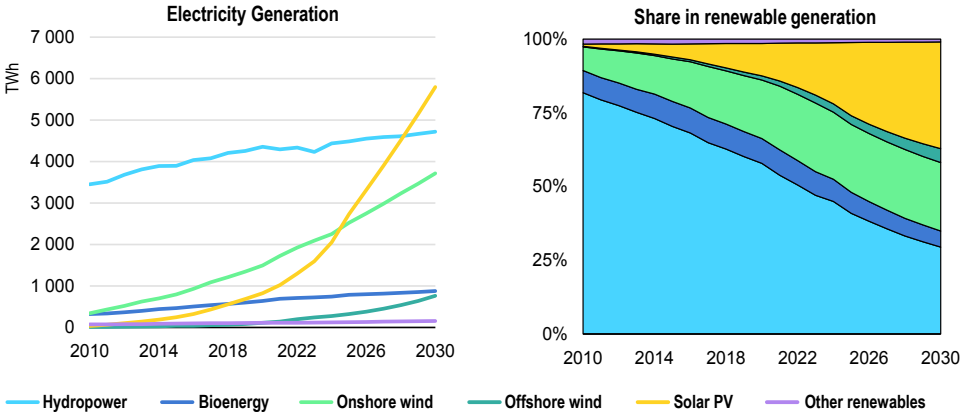

Figure 1.3: Global renewable electricity generation and shares by source, 2010–2030.

Note: This chart is taken from [15].

renewable energy systems that harness resources such as solar, wind, water, biomass, and geothermal energy to produce electricity without greenhouse gas emissions. Since the power sector accounts for the majority of global emissions, renewables remain central to decarbonization and sustainable development [9]. Over the past two decades, significant progress in solar and wind technologies has driven rapid cost declines, photovoltaic electricity costs have fallen by more than 80% since 2010, and substantial performance gains, making both technologies cost-competitive and widely adopted [12, 13, 14]. According to the International Energy Agency's latest outlook, renewable electricity generation is set to almost double by 2030, raising its share of global power supply to nearly 45% [15]. As shown in Fig. 1.3, hydropower will remain the largest contributor, but the expansion is increasingly dominated by solar photovoltaics and wind (both onshore and offshore,) reflecting the accelerating global shift toward variable renewable energy. This rapid growth, while vital for achieving climate goals and enhancing energy security by reducing dependence on fossil fuel imports, also intensifies the need for flexibility and energy storage solutions capable of maintaining system reliability under high variable renewable energy penetration.

Building on the rapid expansion of variable renewable energy outlined above, modern power systems require *flexibility*, i.e., the capability to adjust generation, demand, or power flows across seconds to seasons in response to variability and

forecast uncertainty [16, 17]. The literature identifies three principal flexibility classes [16]: (*i*) *energy storage* that absorbs surplus generation and supplies energy and ancillary services across multiple time scales; (*ii*) *fast-ramping generators* (e.g., hydropower, open-cycle gas turbines, reciprocating engines) that provide operating reserves and ramping capability; and (*iii*) *demand response* that shifts, shapes, or sheds loads to align consumption with renewable availability [18]. Portfolios combining these options mitigate net-load ramps, reduce curtailment, and lower integration costs at high variable renewable energy shares [19].

Among available options, the Energy Storage System (ESS) provides unique, multi-service value: fast frequency control, operating reserves, congestion relief, intertemporal energy shifting, and capacity adequacy, thereby enhancing reliability and enabling efficient market operation [20, 21, 22, 23]. This role strengthens as wind and solar expand toward supplying a large share of electricity by mid-century [24] and as electrification (e.g., electric vehicles) raises system demand [25]. Bloomberg New Energy Finance reports that the fossil share in the global generation mix has begun to decline and could fall to ∼31% by 2050, while renewables rise above 62% [26]. Consistent with this shift, Bloomberg New Energy Finance projects a surge in grid-scale storage from 9 GW/17 GWh in 2018 to about 1,095 GW/2,850 GWh by 2040, an expansion of more than two orders of magnitude and requiring roughly $662 billion in investment, driven in part by battery cost declines exceeding 80% since 2010 (Fig. 1.4) [27]. Together with other flexibility resources, energy storage facilities thus become central to integrating high variable renewable energy shares while maintaining reliability and economic efficiency [19, 22].

The development of energy storage technologies has advanced considerably, from behind-the-meter devices to grid-scale assets, with further details discussed in the next chapter. These technologies support the integration of intermittent renewable energy and provide services such as energy arbitrage, capacity reserve, uninterrupted power supply, and bulk power management. They also supply fast frequency control and synthetic inertia (sub-second response), load-following and ramping reserves (minutes to hours), intraday energy shifting and peak shaving (multi-hour), congestion relief and transmission, distribution deferral, voltage/reactive support, black start, and resource adequacy [21, 28, 29]. The feasible service set depends on technical characteristics, including response time and ramp rate, energy-to-power ratio (duration), round-trip efficiency, self-discharge, cycle life, depth-of-discharge, and cost—so that short-duration

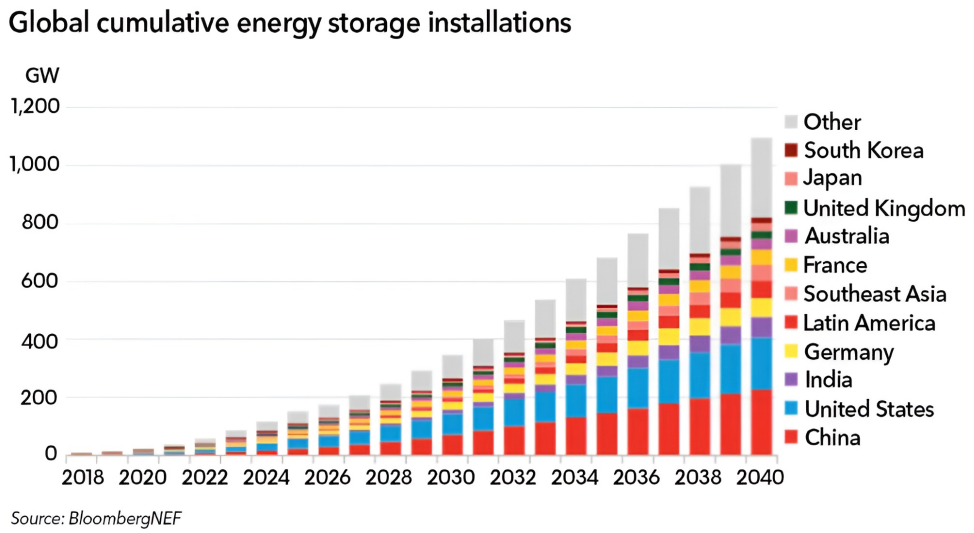

Figure 1.4: Prediction of the worldwide deployment of ESSs by 2040.
Note: This chart is taken from [27].

technologies excel at power-quality and frequency services, while long-duration options enable multi-hour to multi-day shifting, curtailment reduction, and firm capacity provision [20, 23, 22].

Given these characteristics, bulk energy storage[1], with capacities above several tens of megawatts and multi-hour duration, provides system-level benefits essential for integrating high shares of variable renewable energy. It enables energy shifting from surplus periods to peak demand, reduces curtailment, smooths large net-load ramps, and supports adequacy during prolonged renewable shortfalls. In addition, it supplies operating reserves, frequency control, and congestion relief that can postpone network reinforcements. Mature and emerging bulk technologies include pumped-hydro energy storage, Compressed Air Energy Storage (CAES), Liquid Air Energy Storage (LAES), pumped-thermal electricity storage, and large flow- and lithium-ion battery plants. Achieving the storage scale required under high renewable pathways therefore depends on deploying these bulk technologies alongside shorter-duration assets to ensure intertemporal flexibility and maintain system adequacy throughout the energy transition [30].

[1]Bulk energy storage facilities commonly refer to storage facilities with charge/discharge power capacities exceeding several megawatts (e.g., 50 MW) and durations of four hours or more [30].

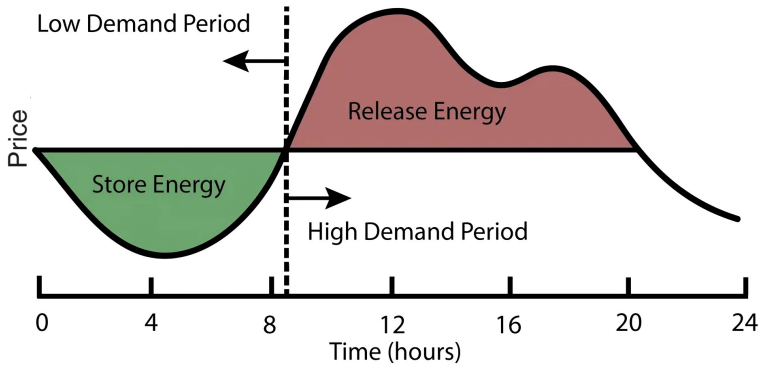

Figure 1.5: Energy arbitrage practice leveraging electricity price fluctuations. *Note:* This figure is taken from [32].

As discussed earlier, a wide spectrum of energy storage technologies exists, encompassing both emerging and mature solutions that collectively strengthen grid reliability and enhance system efficiency. These systems are instrumental in accommodating the growing shares of variable renewable energy sources such as wind and solar. However, as the penetration of these intermittent resources increases, market price volatility intensifies due to their variable and uncertain generation patterns [31]. In this evolving context, bulk ESSs can assume an active role in energy markets, transforming from passive grid assets into market participants and, in doing so, improving their economic viability and investment attractiveness.

In current deregulated electricity markets, large-scale ESSs can receive compensation through various channels such as ancillary service payments, capacity payments, and electricity trading through energy arbitrage. The primary mode of participation for bulk ESSs in electricity markets revolves around energy arbitrage. This strategic practice involves procuring and storing energy during periods of low electricity prices, subsequently selling and discharging the stored energy back into the grid during peak-price periods, as illustrated in Figure 1.5. The widespread deployment of ESSs in electric grids is contingent upon the attainment of attractive revenue streams, primarily derived from market services such as energy arbitrage and ancillary services, which are categorized as external factors. Additionally, facility-related factors, including the round-trip efficiency of ESSs, play a significant role in shaping their investment appeal. These facility-related factors, also known as internal factors, influence the optimal

daily, weekly, and yearly operation strategies of ESSs, thereby impacting their market revenue potential. As elaborated earlier, there is a consensus within the industry that no ideal ESS exists, excelling in all internal facility factors. These factors encompass various parameters, including nominal capacity range, rated discharge duration, round-trip efficiency, lifetime, technology maturity, and geological constraints, among others.

Overall, the external and internal factors discussed above jointly shape the revenue streams of bulk ESSs. As a result, the operation of large-scale storage assets faces pressing challenges in energy markets, particularly under increasing uncertainty, stronger price volatility, and evolving market rules. These challenges directly influence the bankability of storage investments and motivate the need for decision-making tools that support reliable and economically meaningful operation.

In this thesis, the problem is positioned as a market-driven optimization task: bulk storage operation is determined by the interaction between market revenues, operational constraints, and uncertainty. Accordingly, decision-making models are developed and evaluated for three representative settings: (*i*) risk-aware dispatch of grid-scale batteries in short-term electricity markets, (*ii*) market-oriented dispatch of an integrated long-duration storage concept that couples electricity and Liquefied Natural Gas (LNG) through cryogenic processes, and (*iii*) strategic operation of a hybrid storage plant that interacts with market clearing as a price-making participant. This positioning enables contributions to both operational optimization methods and evidence-based insights on the economic potential of emerging storage technologies, as will be detailed in the subsequent section.

Scope Clarification

The thesis focuses on bulk energy storage from the perspective of energy arbitrage within wholesale electricity markets, while other services remain outside its analytical scope.

Scope and boundaries of the thesis. To keep the analysis focused and reproducible, the following scope boundaries are adopted:

- **Market products:** Participation is primarily modeled through energy arbitrage and market bidding. Ancillary services, reserves, and capacity

mechanisms are not explicitly co-optimized in the core models, although several of the studied technologies could provide such products.

- **Decision layers:** The emphasis is placed on operational and strategic decision-making, rather than long-term capacity expansion planning. Economic implications are assessed through operational profits and feasibility indicators.
- **Uncertainty modeling:** Uncertainty in market-relevant variables is represented to the extent required to support risk-aware and strategic decision-making, while maintaining computational tractability and enabling out-of-sample evaluation.
- **Technology fidelity:** The proposed models target the stable design operating regime of the selected technologies. Accordingly, thermo-based storage concepts are represented through dispatch-level constraints and design-point efficiencies, while detailed thermodynamic modeling and off-design behavior are kept outside the scope. This boundary supports a consistent market-oriented analysis and avoids introducing physical detail that would require technology-specific calibration beyond the aims of the thesis.

1.2. Research Questions and Challenges of Bulk Energy Storage Integration in Energy Markets

This thesis investigates the arbitrage potential of bulk energy storage facilities and addresses the main challenges associated with their operation in energy markets. The analysis focuses on the dispatch strategies of both mature and emerging bulk storage technologies, specifically lithium-ion batteries, LAES, and hybrid Compressed Air-Liquid Air Energy Storage (CAES-LAES) systems. Lithium-ion batteries represent the most established electrochemical technology, accounting for over 85% of installations in 2016 [33], due to their maturity, high round-trip efficiency, and applicability across scales ranging from behind-the-meter to grid-level systems. In parallel, this work examines two advanced thermo-mechanical technologies, LAES and hybrid CAES-LAES, as competitive alternatives to pumped hydro and conventional underground CAES. LAES provides key advantages such as scalability, absence of geological constraints, cost-effectiveness, and multi-service capability [34]. The hybrid CAES-LAES

concept mitigates the cost and scalability limitations of above-ground CAES while enhancing flexibility and efficiency [35]. These characteristics have intensified research and industrial interest in thermo-mechanical storage solutions. The following subsections outline the principal challenges in optimizing the dispatch of these bulk storage technologies in wholesale energy markets and define the corresponding research questions that guide this thesis.

1.2.1 Market Dispatch of Grid-Scale Lithium-Ion Batteries

Battery storage systems, spanning from grid-scale installations to small-scale home setups, have become an integral component of today's electricity industry. They play a pivotal role in facilitating the integration of renewable energy sources, enhancing overall system flexibility, providing rapid-response power quality services, and deferring the need for expansion planning. Despite their technological advancements and economies of scale, the widespread adoption of battery storage systems in existing electric grids continues to face significant barriers, primarily due to high investment costs [36]. A critical aspect influencing the revenue streams of battery storage systems, particularly electrochemical batteries like lithium-ion, is their degradation over time [37]. This degradation primarily stems from the diverse discharging and charging cycles they undergo, which diminishes their lifespan and impacts their efficiency. Therefore, implementing appropriate strategies to mitigate degradation is imperative [38]. Several comprehensive studies have investigated the degradation and aging mechanisms of lithium-ion batteries, one of the most widely utilized electrochemical batteries [38, 39].

A complementary approach to promoting battery deployment is to optimize their revenue potential by leveraging the services they provide to the grid. Energy arbitrage, accomplished through market bidding, stands out as a key strategy offering promising economic returns for battery owners. Energy arbitrage, as depicted in Figure 1.5, involves charging and discharging at different times of the day to capitalize on price fluctuations in the electricity market [40]. Under increasing renewable penetration, however, short-term prices become more volatile and more uncertain, which amplifies arbitrage opportunities but also exposes the operator to low-profit realizations. Consequently, the key operational difficulty is not only to maximize expected profit, but to design a dispatch strategy that protects the battery against low-profit outcomes that arise from price uncertainty. In particular, price forecast errors translate into a

dispersed profit distribution, where downside outcomes matter for investment viability.

The literature has addressed risk management in battery bidding using several paradigms, including Conditional Value-at-Risk (CVaR) [41], robust optimization [42], distributionally robust optimization [43], and information gap decision theory [44]. These approaches provide valuable tools, yet they often emphasize either tail events or worst-case protection, which can lead to overly conservative schedules or require risk parameters that are difficult to interpret for market participants. In contrast, stochastic dominance criteria allow the operator to express risk preferences directly at the level of the profit distribution.

Among these, Second-order Stochastic Dominance (SSD) provides a coherent benchmark-based mechanism that can protect against downside profit outcomes while retaining diversification benefits. However, two practical obstacles still limit its routine use in market dispatch models for grid-scale batteries. *First*, SSD requires a benchmark specification, and the literature lacks a generic and well-justified procedure to characterize the feasible benchmark region. When the benchmark lies outside this feasible set, the model becomes infeasible or yields economically meaningless outcomes. *Second*, even within the feasible region, existing works provide limited guidance on how an operator should select a meaningful benchmark, although benchmark choice largely determines the risk–profit trade-off.

These observations motivate the use of stochastic dominance as a distribution-based way to represent risk preferences in battery arbitrage. In particular, SSD offers a benchmark-oriented mechanism to protect the operator against downside profit outcomes under uncertain prices. However, the literature still lacks practical guidance on benchmark feasibility and benchmark selection in SSD-constrained battery dispatch. The following research gaps therefore remain:

(i) Beyond the risk-based bidding structures reviewed above [41, 42, 43, 44], only limited research has used SSD to express the operator's risk preference directly at the level of the profit distribution. The SSD criterion provides a coherent benchmark-oriented way to hedge against uncertainty by requiring the battery's profit distribution to dominate a reference benchmark. However, the existing SSD literature does not provide a generic and well-justified procedure to characterize the feasible set of

benchmarks in SSD-constrained dispatch problems. When the benchmark lies outside this feasible set, the model becomes infeasible or yields economically meaningless outcomes. For instance, in [45], one of the few works applying SSD-constrained optimization, the benchmark-feasibility reasoning is not generalized into a reproducible procedure. A structured derivation of the feasible benchmark region therefore remains necessary for practical adoption.

(ii) Even when benchmark feasibility is guaranteed, the final benchmark choice has received limited attention, although it largely determines the risk–profit trade-off. Prior studies [45, 46, 47] evaluate SSD performance under selected benchmark values, but they do not propose a practical method to identify a meaningful compromise benchmark within the feasible region. As a result, benchmark selection remains ad hoc, which can weaken the risk-management value of the SSD constraint in operational decision-making.

Based on these gaps, this thesis formulates the first research question to develop a structured risk-aware dispatch framework for grid-scale lithium-ion batteries under uncertain and volatile electricity prices.

Research Question 1

How can we design a risk-aware market dispatch strategy for grid-scale lithium-ion batteries to protect them against uncertain and volatile electricity prices?

1.2.2 Market Dispatch of Advanced LAES Facilities

In addition to lithium-ion batteries, several specialized storage systems are designed for long-duration, large-scale power applications. These include pumped hydroelectric storage, CAES, and LAES systems. Unlike electrochemical batteries, pumped-hydro storage, CAES, and LAES do not exhibit intrinsic electrochemical capacity fade with cycling; instead, their long-term performance is primarily governed by equipment aging and wear (e.g., rotating machinery, valves, heat exchangers) and is managed through maintenance and refurbishment. Among these technologies, pumped hydroelectric storages are recognized as high-efficient and cost-effective bulk storages that can only be built in specific locations with favorable geological features, though most viable areas have

been already erected and exploited. On the other hand, compressed air energy storage is another fairly efficient technology that demands: 1) gigantic above-ground air storage tanks, requiring significant investment costs, or 2) natural underground caverns that charge geographical limitations [48].

The foregoing obstacles have drawn increasing attention to LAES[2], that lends itself well to bulk-scale applications. Since liquefied air with high energy density is leveraged as the working fluid in the LAES facility, considerably smaller storage tanks are required, resulting in reduced initial investment costs. Furthermore, the LAES is restricted to no geographical or geological constraints, making it more amenable to industrialization and grid integration purposes [49]. Also, similar to CAES, LAES is deemed a potentially suitable asset for sector coupling or integrating multiple energy carriers [34].

Despite the benefits mentioned above for the LAES [34], its ongoing deployment in energy networks [50], and evolving research, the comparatively low efficiency of standalone LAES facilities is the main barrier to their widespread installation in power and energy networks. Although joint dispatching of LAES alongside renewable resources and other technologies like air separation units increases the system's flexibility [51], the LAES efficiency is not affected by this coordinated operation. Therefore, improving LAES round-trip efficiency has emerged as a crucial area of research, leading to exploring four general pathways and directions within this domain [34, 50].

The first pathway involves integrating LAES with external cold sources, such as the cold released during LNG regasification process to aid air liquefaction during the charging mode [52]. The second strategy involves incorporating external heat sources, like co-firing natural gas with regasified air during discharging [53]. Third, integrating renewables like geothermal [54] and solar thermal [55] systems with LAES can improve power generation efficiency in LAES. Finally, hybridizing LAES with other energy storage technologies, such as pumped thermal energy storage, by sharing/replacing certain components or providing heat and cold sources, represents another promising avenue to enhance the efficiency of LAES [56]. While each pathway offers its specific advantages, significant focus has been placed on harnessing both external cold and heat sources to enhance LAES efficiency within charging and discharging modes [34, 50]. In pursuit of this objective, the integration of LAES with the LNG regasification process has emerged as a notable area of research. This

[2]LAES is a form of "cryogenic energy storage".

integration holds considerable potential, as highlighted in [57, 52, 49]. In this approach, (*i*) during LAES charging, the released cold energy from the LNG regasification is further leveraged in the air liquefication process, and (*ii*) during LAES discharging, the regasified air and natural gas are co-fired to power a gas turbine and generate electricity. As a result, by leveraging the first two pathways mentioned earlier, the performance of the LAES can be simultaneously enhanced, potentially leading to a competitive performance in the energy storage landscape. While thermodynamics and functionality of Liquid Air Energy Storage coupled with LNG regasification (LAES-LNG) have been examined and validated in a broad body of literature [57, 52, 49], the following have remained open issues so far:

(i) The optimal operation strategy of the LAES-LNG facility toward a cost-effective dispatch remains unexplored in the existing literature. Assuring the facility's financial feasibility requires a well-laid mathematical programming setup that has not been presented so far.

(ii) In the context of the LAES-LNG facility, the trading platform involving both electricity and LNG as energy carriers remains uncovered in the relevant literature. While previous works in power system studies have extensively addressed the electricity market, studies involving LNG have primarily focused on its utilization as a natural gas provider [58, 59] or its integration into the natural gas market/network [60, 61], without delving into LNG market setups. Consequently, there is a notable gap in the literature concerning the LNG market as a fundamental component of LNG provision. Additionally, the optimal daily operation of the LAES-LNG facility requires a proper market-oriented sequence-aware decision-making framework in LNG and electricity markets that are usually cleared at different times of the day, which also has not been addressed before.

(iii) Although some economic indicators have been examined for the LAES-LNG facility in [57, 52, 49], the economic viability of the facility can not be assessed without a (*i*) well-laid optimal operation strategy for the LAES-LNG facility and (*ii*) proper market-oriented sequence-aware interaction with electricity and LNG markets as the involved carriers. In this regard, a proper economic feasibility study should be conducted to assess the LAES feasibility and its long-term potential for deployment

in energy markets. Evaluating the *payback period*, which serves as a key metric for assessing economic feasibility, is an essential initial step in the process of LAES commercialization to determine the timeframe for recovering investment costs. It is worth stressing that the *payback period* has not been analyzed for the LAES-LNG facility in [57, 52, 49]. The *payback period* of the LAES is influenced by uncertain investment costs and annual profits, with the former attributed to the project's complex composition and susceptibility to market fluctuations, inflation, technological advancements, and unforeseen events, while the latter is affected by the high price volatility of the involved energy carriers. Earlier studies neglected these sources of uncertainty and treated them as fixed values, leading to a deterministic *payback period* analysis.

Addressing these open challenges, the second research question in this thesis is envisioned to develop an integrated framework that links the operational strategy of the LAES-LNG facility with market-based decision-making to ensure its cost-effective participation under current market conditions.

Research Question 2

How can an optimal market-oriented dispatch framework be developed for the integrated LAES-LNG facility to ensure cost-effective operation under current market designs?

1.2.3 Strategic Market Dispatch of Hybrid CAES-LAES Systems

Following the progress in thermo-mechanical storage concepts such as LAES-LNG, recent research has shifted toward hybrid configurations that CAES and LAES to exploit their complementary advantages in efficiency and cost. Conventional CAES is widely recognized for its cost-effectiveness at large scales; however, underground storage depend on suitable salt caverns, which are geographically limited. In regions lacking such formations, above-ground CAES and cryogenic systems like LAES offer feasible alternatives. Above-ground CAES employs high-pressure steel vessels, but the low energy density of compressed air leads to large tank volumes and high storage costs, limiting capacity compared with underground CAES [62]. In contrast, standalone LAES stores energy in liquid form with much higher density, allowing large-scale

storage in low-pressure cryogenic tanks at significantly lower cost. Nonetheless, cryogenic systems generally exhibit lower round-trip efficiency than CAES [63]. To overcome these trade-offs, research has increasingly focused on hybrid CAES-LAES configurations that integrate the cost advantage of cryogenic storage with the high efficiency of CAES, enabling scalable, efficient, and geographically unconstrained long-duration storage solutions [35, 64, 65, 66].

In line with this concept, the hybrid CAES-LAES design integrates both storage forms to deliver an efficient and scalable solution free from geological limitations. The hybrid plant features: (*i*) an LAES facility equipped with a high-capacity cryogenic tank capable of storing large volumes of energy, (*ii*) a CAES unit utilizing a cost-effective above-ground high-pressure tank with lower energy capacity, and (*iii*) machinery that enables the conversion between liquid air and compressed air storage. This design aims to create a scalable energy storage solution without geological constraints by combining the cost-effectiveness of LAES with the high efficiency of above-ground CAES units. The analyses in the previous subsections adopt a price-taking perspective for bulk storage participation. For the hybrid CAES-LAES configuration, we move beyond this assumption and allow strategic (price-making) behavior: the plant optimizes coordinated offer/bid decisions while accounting for their effect on market clearing. This extension captures the economic reality of large storage assets that can shape prices and dispatched volumes, and it motivates a Stackelberg-type dispatch model aimed at improving profitability under look-ahead market designs.

Building on this strategic (price-making) perspective, and notwithstanding prior examinations and validations of the hybrid plant's thermo-mechanical design, particularly the machinery enabling bi-directional conversion of air storage forms [35, 64, 65], the following modeling and market-design challenges remain open:

(i) Although the economic feasibility of a hybrid CAES-LAES plant has been analyzed using an algorithmic approach in [64], the optimal dispatch strategy for such a plant has yet to be addressed. Effective dispatch requires coordinating internal energy transfers (via machinery) with the distinct operational states of each storage facility.

(ii) Despite extensive studies on the strategic behavior of energy storage facilities [67, 68, 69], no prior research has addressed: (*i*) the *look-ahead strategic* dispatch of a hybrid CAES-LAES plant in electricity markets,

which requires adapting the general dispatch formulation to a Stackelberg game where the plant submits coordinated offers/bids to the market; (*ii*) the impact of varying look-ahead window lengths (on a daily basis) on the social welfare constituents[3] across all entities in the electric grid [69, 70, 71].

(iii) *bi-level* optimization approaches frequently rely on numerous integer variables, resulting in significant computational burdens. However, the potential for leveraging deep learning network to warm-start these integer variables for the solver remains unexplored in the context of *bi-level* programming. While warm-starting techniques[4] have proven to be effective in various power system problems [72, 73, 74], the application of deep learning to warm-start a large number of integer variables in a *bi-level* setup remains uncharted.

To overcome the above limitations, the final research question of this thesis seeks to underscore the importance of an integrated modeling framework that links coordinated operation, strategic bidding behavior, and computational scalability for hybrid CAES-LAES systems.

Research Question 3

How can a strategic market dispatch framework be developed for the hybrid CAES-LAES plant to achieve coordinated operation under look-ahead market designs while improving computational efficiency through learning-based warm-start techniques?

1.3. Research Contributions

As part of the efforts to address the research questions outlined above, this section summarizes the principal contributions of the thesis corresponding to *Research Questions 1–3*. First, a coherent risk-aware day-ahead and intraday market dispatch framework is developed for grid-scale lithium-ion batteries, embedding the SSD criterion and introducing a systematic methodology for feasible benchmark selection. This contribution directly addresses *Research Question 1* and is detailed in Section 1.3.1. Next, to tackle *Research Question 2*,

[3] Suppliers' expected profit and consumers' expected surplus.

[4] Warm-starting {continuous variables, integer variables, active constraints}.

an integrated market-oriented dispatch model is proposed for the LAES-LNG facility, as discussed in Section 1.3.2. The model captures sequence-aware participation across electricity and LNG markets and enables comprehensive assessment of the facility's economic feasibility under uncertainty. Finally, Section 1.3.3 establishes a strategic (price-making) look-ahead dispatch framework for a hybrid CAES-LAES plant, formulated as a *bi-level* Stackelberg problem and enhanced with learning-based warm-start techniques to improve computational scalability. This contribution provides a comprehensive response to *Research Question 3*.

1.3.1 On a Risk-Aware Dispatch of Lithium-Ion Batteries

Addressing *Research Question 1*, we develop a coherent risk-aware dispatch framework for grid-scale lithium-ion batteries operating in day-ahead and intraday markets. The framework advances beyond conventional risk treatments by embedding the SSD criterion within a stochastic bidding formulation. The SSD-constrained model enables the storage operator to articulate risk preferences through a predefined profit benchmark and to enforce decisions that probabilistically dominate this benchmark under uncertainty, thereby aligning operational choices with explicit performance expectations.

The adoption of SSD is motivated by its coherence properties [75] and its intuitive interpretation for market participants. Unlike tail-focused measures such as CVaR, which emphasize extreme-loss aversion, SSD evaluates the entire profit distribution relative to a benchmark and preserves diversification benefits that incoherent metrics, such as value-at-risk, fail to guarantee. In the context of battery dispatch, this property yields operational strategies that remain economically sound across a wide range of price trajectories while still mitigating downside risks relative to an operator-defined target.

A key challenge in implementing SSD lies in the rational selection of the profit benchmark. To address this, a two-stage procedure is introduced that combines a generic derivation of the feasible benchmark region with a preference-informed screening process. First, the admissible set of benchmarks is analytically characterized to ensure feasibility and avoid ill-posed solutions. Second, candidate benchmarks are sampled from this region and assessed through an out-of-sample performance analysis using a regret-based metric, defined as the shortfall relative to the hypothetical best-informed action [76]. This evaluation jointly considers profitability and regret to balance realized performance with

aversion to hindsight loss. The final benchmark is selected using the VIKOR multi-criteria ranking method, yielding a transparent and reproducible rule for benchmark determination.

Embedded within a day-ahead and intraday co-optimization, the resulting SSD-based bidding framework produces risk-consistent and market-feasible schedules that enhance profit distribution relative to the selected benchmark without excessive conservatism. Numerical experiments demonstrate that the model effectively captures the operational dynamics of battery arbitrage under price uncertainty, providing dispatch strategies that remain robust to scenario variations while preserving economic opportunity. These developments collectively offer a practical and implementable response to *Research Question 1*, establishing a coherent risk-aware framework and a principled methodology for feasible benchmark selection in battery market bidding. The development of this model has resulted in the following contribution:

- **H. Khaloie**, J. Faraji, F. Vallée, C. S. Lai, J.-F. Toubeau, and L. L. Lai, "Risk-Aware Battery Bidding With a Novel Benchmark Selection Under Second-Order Stochastic Dominance," *IEEE Transactions on Industry Applications*, vol. 59, no. 3, pp. 3009–3018, May–June 2023.

1.3.2 On an Integrated Operation of the LAES-LNG Facility

As part of the efforts to tackle *Research Question 2*, we propose an integrated, market-oriented dispatch framework for the LAES-LNG facility. The study moves beyond the thermodynamic and design-oriented analyses commonly found in the literature [57, 52, 49] by formulating a mathematical dispatch model that captures the operational behavior of the LAES-LNG system within a market-based context. This framework enables a realistic evaluation of the facility's participation in both the electricity and LNG markets, bridging the gap between conceptual design and market-driven operation.

The first step in this development establishes a comprehensive mathematical formulation for the LAES-LNG facility applicable to power system analyses. While previous studies primarily focused on configuration and thermodynamic efficiency, this model explicitly represents the operational decisions and intertemporal energy exchanges between charging and discharging stages. By treating the LAES-LNG system as a dispatchable asset, the formulation aligns its operation with short-term market optimization problems and multi-energy coordination studies.

Building on this foundation, a day-ahead dispatch model is designed to represent the facility's simultaneous participation in LNG and electricity markets. To reflect real-world conditions, the formulation captures the sequence-aware structure of these markets, recognizing that their clearing times differ. The resulting two-stage stochastic optimization accounts for market-price and operational uncertainties, enabling the LAES-LNG facility to coordinate its bids and offers across both markets while maintaining technical feasibility. This approach introduces a practical short-term LNG trading representation into power system studies, addressing a gap that has persisted in the existing literature.

Finally, the long-term economic viability of the LAES-LNG concept is evaluated through a probabilistic feasibility analysis centered on the *payback period*. In contrast to earlier deterministic assessments, this analysis incorporates uncertainties in both investment cost and annual profit, reflecting market volatility and financial variability. The stochastic framework thus provides a more realistic and transparent measure of the facility's financial performance and deployment potential, marking the first probabilistic payback-period analysis conducted for a thermo-mechanical storage system under uncertainty.

Collectively, these efforts deliver a coherent and implementable response to *Research Question 2*, establishing a sequence-aware market framework and a probabilistic evaluation approach for the LAES-LNG facility. As a result of constructing this model, the research introduces the following contribution:

- **H. Khaloie** and F. Vallée, "Day-Ahead Dispatch of Liquid Air Energy Storage Coupled With LNG Regasification in Electricity and LNG Markets," *IEEE Transactions on Power Systems*, vol. 39, no. 3, pp. 5177–5190, May 2024.

1.3.3 On a Strategic Dispatch of Hybrid CAES-LAES Systems

While moving forward to address *Research Question 3*, we put forth a strategic, look-ahead dispatch framework for a hybrid CAES-LAES system. The study advances beyond design-oriented analyses by formulating an operational model that integrates technical coordination and strategic decision-making within day-ahead electricity markets. The hybrid facility is modeled as a unified price-making entity capable of influencing market-clearing outcomes through coordinated bids and offers from its CAES and LAES subsystems.

The first step establishes a detailed mathematical representation of the hybrid plant, capturing its internal energy exchanges and conversion pathways between compressed air and cryogenic forms. This formulation enables

coordinated operation that combines the cost advantage of LAES with the higher efficiency of CAES, creating a scalable and geographically unconstrained long-duration storage solution. By explicitly modeling shared components and conversion machinery, the framework links thermo-mechanical interactions with market-driven dispatch decisions.

Building upon this foundation, a strategic market dispatch model is formulated in which the hybrid plant acts as a leader in a *bi-level* Stackelberg game, anticipating market responses to its decisions. This look-ahead structure allows the facility to evaluate the impact of different forecasting horizons on system-wide economic indicators, including producer profits and consumer welfare. The formulation departs from conventional price-taking assumptions, offering a realistic representation of how large storage assets may strategically shape electricity market outcomes to their benefit.

To address the computational complexity of the *bi-level* problem, a learning-assisted optimization scheme is introduced. A deep learning model generates high-quality initial solutions for the mixed-integer variables of the market-clearing problem, effectively warm-starting the solver and accelerating convergence. This integration substantially improves scalability, allowing the model to be applied to larger test systems while maintaining numerical precision. The learning framework builds on a comprehensive review of machine learning applications in Optimal Power Flow (OPF), which informs the methodological integration of learning-based initialization within power system optimization.

Together, these developments provide a coherent and scalable response to *Research Question 3*, establishing a Stackelberg-based strategic dispatch model for hybrid CAES-LAES systems enhanced with deep learning techniques for computational efficiency. The development of this framework and its supporting methodological review have resulted in the following contributions:

- **H. Khaloie**, A. Stankovski, B. Gjorgiev, G. Sansavini, and F. Vallée, "Hybrid Energy Storage Dispatch: A Bi-Level Look-Ahead Learning-Assisted Model," *IEEE Transactions on Energy Markets, Policy and Regulation*, vol. 3, no. 3, pp. 376–392, Sept. 2025.

- **H. Khaloie**, M. Dolányi, J.-F. Toubeau, and F. Vallée, "Review of Machine Learning Techniques for Optimal Power Flow," *Applied Energy*, vol. 388, p. 125637, 2025.

1.4. Thesis Organization

This thesis is organized as follows.

1. **Chapter 2** reviews the roles and applications of energy storage, introduces a taxonomy of storage technologies, and discusses their participation in wholesale electricity markets, with emphasis on large-scale technologies relevant to this thesis.

2. **Chapter 3** presents the optimization foundations, including deterministic and stochastic formulations, multi-level models, optimality conditions, and mathematical programs with equilibrium constraints, together with a short overview of machine learning techniques for large-scale optimization.

3. **Chapter 4** develops a market dispatch framework for grid-scale lithium-ion batteries, compares risk-neutral and SSD-constrained bidding models in day-ahead and intraday markets, and evaluates the impact of risk attitudes and benchmark selection on profits and regret.

4. **Chapter 5** investigates an integrated LAES-LNG system, formulates a two-stage stochastic day-ahead dispatch model for electricity and LNG markets, and assesses economic feasibility through a probabilistic payback period under price and demand uncertainty.

5. **Chapter 6** studies the strategic look-ahead dispatch of a hybrid CAES-LAES plant, proposes a *bi-level* market model cast as a mixed-integer Mathematical Program with Equilibrium Constraints (MPEC), and introduces a learning-assisted solution approach that is tested on transmission networks of different sizes.

6. **Chapter 7** concludes the thesis by synthesizing the main findings, relating them to the initial research questions, and outlining prospects and directions for future research on bulk storage in liberalized energy markets.

CHAPTER 2

Energy Storage: Technologies, Applications, and Market Participation

This chapter reviews the roles of energy storage in modern power systems, classifies the main technology families, compares their suitability across applications, and provides focused capsules on lithium-ion batteries, LAES, and CAES. It then introduces the principal wholesale electricity markets in which bulk storage participates and frames energy arbitrage as the dominant revenue stream considered in this thesis. The chapter closes by linking technical capabilities with market needs to motivate the modeling work in Chapters 4–6.

2.1. Energy Storage: Roles and Applications

Although energy storage has been a well-known concept for many decades, its significance has surged in recent years, largely attributed to the widespread integration of renewables into power systems. The increasing penetration of renewable energy sources has introduced challenges related to voltage and frequency quality, system reliability, and power system security. While power systems can function adequately without energy storage, cost-effective energy storage solutions have the potential to enhance network efficiency and reliability, leading to reduced transmission losses. This shift in perspective transforms electricity from a just-in-time commodity to a time-adjustable resource. Furthermore, certain storage technologies offer rapid implementation compared to conventional grid upgrades. Given the current trend of decentralized and fluctuating electricity production, energy storage can play a pivotal role in enhancing generation, transmission, and distribution systems.

The relevance of energy storage can be assessed from both technical and

Table 2.1: Representative power system challenges and indicative storage responses across timescales.

Timescale	**Typical Challenge**	**Potential Storage Response**
Seconds	Power quality and harmonics from variable renewable output	Fast-response, low-capacity storage integrated with generation or transmission assets
Minutes	Rapid changes in wind or solar generation affecting frequency	Medium-scale storage systems providing short-term balancing or frequency support
Hours	Daily demand peaks and electric vehicle charging	High-power bulk storage to meet short-term demand peaks or distributed storage at building level
Hours–Days	Variability of renewable supply and weekly demand fluctuation	Large-scale or decentralized storage to back up renewables and community-level heat storage
Months	Seasonal variation in heat and electricity demand	Long-duration or inter-seasonal heat storage coupled with combined heat and power systems

Note: This table is adapted from [77].

temporal perspectives. Different operational timescales in the grid correspond to specific challenges that require different storage characteristics. Table 2.1 summarizes representative challenges across timescales and illustrates possible storage responses. As shown, fast-response storage is required to maintain power quality and frequency stability on the second-to-minute scale, while bulk storage with longer discharge duration becomes critical for daily or seasonal balancing. Although storage represents a highly versatile solution, it should be considered as part of a broader flexibility portfolio that also includes interconnections, dispatchable generation, and demand-side response [77].

In general, the key factors driving the popularity of energy storage installations include fast charging and discharging times, timely energy provision, and quick installation, giving them an advantage over conventional technologies. However, less favorable aspects of energy storage include high costs, self-discharge, and varying energy densities. Various types of energy storage technologies are under development, with some available commercially and others still in the developmental stage.

The *specific energy* and *specific power*, referring to the energy and power

available per unit weight, respectively, are crucial considerations for certain applications of energy storage, as they directly impact the efficiency, performance, and feasibility of energy storage solutions in meeting diverse operational requirements and constraints. Particularly, *specific energy* denotes the amount of energy stored per unit mass, while *specific power* represents the rate at which energy can be extracted or delivered per unit mass of the storage. Therefore, based on the energy and power ratio, ESSs are commonly classified into energy-type and power-type facilities. Energy-type storage typically offers high energy density but shorter life cycles, encompassing technologies like chemical energy storage and CAES. On the other hand, power-type storage boasts high power density, longer life cycles, and high-rate charge and discharge capabilities, exemplified by electromagnetic and flywheel energy storage.

ESSs offer numerous benefits to power system networks. When considering their applications, they can be categorized based on their ability to fulfill specific functions, as summarized in Table 2.2. While historically, most ESSs targeted bulk or centralized storage for relatively long durations (e.g., pumped hydroelectric storage) or rapid response (e.g., flywheels), there is a growing argument for decentralized or distributed storage embedded within distribution networks or integrated into building electrical systems.

Among the various applications outlined in Table 2.2, energy arbitrage and renewable energy time shifting are the primary contributors to energy storage profitability and widespread deployment in power systems. Additionally, ESSs can generate significant profits by providing voltage regulation and frequency regulation services [78].

2.2. Taxonomy of Energy Storage Technologies

As discussed in the previous section, ESSs serve a wide range of functions across various temporal and operational scales in power systems. These diverse roles are enabled by the existence of multiple storage technologies, each relying on distinct physical principles to store and release energy. To better understand their operational characteristics and potential integration into the energy system, it is essential to classify storage technologies according to the form of energy in which they store electricity. This section provides a taxonomy of ESSs based on their underlying conversion processes and highlights representative technologies within each category.

Electricity, although one of the most versatile and easily transmitted en-

Table 2.2: Energy and power applications of energy storage.

Energy Applications	Power Applications
Energy arbitrage	Frequency regulation
Renewable energy time shift	Voltage support
Demand charge reduction	Small signal stability
Time-of-use charge reduction	Frequency droop
T&D* upgrade deferral	Synthetic inertia
Grid resiliency	Renewable capacity firming

T&D*: Transmission and Distribution. *Note:* This table is taken from [79].

ergy carriers, remains difficult to store directly in large quantities. Therefore, electrical energy is typically converted into another form, mechanical, chemical, thermal, or hybrid, before being stored. The stored energy can later be reconverted into electricity as required [80]. Based on the form of energy stored and the nature of the conversion mechanism, storage technologies can be broadly classified as follows. While individual storage classes are often presented separately, certain technologies combine multiple conversion mechanisms. For instance, thermo-mechanical systems merge both mechanical compression/-expansion and thermal management, bridging the boundary between purely mechanical and thermal categories. The following taxonomy therefore progresses from single-principle technologies to hybrid systems that integrate two or more energy forms.

2.2.1 Mechanical Energy Storage

Mechanical storage systems, such as pumped hydroelectric storage and flywheels, store energy in the form of potential or kinetic energy. This is among the oldest and most mature classes of energy storage. Pumped hydroelectric storage operates by transferring water between two reservoirs at different elevations, converting excess electricity into gravitational potential energy. When electricity is needed, water is released through turbines to generate power. Despite its high round-trip efficiency and capability to provide large-scale, long-duration storage, its implementation is restricted to locations with suitable topographical conditions. Flywheel systems, on the other hand, store kinetic energy in a

rotating mass accelerated by an electric motor. They offer rapid response and high cycle efficiency, making them suitable for power-quality enhancement and frequency-regulation applications [81].

2.2.2 Electrochemical Energy Storage

Electrochemical systems store energy in chemical bonds and retrieve it through reversible redox reactions. Batteries are the most prominent representatives of this class, including lead–acid, sodium-sulfur, lithium-ion, nickel-cadmium, and flow battery technologies. Lithium-ion batteries, in particular, have achieved dominant market penetration due to their high energy density, efficiency, and scalability, representing more than 85% of new energy storage deployments as of 2016 [82]. Flow batteries, which store energy in liquid electrolytes circulated through electrochemical cells, provide flexible energy-power decoupling and long cycle life, making them promising for medium- to large-scale applications.

2.2.3 Electrical Energy Storage

Electrical energy storage encompasses technologies that store energy directly in electric or magnetic fields. This category includes capacitors, supercapacitors, and superconducting magnetic ESSs [80, 83]. Capacitors are suitable for supplying short bursts of power and are commonly used in power electronics for voltage smoothing. Supercapacitors extend this principle by offering higher capacitance in compact form, enabling very fast charge-discharge cycles and long operational lifetimes. Superconducting magnetic ESSs, which store energy in the magnetic field generated by a superconducting coil, offer extremely fast response times and high efficiency, making them suitable for transient stability and frequency control applications [84]. However, their high cost and cryogenic requirements have limited their large-scale deployment.

2.2.4 Chemical Energy Storage

Chemical storage technologies store energy within molecular compounds that can be later transformed into mechanical, thermal, or electrical energy. The most prominent example is hydrogen-based storage, where excess electricity is converted into hydrogen through electrolysis and subsequently used in fuel cells or combustion processes [83, 85]. Other chemical carriers, such as ammonia and synthetic methane, can also serve as long-term storage media and enable

sector coupling between electricity, heat, and transport. Although hydrogen is a promising clean energy vector, its large-scale adoption is currently constrained by the lack of infrastructure, high production costs, safety considerations, and the energy intensity of conversion processes.

2.2.5 Thermal Energy Storage

Thermal ESSs accumulate energy in the form of heat or cold for later use in power generation or heating and cooling applications. These systems are classified into sensible, latent, and thermochemical storage types [83]. Sensible heat storage involves raising the temperature of a medium such as water or rocks without phase change. Latent heat storage stores energy during phase transitions, for instance through melting or solidification of phase-change materials. Thermochemical storage, in contrast, relies on reversible chemical reactions or sorption processes to store heat at high density and for extended periods. Thermal ESSs are widely deployed in concentrated solar power plants [86] and solar tower facilities [87], where stored heat enables dispatchable electricity generation after sunset.

2.2.6 Thermo-Mechanical Energy Storage

This category serves as a hybrid between the mechanical and thermal families, using both compression/expansion work and heat management to maximize efficiency [88]. Prominent examples include CAES, LAES, and pumped thermal energy storage. CAES uses off-peak electricity to compress air and store it in underground caverns or high-pressure vessels. During discharge, the air is heated (either using stored thermal energy or fuel combustion) and expanded through turbines to produce electricity. LAES follows a similar principle but stores energy in the form of liquefied air at cryogenic temperatures, which vaporizes and expands through turbines during discharge. Pumped thermal energy storage, on the other hand, converts electricity into heat using a heat pump, stores it in thermal reservoirs, and reconverts it to electricity through a heat engine when needed. These hybrid systems offer long-duration storage and potential scalability for large-scale grid integration.

In summary, the taxonomy of energy storage technologies demonstrates the diversity of physical principles available for storing electricity in alternative forms. Each category exhibits distinct trade-offs among efficiency, scalability, energy density, and discharge duration. Understanding these differences is

fundamental to assessing their suitability for different system-level applications, which will be analyzed in the following section.

2.3. Suitability of Energy Storage Technologies Across Different Applications

The preceding section illustrated the wide array of technologies available for storing electrical energy, each addressing specific operational requirements within power systems. These technologies not only facilitate the integration of intermittent renewable sources but also serve functions such as energy arbitrage, capacity reserves, uninterrupted power supply, and bulk energy management. Their suitability depends on intrinsic parameters including energy and power density, charge-discharge rate, round-trip efficiency, cycle life, and overall cost-effectiveness [80, 89, 90].

An ideal ESS would be cost-effective, highly efficient, energy- and power-dense, long-lived, and environmentally benign. No single technology, however, satisfies all these attributes simultaneously; consequently, the choice of storage system remains application-dependent. Historically, long-duration storage was almost exclusively provided by large-scale pumped hydroelectric and CAES facilities, both offering mature solutions for multi-hour operation. Recent advances, however, are expanding this domain toward emerging concepts such as LAES, pumped thermal, and hydrogen-based storage, which promise comparable capacity with fewer geographical constraints. At the same time, short-duration and fast-response technologies, including flywheels and supercapacitors, continue to play an essential role in power-quality and ancillary service applications.

Table 2.3 summarizes key cost and performance indicators across major storage technologies, while Figure 2.1 maps these technologies in relation to grid-scale applications. The figure compares discharge duration and power rating, illustrating where each technology family provides the most technical and economic value. The horizontal range of each bar denotes achievable power capacity, while the vertical span represents discharge duration at rated power. This mapping not only delineates current commercial use cases but also indicates potential future deployment windows. Although not all technologies are currently available across the full indicated ranges, their scalability and continuous cost reductions suggest expanding future applicability.

ESSs with high energy capacity, such as pumped hydroelectric and CAES,

can mitigate diurnal supply fluctuations by storing surplus wind or solar energy for later use, thereby extending renewable output beyond daylight hours. Nevertheless, these mature solutions remain constrained by geographical and geological limitations. Conversely, technologies such as LAES and pumped thermal storage exhibit lower siting dependence but require further development to achieve comparable efficiency and cost competitiveness.

Taken together, Figure 2.1 and Table 2.3 illustrate that the practical suitability of a storage technology depends on discharge duration, power rating, efficiency, lifetime, and siting constraints rather than on any single performance metric. The following observations can be derived.

1. **Short-to-medium duration services:** Technologies providing seconds-to-minutes discharge times and high ramp rates, such as flywheels, supercapacitors, and several battery chemistries, are well suited for high-power and rapid-response applications, including frequency regulation, synthetic inertia, and power-quality support. These technologies exhibit high round-trip efficiencies and operational flexibility across a broad range of power ratings and are commercially mature for both grid-connected and behind-the-meter applications [92].

2. **Bulk, multi-hour storage:** Pumped hydro remains the most established solution for multi-hour to day-scale storage. Emerging or early-commercial technologies, including CAES, LAES, and pumped thermal energy storage, expand this operational domain with lower siting constraints and increasing efficiency potential. Among these, pumped hydro and underground CAES are characterized by relatively modest levelized costs but are limited by geographical dependence, while LAES and pumped thermal technologies remain under active demonstration and investment [21]. Hydrogen fuel cells, though offering very long-duration potential, face conversion inefficiencies and infrastructure requirements.

3. **Very long-duration and seasonal storage:** Storage on the order of days to months, requiring GWh–TWh-scale capacities, remains largely undeployed. Addressing these inter-seasonal energy imbalances calls for advances in thermo-mechanical and chemical storage pathways, such as large-scale pumped thermal, LAES clusters, and hydrogen or ammonia-based energy carriers.

Table 2.3: Comparative overview of energy storage technologies.

Technology	Typical Capacity (MW)	Nominal Duration	Cycle Efficiency (%)	Typical Lifetime (yr)	Technology Maturity	Site Constraint	CAPEX ($/kW; $/kWh)
Pumped Hydroelectric Storage	30–5000	Hours–days	70–87	30–60	Commercial	Yes	2,000-4,300; 5-100
Compressed Air Energy Storage	0.5–320	Hours–days	42–70	20–40	Commercial	Yes	400-1000; 2-120
Liquid Air Energy Storage	1–300	Hours–days	45–70	20–40^{+}	Early Commercial	No	900-6,000; 240-640
Pumped Thermal Energy Storage	10–150	Hours–days	48–75^{+}	25–30	Developing	No	1,900-3,300; 190-330
Flywheel	0.4–20	1–15 min	80–95	15–20	Commercial	No	250-350; 1,000-5,000
Hydrogen Fuel Cell	0.1–50	Seconds–days	20–85	5–20	Early Commercial	No	500-10,000; –
Flow Battery	0.03–200	Seconds–10 h	65–85	5–30^{+}	Commercial	No	600-1,500; 150-1,000
Lithium-ion Battery	1–100	0.15–4 h	75–90	5–15	Commercial	No	1,200-4,000; 600-2,500
Metal-air Battery	0.01–50	Seconds–5 h	∼75	(100–10k cycles)	Demonstration	No	1,750-1,900; 10-60
Sodium-Sulfur Battery	0.05–34	Seconds–8 h	75–90	5–15	Commercial	No	1,000-3,000; 300-500
Nickel Battery	0–40	Seconds–hours	60–90	10–20	Commercial	No	500-1,500; 800-1,500
Lead-Acid Battery	0–40	Seconds–10 h	63–90	5–20	Commercial	No	300-600; 150-500
Supercapacitor	0–10	Milliseconds–1 h	75–98	8–20^{+}	Commercial	No	100-300; 300-2,000

Note: The data in this table are collected from [21, 50, 77, 80, 91].

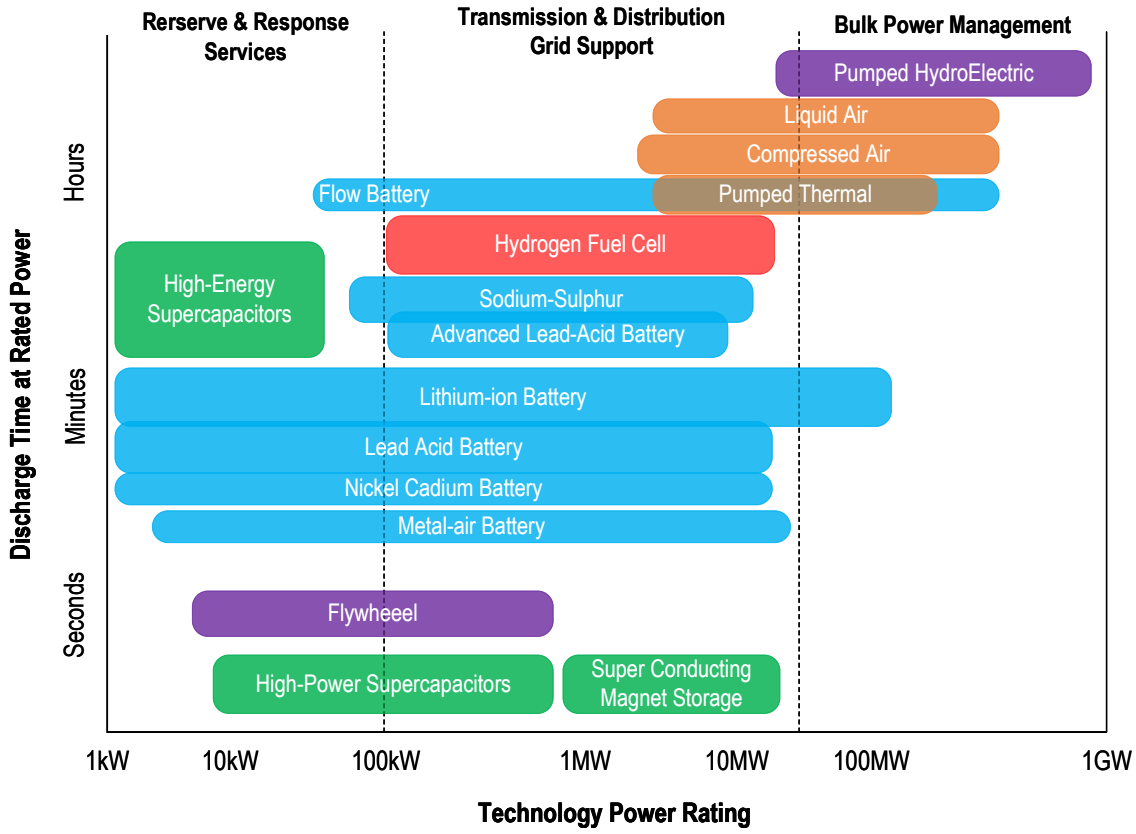

Figure 2.1: Suitability of energy storage technologies across applications: discharge time versus rated power with indicative application zones.

Note: This figure is adapted from [80, 89, 90]. Each block denotes a technology family (Purple: Mechanical; Red: Chemical; Orange: Thermo-mechanical; Blue: Electrochemical; Green: Electrical).

2.4. Technology Capsules

The preceding sections provided a taxonomy and comparative evaluation of major energy storage families. This section narrows the focus to three technologies of particular relevance to this thesis, i.e., lithium-ion batteries, LAES, and CAES. These technologies represent complementary segments of the storage spectrum, spanning short- to long-duration operation and covering both mature and emerging solutions. The following subsections outline their physical principles, technical features, and market relevance, emphasizing parameters that influence their dispatch modeling in later chapters.

2.4.1 Lithium-Ion Batteries

Lithium-ion batteries have become the dominant electrochemical storage technology for both stationary and mobile applications. Their rapid rise stems from significant cost declines, high round-trip efficiency (typically 90–95%), and superior energy and power density compared with other battery chemistries [93]. A lithium-ion cell consists of a graphite anode, a lithium-metal-oxide cathode (commonly $LiCoO_2$, $LiFePO_4$, or $LiNiMnCoO_2$), and a liquid or polymer electrolyte allowing lithium-ion transport during charge and discharge cycles. During charging, lithium ions migrate from the cathode to the anode through the electrolyte, while electrons flow through the external circuit; the reverse occurs during discharge [94]. Figure 2.2 illustrates the internal configuration and operating principle of a typical lithium-ion cell. It shows the graphite anode, lithium-metal-oxide cathode, electrolyte, and separator, together with the direction of lithium-ion movement during charging and discharging. The external circuit allows electron flow opposite to the ionic motion inside the cell, thereby completing the electrochemical cycle and enabling reversible energy conversion.

Grid-scale lithium-ion systems are typically deployed as modular racks integrated with power-conversion systems and battery management units that maintain cell balancing, temperature control, and safety [94]. They are well-suited for frequency regulation, synthetic inertia, and ramp-rate control [94]. When configured for multi-hour discharge, lithium-ion installations also participate in energy arbitrage and renewable time-shifting [21]. Nevertheless, degradation mechanisms such as solid-electrolyte-interface growth and lithium plating cause gradual capacity fade, limiting economic lifetime to approximately

5–15 years or 4,000–10,000 cycles depending on depth-of-discharge and thermal conditions [95].

For real-time balancing, lithium-ion batteries provide very fast response and ramping, as grid-scale systems typically interface with the grid through power-electronic converters. As a result, the dominant operational time constant is the converter and control response, which is in the sub-second range. Reported frequency-regulation battery energy storage deployments indicate a nearly vertical power response, with ramping to full output in well under 200 ms, and the ability to respond to regulation needs within milliseconds [96]. Accordingly, lithium-ion batteries are technically well-suited for fast balancing products, provided that state-of-charge and thermal limits remain available for sustained activation.

Despite these drawbacks, continuous improvements in electrode materials and recycling processes are reducing environmental impacts and extending lifespans [97]. Global average battery pack costs have declined from above 1000 \$/kWh in 2010 to below 150 \$/kWh in 2023 [98]. Consequently, lithium-ion systems dominate new stationary storage capacity additions, particularly in fast-responding markets such as California, the United Kingdom, and Australia. Their role in this thesis is to represent the benchmark short-duration, high-efficiency storage technology for market-based operation under stochastic conditions.

2.4.2 LAES (Liquid Air Energy Storage)

LAES is a thermo-mechanical technology that stores electricity by liquefying ambient air and recovering its stored exergy during re-gasification and expansion. It is considered a promising long-duration storage solution due to its scalability, siting flexibility, and compatibility with industrial waste heat or cold sources. An LAES facility consists of three main subsystems: charging, storage, and discharging. Figure 2.3 depicts a typical layout.

During the charging stage, grid electricity drives multi-stage compressors that pressurize ambient air before delivering it to the liquefaction unit. The air is cooled through a series of heat exchangers until it reaches cryogenic temperatures of approximately $-196°C$, after which it is stored in atmospheric liquid air (cryogenic) tanks. The storage subsystem keeps the liquid air at low pressure and near-boiling temperature, enabling multi-hour to daily-scale energy retention.

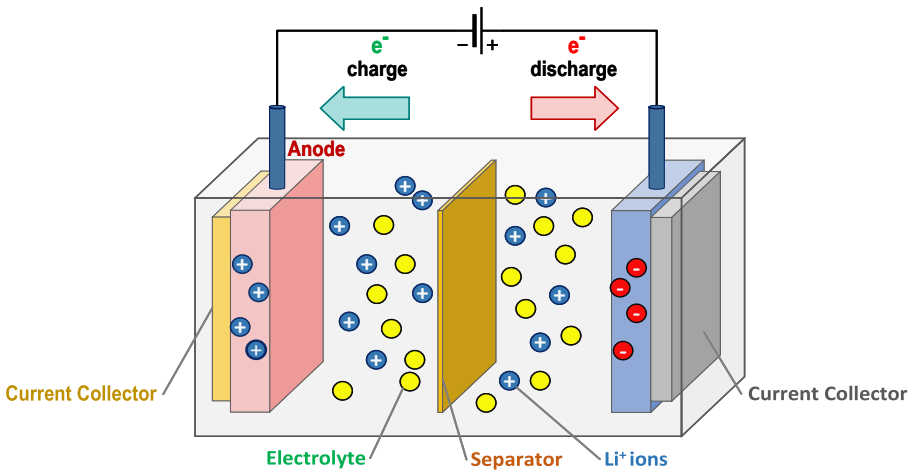

Figure 2.2: Schematic structure of a lithium-ion cell showing its main components and charge-discharge process.

Note: This figure is taken from [99].

The discharge subsystem reverses the process. A cryogenic pump first raises the pressure of the stored liquid air with minimal energy input due to the low fluid temperature. The high-pressure liquid then passes through an evaporator, where it absorbs heat and returns to the gaseous state. The gaseous air subsequently expands through one or multiple turbine stages to generate electricity. Throughout this process, the compression heat from charging and the cold energy released during evaporation are stored in dedicated thermal reservoirs. These thermal stores improve the round-trip efficiency by preheating or pre-cooling the working fluid as needed. Even with this heat and cold recovery, the round-trip efficiency of standalone LAES systems typically ranges between 45% and 55%, which is lower than that of many electrochemical systems. This has driven increasing interest in hybrid concepts that integrate LAES with external heat or cold sources such as LNG regasification terminals, industrial waste heat streams, or cryogenic processes [57, 52, 49], with the LAES-LNG configuration addressed in detail in Chapter 5.

Beyond energy and efficiency characteristics, the dynamic performance and response time of LAES are strongly influenced by the underlying thermomechanical plant configuration and operating mode. Vendor-reported characteristics indicate that, in a standard operating mode, an LAES plant can deliver power to the grid within less than 5 minutes with an indicative ramp rate of

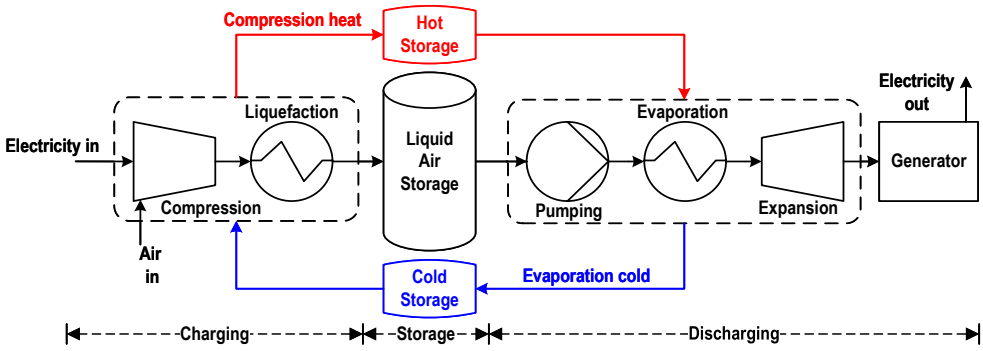

Figure 2.3: Schematic layout of an LAES facility.

about 20% P^{nominal}/min [100]. If operated in a spinning/standby configuration, power delivery within less than 30 seconds and ramping of about 5% P^{nominal}/s have been reported, which can support slower real-time services when the plant is maintained in a high-readiness state [100].

The development of LAES may be broken down into a number of turning points along the way. The origin of storing energy via liquid air can be traced back to 1977 [101], but it was not until years later that Mitsubishi Heavy Industries conducted practical research into the notion [102]. With an eye to storing electricity through liquid air, the University of Birmingham is home to the first LAES pilot facility, developed between 2009-2012, with power and energy storage capacities of 350 kW and 2.5 MWh, respectively. In 2018, a 5 MW/15 MWh demonstration-scale LAES facility was launched in Manchester, leading to the first commercial 50 MW/300 MWh LAES project set for grid connection in Northern England during 2023-2024 [50, 103]. The project is being developed by Highview Power, a UK-based company that specializes in cryogenic energy storage facilities [103]. Highview Power is currently at the forefront of commercial LAES projects worldwide, leading the way in their implementation. The company has an extensive portfolio of LAES projects under development across the globe, including a 200 MW/2.5 GWh facility in Yorkshire [103], UK, a 50 MW/400 MWh facility in Vermont, USA [104], seven 50 MW/300 MWh facilities in Spain [104], and a 50 MW/600 MWh facility in Chile [105].

From the perspective of this thesis, LAES serves as a representative thermo-mechanical long-duration storage technology that offers high energy capacity and minimal siting restrictions. Its ability to exploit external heat or cold

sources makes it suitable for sector-coupled configurations, including LNG terminals and industrial clusters. This flexibility, combined with its multi-hour discharge capability, positions LAES as a strong candidate for future bulk storage services and motivates its detailed market-oriented modeling in subsequent chapters.

2.4.3 CAES (Compressed Air Energy Storage)

CAES is a thermo-mechanical storage technology that converts electrical energy into compressed air during charging and recovers it through expansion turbines during discharge [106]. CAES systems rely on the thermodynamic advantages of storing energy in pressurized air reservoirs and using staged compression and expansion processes to increase the efficiency and flexibility of power system operations. Figure 2.4 illustrates the general configuration of an above-ground CAES facility, showing the charging and discharging subsystems together with the compressed air storage tanks.

During the charging stage, grid electricity powers multi-stage compressors that elevate the pressure of ambient air. The compressed air is then cooled in intercoolers and directed into a storage reservoir. In classical CAES systems, compression heat is rejected to the environment, although advanced concepts store this heat for later use. The discharged energy is recovered by reversing the process. High-pressure air exits the reservoir and passes through recuperators and a combustor before expanding through turbine stages that drive an electrical generator. The combustion process is used to reheat the air to prevent excessive cooling during expansion, thereby enhancing the specific work output. The discharging subsystem in Figure 2.4 shows these major components, including the combustor, expansion block, and generator. Although this configuration relies on supplementary natural gas, research continues toward adiabatic CAES systems that capture and reuse compression heat to avoid fuel consumption [106, 107].

CAES dynamics are governed by turbo-machinery and plant-level operating procedures. Reported operating characteristics indicate that the McIntosh CAES plant can ramp at approximately 18 MW/min, which corresponds to about 16% P^{nominal}/min for a 110 MW unit [108]. Mode transitions can also be limiting: the same reference reports that the Huntorf CAES plant requires a minimum of about 20 minutes to switch between compression and generation modes, during which the plant neither generates nor compresses [108]. These

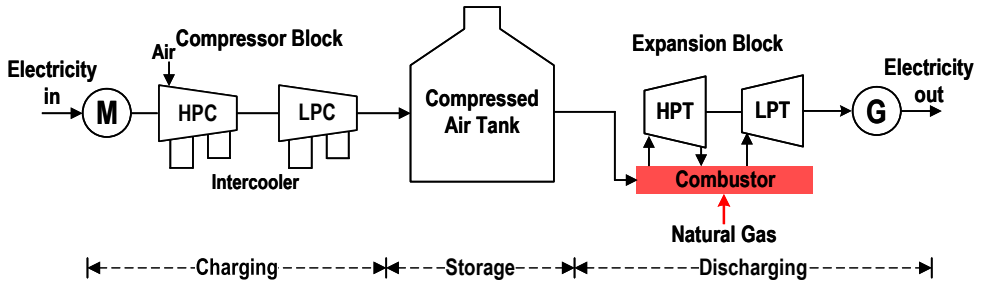

Figure 2.4: Schematic layout of an above-ground CAES facility.

time constants suggest that CAES is generally better aligned with slower reserve products than with sub-minute regulation, unless additional design measures are adopted.

CAES plants can be categorized into two distinct forms based on the type of air storage:

(i) Underground cavern-based CAES: Historically, commercial CAES has relied on large underground caverns, such as salt domes or aquifers, that provide sufficient volume at relatively low cost. These caverns can support multi-hour energy storage at the scale of hundreds of megawatts. The Huntorf plant in Germany, commissioned in 1978, was the first commercial CAES facility and remains operational with a rated capacity of 290 MW and discharge duration of up to two hours [109, 110, 111]. The McIntosh plant in Alabama, USA, commissioned in 1991, offers 110 MW of power and uses a diabatic configuration with natural gas combustion [112, 113]. These plants demonstrate the long-term technical viability and durability of cavern-based CAES systems.

(ii) Above-ground high-pressure tank CAES: More recent developments aim to eliminate geological restrictions by using engineered above-ground pressure vessels or modular high-pressure tanks. These systems are more flexible in siting and can be deployed in regions without suitable caverns. Although they typically store less energy than cavern-based installations, they offer faster deployment and potential scalability for distributed or urban applications. Figure 2.4 represents this above-ground configuration, where compressed air is stored in engineered tanks rather than geological formations. Ongoing research focuses on optimizing tank design, thermal management, and integration with renewable energy sources [106, 114].

Beyond these two variants, several advanced concepts aim to improve round-

trip efficiency by recovering compression heat. Adiabatic CAES systems store the heat generated during compression and re-inject it before expansion, potentially increasing efficiency to 70% or higher. Hybrid CAES systems incorporate thermal storage, renewable heating sources, or waste heat from industrial processes, expanding the range of possible applications. These advanced designs remain under active research and require further demonstration before large-scale commercial deployment.

From the perspective of this thesis, both underground and above-ground CAES are promising long-duration storage options. Cavern-based systems can store large amounts of energy but require suitable geological formations, while above-ground configurations offer full siting flexibility at the cost of more limited storage volume. This thesis focuses on the above-ground variant and investigates how its storage limitation can be mitigated through hybridization with liquid air tanks, which will be detailed in Chapter 6.

2.5. Energy Storage in Wholesale Electricity Markets

The large-scale deployment of energy storage in electric grids ultimately depends on its investment appeal. Storage technologies will only be integrated at scale if they offer sufficiently attractive and predictable revenue streams to investors. In liberalized power systems, these revenues arise from the participation of storage units in electricity markets, where they can trade energy and, in some cases, system services. The remainder of this section introduces the main market layers relevant for bulk storage participation, the logic of storage bidding behavior, and the arbitrage focus adopted in this thesis.

2.5.1 Market Layers

Within any power system, energy storage can contribute in three general domains [77]. First, it can deliver short-duration reserve or frequency-response services, which enable the system operator to maintain the instantaneous balance between production and consumption. Second, it can increase the efficiency of existing grid assets; depending on its location, storage may substitute for additional backup plants or defer reinforcement of network infrastructure. Third, it can engage in energy arbitrage by charging when electricity prices are low and discharging at higher prices. This function moderates peaks and troughs in systems with significant renewable penetration and supports more

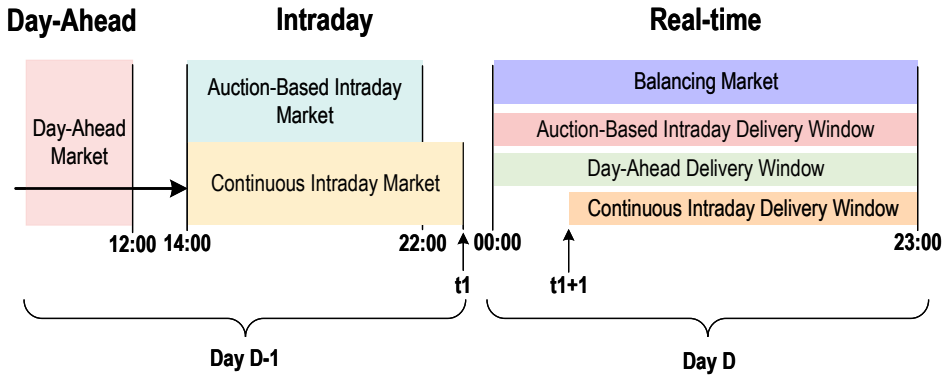

Figure 2.5: Schematic representation of short-term trading floors in coupled wholesale electricity markets: day-ahead market, auction-based intraday sessions, continuous intraday market, and balancing stage.

reliable integration of variable resources. Storage assets may be connected at different points along the power system chain, from generation buses to transmission and distribution networks, and finally to demand locations. The most suitable placement depends on the intended services and the prevailing market or regulatory framework.

Since this thesis focuses on bulk storage technologies with multi-hour discharge capability, the storage units considered here are assumed to connect at the transmission level. They therefore participate in wholesale electricity markets rather than in purely distribution-level or behind-the-meter contexts. Their main revenue streams arise from trading energy across short-term wholesale market layers.

Figure 2.5 schematically illustrates the trading floors of the coupled short-term electricity markets considered in this thesis. The sequence begins with the day-ahead market and proceeds through auction-based and continuous intraday markets, followed by real-time balancing actions. Each layer offers specific opportunities for storage to adjust its schedule and monetize its flexibility.

The day-ahead market is the first short-term trading floor. The day-ahead auction for most European bidding zones closes at 12:00 Central European Time (CET) on day $D-1$ [115]. Market participants submit hourly buy and sell orders for the whole 24-hour delivery horizon of day D. After gate closure, the nominated electricity market operator (for example, European Power Exchange (EPEX SPOT) in Central Western Europe) aggregates the

offers and bids, constructs the supply and demand curves, and clears the market by computing the equilibrium prices and accepted quantities for each delivery hour. The day-ahead results are published shortly after market closure and provide the reference schedule and price signal for the next day.

Once day-ahead results are known, participants can refine their positions in the intraday markets, which operate closer to real time. Intraday trading is organized in two main forms: auction-based sessions and a continuous intraday market.

The auction-based intraday market is currently structured into three discrete sessions with the following characteristics:

- **Session 1:** Opens at 14:00 CET on day $D-1$ and closes at 15:00 CET on day $D-1$. Results are published before 15:20 CET. The delivery horizon covers the entire next day D.
- **Session 2:** Opens at 21:00 CET on day $D-1$ and closes at 22:00 CET on day $D-1$. Results are published before 22:20 CET. The delivery horizon again covers the entire next day D. For visual clarity, Figure 2.5 represents this second auction session as the reference intraday auction.
- **Session 3:** Opens at 09:00 CET on day D and closes at 10:00 CET on day D. Results are published before 10:20 CET. The delivery horizon spans the second half of day D, from 12:00 to 23:00.

In parallel with these auctions, a continuous intraday market provides a more flexible adjustment platform. The continuous intraday market, often implemented through single intraday coupling, typically opens at 14:00 CET on day $D-1$ and remains open up to 0–1 hour before delivery, depending on the region [115]. Market participants can submit or update orders in near real time, subject to available transmission capacity between bidding zones. Compared with the intraday auctions, the continuous market exhibits two key features:

- It grants access to both local and cross-border liquidity, as participants may trade with counterparts in other European bidding zones when inter-connector capacity is available.
- It allows continuous portfolio adjustments up to one hour before physical delivery, enabling participants to manage forecast errors and operational uncertainties more dynamically than in discrete auctions.

The main objective of the continuous intraday market is to facilitate efficient cross-zonal energy trading close to real time and to improve the overall efficiency of short-term transactions across Europe.

Nominated electricity market operators operate both the day-ahead and intraday markets. To secure the final real-time balance, the transmission system operator runs the balancing market. In this market, the system operator activates upward and downward reserve products to correct residual imbalances and maintain system security [116]. Although balancing markets are essential for system operation, their detailed design and products fall outside the scope of this thesis. The modeling work in later chapters focuses on the interaction of bulk storage with the day-ahead and intraday trading floors.

2.5.2 Participation Logic

The way bulk storage assets interact with wholesale markets depends not only on the available trading floors but also on their bidding behavior. In general, the market participation of a storage unit can be framed under two alternative logics: price-taking and price-making [117].

In a *price-taking* framework, the storage operator behaves as a small market participant without significant market power. It submits offers and bids under the assumption that individual actions do not influence market-clearing prices. The storage unit observes exogenous price forecasts or historical statistics and optimizes its charging and discharging schedule accordingly. This representation is appropriate for most current storage installations, which typically account for a small share of total system capacity. From a market-clearing perspective, price-taking behavior is consistent with submitting quantities at prices close to marginal cost (or marginal willingness-to-pay), so that the bid lies below the expected clearing price when the unit intends to be dispatched. As illustrated in Fig. 2.6a, when a producer submits an offer at a marginal cost lower than the market-clearing price, the offer is accepted and the cleared quantity is remunerated at the uniform market-clearing price.

In a *price-making* or *strategic* framework, the storage operator recognizes that its bids and offers can influence market-clearing outcomes. The participant embeds the market-clearing mechanism in its decision problem and selects bid quantities and prices to steer the market-clearing price to more favorable levels. When implemented effectively, such strategic bidding can increase profits compared with purely price-taking behavior, especially for large-scale storage

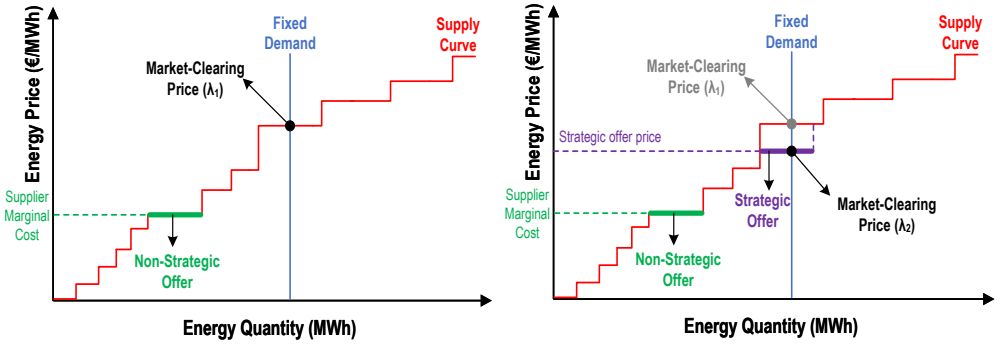

(a) Price-taking participation.

(b) Price-making participation.

Figure 2.6: Market-perspective illustration of price-taking and price-making participation in a uniform-price market.

plants in concentrated markets. However, it also requires more detailed modeling of market coupling and of the reactions of other participants. Fig. 2.6b illustrates this logic: by submitting a quantity at a strategic price, the participant shifts the effective supply curve and thereby displaces the market equilibrium. Depending on whether the participant is predominantly selling or buying, this mechanism can be used to move the clearing price upward or downward; in the illustrated example, the equilibrium is shifted downward, which increases the participant's cleared share while reducing the market-clearing price.

In this thesis, both logics are considered, but in different contexts. The bidding models developed in Chapter 4 for grid-scale lithium-ion batteries and in Chapter 5 for bulk thermo-mechanical storage (including LAES and LAES-LNG configurations) adopt a price-taking perspective. Storage units in these chapters are modeled as market followers that respond optimally to given price trajectories in day-ahead and, where relevant, intraday markets.

Chapter 6 extends the analysis to *price-making* strategic bidding for a hybrid CAES-LAES facility. In this setting, the hybrid storage plant is treated as a large actor that can influence market prices. A look-ahead market dispatch framework is developed to capture the feedback between the plant's bids, the market-clearing process, and subsequent price evolution. This contrast between price-taking and price-making formulations clarifies how the same physical storage technologies may require different decision-making models depending on their system impact and market share.

2.5.3 Arbitrage Framing

Against the backdrop of the market layers and participation logic described above, this thesis concentrates on the energy arbitrage potential of bulk storage facilities in wholesale markets. The core focus is on how large-scale storage can exploit temporal price differences in day-ahead and intraday markets, subject to realistic technical and operational constraints.

For short-duration electrochemical storage, Chapter 4 develops a bidding strategy for a grid-scale lithium-ion battery that jointly considers energy arbitrage in the day-ahead and intraday markets. The model captures the interaction between day-ahead scheduling and subsequent intraday adjustments, while accounting for state-of-charge dynamics and degradation-related constraints.

For emerging thermo-mechanical technologies, the dispatch formulations are centered on day-ahead energy arbitrage. Chapter 5 formulates a day-ahead market participation model for a standalone LAES plant and then extends it to an advanced LAES facility coupled with an LNG regasification terminal. In the latter case, the arbitrage problem spans both the day-ahead electricity market and the day-ahead LNG market, reflecting the sector-coupled nature of the hybrid configuration.

Chapter 6 finally considers a hybrid CAES-LAES facility that participates in the day-ahead electricity market under a strategic price-making regime with look-ahead constraints. Although additional revenue streams such as reserve provision and balancing services are briefly discussed where relevant, they are not explicitly modeled. Throughout the thesis, bulk storage is therefore analyzed primarily through the lens of energy arbitrage in wholesale markets, while other services remain outside the main scope of the quantitative models.

2.6. Chapter Conclusion

This chapter reviewed the technological foundations and operational roles of energy storage in modern power systems. It outlined the growing need for storage due to increased renewable penetration and described how different technologies address challenges across multiple timescales. The taxonomy of mechanical, electrochemical, electrical, chemical, thermal, and thermo-mechanical options highlighted that each technology offers distinct advantages and limitations. Their suitability depends on efficiency, discharge duration, power rating, lifetime, and siting constraints rather than on any single performance metric.

Within this broad landscape, the chapter focused on lithium-ion batteries, LAES, and CAES. These three technologies represent complementary segments of the storage spectrum and are central to the modeling work that follows. Lithium-ion batteries provide rapid-response, short-duration services and serve as the benchmark mature technology. CAES and LAES represent, respectively, mature and emerging thermo-mechanical alternatives that offer multi-hour capability and, in the case of LAES, opportunities for integration with external heat or cold sources. Their technical characteristics and siting features motivate the hybrid configurations explored later in the thesis.

The chapter concluded by linking storage technologies to wholesale electricity markets. It introduced the day-ahead, intraday, and balancing layers through which bulk storage derives revenues and clarified the distinction between price-taking and price-making participation. Energy arbitrage across day-ahead and intraday markets was identified as the main economic focus of this thesis. The next chapters build on this foundation to develop detailed dispatch and bidding models for lithium-ion batteries, LAES and LAES-LNG systems, and a hybrid CAES-LAES facility.

CHAPTER 3

Optimization Foundations for Market-Based Storage Models

This chapter provides a concise overview of the mathematical principles that underlie the storage models developed in the subsequent chapters. Its purpose is to offer a clear foundation for readers who may not be familiar with these concepts, by introducing basic optimization formulations, their extensions under uncertainty and strategic interaction, and the use of optimality conditions and equilibrium representations. The chapter closes with a brief introduction to learning-based tools that assist large-scale optimization, preparing the ground for their use in later chapters.

3.1. Mathematical Optimization

Mathematical optimization provides the basic language used in this thesis to represent decision-making problems in energy systems. In particular, the short-term scheduling of energy storage in market-based energy systems can be viewed as the systematic selection of decision variables that minimize or maximize a numerical performance index, subject to physical, technical, and market constraints. Standard texts such as Boyd and Vandenberghe [118] and Bazaraa *et al.* [119] offer a rigorous introduction to this framework and motivate its use in a wide range of engineering applications. This framework can be expressed using the following generic constrained optimization problem.

A generic constrained optimization problem can be written as:

$$\begin{aligned} \min_{x \in \mathcal{X}} \quad & f(x) \\ \text{s.t.} \quad & h(x) = 0, \\ & g(x) \leq 0 \end{aligned} \tag{3.1}$$

where $\mathcal{X} \subseteq \mathbb{R}^n$ denotes the domain of the decision vector x, $f : \mathcal{X} \to \mathbb{R}$ is the objective function, $h : \mathcal{X} \to \mathbb{R}^{m_e}$ represents the set of equality constraints, and $g : \mathcal{X} \to \mathbb{R}^{m_i}$ represents the set of inequality constraints. Equality constraints usually encode exact physical relationships, such as balance equations or state transitions, while inequality constraints capture capacity limits, operating ranges, and regulatory requirements. The feasible region is given by all $x \in \mathcal{X}$ that satisfy $h(x) = 0$ and $g(x) \leq 0$ [118, 119].

In the context of this thesis, the vector x may contain, for instance, hourly charging and discharging decisions for a storage unit, its state-of-charge trajectory, and the quantities offered in day-ahead or intraday market bids. The objective function $f(x)$ then represents an economic performance metric such as total profit from energy arbitrage or total operating cost of a system that includes storage. Equality constraints typically impose power balance across the network, intertemporal state-of-charge dynamics, or exact market-clearing rules, while inequality constraints enforce storage power and energy limits and maximum transmission capacity limits. Similar formulations are widely used in short-term scheduling models for energy storage in electricity markets [120, 121, 122].

Problem (3.1) can be classified according to the properties of f, h, and g, and according to the domain of x. When all functions are linear and the variables are continuous, the result is a Linear Programming (LP) problem, which can be solved efficiently for large-scale instances [123]. If some variables are constrained to be integer, for example, to represent the charging or discharging status of storage units participating in energy arbitrage, the problem becomes a Mixed-Integer Mixed-Integer Linear Programming (MILP). When at least one of the functions is nonlinear, the model falls into the general category of Non-Linear Programming (NLP), with convex or nonconvex structure depending on the curvature of the functions involved [118, 119].

The models developed in the subsequent chapters are particular instances of (3.1) formulated as large-scale MILPs. Chapters 4-6 describe the short-term market participation of bulk storage technologies under different information structures and strategic settings, including risk-aware battery dispatch, LAES-LNG co-optimization, and strategic hybrid CAES-LAES bidding with embedded network constraints.

3.2. Stochastic Programming

The formulation in Section 3.1 describes a deterministic optimization problem in which all parameters are assumed to be known with certainty. This assumption is rarely satisfied in short-term power system operation [124] and is particularly restrictive for energy storage, whose value arises from inter-temporal arbitrage under uncertain conditions. In practice, storage operators face volatile electricity prices, fluctuating renewable generation, and variable demand, and they must make decisions before the actual realizations of these quantities. Ignoring these uncertainties can lead to dispatch strategies that are systematically biased or overly myopic [125].

Decision-making in this context has an inherent temporal structure [124]. Storage operators revise their decisions as new information becomes available over time and as markets close sequentially. A typical example is the joint participation of a storage asset in day-ahead and intraday electricity markets. In the first stage, the operator submits offers and bids to the day-ahead auction based on forecasts of day-ahead prices. After the day-ahead market closure, the clearing prices and accepted quantities become known. Then, in the second stage, the operator can adjust the storage schedule and submit additional bids and offers in intraday markets, taking updated information into account. This dynamic view of the problem naturally motivates multi-stage optimization models in which early decisions must anticipate the impact of uncertain future outcomes [126, 127].

Stochastic programming provides a structured way to embed uncertainty into optimization models. The key idea is to represent uncertain parameters, such as prices or wind generation, through a finite set of scenarios that approximate their possible future trajectories and associated probabilities [128]. The decision variables are divided into first-stage variables (*here-and-now* decisions), which must be chosen before uncertainty is revealed, and second-stage variables (*wait-and-see* decisions), which can adapt to each scenario once the uncertain

outcomes are observed. This two-stage structure is widely adopted in short-term scheduling problems in power systems [124], including the operation of energy storage units, and can be extended to multi-stage formulations when required. This structure can be expressed using the following generic two-stage stochastic program [124, 125, 126].

Let x denote the vector of first-stage decisions and let $y(\omega)$ be the vector of second-stage decisions corresponding to scenario ω in a finite scenario set Ω. Each scenario $\omega \in \Omega$ occurs with probability π_ω, where $\pi_\omega \geq 0$ and $\sum_{\omega\in\Omega} \pi_\omega = 1$. A generic two-stage stochastic program can be written as:

$$\begin{aligned} \min_{x\in\mathcal{X}, y(\omega)\in\mathcal{Y}(\omega)} \quad & c^\top x + \sum_{\omega\in\Omega} \pi_\omega \, q(\omega)^\top y(\omega) \\ \text{s.t.} \quad & Ax = b, \\ & T(\omega)x + W(\omega)y(\omega) = h(\omega), \quad \forall \omega \in \Omega \end{aligned} \tag{3.2}$$

where c and $q(\omega)$ are cost (or negative revenue) vectors, A, $T(\omega)$, and $W(\omega)$ are appropriate coefficient matrices, and b and $h(\omega)$ collect right-hand-side parameters. The set $\mathcal{X}$ contains the deterministic first-stage (*here-and-now*) variables, that must hold independently of the scenario. The sets $\mathcal{Y}(\omega)$ contain the second-stage (*wait-and-see*) variables, which depend on scenario ω. Problem (3.2) optimizes x and $y(\omega)$ to minimize the sum of the immediate first-stage cost and the expected second-stage cost.

Within the scope of this thesis, the compact structure in (3.2) is used to describe price-taking sequential dispatch of bulk energy storage in market-based environments. In Chapter 4, a two-stage stochastic formulation is adopted for the short-term scheduling of a grid-scale battery that participates as a price-taking unit in day-ahead and intraday markets, where day-ahead offers correspond to x and intraday adjustments correspond to $y(\omega)$ for different realizations of market prices. In Chapter 5, a similar two-stage logic is applied to the LAES-LNG facility. The first stage determines the facility's position in the LNG market, while the second stage governs its operation in the day-ahead electricity market. These models remain aligned with the deterministic framework introduced in Section 3.1, yet they extend it by explicitly capturing the uncertainty that shapes the economic value of storage in modern energy

markets.

3.3. Multi-Level Optimization

The deterministic and stochastic formulations introduced in Sections 3.1 and 3.2 describe decision problems for a single decision-maker (storage operator) who optimizes an objective subject to physical and operational constraints, possibly under uncertainty. In liberalized electricity markets, however, market outcomes arise from the interaction between individual participants and a central market operator like EPEX SPOT [115]. When a bulk storage facility is large enough to influence prices, its actions affect the market-clearing result, and the resulting prices feed back into its profit. This feedback loop cannot be captured by a single-level optimization model and motivates the use of multi-level (in particular, *bi-level*) optimization frameworks [129, 130]. Multi-level optimization explicitly represents this hierarchical interaction by coupling one upper-level problem, which models the strategic decisions of a leader, with one or several lower-level problems that capture the market-clearing or system-response behavior of the followers.

In the context of this thesis, the upper-level problem represents a bulk energy storage operator that behaves as a price-making market participant. The operator selects bidding strategies and look-ahead schedules to maximize expected profit. The lower-level problem represents the market-clearing problem solved by a market operator. In the lower-level optimization, the market operator determines the dispatch of all generators and storage units, as well as the corresponding nodal prices, by solving a welfare maximization or cost minimization problem subject to network and operational constraints. The upper-level decisions enter the lower-level model as offer parameters and technical limits, while the lower-level solution determines accepted quantities and prices that appear in the upper-level profit function [131, 132]. This interaction between upper- and lower-level decisions can be expressed using the following generic multi-level formulation.

To formalize this structure, let x^U denote the vector of upper-level decisions (e.g., price-quantity pairs for day-ahead offers) and let x^L collect all lower-level decision variables, for example, generation dispatch, in a market-clearing model. A generic multi-level formulation with a single lower-level problem can be written in compact form as:

$$\begin{aligned} \max_{x^U \in \mathcal{X}^U, x^L \in \mathcal{X}^L} \quad & F^U\big(x^U, x^L\big) \\ \text{s.t.} \quad & H\big(x^U, x^L\big) = 0, \\ & G\big(x^U, x^L\big) \leq 0, \\ & x^L \in \arg\min_{y \in \mathcal{X}^L} \Big\{ f^L\big(x^U, y\big) \,:\, h\big(x^U, y\big) = 0 \;(\lambda), \\ & \qquad\qquad g\big(x^U, y\big) \leq 0 \;(\mu) \Big\} \end{aligned} \tag{3.3}$$

where F^U and f^L denote the upper- and lower-level objective functions, while H and G represent the upper-level equality and inequality constraints. The notation (λ) and (μ) indicates that λ and μ are the Lagrange multipliers associated with the lower-level equality and inequality constraints, respectively. The implicit condition $x^L \in \arg\min\{\cdot\}$ ensures that x^L is an optimal solution to the lower-level problem parameterized by x^U.

The formulation in (3.3) can be extended to handle several lower-level problems, for example, when a strategic storage operator interacts with multiple coupled markets or with a sequence of clearing mechanisms. In that case, x^L, λ, and μ can be interpreted as stacked vectors that gather primal and dual variables from all lower-level problems, each of which follows the same generic form. In this thesis, the focus remains on *bi-level* structures where a single upper-level storage operator interacts with one or more market-clearing models. In particular, Chapter 6 instantiates (3.3) for a hybrid CAES-LAES facility that acts as a price-making leader in a Stackelberg game. The hybrid plant submits coordinated look-ahead offers to the day-ahead electricity market, while the lower-level represents the market equilibrium that maps these offers to dispatch schedules and prices. Subsequent sections show how the optimality conditions of the lower-level problems, through the dual variables λ and μ, allow this hierarchical formulation to be recast as a single-level MPEC suitable

for numerical implementation.

3.4. Optimality Conditions

The multi-level optimization structure in Section 3.3 models the interaction between a strategic storage operator and the market-clearing problem solved by the market operator. In order to solve such models numerically, it is convenient to replace the lower-level optimization problem with algebraic conditions that characterize its optimal solutions. The Karush-Kuhn-Tucker (KKT) conditions provide this characterization for a broad class of constrained optimization problems and form the standard link between *bi-level* models and single-level reformulations [118, 119, 131].

For a given upper-level decision vector x^U, the lower-level problem in (3.3) can be written as:

$$\begin{aligned} \min_{x^L \in \mathcal{X}^L} \quad & f^L\big(x^U, x^L\big) \\ \text{s.t.} \quad & h\big(x^U, x^L\big) = 0 \quad (\lambda), \\ & g\big(x^U, x^L\big) \leq 0 \quad (\mu), \end{aligned} \tag{3.4}$$

where x^L collects the lower-level variables (generator and storage dispatch, nodal injections, and flows) and f^L represents the system-wide objective, such as total production cost or negative social welfare [124, 120]. Let λ and μ denote the Lagrange multipliers associated with h and g, respectively. The Lagrangian of (3.4) is

$$\mathcal{L}^L\big(x^U, x^L, \lambda, \mu\big) = f^L\big(x^U, x^L\big) + \lambda^\top h\big(x^U, x^L\big) + \mu^\top g\big(x^U, x^L\big) \tag{3.5}$$

Assume that f^L, h, and g are continuously differentiable and that a suitable constraint qualification holds at an optimal solution of (3.4). Then any optimal solution (x^L, λ, μ) must satisfy the KKT conditions [118, 119]. These optimality requirements are summarized by the KKT conditions shown below.

For a fixed x^U, the KKT conditions of (3.4) associated with (3.5) are:
Stationarity:

$$\nabla_{x^L} f^L\big(x^U, x^L\big) + \big(\nabla_{x^L} h\big(x^U, x^L\big)\big)\lambda^\top + \big(\nabla_{x^L} g\big(x^U, x^L\big)\big)\mu^\top = 0, \quad (3.6)$$

Primal feasibility:

$$h\big(x^U, x^L\big) = 0, \qquad g\big(x^U, x^L\big) \leq 0, \quad (3.7)$$

Dual feasibility:

$$\mu \geq 0, \quad (3.8)$$

Complementary slackness:

$$\mu^\top g\big(x^U, x^L\big) = 0. \quad (3.9)$$

Equivalently, (3.8)–(3.9), together with the inequality part of (3.7), can be expressed component-wise as:

$$0 \leq \mu \perp g\big(x^U, x^L\big) \leq 0. \quad (3.10)$$

In electricity market models, the multipliers in λ and μ have a direct economic interpretation as marginal prices and scarcity values of network and resource constraints [120, 124, 131]. In systems with bulk energy storage, they quantify the marginal value of relaxing power and energy limits, which is closely related to the opportunity cost of shifting energy across time. When the lower-level problem is convex, the KKT conditions (3.6)-(3.10) are both necessary and sufficient for optimality [118, 119]. This property allows the replacement of the implicit optimality condition in (3.3) by the explicit KKT conditions, leading to a single-level formulation with equilibrium constraints. The following section uses this idea to introduce MPEC for strategic storage participation in market-based energy systems.

3.5. Mathematical Programming with Equilibrium Constraints (MPEC)

Section 3.4 showed how the optimality of the lower-level problem can be described explicitly through the KKT conditions. This observation is central for

transforming the *bi-level* structure in (3.3) into a single optimization model that can be handled by standard solvers. MPEC provide this single-level representation by embedding the equilibrium conditions of one or more optimization problems directly as constraints [131, 133, 134]. An MPEC is an optimization problem in which part of the constraint set consists of complementarity or KKT conditions that characterize an equilibrium or an optimal response of another problem. In the present context, the equilibrium corresponds to the solution of the lower-level market-clearing model, typically formulated as a linear or convex program that minimizes total system cost or maximizes social welfare [120].

Starting from the *bi-level* formulation in (3.3), the lower-level optimality condition

$$x^L \in \arg\min_{y \in \mathcal{X}^L} \{\cdot\}$$

can be replaced by the KKT conditions of the lower-level problem described in (3.6)–(3.9) [131]. This substitution yields a single-level MPEC in which the upper-level variables, the lower-level primal variables, and the associated dual variables appear jointly in one optimization problem [131].

With x^U and x^L denoting the upper- and lower-level decisions and (λ, μ) the multipliers of the lower-level equality and inequality constraints, the resulting single-level MPEC can be written as:

A compact MPEC representation of the structure in (3.3) is:

$$\begin{aligned}
\max_{x^U,\, x^L,\, \lambda,\, \mu} \quad & F^U\big(x^U, x^L\big) \\
\text{s.t.} \quad & H\big(x^U, x^L\big) = 0, \\
& G\big(x^U, x^L\big) \le 0, \\
& h\big(x^U, x^L\big) = 0, \\
& \nabla_{x^L} f^L\big(x^U, x^L\big) + \big(\nabla_{x^L} h\big(x^U, x^L\big)\big)\lambda^\top + \big(\nabla_{x^L} g\big(x^U, x^L\big)\big)\mu^\top = 0, \\
& 0 \le \mu \perp g\big(x^U, x^L\big) \le 0
\end{aligned} \tag{3.11}$$

The first two sets of constraints in (3.11) impose the upper-level feasibility conditions H and G, which restrict the leader's decisions to a permissible region defined by physical, operational, or structural requirements. The equality constraint $h\big(x^U, x^L\big) = 0$ enforces the primal feasibility of the lower-level

problem and ensures that any candidate (x^U, x^L) pair satisfies the underlying system equations. The stationarity condition links the gradient of the lower-level objective with the gradients of the constraints through the multipliers (λ, μ), which is the core mechanism through which the lower-level optimality is represented analytically [118, 135]. The primal and dual feasibility conditions, $g\big(x^U, x^L\big) \leq 0$ and $\mu \geq 0$, together with the complementary slackness relation $\mu^\top g\big(x^U, x^L\big) = 0$, can be written compactly as $0 \leq \mu \perp g\big(x^U, x^L\big) \leq 0$. This formulation expresses, in a single relation, the interaction between each inequality constraint and its associated multiplier. Together, these conditions fully characterize the solution of the lower-level convex program and allow the MPEC to reproduce the exact follower response within a single-level structure [131].

From a numerical point of view, MPEC problems are challenging because complementarity constraints create nonconvex feasible regions and can violate standard regularity conditions [133, 134]. In practice, these relations are often reformulated with binary variables and big-M constraints or other disjunctive schemes, which convert (3.11) into a large-scale MILP or mixed-integer nonlinear program suitable for input to modern solvers [131, 132]. The strategic storage models in Chapter 6 follow this approach and implement the single-level MPEC as a mixed-integer representation of hybrid CAES-LAES participation in day-ahead electricity markets under price-making behavior.

3.6. Machine Learning for Optimization

The optimization frameworks introduced in Sections 3.1–3.5, whether deterministic, stochastic, or multi-level with equilibrium constraints, can become computationally demanding when applied to realistic energy market models. In practice, large-scale formulations often combine several sources of difficulty. *Nonlinear* terms, for instance, quadratic cost or alternating current network constraints, destroy convexity or require iterative linearization. *Integer variables*, such as binary commitment, on/off charging decisions, or complementarity representations of equilibrium, create combinatorial complexity. Stochastic programming and *bi-level* MPEC structures further increase problem size through scenario expansion and additional primal-dual variables. When these models support short-term decision-making, such as short-term dispatch of energy storage in market-based environments, their direct solution may be intractable or too slow to be practical.

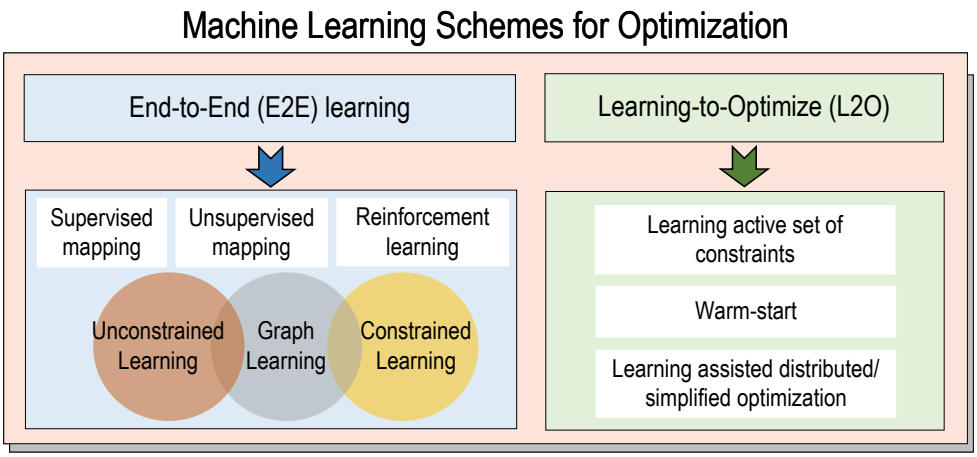

Figure 3.1: Overview of machine learning schemes for optimization.

Recent work has therefore explored machine learning models as auxiliary tools that reduce the online computational burden. The central idea is to move most of the computational burden to an offline training phase that relies on historical data or simulated optimal solutions, so that the online phase reduces to a computationally light prediction task or a learned component that accelerates the solver's optimization process [136]. Within this general perspective, learning-based schemes for assisting optimization can be grouped into two main families: End-to-End (E2E) learning and Learning-to-Optimize (L2O) [136]. Figure 3.1 provides an overview of these families and their main subclasses, while Table 3.1 summarizes their main characteristics, advantages, and limitations in a generic optimization setting.

3.6.1 End-to-End (E2E) Learning Schemes

E2E learning schemes aim to bypass explicit optimization at run time by learning a direct mapping from problem inputs, such as demand profiles, forecasts, or market conditions, to optimal or near-optimal decisions, such as dispatch schedules or bidding strategies. A generic workflow first generates a large dataset of input–solution pairs, typically by solving the original optimization model offline for many realizations of the uncertain parameters or operating conditions, although this step can be significantly reduced or bypassed when a sufficiently large historical record of past operating decisions and associated system conditions is available. A *supervised* [137], *unsupervised* [138], or

reinforcement learning [139] model then approximates the relationship between inputs and decisions. Once trained, the model provides decisions with very low computational cost, which is attractive for applications that require fast responses or repeated solutions of similar problem instances.

Within this family, one can distinguish three primary learning mechanisms. The first class, *supervised mapping*, uses labeled data and treats the optimization solver as an oracle that provides target decisions during training. The second class, *unsupervised mapping*, often relies on generative models [140] that learn the distribution of decisions or trajectories and can then sample new candidate decisions that are consistent with historical patterns. The third primary class, *reinforcement learning*, frames the decision problem as a sequential interaction between an agent and a simulated environment, where the agent learns a policy that maximizes an accumulated reward. Orthogonal to these three primary classes, the literature introduces several subcategories that describe how constraints and structure are handled [136]. *Unconstrained* models focus on predictive accuracy without enforcing technical constraints, which may require post-processing. *Constrained* models embed physical or operational constraints into the training loss or architecture, which improves the feasibility of the predicted solutions [141]. *Graph-based* models exploit the underlying network structure, for example in transmission networks or gas grids, by representing the system as a graph and learning on that representation [142]. The E2E schemes in Figure 3.1 and Table 3.1 capture these primary classes and their subcategories in a compact way.

3.6.2 Learning-to-Optimize (L2O) Schemes

L2O schemes follow a different philosophy. Rather than replacing the optimization model, they learn auxiliary information or strategies that support and accelerate traditional solvers. The explicit mathematical formulation remains central, while the learning component augments it with data-driven predictions that reduce problem size, improve initialization, or tune algorithmic parameters. This family is often referred to as hybrid learning and optimization, or learning-assisted optimization, and can be broadly grouped into three categories: *learning active sets of constraints*, *warm-start* approaches, and *learning-assisted distributed or simplified optimization* schemes [136].

The first category, learning active sets of constraints, focuses on identifying inequality constraints that are binding at the optimum [143]. In many large-

Table 3.1: Representative machine learning schemes for optimization.

E2E learning schemes	**Description**	Learn a direct mapping from features to decisions without explicitly solving the optimization		
	Pros	Ability to capture complex nonlinear relationships, very low online computational cost		
	Cons	Often reduced interpretability, limited robustness to rare instances, feasibility not always guaranteed		
	Delegate classes	***Supervised mapping:*** Learn the mapping from inputs to optimal or near-optimal decisions by training on labeled data	***Unsupervised mapping:*** Use generative models to learn the distribution of decisions or trajectories from unlabeled data	***Reinforcement learning:*** Train an agent that interacts with a simulated environment and learns a policy that produces good decisions
	Delegate subclasses	Each main class can be further categorized as *unconstrained*, *constrained*, and/or *graph-based* learning		
		Unconstrained learning: Learn the mapping without enforcing operational or physical constraints during training	***Constrained learning:*** Learn the mapping while embedding selected or all constraints into the learning process	***Graph learning:*** Learn the mapping while exploiting graph representations of the underlying network or system structure
L2O schemes	**Description**	Learn algorithms or strategies that assist or accelerate the solution of an explicit optimization model		
	Pros	Preserve model-based structure and feasibility guarantees (depending on the scheme) while exploiting data to improve computational performance		
	Cons	Need for representative training data, possible loss of performance for rare or highly stressed instances		
	Delegate classes	***Learning active set of constraints:*** Predict the subset of inequality constraints that will be active at the optimum, then solve a reduced problem	***Warm-start:*** Use pre-trained models to generate good initial points or candidate solutions for optimization solvers	***Learning-assisted distributed/simplified optimization:*** Combine decomposition, relaxation, or simplified models with learning components to improve convergence or accuracy

scale models, only a small subset of inequality constraints is active, while the remaining ones are slack and do not influence the solution, yet they still introduce extra variables and dual conditions that increase computational effort. Active-set L2O schemes train a classifier to predict which constraints are likely to be active for a given problem instance, based on features such as electricity prices, renewable energy outputs, or past solutions. The solver then processes a reduced optimization problem that includes only the predicted active constraints. This reduction can significantly decrease solution times, while the explicit optimization model still enforces exact feasibility on the reduced set.

The second category, warm-start approaches, centers on learning high-quality initial points for the underlying solver [73, 144]. A learning model produces an initial solution or a set of candidate solutions that lie close to the optimum of the full optimization problem. Standard solvers, such as mixed-integer or nonlinear programming solvers like Gurobi, then use these predictions as starting points. Warm-start information can include primal variables, dual variables, or both. In sequential decision settings, for example, rolling-horizon dispatch or repeated market-clearing, training data can be collected from historical or simulated solutions that correspond to similar operating conditions. By providing initial points that are already near-optimal, the solver requires fewer iterations and explores a smaller portion of the search space, thereby reducing online computational cost without altering the mathematical formulation.

The third category comprises learning-assisted distributed or simplified optimization schemes [145, 146]. Large energy systems are often decomposed into subsystems or approximated by relaxed models to achieve scalability. Typical examples include decomposition methods based on alternating direction techniques or Lagrangian relaxation, and surrogate models that approximate complex physics. Learning models can assist these algorithms in several ways. They can tune penalty parameters or step sizes to improve convergence, predict suitable decompositions or aggregation structures, or correct systematic biases introduced by simplified models. In all these cases, the data-driven component operates alongside a model-based algorithm that preserves the physical and economic structure of the optimization problem.

Within the scope of this thesis, the L2O perspective is particularly relevant for the computational treatment of the MPEC formulations introduced in Section 3.5. The strategic dispatch of the hybrid CAES-LAES facility in Chapter 6 leads to large mixed-integer MPEC instances that must be solved

repeatedly for different market scenarios and parameter sets. In that context, this thesis adopts warm-start techniques as the main L2O tool. Machine learning models are used to provide high-quality initial points for the single-level MPEC solver, thereby reducing the number of iterations and overall solution time while preserving the exact mixed-integer representation of strategic storage participation in electricity markets.

3.7. Chapter Conclusion

The objective of this chapter has been to assemble the optimization tools required for the storage models developed in the remainder of the thesis. Starting from a generic constrained optimization problem, the chapter has clarified how objectives, equality constraints, and inequality constraints provide a common language to describe storage scheduling in market-based energy systems, with a focus on large-scale linear and mixed-integer formulations. It has then extended this deterministic viewpoint to two-stage stochastic programming to account for uncertainty in sequential markets. Building on this foundation, the chapter has introduced multi-level optimization, which can be used to represent strategic storage participation in liberalized electricity markets. The derivation of the KKT optimality conditions and their use in MPEC formulations have completed the transition from implicit *bi-level* structures to explicit single-level models with equilibrium constraints that remain suitable for numerical implementation.

The final part of the chapter has addressed the computational implications of previously introduced formulations and has motivated the use of machine learning as a complementary tool. E2E learning schemes and L2O approaches have been positioned as two broad families that either approximate the decision mapping directly or assist in solving explicit optimization models by predicting active sets, generating warm-start solutions, or supporting distributed and simplified optimization schemes. In this way, the chapter has framed machine learning not as a replacement for mathematical programming, but as a means to preserve the structure and interpretability of model-based formulations while reducing their online computational burden.

Within the thesis, the above concepts support the specific applications developed in Chapters 4–6. Chapter 4 and Chapter 5 instantiate the stochastic framework for price-taking battery and LAES-LNG operation in sequential energy markets. Chapter 6 relies on the multi-level and MPEC machinery, together with warm-start L2O schemes, to model the strategic participation of

a hybrid CAES-LAES facility as a price-making market player. In this way, the chapter provides a consistent methodological basis that will be used throughout the subsequent chapters.

Chapter Publication

- **H. Khaloie**, M. Dolányi, J.-F. Toubeau, and F. Vallée, "Review of Machine Learning Techniques for Optimal Power Flow," *Applied Energy*, vol. 388, p. 125637, 2025.

CHAPTER 4

Risk-Aware Market Dispatch of Grid-Scale Batteries

Chapters 2 and 3 have provided the technical and methodological background for the storage models developed in this thesis. Building on this foundation, the present chapter makes the first methodological contribution by studying how a grid-scale battery storage system should bid in coupled day-ahead and intraday electricity markets when price uncertainty and risk preferences are explicitly accounted for.

Increasing shares of variable renewable generation have raised short-term price volatility, which amplifies arbitrage opportunities and financial risk for battery storage owners. Aggressive cycling can increase expected profit but may lead to undesirable low-profit outcomes and faster degradation, so a purely risk-neutral model is not suitable for a risk-averse operator. This chapter addresses *Research Question 1* from Chapter 1 by formulating a two-stage stochastic battery bidding framework based on SSD, equipped with a novel benchmark selection method that combines SSD with regret-based considerations. The resulting model delivers bidding strategies that balance expected revenue and downside protection in a way that reflects the preferences of the battery operator.

The remainder of the chapter is organized as follows. Section 4.1 reviews the literature on battery bidding models in short-term electricity markets, with a focus on both risk-neutral and risk-aware formulations. In Section 4.2, a stochastic risk-neutral battery bidding model is formulated to co-optimize day-ahead and intraday decisions. Section 4.3 then extends this setup to a risk-aware framework by imposing SSD-based constraints. The proposed benchmark selection method and its integration into the SSD-constrained model are detailed in Section 4.4. Section 4.5 turns to the case study and the corresponding numerical results. Finally, Section 4.6 concludes the chapter and outlines the implications for the remainder of the thesis.

4.1. Literature Review on Battery Bidding Models

A substantial body of work has examined how battery storage systems should bid into short-term electricity markets. Most studies adopt a price-taking perspective and formulate the bidding problem as a deterministic or stochastic optimization model that co-optimizes charging and discharging schedules subject to inter-temporal energy constraints. Early contributions focus on day-ahead energy arbitrage and incorporate degradation-aware formulations based on cycle aging or cost functions embedded in the operational model [147, 148]. Multi-scenario stochastic formulations have also been explored to capture uncertainty in day-ahead and ancillary service prices [149].

Bi-level structures have also been proposed to couple the battery profit-maximization problem with the market-clearing mechanism, in which the upper-level problem optimizes arbitrage profit, while the lower-level problem represents market operations. These models often include degradation terms to improve revenue evaluation [69]. Several studies extend the bidding problem to multiple trading floors, such as combining day-ahead arbitrage with balancing services or fast frequency response [150]. Learning-based approaches have also been investigated, including reinforcement learning methods designed to map price observations into operational decisions while accounting for losses and battery lifetime [151]. Other contributions consider distribution-level and transmission-level bidding through bi-level or decomposition-based structures to improve computational efficiency [152, 153]. Deterministic co-optimized sizing and bidding models have been developed for energy and frequency regulation markets [154], and joint bidding and clearing models have been proposed to manage cycling mileage [155]. These studies collectively establish the main modeling practices for battery bidding in wholesale markets.

A second group of studies incorporates risk preferences into market participation strategies. CVaR has been the most widely adopted approach for managing downside risk in storage and hybrid wind-storage bidding models [156, 157]. CVaR has also been integrated into robust and hybrid stochastic-robust formulations [158, 159], while distributionally robust bidding has been proposed for wind-storage aggregators participating in day-ahead markets [160]. Beyond CVaR, SSD has been introduced as a coherent risk metric in market bidding for renewable generators [45], although its application to battery bidding remains limited. Information gap decision theory has been applied to manage risk-averse and risk-seeking strategies in day-ahead markets [161].

Together, these works demonstrate the relevance of risk-aware modeling for bidding problems under uncertainty.

Despite these contributions, two issues remain relevant for the present chapter. First, existing SSD-based formulations provide limited guidance on how to derive the feasible region of admissible benchmarks, although benchmark selection directly affects the performance and tractability of SSD-constrained models. Second, there is no systematic method for selecting a final benchmark that reflects the decision-maker's preferences while preserving consistency with the SSD framework.

In response, this chapter develops an SSD-constrained battery bidding model for day-ahead and intraday markets and introduces a practical benchmark selection procedure based on regret analysis and out-of-sample evaluation. This approach enables the operator to balance expected revenue with downside protection while ensuring that the chosen benchmark is both feasible and aligned with the decision-maker's risk preferences for a risk-averse battery operator.

4.2. Risk-Neutral Battery Bidding Model

4.2.1 Market Model

This section considers a lithium-ion battery that participates as a price-taker in the wholesale electricity market. The analysis focuses on two trading venues that are representative of the European market design: the day-ahead market and an auction-based intraday market. Both markets clear energy for the same delivery horizon, indexed here as day D with an hourly resolution.

In line with current European practice, the day-ahead market for day D closes at 12:00 CET on day $D-1$ [115]. At this time, the battery operator submits its energy offer schedule for each hour of the next day. After market closure, the day-ahead auction is cleared and the resulting prices and accepted quantities are published. The intraday market then provides an additional trading opportunity to adjust positions before physical delivery. Among the several auction sessions implemented in practice, this chapter models the second intraday auction. This session closes later on day $D-1$ while still covering the full delivery horizon of day D, which makes it particularly relevant for refining the battery schedule on the basis of updated information. The first intraday auction is closer in time to the day-ahead auction and would provide

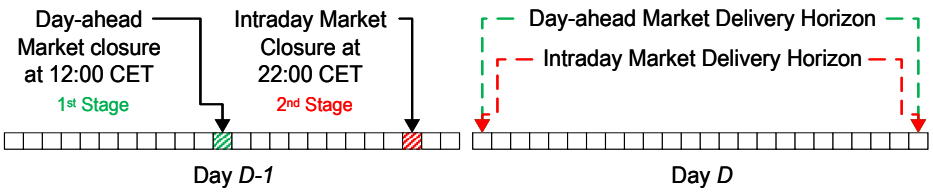

Figure 4.1: Time line of the two-stage battery bidding problem in coupled day-ahead and intraday markets.

less additional information, whereas the third auction does not cover the entire next day and is therefore not considered here for the sake of consistency.

Figure 4.1 summarizes the timeline of these trading activities. The first stage of the decision process corresponds to the submission of day-ahead bids at 12:00 CET of day $D-1$. The second stage corresponds to the participation in the intraday auction, which closes at 22:00 CET of day $D-1$. In both stages, the decisions concern the hourly charging and discharging schedules of the battery over the delivery horizon of day D, subject to its technical limits and state-of-charge dynamics. The resulting two-stage structure is the basis for the stochastic programming model presented in Section 4.2.2 and later extended to a risk-aware formulation in Section 4.3.

4.2.2 Mathematical Formulation

In line with the scope of this chapter, this section formulates a risk-neutral, price-taking bidding model for a lithium-ion battery participating in coupled day-ahead and intraday electricity markets. The battery is exposed to exogenous market prices that are represented through a finite set of scenarios. Lithium-ion battery storage systems are widely deployed, from residential to grid-scale, because of their favorable technical characteristics, such as low self-discharge and high energy density. At the same time, aging effects remain a key limitation. As discussed in Chapter 2, a large body of research has focused on modeling degradation and embedding it into operational strategies. Among the different approaches proposed in the literature, this chapter adopts the cycle-aging cost model of [147], in which degradation cost is represented as a piecewise linear function of the depth-of-discharge.

On this basis, the energy arbitrage problem is formulated as a two-stage stochastic program. The stochastic parameters are the day-ahead and intraday electricity prices, which are modeled through a set of scenarios $\omega \in \{1, \ldots, \Omega\}$

with associated probabilities π_ω. Several scenario generation techniques are available in the literature [162]. Here, the method proposed in [163] is employed to construct a discrete set of price trajectories that jointly describe day-ahead and intraday prices over the delivery horizon.

The objective function of the resulting optimization problem is given in (4.1):

$$\max_{\Xi^{1^{\text{st}}},\Xi^{2^{\text{nd}}}} \sum_{\omega=1}^{\Omega} \pi_\omega \left(\sum_{t=1}^{\mathcal{T}} \left[\underbrace{\lambda_{t,\omega}^{\text{DA}} \left(P_t^{\text{DA,dis}} - P_t^{\text{DA,ch}} \right)}_{\mathcal{O}_1} + \underbrace{\lambda_{t,\omega}^{\text{ID}} \left(P_{t,\omega}^{\text{ID,dis}} - P_{t,\omega}^{\text{ID,ch}} \right)}_{\mathcal{O}_2} \right. \right. \\ \left. \left. - \sum_{s=1}^{\mathcal{S}} \underbrace{\Phi_s \left(\xi_{s,t}^{\text{DA,dis}} + \xi_{s,t,\omega}^{\text{ID,dis}} \right)}_{\mathcal{O}_3} \right] \right) \tag{4.1}$$

where π_ω is the probability of scenario ω, $P_t^{\text{DA,ch}}$ and $P_t^{\text{DA,dis}}$ represent the battery charge and discharge bids in the day-ahead market, and $P_{t,\omega}^{\text{ID,ch}}$ and $P_{t,\omega}^{\text{ID,dis}}$ denote the corresponding bids in the intraday market. The parameters $\lambda_{t,\omega}^{\text{DA}}$ and $\lambda_{t,\omega}^{\text{ID}}$ are the day-ahead and intraday prices, and Φ_s is the slope of block s in the piecewise linear function that represents the battery aging cost [147].

With the above definitions, the objective function in (4.1) consists of three terms. Terms $\mathcal{O}_1$ and $\mathcal{O}_2$ capture the profits from energy arbitrage in the day-ahead and intraday markets, respectively. Term $\mathcal{O}_3$ represents the degradation cost of the lithium-ion battery as a function of the discharged energy in each depth-of-discharge segment, covering both day-ahead and intraday actions.

The two-stage stochastic structure reflects the sequence of decisions illustrated in Fig. 4.1. The decision stages are organized as follows:

1. **First-stage (*here-and-now*) decisions:** Before the realization of the day-ahead and intraday prices, and before the day-ahead market closure at 12:00 CET of day $D-1$, the battery operator decides on its energy offer and bid schedule in the day-ahead market, together with the commitment status of the storage unit. The set of first-stage decision variables is:

$$\Xi^{1^{\text{st}}} = \left\{ P_t^{\text{DA,dis}},\, P_t^{\text{DA,ch}},\, \beta_t,\, \xi_{s,t}^{\text{DA,dis}},\, \xi_{s,t}^{\text{DA,ch}} \right\}.$$

2. **Second-stage (*wait-and-see*) decisions:** After the day-ahead market has been cleared and before the intraday market closure at 22:00 CET of day $D-1$, the battery operator determines its participation in the intraday market for each price scenario. At this stage, the intraday prices for the considered session are still uncertain, and the decisions are scenario dependent and conditional on the first-stage schedule. For each scenario ω, the operator chooses intraday charging and discharging powers, segment-wise quantities, and the resulting state-of-charge. The corresponding set of second-stage decision variables is:

$$\Xi^{2^{\text{nd}}} = \left\{ P_{t,\omega}^{\text{ID,dis}},\, P_{t,\omega}^{\text{ID,ch}},\, \xi_{s,t,\omega}^{\text{ID,dis}},\, \xi_{s,t,\omega}^{\text{ID,ch}},\, \delta_{s,t,\omega}^{\text{SoC}},\, \Delta_{t,\omega}^{\text{SoC}} \right\}.$$

The relationships between aggregated charge and discharge bids and segment-wise power variables are enforced by (4.2)–(4.5). These constraints define the charge and discharge powers in the day-ahead and intraday markets as the sum of the corresponding powers over all segments $s \in \{1, \ldots, \mathcal{S}\}$ of depth of discharge:

$$P_t^{\text{DA,dis}} = \sum_{s=1}^{\mathcal{S}} \xi_{s,t}^{\text{DA,dis}} \qquad \forall t, \tag{4.2}$$

$$P_t^{\text{DA,ch}} = \sum_{s=1}^{\mathcal{S}} \xi_{s,t}^{\text{DA,ch}} \qquad \forall t, \tag{4.3}$$

$$P_{t,\omega}^{\text{ID,dis}} = \sum_{s=1}^{\mathcal{S}} \xi_{s,t,\omega}^{\text{ID,dis}} \qquad \forall t, \forall \omega, \tag{4.4}$$

$$P_{t,\omega}^{\text{ID,ch}} = \sum_{s=1}^{\mathcal{S}} \xi_{s,t,\omega}^{\text{ID,ch}} \qquad \forall t, \forall \omega. \tag{4.5}$$

The charging and discharging powers of the lithium-ion battery are constrained by the converter ratings in both markets, as specified in (4.6)–(4.9):

$$0 \leq P_t^{\text{DA,dis}} \leq P^{\text{dis}} \beta_t \qquad \forall t, \tag{4.6}$$

$$0 \leq P_t^{\text{DA,dis}} + P_{t,\omega}^{\text{ID,dis}} \leq P^{\text{dis}} \beta_t \qquad \forall t, \forall \omega, \tag{4.7}$$

$$0 \leq P_t^{\text{DA,ch}} \leq P^{\text{ch}} (1 - \beta_t) \qquad \forall t, \tag{4.8}$$

$$0 \leq P_t^{\text{DA,ch}} + P_{t,\omega}^{\text{ID,ch}} \leq P^{\text{ch}} (1 - \beta_t) \qquad \forall t, \forall \omega. \tag{4.9}$$

Here, P^{ch} and P^{dis} denote the maximum charging and discharging powers of the battery, and β_t is a binary decision variable indicating the discharging mode. Constraints (4.6)–(4.9) ensure that the storage system does not charge and discharge simultaneously and that its power schedules remain within technical limits.

In addition, it is important to limit the intraday charging and discharging powers relative to the day-ahead schedule [163]. This is enforced by (4.10) and (4.11):

$$0 \leq P_{t,\omega}^{\text{ID,dis}} \leq \theta \, P_t^{\text{DA,dis}} \qquad \forall t, \forall \omega, \tag{4.10}$$

$$0 \leq P_{t,\omega}^{\text{ID,ch}} \leq \theta \, P_t^{\text{DA,ch}} \qquad \forall t, \forall \omega, \tag{4.11}$$

where θ is a coefficient that limits the magnitude of intraday adjustments relative to the day-ahead positions. Segment-wise charging and discharging powers in both markets must be non-negative, as stated in (4.12):

$$\xi_{s,t}^{\text{DA,dis}}, \; \xi_{s,t}^{\text{DA,ch}}, \; \xi_{s,t,\omega}^{\text{ID,dis}}, \; \xi_{s,t,\omega}^{\text{ID,ch}} \geq 0 \quad \forall s, \forall t, \forall \omega. \tag{4.12}$$

The state-of-charge dynamics are modeled at the level of each segment s and aggregated to yield the total state-of-charge. Equations (4.13) and (4.14) describe the hourly state-of-charge in block s and the total hourly state of charge of the battery, respectively:

$$\delta_{s,t,\omega}^{\text{SoC}} = \delta_{s,t-1,\omega}^{\text{SoC}} - \frac{\xi_{s,t}^{\text{DA,dis}} + \xi_{s,t,\omega}^{\text{ID,dis}}}{\eta^{\text{dis}}} + \eta^{\text{ch}} \left(\xi_{s,t}^{\text{DA,ch}} + \xi_{s,t,\omega}^{\text{ID,ch}} \right) \qquad \forall s, \forall t, \forall \omega, \tag{4.13}$$

$$\Delta_{t,\omega}^{\text{SoC}} = \sum_{s=1}^{\mathcal{S}} \delta_{s,t,\omega}^{\text{SoC}} \qquad \forall t, \forall \omega. \tag{4.14}$$

In (4.13), $\delta_{s,t,\omega}^{\text{SoC}}$ denotes the state of charge in block s of depth of discharge for scenario ω at time t, while η^{ch} and η^{dis} are the charging and discharging efficiencies of the battery storage system. In (4.14), $\Delta_{t,\omega}^{\text{SoC}}$ represents the total state of charge at time t in scenario ω.

The state-of-charge must remain within acceptable bounds [164], which are

expressed in (4.15) and (4.16):

$$0 \leq \delta^{\mathrm{SoC}}_{s,t,\omega} \leq \varkappa^{\mathrm{SoC}}_{s} \qquad \forall s, \forall t, \forall \omega, \tag{4.15}$$

$$0 \leq \Delta^{\mathrm{SoC}}_{t,\omega} \leq E^{\mathrm{SoC}} \qquad \forall t, \forall \omega. \tag{4.16}$$

Here, $\varkappa^{\mathrm{SoC}}_{s}$ is the maximum allowable state-of-charge in block s of depth of discharge, and E^{SoC} is the maximum energy capacity of the battery storage system.

Taken together, (4.1)–(4.16) define the risk-neutral two-stage stochastic battery bidding model that serves as the reference for the risk-aware SSD-based formulation presented in the following Section.

4.3. SSD-Constrained Battery Bidding Model

The risk-neutral model in (4.1)–(4.16) maximizes the expected profit of the battery across all price scenarios in the two-stage stochastic setting. This formulation captures the physical and market constraints in detail, but it does not control how profits are distributed across scenarios. In particular, it may produce solutions with high expected revenue but a non-negligible probability of very low profits. A risk-averse storage operator may prefer to sacrifice part of the expected profit in exchange for improved protection against such undesirable outcomes.

This section extends the risk-neutral model by incorporating a risk criterion based on SSD. The objective remains the maximization of expected profit, while SSD-type constraints restrict the set of admissible profit distributions to those that stochastically dominate a preset benchmark. The resulting formulation provides a systematic way to trade expected revenue against downside protection in a way that remains consistent with the axioms of coherent risk measures.

4.3.1 Mathematical Formulation

In the two-stage stochastic program of Section 4.2, price uncertainty is represented by a finite set of scenarios for day-ahead and intraday electricity markets. This representation naturally emphasizes the need for risk management. A standard approach is to introduce a risk measure in addition to the expectation operator and to optimize a risk-adjusted objective or impose risk constraints. Widely used risk criteria include variance, probability of shortfall, expected

shortage, value-at-risk, and CVaR [45]. Among these, CVaR is the only measure that is coherent in the sense of [124], which explains its widespread use in power-system and energy-market applications.

The SSD criterion provides an alternative way to represent risk preferences. While CVaR focuses on the lower tail of the profit distribution, SSD compares entire distributions against a benchmark. In intuitive terms, SSD ensures that, for any profit threshold, the probability of obtaining a profit below this threshold is no larger than under the benchmark. A decision-maker who prefers more profit to less and exhibits risk aversion should always prefer a distribution that SSD-dominates another [124]. In the present context, this property allows the battery operator to specify a reference profit distribution and restrict attention to bidding strategies whose profits stochastically dominate this benchmark.

To formalize this idea, it is convenient to introduce an explicit variable for the scenario-wise profit. Let

$$R_\omega = \sum_{t=1}^{\mathcal{T}} \left[\lambda_{t,\omega}^{\mathrm{DA}} \left(P_t^{\mathrm{DA,dis}} - P_t^{\mathrm{DA,ch}} \right) + \lambda_{t,\omega}^{\mathrm{ID}} \left(P_{t,\omega}^{\mathrm{ID,dis}} - P_{t,\omega}^{\mathrm{ID,ch}} \right) - \sum_{s=1}^{\mathcal{S}} \Phi_s \left(\xi_{s,t}^{\mathrm{DA,dis}} + \xi_{s,t,\omega}^{\mathrm{ID,dis}} \right) \right] \quad \forall \omega. \tag{4.17}$$

By construction, the risk-neutral objective in (4.1) can be written as the maximization of the expected profit,

$$\max_{\Xi^{1^{\mathrm{st}}}, \Xi^{2^{\mathrm{nd}}}} \sum_{\omega=1}^{\Omega} \pi_\omega R_\omega, \tag{4.18}$$

subject to the operational constraints (4.2)–(4.16) and the definition of R_ω in (4.17).

The SSD-constrained version of this model is obtained by adding dominance constraints that relate the profit distribution $\{R_\omega, \pi_\omega\}$ to a benchmark distribution $\{k_b, \eta_b\}$. Here, k_b denotes the profit level in benchmark scenario b, and η_b is the associated probability. Let $\zeta_{\omega,b}$ be a non-negative auxiliary variable that measures the shortfall of scenario ω relative to benchmark level k_b. A linear characterization of SSD between the model outcome and the benchmark

can then be written as [45]

$$R_\omega \geq k_b - \zeta_{\omega,b} \qquad \forall\omega,\ \forall b, \tag{4.19a}$$

$$\sum_{\omega=1}^{\Omega} \pi_\omega \zeta_{\omega,b} \leq \sum_{b'=1}^{B} \eta_{b'}\ \max(k_b - k_{b'}, 0) \qquad \forall b, \tag{4.19b}$$

$$\zeta_{\omega,b} \geq 0 \qquad \forall\omega,\ \forall b. \tag{4.19c}$$

Constraint (4.19a) defines the shortfall variables as the amount by which scenario profit R_ω falls below each benchmark level k_b. Constraint (4.19b) restricts the expected shortfall of the model relative to each benchmark point k_b so that the resulting profit distribution SSD-dominates the benchmark distribution $\{k_b, \eta_b\}_{b=1}^{B}$. Non-negativity of the shortfall variables is enforced by (4.19c).

Combining (4.17), (4.18), and (4.19) with the operational constraints leads to the full SSD-constrained battery bidding model:

$$\max_{\Xi^{1\text{st}},\Xi^{2\text{nd}}} \sum_{\omega=1}^{\Omega} \pi_\omega R_\omega, \tag{4.20a}$$

$$\text{s.t. Definition of scenario profits } R_\omega \text{ in (4.17)}, \tag{4.20b}$$

$$\text{SSD constraints (4.19a)} - \text{(4.19c)}, \tag{4.20c}$$

$$\text{Operational constraints (4.2)} - \text{(4.16)}. \tag{4.20d}$$

The objective function in (4.20a) remains identical to that of the risk-neutral model. The additional constraints in (4.20b)–(4.20c) implement the SSD criterion with respect to the chosen benchmark, while preserving the linear or mixed-integer structure of the problem.

In principle, the decision-maker can specify any number of benchmark scenarios B with associated probabilities η_b. Figure 4.2 illustrates three examples of benchmark distributions, with one, two, and three scenarios, respectively.[1] As the number of benchmark scenarios increases, the benchmark distribution can approximate a smooth cumulative distribution function. This provides a fine-grained way to shape the range and curvature of the admissible profit distributions. Conversely, a benchmark with a small number of scenarios leads to a simpler representation that still controls the range of profits but allows

[1]The benchmark distributions in Fig. 4.2 are represented through their cumulative probabilities, and the corresponding lower and upper bounds are discussed in Section 4.3.2.

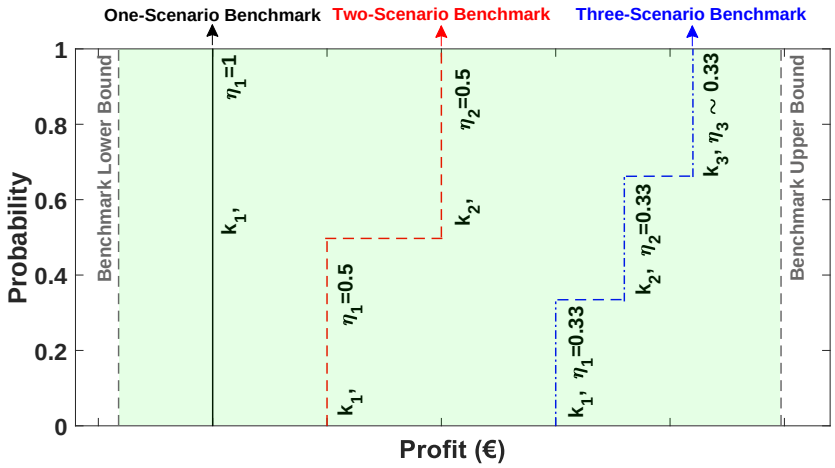

Figure 4.2: Examples of benchmark distributions with different numbers of scenarios in an SSD-constrained problem.

more flexibility in the shape of the resulting distribution.

In the remainder of this chapter, a single-scenario benchmark is adopted. This choice corresponds to $B = 1$ and $\eta_1 = 1$ and keeps the economic interpretation of the SSD constraint transparent. The benchmark then reduces to a single profit level that the entire profit distribution of the model must SSD-dominate, while the benchmark selection procedure described next ensures that this level remains both feasible and meaningful.

4.3.2 Deriving the Benchmark Feasible Region under the SSD Criterion

The performance of the SSD-constrained model in (4.20) depends critically on the choice of benchmark. If the benchmark is too conservative or too ambitious, the optimization problem may become trivial or infeasible. It is therefore essential to characterize the range of benchmark values that lead to a well-posed problem. This subsection describes a generic procedure to derive a feasible interval for a single-scenario benchmark, which will later be combined with regret-based arguments in Section 4.4.

The feasible region can be visualized on the Cumulative Distribution Function (CDF) of the profit variable. Figure 4.3 shows an illustrative example, where the CDF of the risk-neutral solution and that of an SSD-constrained solution are plotted together with the benchmark and its feasible region. The

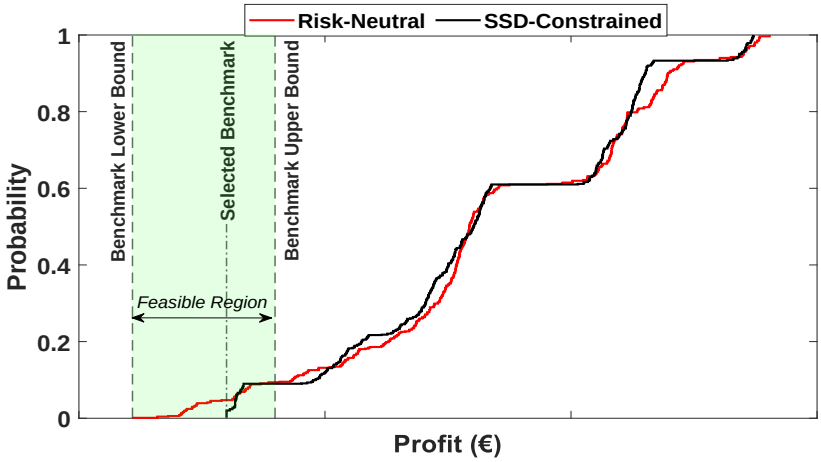

Figure 4.3: Illustrative example of CDFs and benchmark feasible region in an SSD-constrained problem.

admissible interval for the benchmark is the rectangular region between a lower and an upper bound on the profit axis. Any benchmark outside this interval either has no impact on the solution or cannot be dominated by any feasible bidding strategy.

The lower bound of the benchmark interval is obtained from the risk-neutral solution. Let R_ω^{RN} denote the scenario-wise profits produced by the risk-neutral model (4.1)–(4.16). The benchmark lower bound is defined as the smallest of these profits:

$$k^{\mathrm{L}} = \min_{\omega} R_\omega^{\mathrm{RN}}. \tag{4.21}$$

Any benchmark k_1 smaller than k^{L} is automatically dominated by the risk-neutral solution itself. In that case, the SSD-constrained model in (4.20) reduces to the risk-neutral formulation, because the added constraints are non-binding.

The upper bound is derived from an auxiliary optimization problem in which the operator maximizes a CVaR-type criterion at a confidence level β close to one. Let ξ denote the value-at-risk at level β and let φ_ω be non-negative variables representing the shortfall of scenario profits below ξ. A standard

CVaR maximization model can be written as

$$\max_{\Xi^{1^{\text{st}}},\Xi^{2^{\text{nd}}}} \ \xi - \frac{1}{1-\beta}\sum_{\omega=1}^{\Omega}\pi_\omega\varphi_\omega, \tag{4.22a}$$

$$\text{s.t. } R_\omega \geq \xi - \varphi_\omega \qquad \forall\omega, \tag{4.22b}$$

$$\varphi_\omega \geq 0 \qquad \forall\omega, \tag{4.22c}$$

$$\text{Operational constraints (4.2)} - \text{(4.16)}. \tag{4.22d}$$

Here, β is chosen close to one (for instance $\beta = 0.99$), so that the model focuses on the extreme low-profit realizations [165]. The resulting solution can be interpreted as the most conservative bidding strategy that a highly risk-averse decision-maker would adopt within the given operational constraints.

Let R_ω^{CVaR} denote the scenario-wise profits obtained from (4.22). The benchmark upper bound is then defined as

$$k^{\text{U}} = \min_{\omega} R_\omega^{\text{CVaR}}. \tag{4.23}$$

Any benchmark k_1 larger than k^{U} cannot be SSD-dominated by any feasible strategy, because even the most conservative CVaR-maximizing solution fails to reach that level in all scenarios. In this case, the SSD-constrained model has no feasible solution.

Combining (4.21) and (4.23) yields a practical benchmark feasible region,

$$k^{\text{L}} \leq k_1 \leq k^{\text{U}}, \tag{4.24}$$

within which the single-scenario benchmark k_1 can be selected. The lower bound k^{L} corresponds to the worst-case profit of the risk-neutral strategy, while the upper bound k^{U} corresponds to the worst-case profit of an extremely risk-averse CVaR-maximizing strategy. This interval is highlighted as the shaded region in Fig. 4.3. In Section 4.4, this feasible region is combined with regret-based metrics and out-of-sample evaluation to select benchmarks that are not only feasible but also aligned with the preferences of the battery operator.

4.4. Proposed Benchmark Selection Method for SSD-Constrained Problems

Sections 4.3.1 and 4.3.2 have shown how to embed the SSD criterion into the battery bidding model and how to construct a feasible interval for the single-scenario benchmark k_1, namely $[k^{\mathrm{L}}, k^{\mathrm{U}}]$. Within this interval, any value of k_1 yields a well-posed SSD-constrained problem. However, the choice of a specific benchmark remains non-trivial, because different values of k_1 lead to different trade-offs between expected profit and downside protection.

The literature on SSD-based models has mostly focused on the properties of the dominance criterion itself, while benchmark selection has often relied on ad hoc or purely empirical choices. In this thesis, a more systematic procedure is proposed. The method combines two complementary performance metrics:

- an *ex-ante* evaluation based on the notion of regret, which measures how far the strategy induced by a given benchmark is from an ideal solution with perfect information, and
- an *ex-post* out-of-sample evaluation, which tests how the same strategy performs under an external set of price scenarios that is not used in the original optimization.

Both metrics are evaluated for a finite set of candidate benchmarks within $[k^{\mathrm{L}}, k^{\mathrm{U}}]$. The resulting two-criterion decision problem is then assessed by the VIKOR method, a multi-criteria ranking technique that identifies a compromise solution that is closest to the ideal performance along both dimensions.

4.4.1 Regret-Based Ex-Ante Evaluation

For a given benchmark k_1 in the feasible interval $[k^{\mathrm{L}}, k^{\mathrm{U}}]$, the SSD-constrained model (4.20) produces a set of scenario-wise profits $R_\omega(k_1)$ and their expectation $\sum_\omega \pi_\omega R_\omega(k_1)$. To assess how robust this solution is to price uncertainty, it is useful to compare it to an ideal strategy that would be available if the operator had perfect foresight of future prices.

Let $F_\omega^{\mathrm{ideal}}$ denote the maximum profit that can be obtained in scenario ω when all decisions are allowed to depend on the realization of prices. This quantity is computed by solving a single-stage, perfect-information version of the battery bidding problem, in which all decision variables are indexed by

ω and the two-stage structure is relaxed. The corresponding formulation is reported in Appendix A.1. For each benchmark k_1, the scenario-wise regret is then defined as

$$\mathcal{G}_\omega(k_1) = F_\omega^{\text{ideal}} - R_\omega(k_1) \quad \forall\omega. \tag{4.25}$$

Regret quantifies the profit loss incurred when the SSD-constrained two-stage strategy replaces an ideal benchmark that would make decisions with perfect price foresight. This benchmark is unattainable in practice, as future prices and their uncertainties can never be known with complete accuracy.

The average regret associated with benchmark k_1 is obtained by taking the expectation of (4.25):

$$\bar{\mathcal{G}}(k_1) = \sum_{\omega=1}^{\Omega} \pi_\omega \mathcal{G}_\omega(k_1). \tag{4.26}$$

Decision-makers naturally prefer benchmarks that lead to smaller values of $\bar{\mathcal{G}}(k_1)$, because they correspond to strategies that remain closer to the ideal, perfect-foresight outcome. The average regret in (4.26) can also be interpreted as the objective value of an auxiliary optimization problem in which the operator minimizes expected regret subject to the same SSD and operational constraints as in (4.20). In this chapter, (4.26) is used as an ex-ante performance metric for each candidate benchmark.

4.4.2 Out-of-Sample Evaluation

Expected profit and average regret are computed with respect to the scenario set that defines the original stochastic program. To assess the robustness of the resulting strategies, it is important to evaluate them under alternative realizations of prices that do not appear in the training set. This step is standard in stochastic programming and in data-driven decision problems [124, 166].

Consider an external scenario set indexed by $\tilde{\omega} \in \{1, \ldots, \tilde{\Omega}\}$, with associated probabilities $\tilde{\pi}_{\tilde{\omega}}$. This set may contain a larger number of scenarios, historical samples, or simulated trajectories generated by a different model. For each candidate benchmark k_1, the SSD-constrained model (4.20) is first solved once, using the original scenario set. The resulting first-stage decisions and decision rules are then simulated under the external scenarios to compute an

out-of-sample expected profit,

$$\bar{R}^{\mathrm{OOS}}(k_1) = \sum_{\tilde{\omega}=1}^{\tilde{\Omega}} \tilde{\pi}_{\tilde{\omega}} \tilde{R}_{\tilde{\omega}}(k_1), \tag{4.27}$$

where $\tilde{R}_{\tilde{\omega}}(k_1)$ denotes the profit realized when the strategy associated with benchmark k_1 is exposed to scenario $\tilde{\omega}$ in the external set.

A higher out-of-sample expected profit $\bar{R}^{\mathrm{OOS}}(k_1)$ indicates that the benchmark leads to decisions that generalize better beyond the training scenarios. In the benchmark selection problem, $\bar{R}^{\mathrm{OOS}}(k_1)$ therefore acts as an ex-post performance metric that complements the ex-ante regret measure $\bar{\mathcal{G}}(k_1)$.

4.4.3 Multi-Criteria Benchmark Ranking with the VIKOR Method

The two metrics introduced above often point in different directions. A benchmark that yields very low average regret may also be very conservative and produce modest out-of-sample profits. Conversely, a benchmark that gives high out-of-sample profits may do so at the cost of a larger distance from the ideal solution. Selecting a single benchmark thus requires a compromise between these criteria.

To construct this compromise, the feasible interval $[k^{\mathrm{L}}, k^{\mathrm{U}}]$ is discretized into n candidate benchmarks $\{k_1^{(j)}\}_{j=1}^{n}$, spaced uniformly or according to a desired resolution. For each candidate $k_1^{(j)}$:

1. the SSD-constrained model (4.20) is solved once to obtain scenario-wise profits and the corresponding expected profit,
2. the average regret $\bar{\mathcal{G}}\big(k_1^{(j)}\big)$ is computed using (4.25)–(4.26), and
3. the out-of-sample expected profit $\bar{R}^{\mathrm{OOS}}\big(k_1^{(j)}\big)$ is evaluated using (4.27).

This procedure yields, for each candidate benchmark j, a pair of performance indicators

$$f_{1,j} = -\bar{\mathcal{G}}\big(k_1^{(j)}\big), \qquad f_{2,j} = \bar{R}^{\mathrm{OOS}}\big(k_1^{(j)}\big),$$

where the minus sign in $f_{1,j}$ ensures that larger values are preferred for both criteria. The benchmark selection problem can then be viewed as a two-criterion ranking problem over the n candidates. To solve this problem, the VIKOR

method is adopted [167, 168]. VIKOR has been widely used in multi-criteria decision-making and is well suited to the present setting, since it explicitly constructs a compromise solution that is closest to the ideal performance vector.

Let $f_{i,j}$ denote the value of criterion i (here $i = 1$ for transformed regret and $i = 2$ for out-of-sample profit) for benchmark $j \in \{1, \ldots, n\}$. The first step in VIKOR is to identify the best and worst values for each criterion:

$$f_i^* = \max_j f_{i,j}, \tag{4.28a}$$

$$f_i^- = \min_j f_{i,j}, \tag{4.28b}$$

with the usual adaptation for cost-type criteria if needed. Each criterion can be assigned a non-negative weight w_i such that $\sum_i w_i = 1$. In this chapter, equal weights are used for simplicity.

For each benchmark j, the VIKOR method then computes a group utility measure S_j and an individual regret measure R_j as:

$$S_j = \sum_i w_i \frac{f_i^* - f_{i,j}}{f_i^* - f_i^-}, \tag{4.29a}$$

$$R_j = \max_i \; w_i \frac{f_i^* - f_{i,j}}{f_i^* - f_i^-}. \tag{4.29b}$$

Here, S_j measures the overall distance of benchmark j from the ideal point across all criteria, while R_j captures the worst normalized deviation on any single criterion. Small values of S_j and R_j correspond to more attractive benchmarks.

Let

$$S^* = \min_j S_j, \quad S^- = \max_j S_j, \quad R^* = \min_j R_j, \quad R^- = \max_j R_j. \tag{4.30}$$

The VIKOR index Q_j for each benchmark j is then defined as

$$Q_j = v \frac{S_j - S^*}{S^- - S^*} + (1 - v) \frac{R_j - R^*}{R^- - R^*}, \tag{4.31}$$

where $v \in [0, 1]$ is a parameter that reflects the relative importance of the group utility measure versus the individual regret measure. Following [168], a typical choice is $v = 0.5$, which gives equal weight to both.

The benchmarks are then sorted in ascending order of Q_j. The candidate

Algorithm 1 VIKOR method for benchmark ranking

1: **Input:** candidate benchmarks $k_1^{(j)}$, $j = 1, \ldots, n$, with associated criteria values $f_{1,j} = -\bar{\mathcal{G}}\big(k_1^{(j)}\big)$ and $f_{2,j} = \bar{R}^{\mathrm{OOS}}\big(k_1^{(j)}\big)$, and criterion weights w_1, w_2.
2: For each criterion i, compute the best and worst values using (4.28a)–(4.28b).
3: For each benchmark j, compute the group utility measure S_j and the individual regret measure R_j using (4.29a)–(4.29b).
4: Compute S^*, S^-, R^*, and R^- according to (4.30).
5: For each benchmark j, compute the VIKOR index Q_j using (4.31) with a chosen value of v (here $v = 0.5$).
6: Rank all benchmarks in ascending order of Q_j.
7: **Output:** ranking of candidate benchmarks and the compromise benchmark corresponding to the smallest Q_j.

with the smallest value of Q_j is identified as the most desirable compromise solution. In the context of this chapter, this benchmark provides a balanced trade-off between low average regret and high out-of-sample expected profit, and it is therefore selected as the reference benchmark for the SSD-constrained battery bidding model.

For completeness, Algorithm 1 summarizes the implementation of the VIKOR procedure used to rank candidate benchmarks.

4.5. Case Study and Numerical Results

This section evaluates the proposed risk-averse SSD-constrained bidding framework on a representative grid-scale battery storage system. The case study illustrates how the benchmark feasible region is constructed, how the benchmark selection method of Section 4.4 operates in practice, and how the resulting bidding strategies compare with conventional deterministic, stochastic, and robust formulations.

4.5.1 Case Study Setup

The numerical experiments consider a lithium-ion battery storage with a rated power of 35 MW and an energy capacity of five hours, corresponding to a maximum stored energy of 175 MWh. Charging and discharging efficiencies

are set to $\eta^{\mathrm{ch}} = \eta^{\mathrm{dis}} = 0.95$ [169]. The cycle-aging cost function is taken from [147] and represented in the optimization model through a piecewise-linear approximation with $\mathcal{S} = 20$ depth-of-discharge segments.

Day-ahead and intraday electricity prices correspond to the Spanish wholesale market on 16 May 2022 [170]. For the ex-ante analysis, 1000 day-ahead and 1000 intraday price trajectories are generated following the general scenario generation and reduction framework of [163, 171]. Specifically, we model hourly price uncertainty using Gaussian distributions fitted to historical observations from May 2022. This procedure yields 24 hour-specific distributions for the day-ahead market and 24 for the intraday market, parameterized by the empirical mean and standard deviation estimated for each delivery hour. We then generate synthetic price trajectories by independently sampling each hourly price from its corresponding distribution and assembling the 24 sampled values into a daily trajectory. Day-ahead and intraday trajectories are generated in the same manner, without imposing an explicit dependence structure between the two markets. This approach captures hour-by-hour marginal uncertainty but does not explicitly enforce temporal dependence across hours. The resulting sets are reduced to 20 representative scenarios for each market using the reduction method in [163, 171]. The reduced scenario sets are illustrated in Fig. 4.4, which shows the reduced hourly prices in the day-ahead and intraday markets for the delivery day. For the ex-post out-of-sample analysis, an additional set of 1000 scenarios is generated using the same approach, without reduction. Figure 4.5 displays these out-of-sample price trajectories.

The coefficient that limits intraday adjustments relative to the day-ahead positions, denoted by θ in constraints (4.10)–(4.11), is set to $\theta = 0.3$ [168]. This choice restricts the intraday charging and discharging powers to at most 30% of the corresponding day-ahead bids, which reflects the design of the intraday auction under study. All optimization models in this chapter are formulated as MILP and implemented in GAMS [172]. All simulations are conducted on a laptop equipped with an 11th-generation Intel Core i7 processor (2.50 GHz) and 16 GB of memory. They are solved with the CPLEX solver using default settings.

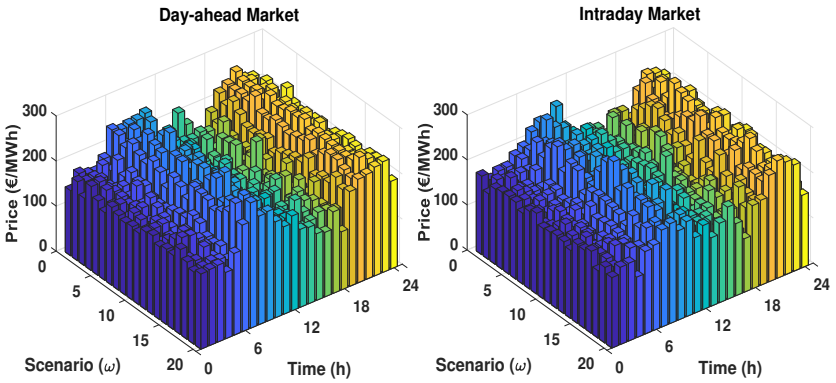

Figure 4.4: Reduced day-ahead and intraday price scenarios for the ex-ante analysis.

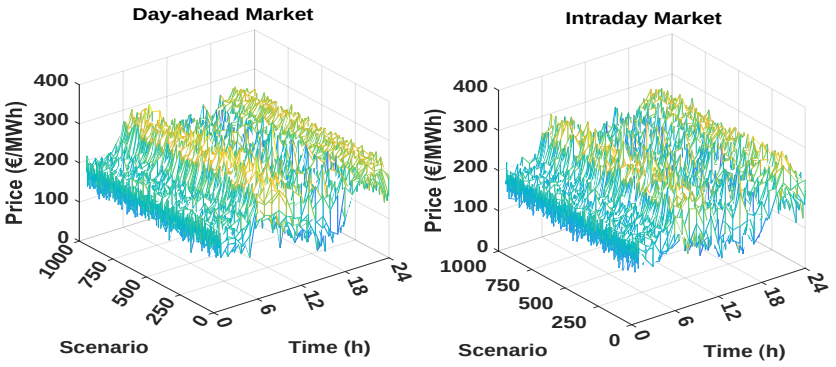

Figure 4.5: One thousand day-ahead and intraday price scenarios for the ex-post out-of-sample analysis.

4.5.2 Step-by-Step Implementation of the Benchmark Selection Method

The first step in applying the SSD-constrained model is to compute the feasible interval for the single-scenario benchmark k_1, as described in Section 4.3.2. This interval is defined by a lower bound k^{L} derived from the risk-neutral strategy and an upper bound k^{U} derived from a highly risk-averse CVaR-maximizing strategy.

Benchmark lower bound. The benchmark lower bound k^{L} is obtained from the risk-neutral model (4.1)–(4.16). Solving this model for the case study yields

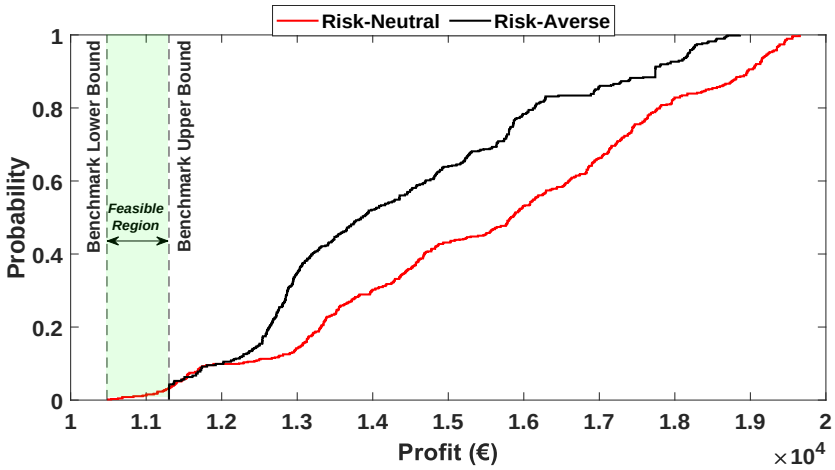

Figure 4.6: Benchmark feasible region in the SSD-constrained bidding problem.

a set of scenario-wise profits, whose minimum value is:

$$k^{\mathrm{L}} = \text{€ } 10{,}480.$$

Figure 4.6 shows the CDF of the risk-neutral profit together with this lower bound. Any benchmark $k_1 < k^{\mathrm{L}}$ would be trivially dominated by the risk-neutral strategy, so the SSD constraints would be non-binding and the SSD-constrained model would reduce to the risk-neutral formulation.

Benchmark upper bound. The upper bound k^{U} is obtained from the CVaR-maximization model in (4.22), with a confidence level β close to one (here $\beta = 0.99$). This auxiliary problem yields an extremely conservative strategy that emphasizes the worst profit realizations. The minimum scenario-wise profit under this strategy is:

$$k^{\mathrm{U}} = \text{€ } 11{,}301.$$

The associated CDF is also plotted in Fig. 4.6 and labelled as "Risk-averse". Any benchmark $k_1 > k^{\mathrm{U}}$ would be impossible to dominate in the SSD sense, so the SSD-constrained model would become infeasible.

The resulting benchmark feasible region is therefore the interval $\text{€}[10480, 11301]$. Following the procedure described in Section 4.4.3, this interval is discretized into $n = 11$ candidate benchmarks. The spacing between

Table 4.1: Performance of the SSD-constrained model for eleven different benchmarks.

$\mathbf{k_1}$ (€)	**Average profit (€)**	**Average regret (€)**	**Maximum regret (€)**	**Average out-of-sample profit (€)**
10,480	15,594.69	2,401.64	5,365.82	15,463.46
10,562.1	15,591.96	2,404.37	5,453.79	15,524.28
10,644.2	15,588.53	2,407.79	5,457.35	15,537.21
10,726.3	15,585.01	2,411.31	5,460.94	15,500.14
10,808.4	15,580.14	2,416.18	5,458.81	15,547.38
10,890.5	15,560.87	2,435.45	5,588.63	15,502.29
10,972.6	15,533.90	2,462.42	5,805.69	15,465.32
11,054.7	15,499.56	2,496.76	6,101.99	15,486.25
11,136.8	15,450.54	2,545.78	6,296.46	15,429.22
11,218.9	15,220.55	2,775.77	6,472.73	15,177.73
11,301	14,901.59	3,094.74	6,695.22	14,699.97

consecutive benchmarks is:

$$\Delta k = \frac{11{,}301 - 10{,}480}{10} = 82.1,$$

so that the candidate benchmarks are

$$k_1^{(j)} = 10{,}480 + (j-1)\Delta k, \quad j = 1, \ldots, 11.$$

These values appear in the first column of Table 4.1.

For each candidate benchmark $k_1^{(j)}$, the SSD-constrained model (4.20) is solved once using the reduced scenario set of Fig. 4.4. The resulting strategy is then evaluated in terms of:

- the average profit over the training scenarios,

- the average and maximum regrets defined in (4.25)–(4.26), using the ideal profits $F_{\omega}^{\text{ideal}}$ from Appendix A.1, and
- the out-of-sample expected profit obtained under the external scenario set of Fig. 4.5, as defined in (4.27).

The numerical values of these metrics for all benchmarks are reported in Table 4.1. Several qualitative observations can be drawn:

1. Average profit decreases as the benchmark increases. This effect becomes more pronounced when benchmarks approach the upper bound k^{U}, since the model must sacrifice more expected profit in order to dominate a very ambitious benchmark.
2. Both average and maximum regrets tend to increase with the benchmark. When the benchmark moves closer to k^{U}, the model pushes the strategy toward more conservative profit distributions, which remain further from the ideal perfect-foresight solution.
3. The impact of the benchmark on the out-of-sample expected profit does not follow a monotone pattern. For moderate benchmark values, the out-of-sample profit remains relatively stable, but it declines sharply when the benchmark approaches k^{U}, reflecting the cost of extreme risk aversion.

These trends highlight the need for a structured multi-criteria approach to benchmark selection, since no single benchmark is uniformly best across all metrics.

To select a single benchmark, the VIKOR method of Algorithm 1 is applied to the set of candidates, using two alternative decision-making strategies with equal weighting parameter $v = 0.5$:

1. **Strategy 1:** criteria are [average regret] and [average out-of-sample profit].
2. **Strategy 2:** criteria are [maximum regret] and [average out-of-sample profit].

For each strategy, the VIKOR index Q_j in (4.31) is computed for all benchmarks and used to rank them in ascending order. The results are summarized

Table 4.2: Ranking of input benchmarks under two decision-making strategies with $v = 0.5$.

$\mathbf{k_1}$ (€)	**Strategy 1** [Average regret + out-of-sample profit]		**Strategy 2** [Maximum regret + out-of-sample profit]	
	Q_j	**Ranking**	Q_j	**Ranking**
10,480	0.063785491	6	0.025124936	5
10,562.1	0.010322632	3	0.006080420	3
10,644.2	**0**	**1**	0.004257288	2
10,726.3	0.034473287	4	0.017734863	4
10,808.4	0.004578009	2	**0.002023471**	**1**
10,890.5	0.041348686	5	0.093387681	6
10,972.6	0.084279533	7	0.234411984	7
11,054.7	0.111004155	8	0.405093215	8
11,136.8	0.181665151	9	0.538744749	9
11,218.9	0.508405027	10	0.720974034	10
11,301	1	11	1	11

in Table 4.2. Under Strategy 1, the compromise solution corresponds to benchmark $k_1 =$ €10,644.2, whereas under Strategy 2 it corresponds to benchmark $k_1 =$ €10,808.4. These compromise benchmarks and their associated Q_j values are highlighted in Table 4.2.

Table 4.3 compares the two compromise benchmarks in terms of average profit, average and maximum regret, and out-of-sample expected profit. Strategy 1 yields slightly higher average profit and lower regret values, while Strategy 2 achieves a marginally higher out-of-sample profit. Figure 4.7 shows the corresponding profit CDFs. The benchmark selected under Strategy 1 leads to a somewhat broader profit range and higher expected profit, whereas Strategy 2 delivers a more conservative distribution. Consistently with the benchmark values, Strategy 2 is therefore more risk-averse than Strategy 1.

Table 4.3: Comparison between compromise benchmarks under decision-making Strategies 1 and 2.

Strategy	Average profit (€)	Average regret (€)	Maximum regret (€)	Average out-of-sample profit (€)
Strategy 1	15,588.53	2,407.79	5,457.35	15,537.21
Strategy 2	15,580.14	2,416.18	5,458.81	15,547.38

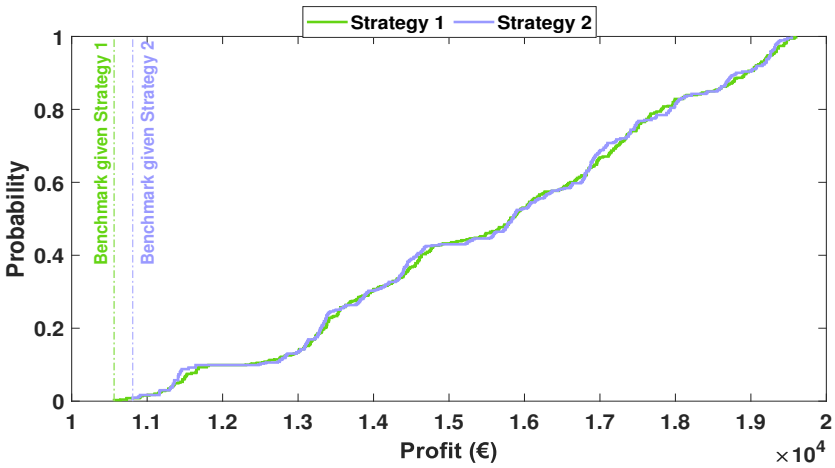

Figure 4.7: CDF of battery storage profit for the compromise benchmarks obtained under Strategies 1 and 2.

4.5.3 Performance Analysis: Comparative Study

The final step is to compare the proposed SSD-constrained model with alternative bidding approaches. Four formulations are considered:

- A deterministic model, in which the scenario set is replaced by the single time series of realized prices on 16 May 2022;
- A pure stochastic programming model, corresponding to the regret-based formulation without SSD constraints;
- A robust programming model, in which uncertainties are represented by uncertainty sets and a robustness parameter; and

Table 4.4: Comparative analysis of different bidding approaches.

Approach	**Average regret (€)**	**Maximum regret (€)**	**Average out-of-sample profit (€)**
Deterministic	2,664.66	6,881.12	15,457.66
Stochastic Programming	2,401.64	5,365.82	15,458.49
Robust programming	3,525.39	7,741.84	15,449.27
Proposed model (Strategy 1)	2,407.79	5,457.35	15,537.21
Proposed model (Strategy 2)	2,416.18	5,458.81	15,547.38

- The proposed SSD-constrained model with the compromise benchmarks selected under Strategies 1 and 2.

The robust formulation and the associated robustness parameters are detailed in Appendix A.2, where the VIKOR method is also used to identify a compromise robustness level. For each approach, average and maximum regrets are computed with respect to the ideal profits $F_{\omega}^{\text{ideal}}$, and out-of-sample expected profit is evaluated using the 1000 external scenarios of Fig. 4.5. The results are summarized in Table 4.4. From a computational perspective, all formulations reported in this section require limited CPU time, since the resulting MILP instances remain small. Based on the CPU time reported by GAMS, the deterministic and robust formulations solve in sub-second time (approximately 0.21 s). The stochastic programming and the SSD-constrained formulations increase the number of continuous variables due to scenario replication. However, the binary decisions remain scenario-independent (24 hourly binary variables). As a result, each MILP instance at a given benchmark level solves within a few seconds, with an average CPU time of about 2.86 s.

Several conclusions emerge from Table 4.4. First, the robust programming model performs poorly in terms of both regret and out-of-sample profit. Since robust optimization focuses on the worst-case realization within the uncertainty set, it tends to produce very conservative strategies that are rarely optimal in typical scenarios, which inflates regret and reduces profitability. When regret is part of the evaluation, such extreme conservatism is difficult to justify.

Second, the deterministic model, which relies on a single point forecast of prices, performs better than the robust model but still exhibits higher regrets than the stochastic approaches. This result reflects the limitations of relying on a single forecast in the presence of significant price uncertainty.

Third, the pure stochastic programming model attains the lowest regret values, since its formulation explicitly minimizes expected regret without additional SSD constraints. However, its out-of-sample profit is lower than that of the proposed model. The introduction of an SSD benchmark therefore slightly deteriorates the regret metrics but improves the robustness of profits when evaluated on external scenarios.

Finally, the proposed SSD-constrained model under both Strategies 1 and 2 delivers the highest out-of-sample expected profits while keeping regret at levels that are close to those of pure stochastic programming. This outcome confirms that the combination of SSD constraints with the benchmark selection method of Section 4.4 provides a favourable balance between downside protection and profitability for the battery storage operator.

4.6. Chapter Conclusion

This chapter has provided the first methodological contribution of the thesis by addressing how a grid-scale battery should bid in day-ahead and intraday markets when price uncertainty and risk aversion are explicitly taken into account. Building on the optimization concepts of Chapter 3 and the storage background of Chapter 2, the chapter has first formulated a two-stage, risk-neutral bidding model for a lithium-ion battery that co-optimizes day-ahead and intraday decisions under inter-temporal energy constraints and degradation costs. It has then extended this formulation to a risk-aware framework based on SSD, in which the profit distribution of the battery is constrained to dominate a benchmark distribution specified by the operator.

A central contribution of the chapter has been to clarify how benchmarks should be handled in SSD-constrained models. On the modelling side, the chapter has shown how to embed SSD constraints in a linear way, how to define a single-scenario benchmark that remains tractable, and how to construct a feasible interval for this benchmark by combining the worst-case outcomes of a risk-neutral and a CVaR-maximizing strategy. On the decision-support side, it has proposed a benchmark selection method that relies on two complementary metrics: an ex-ante regret index that measures the distance to a perfect-foresight

ideal solution, and an ex-post out-of-sample profit that measures generalization to external price scenarios. The VIKOR method has been used to combine these metrics and identify compromise benchmarks that balance downside protection and revenue maximization.

The case study on the Spanish wholesale market has illustrated how these elements fit together in practice. The numerical results have shown that defining a benchmark feasible region helps avoid infeasible or uninformative SSD-constrained problems and guides the search toward economically meaningful benchmarks. They have also confirmed that higher benchmarks tighten the dominance constraints, which reduces average profit and increases both average and maximum regret, especially close to the upper bound of the feasible interval. At the same time, the proposed SSD-constrained model, equipped with the benchmark selection procedure, has delivered higher out-of-sample profits than deterministic, pure stochastic, and robust formulations, while keeping regret at levels that remain close to those of pure stochastic programming. The comparison has further indicated that robust formulations are difficult to justify when regret is part of the evaluation, because worst-case optimization tends to generate strategies that perform poorly in typical conditions.

Overall, this chapter has demonstrated that SSD-based constraints, combined with a structured benchmark selection method, provide a practical way to tailor battery bidding strategies to the preferences of a risk-averse operator. The framework remains compatible with standard MILP tools and can be adapted to alternative market designs or storage technologies. The next chapter builds on these foundations and extends the analysis from lithium-ion batteries to advanced, next-generation storage technologies, where optimization across multi-energy markets becomes central.

Chapter Publication

- **H. Khaloie**, J. Faraji, F. Vallée, C. S. Lai, J.-F. Toubeau, and L. L. Lai, "Risk-Aware Battery Bidding With a Novel Benchmark Selection Under Second-Order Stochastic Dominance," *IEEE Transactions on Industry Applications*, vol. 59, no. 3, pp. 3009–3018, May–June 2023.

CHAPTER 5

Integrated Dispatch of LAES-LNG in Power and LNG Markets

The previous chapter developed a stochastic, risk-aware bidding framework for a grid-scale lithium-ion battery participating in day-ahead and intraday electricity markets. While such batteries provide fast response and short discharge duration, they are not sufficient on their own to cover the multi-hour and multi-day flexibility needs of highly decarbonized energy systems. In addition, their operation can be represented with relatively simple efficiency models, which facilitates market-based dispatch but does not capture the broader class of emerging long-duration storage technologies. By contrast, advanced storage concepts such as LAES thermally coupled with LNG regasification exhibit strong thermo-mechanical interactions, part-load efficiency variations, and multi-energy inputs and outputs that depend on both electricity and LNG flows. These features create new modeling challenges for the dispatch problem, since the plant must be scheduled consistently across coupled markets, under uncertainty in both price processes, and with realistic representations of design performance. Addressing these challenges is important to obtain reliable estimates of project profitability, to reveal the actual system value of LAES-LNG integration, and to provide credible decision-making tools for investors, terminal operators, and policymakers who consider long-duration, sector-coupled storage as part of future net-zero energy systems.

The remainder of this chapter is structured as follows. Section 5.1 reviews the literature on LAES dispatch models and on efficiency improvement strategies for LAES plants, with emphasis on sector-coupled configurations and LNG regasification. Section 5.2 presents the advanced LAES-LNG system description, the market setup, and the main modeling assumptions. Section 5.3 formulates

the two-stage stochastic day-ahead dispatch model for the LAES-LNG facility. Section 5.4 introduces the economic feasibility framework based on a probabilistic payback period under price uncertainty. Section 5.5 describes the case study and reports numerical results. Section 5.6 concludes the chapter and outlines implications for the integration of LAES-LNG systems into future multi-energy markets.

5.1. Literature Review on LAES Dispatch and Efficiency Enhancement

Building on the general overview of LAES technologies provided in Chapter 2, this section focuses on studies that address the dispatch of LAES plants and the improvement of their thermodynamic efficiency. The existing literature can be grouped into works that consider standalone LAES facilities and works that integrate LAES with other processes or energy carriers.

Early contributions on LAES operation investigate standalone plants that participate only in electricity markets and are modeled as bulk storage units with relatively simple efficiency representations [173, 174, 175, 176, 177]. These studies typically optimize the charging and discharging schedules of the plant for arbitrage and, in some cases, for ancillary services, under deterministic or scenario-based electricity prices. They confirm that LAES can provide system value through arbitrage and flexibility, but they also show that investment profitability is difficult to achieve when the plant is operated as a standalone facility with current technology costs and constant round-trip efficiency assumptions. In some cases, the estimated payback period exceeds the technical lifetime of the plant, which highlights the need for efficiency gains or additional revenue streams [173, 174, 175, 176, 177].

A second group of works couples LAES with other processes in order to increase asset utilization and improve overall energy efficiency. Examples include LAES plants integrated with photovoltaic systems or air separation units, where the storage facility absorbs surplus electricity or shares equipment and thermal resources with the co-located process [178, 179, 180]. These configurations can increase the effective round-trip efficiency of LAES by exploiting synergies in compression, liquefaction, and cold recovery. However, most of these studies focus on steady-state operation or simplified scheduling problems and often treat the external process as a fixed boundary condition. Explicit interactions

with multiple energy markets are usually not modeled, and the analysis of long-term project profitability remains limited.

In parallel, several thermodynamic studies examine advanced LAES cycles and component-level performance. These works propose design improvements such as multi-stage compression and expansion, enhanced regeneration, and advanced heat and cold recovery schemes, and assess their impact on cycle efficiency [52, 53, 54, 55, 56]. Other contributions develop detailed models for the steady-state and off-design behavior of LAES components and complete plants, and use these models to analyze part-load operation, start-up and shut-down behavior, or the provision of ancillary services [58, 59, 60, 61]. These studies provide important insight into the technical potential of LAES, but they usually remain disconnected from explicit market design models and do not address the optimal dispatch of LAES under uncertain prices.

LAES has also been proposed as a suitable candidate for sector coupling, in particular through integration with LNG regasification. In such configurations, the large cold exergy released during LNG regasification can be used to assist the liquefaction or power generation processes of the LAES cycle, which may lead to significant efficiency gains [57, 52, 49]. The majority of these works concentrate on thermodynamic performance indicators and on the design of the integrated LAES-LNG facility, often under design or near-design operating conditions. The dispatch of the combined system in coupled electricity and LNG markets, and its profitability under price uncertainty, have received much less attention.

Several authors have pointed out that the performance of LAES is sensitive to the operating point and that off-design operation may significantly reduce effective round-trip efficiency [179, 178, 180, 51]. When dispatch models ignore this behavior and rely on constant efficiency parameters, they may overestimate the energy output and the revenue of LAES projects [179, 173, 174, 175, 176, 177, 178, 180]. Recent reviews on long-duration storage and sector-coupled energy systems recognize LAES as a promising candidate for multi-hour to multi-day flexibility and for the integration of electricity and gas infrastructures [34, 50]. At the same time, they underline the need for market-based models that combine realistic efficiency representations with explicit participation in multiple markets.

Despite this growing body of work, important gaps remain in the dispatch and economic assessment of LAES facilities thermally integrated with LNG regasification. Existing dispatch studies either focus on standalone LAES plants

or consider simplified couplings with other processes, and thermodynamic analyses of LAES-LNG integration rarely include a consistent market-based operation model. Economic assessments often rely on deterministic payback or net present value calculations and do not account for the joint uncertainty of electricity and LNG prices. In this chapter, these gaps are addressed by developing a two-stage stochastic day-ahead dispatch model for an LAES-LNG facility that participates simultaneously in electricity and LNG markets and evaluates investment attractiveness using a probabilistic payback period under price uncertainty.

5.2. Advanced LAES-LNG System, Market Environment, and Modeling Assumptions

The literature reviewed in Section 5.1 highlights that the technical performance and economic prospects of LAES strongly depend on plant configuration and the way the facility interacts with energy markets. These aspects become even more critical when LAES is thermally coupled with LNG regasification, since the combined system relies on multiple energy carriers and exhibits tightly coupled thermo-mechanical processes. To support the dispatch model developed in Section 5.3 and the subsequent economic feasibility analysis, this section describes the configuration of the proposed LAES-LNG facility, introduces the day-ahead electricity and LNG market environment in which it operates, and states the main modeling assumptions adopted in this chapter.

5.2.1 System Description

Figure 5.1 shows the layout of the proposed LAES-LNG facility. In addition to the three subsystems already discussed in Chapter 2 for standalone LAES, namely charging, storage, and discharging, the integrated facility includes three additional components: LNG storage, a regasification unit, and a combustor. These components are responsible for the physical coupling between the electricity and LNG chains within the plant.

Similar to a standalone LAES installation, the charging subsystem draws electricity from the grid to drive air compressors. The compressed ambient air then enters the liquefaction unit, where it is cooled and converted into liquid air, which is stored in a cryogenic liquid air tank. The cold energy required by the liquefaction unit is supplied from two sources: (i) the cold released during

liquid air evaporation and (*ii*) the cold exergy available from LNG regasification. The second source is specific to the LAES-LNG configuration and creates a first point of interaction between the electricity-based charging process and the LNG system.

In parallel, an authorized terminal supplies LNG to the on-site LNG storage. When the plant operator schedules electricity generation, the liquefied air stored in the liquid air tank is pressurized and sent to the combustor. At the same time, LNG is routed through the regasification unit, where it is converted into natural gas, and then conveyed to the combustor. Inside the combustor, the high-pressure air and natural gas are mixed and co-fired. The resulting high-temperature working fluid expands in a gas turbine that drives an electrical generator. In this way, the discharge process of the LAES subsystem is directly linked to the LNG stream, and the energy flows between the LNG system and the LAES discharging subsystem become strongly interconnected. A high-level estimate of the direct combustion-related CO_2 emissions indicates that, under the adopted heat rate assumption, the LAES-LNG discharge block emits approximately 63% less CO_2 per MWh than a reference simple-cycle gas turbine; Appendix A.3 provides the detailed calculation.

Compared with a standalone LAES plant, the proposed LAES-LNG configuration exploits the large cold exergy of LNG regasification to assist liquefaction and to improve the overall thermodynamic efficiency of the cycle. At the same time, the combined use of electricity and LNG as inputs, and electricity and regasified gas as outputs, requires a dispatch model that captures the joint scheduling of these flows in a consistent way. The schematic layout in Fig. 5.1 provides the physical basis for the mathematical formulation developed in Section 5.3.

5.2.2 Market Setup

The day-ahead dispatch of the LAES-LNG facility requires a consistent representation of its interaction with the markets of the involved energy carriers, namely electricity and LNG. In deregulated environments, both electricity and gas derivatives, including LNG, can be traded in organized markets to meet the needs of suppliers and consumers. This chapter adopts the Spanish market framework as a representative example, given the country's liquid LNG market enabled by multiple operational regasification terminals, while keeping the modeling approach adaptable to other market designs.

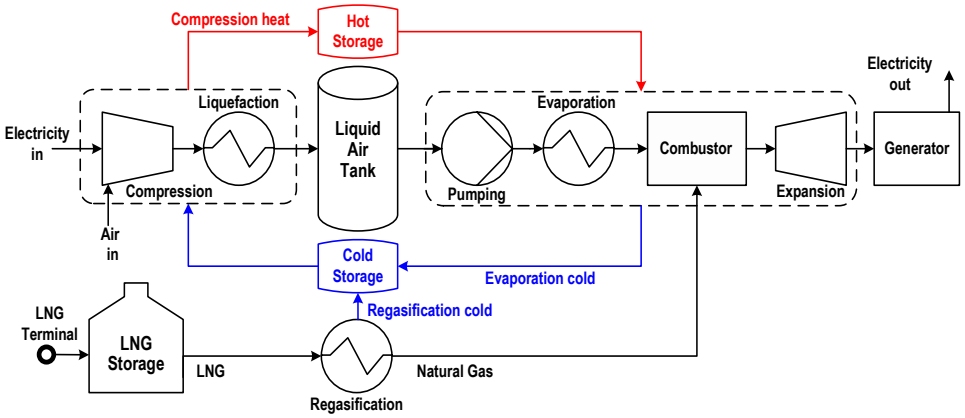

Figure 5.1: Schematic layout of the proposed LAES-LNG facility.

In the Spanish context, electricity is traded in the Iberian electricity market operated by OMIE,[1] whereas LNG is traded in the Iberian gas derivatives market operated by MIBGAS.[2] Both commodities can be traded one day in advance, and additional products are available for longer and shorter time frames. A distinctive feature of the Iberian LNG market is the presence of the *virtual balancing tank* (TVB[3]), which allows any market participant to trade LNG without being tied to a specific physical terminal.

Before the introduction of the TVB, LNG transactions were fragmented and linked to individual LNG terminals or regasification plants. The TVB, which has been in operation since April 1, 2020, aggregates the storage capacities of all Spanish regasification plants into a single virtual tank. In practice, this integration creates a unified LNG hub where market participants can buy and sell LNG independently of the physical location where the LNG is stored. The consolidation of storage capacity and the removal of terminal-specific constraints increase the number of potential counterparties and enhance market liquidity and efficiency.

Figure 5.2 illustrates the day-ahead market setup for electricity and LNG. The day-ahead LNG market is cleared at 11:00 a.m., while the day-ahead electricity market is cleared one hour later, at noon. As a result, the LAES-LNG facility must submit its LNG bids for the next day before 11:00 a.m. The results of the LNG market are published shortly after closure, which provides the facility

[1]OMIE (Operador del Mercado Ibérico de Energía): https://www.omie.es/.
[2]MIBGAS (Mercado Ibérico de Gas): https://www.mibgas.es/.
[3]Tanque Virtual de Balance.

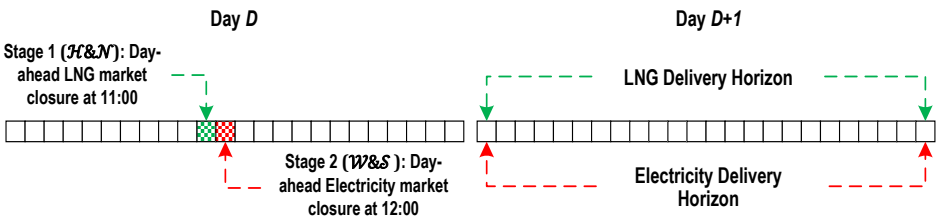

Figure 5.2: Market setup for day-ahead electricity and LNG trading.

with perfect information on next-day LNG prices when submitting its day-ahead electricity bids and offers[4] before noon. Immediately after the electricity market is cleared, the operator receives the accepted quantities and prices, and fixes the next-day schedule of the LAES-LNG facility. This sequential structure underpins the two-stage stochastic dispatch formulation described in Section 5.3.

5.2.3 Model Assumptions

The day-ahead dispatch model for the LAES-LNG facility relies on the following assumptions:

- The LAES-LNG facility is modeled as a perfectly competitive market participant in both electricity and LNG markets. It takes market prices as given, has no market power, and operates under steady-state conditions at the time scale of the day-ahead schedule.
- A two-stage stochastic program is used to represent sequential decision-making in the presence of uncertain day-ahead electricity and LNG prices, consistent with the market sequence in Fig. 5.2. The uncertainties are represented by discrete scenarios generated from Gaussian distributions [181, 182, 183]. For a daily dispatch horizon, a set of 24 individual Gaussian distributions is employed to generate electricity price scenarios, with each distribution corresponding to a specific hour of the next day. Since the LNG price is assumed to remain constant throughout the day, a single Gaussian distribution is used to generate LNG price scenarios.
- The economic feasibility study, and in particular the payback period analysis, accounts for uncertainty in both investment cost and annual

[4]Throughout this chapter, bids and offers refer to buying and selling quantities, respectively.

profit. These quantities are modeled as Gaussian random variables. Using probability distributions for investment cost and annual profit allows decision-makers to characterize the range of plausible outcomes and their associated probabilities, rather than relying on single-point estimates. This is particularly relevant for LAES-LNG projects, where annual profit depends on volatile electricity and LNG prices, and where cost estimation is subject to significant uncertainty due to the scale and complexity of the required infrastructure. The choice of Gaussian distributions is supported by three arguments: (*i*) the central limit theorem, which states that the sum of many independent and identically distributed random variables tends to a normal distribution [184]; (*ii*) extensive empirical evidence indicating that many economic variables, including investment costs and profits, can be approximated reasonably well by Gaussian distributions [185, 186]; and (*iii*) the widespread use of Gaussian models in engineering practice, which benefits from their convenient analytical properties.

These assumptions provide a tractable yet informative representation of the LAES-LNG facility and its market environment. They form the basis for the stochastic dispatch formulation presented in Section 5.3 and for the probabilistic payback period analysis developed in Section 5.4.

5.3. Two-Stage Stochastic Day-Ahead Dispatch Model for LAES-LNG Coupled Operation

Building on the physical configuration and market environment described in Section 5.2, this section develops the day-ahead dispatch model for the LAES-LNG facility. The formulation follows the two-stage stochastic programming framework introduced in Chapter 3, with first-stage decisions that must be taken before the LNG market is cleared and second-stage decisions that are adjusted once LNG prices are revealed and before the day-ahead electricity market closure. For completeness, Appendix A.4 summarizes the corresponding dispatch model for a standalone LAES facility, adapted from [173], which provides a useful reference for assessing the added value of the LAES-LNG integration.

The market setup described in Fig. 5.2 requires a sequential interaction with LNG and electricity markets. To capture this sequence, the day-ahead dispatch problem is formulated as a two-stage stochastic program with the following decision structure.

1. ***Here-and-now* ($\mathcal{H}\&\mathcal{N}$) decisions**: Before 11:00 a.m. of the current day, the facility must submit its LNG bids for the next day. The corresponding $\mathcal{H}\&\mathcal{N}$ decisions include the quantities of LNG to be purchased in the day-ahead LNG market, denoted by h_t, and the associated charging status of the LNG storage. LNG can only be transferred from the TVB to the on-site LNG storage if the storage is in charging mode, so the binary variable β_t^{ch} is modeled as a first-stage decision that is linked to the values of h_t. These decisions are taken before the realization of LNG prices and before the first market closure at 11:00 a.m. The set of *here-and-now* decision variables $\Xi^{\mathcal{H}\&\mathcal{N}}$ is:

$$\Xi^{\mathcal{H}\&\mathcal{N}} = \left\{ h_t,\, H^{\text{tot}},\, \beta_t^{\text{ch}} \right\}.$$

2. ***Wait-and-see* ($\mathcal{W}\&\mathcal{S}$) decisions**: Shortly after 11:00 a.m., the results of the day-ahead LNG market are revealed. Between this time and the electricity market closure at noon, the facility must decide on its day-ahead electricity bids and offers for the next day. The $\mathcal{W}\&\mathcal{S}$ decisions include the quantities offered and bid in the day-ahead electricity market and the operational schedule of the LAES-LNG facility, such as the discharging status of the LNG storage, the charging and discharging of the LAES plant, and the evolution of both storage inventories. These decisions are adapted to the realization of LNG and electricity price scenarios and are therefore modeled as second-stage variables. The set of *wait-and-see* decision variables $\Xi^{\mathcal{W}\&\mathcal{S}}$[5] includes:

$$\Xi^{\mathcal{W}\&\mathcal{S}} = \left\{ P_{l,d,t}^{\text{dis}},\, P_{l,d,t}^{\text{ch}},\, q_{l,d,t}^{\text{LNG}},\, q_{l,d,t}^{\text{LAES}},\, \alpha_{l,t}^{\text{dis}},\, \alpha_{l,t}^{\text{ch}}, \beta_{l,t}^{\text{dis}} \right\}.$$

The day-ahead dispatch model maximizes the expected profit of the LAES-LNG facility over a 24-hour horizon ($\mathcal{T} = 24$ time periods of length $k_t = 1$ hour) under the two-stage stochastic setup described above:

[5] All *wait-and-see* decision variables are introduced and defined at their first appearance in the mathematical formulation that follows.

$$\max_{\Xi^{\mathcal{H}\&\mathcal{N}},\Xi^{\mathcal{W}\&\mathcal{S}}} \mathbb{E}\,\mathcal{F}(y,\theta_l,\theta_d) = \sum_{t\in\mathcal{T}}\Bigg[\mathbb{E}_{\mathcal{H}\&\mathcal{N}}\Big[\underbrace{-h_t k_t \lambda_l^{\mathrm{LNG}}}_{\mathcal{O}_1} + \mathbb{E}_{\mathcal{W}\&\mathcal{S}|\mathcal{H}\&\mathcal{N}}\big[\underbrace{P_{l,d,t}^{\mathrm{dis}} k_t \lambda_{d,t}^{\mathrm{Elec}}}_{\mathcal{O}_2} \underbrace{-P_{l,d,t}^{\mathrm{ch}} k_t \lambda_{d,t}^{\mathrm{Elec}}}_{\mathcal{O}_3} - \underbrace{P_{l,d,t}^{\mathrm{dis}} k_t \vartheta^{\mathrm{dis}}}_{\mathcal{O}_4} - \underbrace{P_{l,d,t}^{\mathrm{ch}} k_t \vartheta^{\mathrm{ch}}}_{\mathcal{O}_5}\big]\Big]\Bigg] \tag{5.1}$$

where $\mathcal{F}(y,\theta_l,\theta_d)$ denotes the profit function of the facility, y is the vector of decision variables, and θ_l and θ_d collect the parameters associated with LNG and electricity price scenarios, respectively. The outer expectation $\mathbb{E}_{\mathcal{H}\&\mathcal{N}}[\cdot]$ is taken with respect to LNG price scenarios, while $\mathbb{E}_{\mathcal{W}\&\mathcal{S}|\mathcal{H}\&\mathcal{N}}[\cdot]$ represents the conditional expectation with respect to electricity price scenarios given a particular LNG price realization.

For each time period t, term $\mathcal{O}_1$ represents the expected cost of purchasing LNG in the day-ahead LNG market to load the on-site LNG storage. Since h_t does not depend on any scenario realization, $\mathcal{O}_1$ corresponds to the first-stage component of the objective function in the terminology of two-stage stochastic programming. Term $\mathcal{O}_2$ is the expected revenue from selling electricity generated by the gas turbine to the day-ahead electricity market. Term $\mathcal{O}_3$ corresponds to the cost of buying electricity from the grid to liquefy air and store it in the liquid air tank. Finally, $\mathcal{O}_4$ and $\mathcal{O}_5$ represent the variable operating costs in discharging and charging modes, respectively. Together, $\mathcal{O}_2$ to $\mathcal{O}_5$ define the recourse function, that is, the second-stage profit associated with a given realization of LNG prices.

The objective function in (5.1) is subject to technical and market constraints that describe the operation of the LNG storage, the LAES plant, and the participation of the facility in the day-ahead electricity market.

LNG market and storage constraints. Equation (5.2) specifies the total quantity of LNG transferred from the TVB to the on-site LNG storage over the dispatch horizon. The parameter H^{tot} denotes the total daily LNG volume

purchased by the facility:

$$\sum_{t\in\mathcal{T}} h_t k_t = H^{\text{tot}}, \quad h_t \geq 0. \tag{5.2}$$

According to the rules of the Iberian LNG derivatives market, the daily volume of LNG purchased by a participant must lie within a prescribed range. This requirement is captured by

$$\underline{\Psi^{\text{LNG}}} \leq H^{\text{tot}} \leq \overline{\Psi^{\text{LNG}}} \tag{5.3}$$

where $\underline{\Psi^{\text{LNG}}}$ and $\overline{\Psi^{\text{LNG}}}$ denote the minimum and maximum allowed total purchases, respectively.

The liquid level of the on-site LNG storage at each period depends on four factors: (*i*) the previous liquid level, (*ii*) the boil-off rate of the storage tank, (*iii*) the quantity of LNG injected from the TVB, and (*iv*) the quantity of LNG withdrawn and sent to the regasification unit. The boil-off rate represents the fraction of LNG that evaporates naturally and is lost as gas. The inventory dynamics for the first period and the remaining periods are as follows:

$$\begin{aligned} q^{\text{LNG}}_{l,d,t} = q^{\text{LNG}}_0 \left(1 - \frac{\mathcal{R}^{\text{LNG}}}{24}\right) + \frac{h_t k_t \times 3600}{\text{LHV} \times \varpi} - \\ \frac{P^{\text{dis}}_{l,d,t} k_t \times \text{HR} \times 3600}{\eta \times \text{LHV} \times \varpi} \quad \forall t = 1, \forall l, \forall d \end{aligned} \tag{5.4}$$

$$\begin{aligned} q^{\text{LNG}}_{l,d,t} = q^{\text{LNG}}_{l,d,t-1} \left(1 - \frac{\mathcal{R}^{\text{LNG}}}{24}\right) + \frac{h_t k_t \times 3600}{\text{LHV} \times \varpi} - \\ - \frac{P^{\text{dis}}_{l,d,t} k_t \times \text{HR} \times 3600}{\eta \times \text{LHV} \times \varpi} \quad \forall t \geq 2, \forall l, \forall d \end{aligned} \tag{5.5}$$

where the factor 3600 converts MWh to MJ, LHV is the lower heating value of LNG, ϖ is the density, $\mathcal{R}^{\text{LNG}}$ is the hourly boil-off rate, HR is the heat rate of the gas turbine, and η is its efficiency.

The storage level must be cyclic and respect operational bounds:

$$q^{\text{LNG}}_{l,d,t} = q^{\text{LNG}}_0 \quad \forall t = 24, \forall l, \forall d \tag{5.6}$$

$$\underline{\mathcal{Q}^{\mathrm{LNG}}} \leq q_{l,d,t}^{\mathrm{LNG}} \leq \overline{\mathcal{Q}^{\mathrm{LNG}}} \quad \forall t, \forall l, \forall d \tag{5.7}$$

where $\underline{\mathcal{Q}^{\mathrm{LNG}}}$ and $\overline{\mathcal{Q}^{\mathrm{LNG}}}$ represent the minimum and maximum admissible LNG inventory.

The instantaneous LNG transfer from the TVB to the LNG storage cannot exceed the loading capacity of the storage:

$$0 \leq \frac{h_t k_t \times 3600}{\mathrm{LHV} \times \varpi} \leq \xi^{\ell} \beta_t^{\mathrm{ch}} \quad \forall t, \left\{\beta_t^{\mathrm{ch}}\right\} \in \{0,1\} \tag{5.8}$$

where ξ^{ℓ} denotes the maximum loading rate. Conversely, the LNG sent from the storage to the regasification unit must not exceed the unloading capacity:

$$\frac{P_{l,d,t}^{\mathrm{dis}} k_t \times \mathrm{HR} \times 3600}{\eta \times \mathrm{LHV} \times \varpi} \leq \xi^{\wp} \beta_{l,t}^{\mathrm{dis}} \quad \forall t, \forall l, \left\{\beta_{l,t}^{\mathrm{dis}}\right\} \in \{0,1\} \tag{5.9}$$

where $\xi^{\wp}$ is the maximum unloading rate. The following constraint prevents simultaneous charging and discharging of the LNG storage:

$$\beta_{l,t}^{\mathrm{dis}} + \beta_t^{\mathrm{ch}} \leq 1 \quad \forall t, \forall l, \left\{\beta_{l,t}^{\mathrm{dis}}, \beta_t^{\mathrm{ch}}\right\} \in \{0,1\} \tag{5.10}$$

As discussed above, the charging status β_t^{ch} is a $\mathcal{H}\&\mathcal{N}$ decision linked to the LNG bids h_t, whereas the discharging status $\beta_{l,t}^{\mathrm{dis}}$ is a $\mathcal{W}\&\mathcal{S}$ decision that depends on the realization of LNG prices and on the electricity dispatch schedule.

LAES power limits and inventory dynamics. Constraints (5.11) and (5.12) impose lower and upper bounds on the power sold and bought by the LAES plant in the day-ahead electricity market, through offers and bids:

$$\underline{\mathcal{P}^{\mathrm{dis}}} \alpha_{l,t}^{\mathrm{dis}} \leq P_{l,d,t}^{\mathrm{dis}} \leq \overline{\mathcal{P}^{\mathrm{dis}}} \alpha_{l,t}^{\mathrm{dis}} \quad \forall t, \forall l, \forall d \tag{5.11}$$

$$\underline{\mathcal{P}^{\mathrm{ch}}} \alpha_{l,t}^{\mathrm{ch}} \leq P_{l,d,t}^{\mathrm{ch}} \leq \overline{\mathcal{P}^{\mathrm{ch}}} \alpha_{l,t}^{\mathrm{ch}} \quad \forall t, \forall l, \forall d \tag{5.12}$$

where $\underline{\mathcal{P}^{\mathrm{dis}}}$ and $\overline{\mathcal{P}^{\mathrm{dis}}}$ are the minimum and maximum discharge powers, and $\underline{\mathcal{P}^{\mathrm{ch}}}$ and $\overline{\mathcal{P}^{\mathrm{ch}}}$ are the corresponding charging limits. The binary variables $\alpha_{l,t}^{\mathrm{dis}}$ and $\alpha_{l,t}^{\mathrm{ch}}$ indicate whether the plant is in discharging or charging mode in period t for LNG scenario l.

Simultaneous charging and discharging of the LAES plant is prevented by

$$\alpha_{l,t}^{\mathrm{dis}} + \alpha_{l,t}^{\mathrm{ch}} \leq 1 \quad \forall t, \forall l, \left\{\alpha_{l,t}^{\mathrm{dis}}, \alpha_{l,t}^{\mathrm{ch}}\right\} \in \{0,1\} \tag{5.13}$$

The liquid energy level in the liquid air tank evolves according to the previous inventory, the boil-off losses, the energy associated with liquefying air during charging, and the energy withdrawn during discharging. For the first and subsequent periods, the dynamics are

$$q_{l,d,t}^{\mathrm{LAES}} = q_0^{\mathrm{LAES}} \left(1 - \frac{\mathcal{R}^{\mathrm{LAES}}}{24}\right) + P_{l,d,t}^{\mathrm{ch}} k_t - P_{l,d,t}^{\mathrm{dis}} k_t \mathrm{ER} \quad \forall t = 1, \forall l, \forall d \tag{5.14}$$

$$q_{l,d,t}^{\mathrm{LAES}} = q_{l,d,t-1}^{\mathrm{LAES}} \left(1 - \frac{\mathcal{R}^{\mathrm{LAES}}}{24}\right) + P_{l,d,t}^{\mathrm{ch}} k_t - P_{l,d,t}^{\mathrm{dis}} k_t \mathrm{ER} \quad \forall t \geq 2, \forall l, \forall d \tag{5.15}$$

where $\mathcal{R}^{\mathrm{LAES}}$ denotes the boil-off rate of the liquid air tank and ER is the energy ratio, defined as the ratio between the energy produced during expansion and the electrical energy consumed in liquefaction. The energy ratio captures the effective round-trip efficiency of the LAES subsystem under the selected operating point.

As for the LNG storage, the liquid air inventory is required to be cyclic and to remain within design limits:

$$q_{l,d,t}^{\mathrm{LAES}} = q_0^{\mathrm{LAES}} \quad \forall t = 24, \forall l, \forall d \tag{5.16}$$

$$\underline{\mathcal{Q}^{\mathrm{LAES}}} \leq q_{l,d,t}^{\mathrm{LAES}} \leq \overline{\mathcal{Q}^{\mathrm{LAES}}} \quad \forall t, \forall l, \forall d \tag{5.17}$$

Non-anticipativity and structure of offering and bidding curves. Because the LAES-LNG facility participates in day-ahead markets, it must submit offering and bidding curves rather than single dispatch quantities. The variables $P_{l,d,t}^{\mathrm{ch}}$ and $P_{l,d,t}^{\mathrm{dis}}$ therefore carry the index of electricity price scenarios d even though they are second-stage decisions. This representation allows the optimization model to determine the energy-price pairs that form the bidding and offering curves, while respecting non-anticipativity.

Non-anticipativity requires that decisions cannot discriminate between scenarios that are indistinguishable at the time the decision is made. For LNG price scenarios l and l' that lead to identical price realizations, the offered and bid power levels must be equal:

$$P^{\text{dis}}_{l,d,t} = P^{\text{dis}}_{l',d,t} \quad \text{if} \quad \lambda^{\text{LNG}}_{l} = \lambda^{\text{LNG}}_{l'} \quad \forall t, \forall l, \forall l', d \tag{5.18}$$

$$P^{\text{ch}}_{l,d,t} = P^{\text{ch}}_{l',d,t} \quad \text{if} \quad \lambda^{\text{LNG}}_{l} = \lambda^{\text{LNG}}_{l'} \quad \forall t, \forall l, \forall l', d \tag{5.19}$$

Similarly, when two electricity price scenarios d and d' yield the same price at a given period, the facility must submit identical offering and bidding quantities:

$$P^{\text{dis}}_{l,d,t} = P^{\text{dis}}_{l,d',t} \quad \text{if} \quad \lambda^{\text{Elec}}_{d,t} = \lambda^{\text{Elec}}_{d',t} \quad \forall t, \forall l, \forall d, d' \tag{5.20}$$

$$P^{\text{ch}}_{l,d,t} = P^{\text{ch}}_{l,d',t} \quad \text{if} \quad \lambda^{\text{Elec}}_{d,t} = \lambda^{\text{Elec}}_{d',t} \quad \forall t, \forall l, \forall d, d' \tag{5.21}$$

The day-ahead electricity market operator also specifies that offering and bidding curves must satisfy monotonicity properties to ensure well-behaved aggregate supply and demand and to facilitate price discovery. The following constraints enforce an increasing structure for offers and a decreasing structure for bids:

$$P^{\text{dis}}_{l,d,t} \geq P^{\text{dis}}_{l,d',t} \quad \text{if} \quad \lambda^{\text{Elec}}_{d,t} \geq \lambda^{\text{Elec}}_{d',t} \quad \forall t, \forall l, \forall d, d' \tag{5.22}$$

$$P^{\text{ch}}_{l,d,t} \leq P^{\text{ch}}_{l,d',t} \quad \text{if} \quad \lambda^{\text{Elec}}_{d,t} \geq \lambda^{\text{Elec}}_{d',t} \quad \forall t, \forall l, \forall d, d' \tag{5.23}$$

In the literature, decision variables such as $P^{\text{ch}}_{l,d,t}$ and $P^{\text{dis}}_{l,d,t}$, which appear in the second stage but depend on price scenarios through offering and bidding curves, are sometimes referred to as "special" $\mathcal{W}\&\mathcal{S}$ variables [166]. They are still classified as second-stage variables, but they play a dual role by both responding to realized prices and defining the schedule-dependent structure of the submitted curves.

Summarizing, variables h_t and β^{ch}_t are $\mathcal{H}\&\mathcal{N}$ decisions, while variables $\beta^{\text{dis}}_{l,t}$, $\alpha^{\text{ch}}_{l,t}$, $\alpha^{\text{dis}}_{l,t}$, $P^{\text{ch}}_{l,d,t}$, $P^{\text{dis}}_{l,d,t}$, $q^{\text{LNG}}_{l,d,t}$, and $q^{\text{LAES}}_{l,d,t}$ are $\mathcal{W}\&\mathcal{S}$ decisions in the proposed two-stage day-ahead dispatch model.

Figure 5.3 provides a high-level view of the dispatch process. Input param-

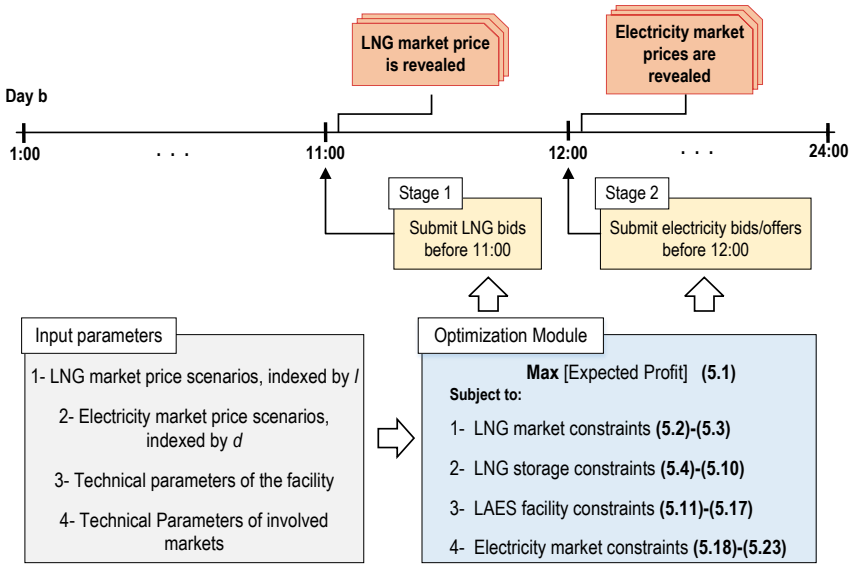

Figure 5.3: High-level diagram of the day-ahead LAES-LNG dispatch process.

eters such as LNG and electricity price scenarios, technical parameters of the LAES-LNG facility, and market specifications are fed into the optimization module that implements the objective function (5.1) subject to constraints (5.2)-(5.23). The module produces optimal LNG purchase quantities h_t and electricity offering and bidding curves $P^{\text{dis}}_{l,d,t}$ and $P^{\text{ch}}_{l,d,t}$. In practice, the facility first submits its LNG bids before 11:00 a.m. based on the optimal h_t. Once the LNG market results are published, it submits its electricity offers and bids before noon based on the optimized curves. The resulting schedule is then used in the subsequent economic feasibility analysis of Section 5.4.

5.4. Economic Feasibility Assessment via Probabilistic Payback Period

The day-ahead dispatch model developed in Section 5.3 provides the short-term operating strategy and the associated annual profit of the LAES-LNG facility under price uncertainty. For substantive deployment, however, investors, system operators, or public agencies also need to assess whether such a project is economically attractive over its lifetime. An economic feasibility study evaluates the viability of undertaking the project by comparing its investment cost with

$$f(g) = \frac{\sqrt{1-\rho^2}}{\pi\sigma_z\sigma_x a^2(g)} \exp\left(\frac{-m}{2\left(1-\rho^2\right)}\right) + \frac{b(g)n(g)}{2\sqrt{2\pi}\sigma_x\sigma_z a^3(g)} \times \left[\Theta\left(\frac{b(g)}{a(g)\sqrt{2\left(1-\rho^2\right)}}\right) - \Theta\left(\frac{-b(g)}{a(g)\sqrt{2\left(1-\rho^2\right)}}\right)\right] \tag{5.24a}$$

where

$$a(g) = \sqrt{\frac{g^2}{\sigma_x^2} - \frac{2\rho g}{\sigma_x\sigma_z} + \frac{1}{\sigma_z^2}}, \quad b(g) = \frac{\mu_x g}{\sigma_x^2} - \frac{\rho\left(\mu_x + \mu_z g\right)}{\sigma_x\sigma_z} + \frac{\mu_z}{\sigma_z^2},$$
$$m = \frac{\mu_x^2}{\sigma_x^2} - \frac{2\rho\mu_x\mu_z}{\sigma_x\sigma_z} + \frac{\mu_z^2}{\sigma_z^2}, \quad n(g) = \exp\left(\frac{b^2(g) - m a^2(g)}{2\left(1-\rho^2\right)a^2(g)}\right),$$
$$\Theta(\psi) = \frac{2}{\sqrt{\pi}} \int_0^{\psi} \exp\left(-u^2\right) du \tag{5.24b}$$

---

the expected stream of benefits. A primary metric in this context is the *payback period*, which measures the time required for an investment to recover its initial cost through accumulated profits.

Let X denote the total investment cost in euro [€] and Z the annual profit in euro per year [€/year]. The payback period G in years is defined as:

$$G = \frac{X}{Z}$$

In a deterministic assessment, X and Z would be treated as fixed values and G would be a single number. In practice, both quantities are subject to uncertainty. Investment cost depends on equipment prices, engineering and construction costs, and financing conditions, while annual profit depends on volatile electricity and LNG prices and on the operational flexibility of the facility. As discussed in Section 5.2, these uncertainties are modeled as Gaussian random variables for investment cost and annual profit. In this setting, it is more informative to characterize the full probability distribution of the payback period G rather than a single point estimate.

The probability density function of G can be obtained in several ways, including analytical, simulation-based, or purely statistical approaches. In

this work, a statistical method is adopted in which both the investment cost and the annual profit are modeled as correlated Gaussian random variables, $X \sim \mathcal{N}(\mu_x, \sigma_x)$ and $Z \sim \mathcal{N}(\mu_z, \sigma_z)$ [187]. The method, known as the Hinkley approach [187], provides a closed-form expression for the probability density function of the ratio of two Gaussian variables. It offers a sound and computationally efficient way to estimate the distribution of G and can handle censored and uncensored data [188]. The correlation coefficient between X and Z is denoted by ρ[6]. Although the method is applied here to the payback period of the LAES-LNG facility, it is general and can be used for any quantity defined as the ratio of two Gaussian random variables. According to the Hinkley approach, the resulting probability density function of the payback period G is given in Formula (5.24), where the expression for $f(g)$ is presented.

Once (5.24) is evaluated, the resulting density $f(g)$ provides a complete probabilistic description of the payback period. From this density, standard summary statistics such as the mean payback period μ_g [year(s)] and its standard deviation σ_g [year(s)] can be computed as

$$\mu_g = \int_{-\infty}^{+\infty} g f(g)\, dg \tag{5.25}$$

$$\sigma_g = \sqrt{\int_{-\infty}^{+\infty} (g - \mu_g)^2 f(g)\, dg} \tag{5.26}$$

In addition, the cumulative distribution associated with $f(g)$ can be used to answer practical questions such as the probability that the payback period is below a given threshold, for example 15 years, or to quantify the risk that the project fails to recover its investment within a target horizon.

Other financial indicators are also widely used in economic feasibility studies, such as net present value and internal rate of return [163]. These indicators provide complementary information on the long-term profitability of investment projects. A detailed analysis based on these metrics is beyond the scope of this chapter, which focuses on the probabilistic payback period as a transparent and intuitive measure to summarize the economic attractiveness of the LAES-LNG facility under uncertainty. The resulting distribution of G will be used in Section 5.5 to interpret the numerical results of the case study and to discuss the conditions under which LAES-LNG projects can become financially viable.

[6]This coefficient takes values $-1 \leq \rho \leq +1$.

5.5. Case Study Setup and Numerical Results

The stochastic dispatch model and the probabilistic payback framework developed in Sections 5.3 and 5.4 provide the methodological basis for assessing the economic performance of the proposed LAES-LNG facility. This section applies these tools to a representative case study in the Spanish electricity and LNG markets and quantifies both short-term profitability and long-term economic feasibility.

The analysis proceeds in two steps. First, a detailed day-ahead dispatch study evaluates the expected profit of the LAES-LNG facility under a representative price profile and compares its performance with two benchmark standalone LAES plants. The comparison isolates the impact of thermal integration with LNG regasification on market revenues and operating patterns. Second, an economic feasibility study combines the dispatch model with observed electricity and LNG prices in 2021 and 2022 to estimate the probability distribution of the payback period based on the Hinkley approach introduced in Section 5.4. This step connects the short-term arbitrage opportunities of the integrated facility with long-term investment risk.

Technical configuration and model implementation

Table 5.1 summarizes the technical characteristics of the LAES-LNG facility considered in the case study [57]. The plant consists of an LNG storage tank, a liquid air tank, an LNG regasification unit, and a LAES system whose charging and discharging processes follow the configuration described in Section 5.2. The average USD-EUR exchange rate in 2021, equal to 0.8458, is used to convert all cost-related parameters to euro [189].

The LAES-LNG facility includes an LNG storage tank of 217 m^3, a liquid air tank with an energy capacity of 480 MWh, an LNG regasification unit with 97% efficiency [190], and a LAES system with discharge and charge rates of 122.2 MW and 60 MW, respectively. The lower bounds on the liquid levels in both the liquid air tank and the LNG storage are set to 10% of their respective upper bounds [173], and the initial levels are chosen slightly above these lower limits. Following [173], the minimum charging and discharging powers are defined as 80% and 3% of their corresponding upper bounds. The LNG storage has a loading capacity of 16.19 m^3/h and an initial LNG level of 21.683 m^3, which corresponds to a filling time of about 12 hours.

Table 5.1: Characteristics of the LAES-LNG facility.

Parameter	**Value**	**Unit**	**Parameter**	**Value**	**Unit**
$\overline{\mathcal{P}^{\text{dis}}}$	122.2	MW	q_0^{LAES}	50	MWh
$\underline{\mathcal{P}^{\text{dis}}}$	3.66	MW	$\overline{\mathcal{Q}^{\text{LNG}}}$	217	m^3
$\overline{\mathcal{P}^{\text{ch}}}$	60	MW	$\underline{\mathcal{Q}^{\text{LNG}}}$	21.7	m^3
$\underline{\mathcal{P}^{\text{ch}}}$	48	MW	q_0^{LNG}	21.863	m^3
ϑ^{dis}	3.72	€/MWh	$\xi^{\wp}$, ξ^{ℓ}	16.19	m^3/h
ϑ^{ch}	3.72	€/MWh	η	0.97	-
$\mathcal{R}^{\text{LAES}}$	0.05	day^{-1}	$\underline{\Psi^{\text{LNG}}}$	10	MWh
$\mathcal{R}^{\text{LNG}}$	0.05	day^{-1}	$\overline{\Psi^{\text{LNG}}}$	20,000	MWh
$\overline{\mathcal{Q}^{\text{LAES}}}$	480	MWh	HR	1.066	$\frac{\text{MWh}_{\text{thermal}}}{\text{MWh}_{\text{out}}}$
$\underline{\mathcal{Q}^{\text{LAES}}}$	48	MWh	ER	0.491	$\frac{\text{MWh}_{\text{in}}}{\text{MWh}_{\text{out}}}$
LHV	48.6	MJ/kg	ϖ	457.4	kg/m^3

The LNG lower heating value LHV and density ϖ are taken from [191] and [192], respectively. In the day-ahead LNG derivatives market, the facility is allowed to submit daily LNG bids between 10 and 20,000 MWh, in line with Iberian market rules. The dispatch formulation (5.1)-(5.23) has a mixed-integer linear structure and is implemented in a commercial optimization environment. All numerical results reported in this section are obtained by solving the corresponding MILP with the CPLEX solver. All simulations are conducted on a laptop equipped with an 11th-generation Intel Core i7 processor (2.50 GHz) and 16 GB of memory.

The numerical investigation focuses on two main questions:

1. How does the integrated LAES-LNG facility perform in the day-ahead electricity and LNG markets compared with realistic and ideal standalone LAES plants?

2. Given observed price conditions in 2021 and 2022, what is the probabilistic payback period of the LAES-LNG facility, and how sensitive is it to key

design choices such as LNG loading and unloading capacities?

These questions are addressed in the next two subsections.

5.5.1 Day-Ahead Dispatch Study

This subsection evaluates the cost-effectiveness of the LAES-LNG facility over a representative day and compares it against benchmark standalone LAES configurations.

Scenario generation and reduction. One thousand initial scenarios are generated for day-ahead electricity and LNG prices using Gaussian distributions. For each hour of the day, the electricity price is modeled as a Gaussian random variable with mean equal to the observed price on 21 January 2021 and standard deviation equal to the empirical standard deviation of hourly prices recorded during January 2021. The LNG price is modeled as a daily Gaussian variable with mean and standard deviation derived from the same period.

The scenario tree is then reduced with the SCENRED2 tool [171]. The reduction yields $\mathcal{L} = 10$ representative scenarios for LNG prices and $\mathcal{D} = 25$ representative scenarios for electricity prices. The choice of 25 electricity scenarios is consistent with the requirement of the Iberian day-ahead electricity market to submit offering and bidding curves with 25 blocks per hour. The reduced scenarios serve as inputs to the two-stage stochastic dispatch formulation of Section 5.3.

Case definitions. To interpret the value of LAES-LNG integration, three case studies are defined:

- **Case 1**: the proposed LAES-LNG facility with technical characteristics given in Table 5.1 [57]. This case represents the integrated configuration analyzed in this chapter.
- **Case 2**: a realistic standalone LAES facility that is economically equivalent to Case 1 [57]. The standalone and integrated facilities are compared under identical market conditions to ensure a fair assessment of their economic feasibility. The technical specifications of this realistic benchmark are listed in Table A.1 in Appendix A.5. Case 2 reflects a plant with 55% round-trip efficiency, reduced operating expenditures, and a lower discharge rate.

- **Case 3**: an ideal standalone LAES facility with 70% round-trip efficiency and low operating costs, as proposed in [173]. Its technical parameters, reported in Table A.2 in Appendix A.5, are derived from [173] and represent an optimistic benchmark for future technology.

Both Case 2 and Case 3 follow the mixed-integer formulation (A.9)-(A.20) outlined in Appendix A.4 for the day-ahead dispatch of a standalone LAES plant. From a computational standpoint, all three case studies rely on MILP formulations and remain computationally tractable. Based on the CPU time reported by CPLEX, solving Case 1 requires 57.92 s. In contrast, the reduced problem size in Case 2 and Case 3 leads to sub-second solution times, with an average CPU time of about 0.64 s.

Expected profit and interaction with markets. Tables 5.2 and 5.3 report, for the three cases, the expected daily profit, the total daily LNG bids, the total expected electricity charging and discharging quantities, and all components of the objective functions (5.1) and (A.9). The comparison reveals that the proposed LAES-LNG facility (Case 1) achieves the highest expected profit.

Despite an expenditure of €15,164.1 for LNG purchases in the day-ahead LNG market, Case 1 attains a revenue of €39,378.6 from electricity sales, which translates into a daily expected profit of €15,797.0. In contrast, the standalone LAES facilities reach maximum electricity market revenues of €10,797.8 (Case 2) and €14,357.7 (Case 3). The financial gain of the LAES-LNG facility relative to its economically equivalent standalone counterpart (Case 2) is approximately 3.1 times higher, which makes the integrated configuration a much more competitive option for grid deployment. Even when compared with the optimistic benchmark of Case 3, which assumes 70% round-trip efficiency and low variable costs, Case 1 yields a 91.4% increase in daily expected profit.

Figure 5.4 details the hourly electricity bids and offers in the three cases. All facilities follow a broadly similar temporal pattern, with charging concentrated in low-price hours and discharging in higher-price hours. The main difference lies in the magnitude of the interactions. The LAES-LNG facility in Case 1 exhibits much more active participation in the electricity market, which reflects the additional flexibility provided by the LNG integration.

Interestingly, although the total expected daily charging of Case 1 exceeds that of the ideal standalone system in Case 3, the cost of purchased electricity is higher in Case 3. This outcome is linked to the limited charging capacity of

Table 5.2: Expected profit and components of the objective functions in Case 1–3.

Case Study	**Profit**	$\sum_t \mathbb{E}[\mathcal{O}_1]$	$\sum_t \mathbb{E}[\mathcal{O}_2]$	$\sum_t \mathbb{E}[\mathcal{O}_3]$	$\sum_t \mathbb{E}[\mathcal{O}_4]$	$\sum_t \mathbb{E}[\mathcal{O}_5]$
	[€]	[€]	[€]	[€]	[€]	[€]
Case 1	15,797.0	−15,164.1	39,378.6	−5,035.5	−2,265.8	−1,116.0
Case 2	4,976.8	–	10,797.8	−4,681.9	−403.29	−735.76
Case 3	8,252.5	–	14,357.7	−6,012.1	−27.0	−66.0

Table 5.3: Daily electricity bids and offers and total LNG procurement in Case 1–3.

Case Study	$\sum_t P^{\text{dis}}$	$\sum_t P^{\text{ch}}$	H^{tot}
	[MWh]	[MWh]	[MWh]
Case 1	609.10	300.00	671.26
Case 2	158.77	289.66	–
Case 3	204.62	292.57	–

Case 3, which forces the plant to replenish its storage at hour $t = 14$, when the day-ahead electricity price is relatively high. The integrated facility can shift more charging to cheaper hours and rely on the LNG stream to sustain higher discharging levels.

Figure 5.5 shows offering and bidding curves for two representative hours ($t = 5$ and $t = 9$). The offering curves increase in both energy and price, which reflects the standard supply behavior of the plant as prices rise. The bidding curves display the opposite trend. For instance, at an electricity price of €70/MWh, the offered power in Case 1 is roughly three times larger than in the benchmark standalone configurations, which illustrates the enhanced ability of the LAES-LNG facility to monetize high-price periods.

Finally, Figure 5.6 reports the liquid level of the liquid air tank. All three

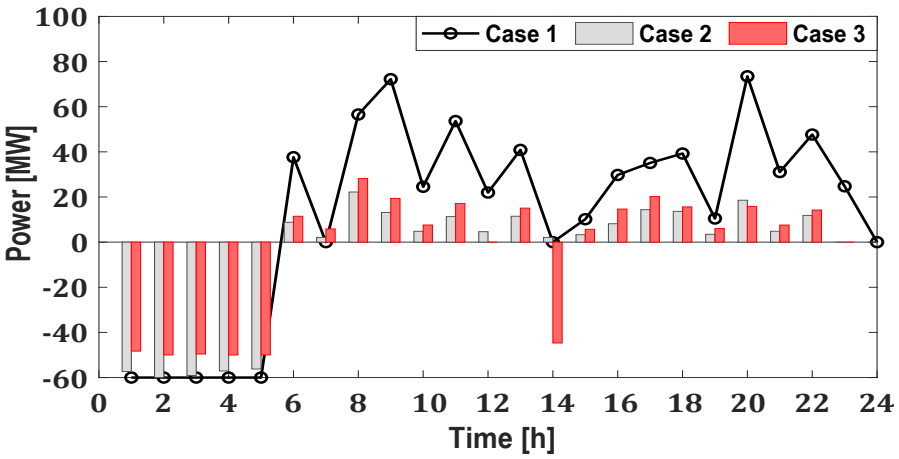

Figure 5.4: Hourly electricity bids and offers in Case 1–3.

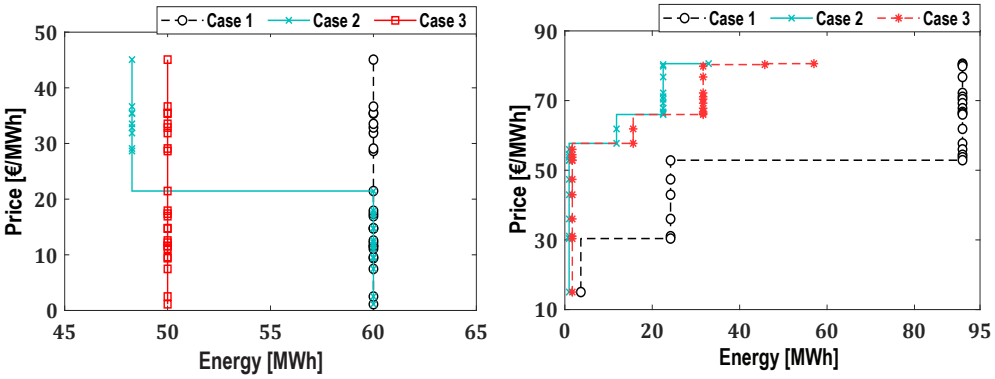

(a) Bidding curve at $t = 5$.

(b) Offering curve at $t = 9$.

Figure 5.5: Day-ahead offer and bid curves in Case 1–3 for two selected periods.

plants fill the storage during the first hours and gradually discharge it towards the end of the day, when electricity prices are higher. The integrated facility, however, operates at higher inventory levels and can support more extensive discharging in peak-price periods, which contributes to its superior profitability.

Sensitivity to LNG loading and unloading capacities. Motivated by the strong economic performance of Case 1, two additional cases investigate the impact of LNG loading and unloading capacities on the bottom line of the LAES-LNG facility. The focus is on the parameters $\xi^{\wp}$ and ξ^{ℓ} that define the

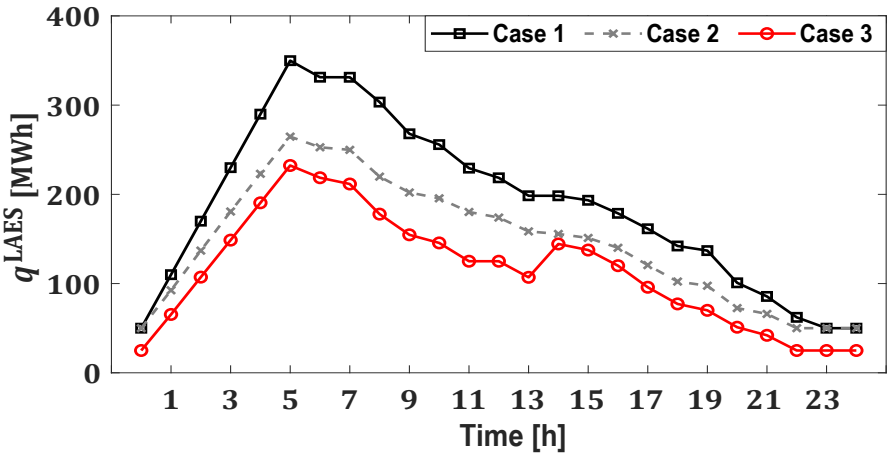

Figure 5.6: Liquid level of the liquid air tank in Case 1–3.

maximum LNG transfer rates between the TVB and the on-site storage, and between the storage and the regasification unit.

- **Case 4**: a LAES-LNG facility with $\xi^{\wp} = \xi^{\ell} = 12.95$ m^3/h.
- **Case 5**: a LAES-LNG facility with $\xi^{\wp} = \xi^{\ell} = 19.43$ m^3/h.

Cases 4 and 5 therefore represent a decrease and an increase of 3.24 m^3/h in the loading and unloading capacities with respect to Case 1, where $\xi^{\wp} = \xi^{\ell} = 16.19$ m^3/h. Note that a change of 3.24 m^3/h in LNG transfer approximately corresponds to a variation of 20 MW in input or output energy.[7]

Table 5.4 summarizes the expected profit, the total daily electricity bids and offers, and the total daily LNG purchases for Case 1, Case 4, and Case 5. The results highlight the strong influence of loading and unloading capacities on the facility's profit. Higher transfer rates allow the plant to concentrate LNG withdrawals and electricity generation in the most favorable hours, which enhances arbitrage opportunities.

A comparison between Case 1 and Case 4 is particularly instructive. Although their total interactions with the electricity and LNG markets are very similar in aggregate terms, the higher loading and unloading capacities in Case 1 yield an additional profit of €2,306.13. Figure 5.7 explains this effect by plotting

[7] $3.24 = \begin{cases} 16.19 - 12.95 \\ 19.43 - 16.19 \end{cases}$ m^3/h.

Table 5.4: Expected profit, daily bought LNG, and daily electricity bids and offers in Case 1, 4, and 5.

Case Study	Profit [€]	$\sum_t P^{\text{dis}}$ [MWh]	$\sum_t P^{\text{ch}}$ [MWh]	H^{tot} [MWh]
Case 1	15,797.00	609.10	300.00	671.26
Case 4	13,490.87	608.99	300.00	671.07
Case 5	17,415.23	729.66	359.19	803.96

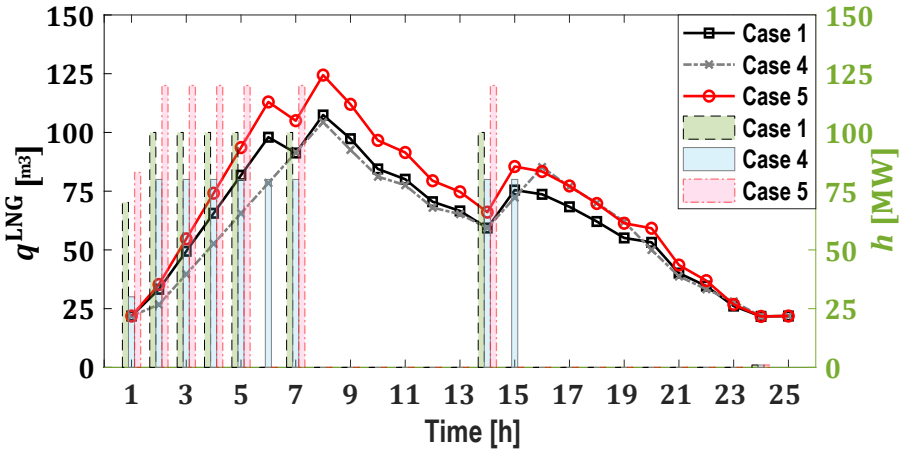

Figure 5.7: Liquid level of LNG storage (lines) and LNG bids (bars) in Case 1, Case 4, and Case 5.

Note: The left and right y-axes correspond to the storage level and the hourly bids, respectively.

the liquid level of the LNG storage and the hourly LNG bids for the three cases. The reduced capacities in Case 4 force the facility to acquire its target LNG volume over a larger number of periods. In particular, the facility in Case 4 needs to purchase LNG during periods 6 and 15 to compensate for the lack of flexibility, whereas Case 1 can concentrate LNG purchases in periods with more favorable LNG prices. Case 5, with higher capacities, interacts even more actively with the LNG market and maintains a higher average LNG inventory, which supports higher electricity generation and profit.

Overall, the day-ahead dispatch study shows that integrating LAES with

LNG regasification provides a substantial profit increase relative to standalone LAES plants, and that the design of loading and unloading capacities plays a critical role in capturing this value.

5.5.2 Economic Feasibility Study

The promising daily profit results motivate a deeper assessment of the long-term economic feasibility of the LAES-LNG facility, with a particular focus on the probabilistic payback period introduced in Section 5.4. This subsection quantifies the distribution of the payback period under realistic market conditions and examines how it depends on the facility design and on the correlation between investment cost and annual profit.

It is important to note that the standalone LAES facilities in Case 2 and Case 3 do not recover their initial investment within a 30-year horizon when evaluated under the same price assumptions. They are therefore excluded from the probabilistic payback analysis. Case 4 is also omitted. The economic feasibility study centers on Case 1 and Case 5, which combine high daily profitability with realistic technology assumptions. In addition, the lower bounds $\underline{\mathcal{P}^{\text{ch}}}$ and $\underline{\mathcal{P}^{\text{dis}}}$ are set to zero in this section, since these minimum power levels are design parameters that can be adjusted in a demonstration plant.

Input parameters for the Hinkley approach. As described in Section 5.4, the Hinkley approach requires four key parameters: the mean and standard deviation of the total investment cost, μ_x and σ_x, and the mean and standard deviation of the annual profit, μ_z and σ_z. In this case study, the investment cost of the LAES-LNG facility is set to €120.61e6 [57]. The standard deviation of the investment cost is assumed equal to 8% of the mean, following [193].

To estimate μ_z and σ_z, the analysis relies on observed electricity and LNG prices in 2021 and 2022. These two years cover the period before and during the recent energy crisis, which was characterized by sustained growth in global energy demand after the COVID-19 outbreak and by geopolitical tensions, including Russia's invasion of Ukraine. Figure 5.8 shows the daily average electricity and LNG prices in the Iberian markets for 2021 and 2022. Both price series increase markedly over 2021. In 2022, electricity prices continue to rise during the first quarter and then decrease, while LNG prices remain relatively stable during the first half of the year, surge in the third quarter, and decline towards the end of the year.

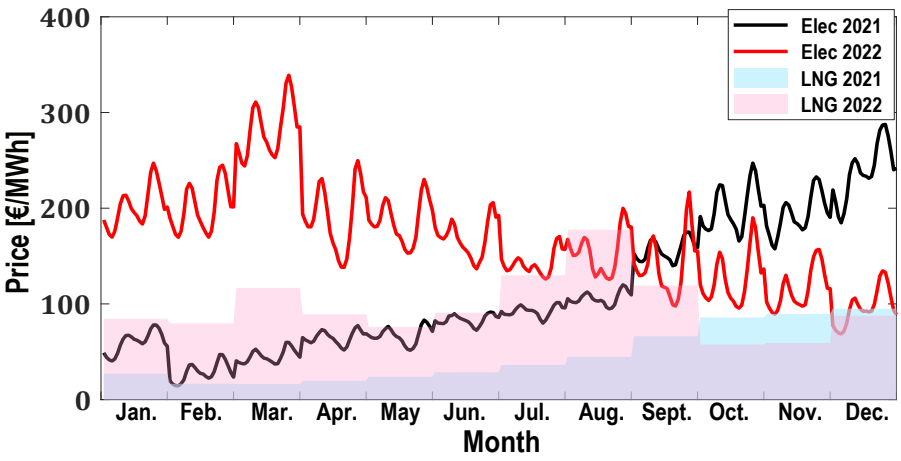

Figure 5.8: Daily average electricity and LNG prices in 2021 and 2022.

As electricity prices increase, the spread between peak and off-peak prices widens, which creates more attractive opportunities for storage-based arbitrage. To quantify the annual profit under these conditions, the procedure proposed in [194] is adapted as follows. First, the historical price data for each year are divided into 12 monthly data sets. Each monthly set is then decomposed into 24 subsets for hourly electricity prices and one subset for the daily LNG price. Each subset is fitted with a Gaussian distribution, which yields 24 hourly fits for electricity prices and one daily fit for the LNG price for each month.

To represent price uncertainty, the same scenario generation and reduction methods described in Section 5.5.1 are applied to these monthly distributions. The resulting representative scenarios are then fed into the dispatch model of Section 5.3 to compute, for each month, the expected profit of the LAES-LNG facility. Summing monthly profits yields the annual profit, from which μ_z and σ_z are obtained.

Tables 5.5 and 5.6 report the monthly and annual mean and standard deviation of the profit for Case 1 and Case 5, respectively, for 2021 and 2022.

The results show that the fourth quarter of 2021 is the most profitable period for the LAES-LNG facility, driven by high electricity prices. December 2021 stands out as the month with the highest profit. In 2022, the picture changes: the first half of the year, with high electricity prices and relatively moderate LNG prices, contributes most to the annual profit. In contrast, the facility incurs losses in July and August 2022, when LNG prices spike and

Table 5.5: Mean and standard deviation of the facility's profit over 2021 and 2022 under Case 1.

Profit	**2021**		**2022**	
	μ_z [€]	σ_z [€]	μ_z [€]	σ_z[€]
January	6.10e5	2.80e5	1.30e6	2.91e5
February	2.74e5	5.88e4	1.29e6	3.85e5
March	4.07e5	9.23e4	2.40e6	8.35e5
April	5.41e5	1.05e5	1.52e6	5.04e5
May	5.66e5	1.15e5	1.23e6	2.08e5
June	4.61e5	1.11e5	5.02e5	3.62e5
July	3.66e5	8.73e4	−8.99e3	4.49e3
August	4.10e5	1.15e5	−1.40e4	1.21e4
September	6.49e5	3.48e5	2.76e5	2.80e5
October	1.30e6	4.12e5	1.17e6	6.77e5
November	1.07e6	3.36e5	7.15e5	4.96e5
December	2.20e6	5.98e5	3.93e5	3.49e5
Annual	8.86e6	9.54e5	1.08e7	1.50e6

electricity prices fall, which makes energy arbitrage unattractive under the given operating costs and constraints. Case 5 systematically attains higher monthly and annual profits than Case 1, which confirms the importance of sizing loading and unloading capacities carefully during the design phase.

Probabilistic payback period. Given μ_x, σ_x, μ_z, and σ_z, the Hinkley approach can be applied to obtain the probability density function $f(g)$ of the payback period G, where $G = X/Z$ with X and Z denoting investment cost and

Table 5.6: Mean and standard deviation of the facility's profit over 2021 and 2022 under Case 5.

Profit	**2021**		**2022**	
	μ_z [€]	σ_z [€]	μ_z [€]	σ_z [€]
January	6.92e5	3.30e5	1.47e6	3.17e5
February	3.13e5	7.22e4	1.47e6	4.28e5
March	4.60e5	1.04e5	2.72e6	1.03e5
April	6.11e5	1.22e5	1.72e6	5.86e5
May	6.35e5	1.24e5	1.43e6	2.48e5
June	5.17e5	1.21e5	5.75e5	4.34e5
July	4.09e5	1.07e5	−8.99e3	4.49e3
August	4.65e5	1.19e5	−1.40e4	1.21e4
September	7.35e5	3.77e5	3.21e5	3.35e5
October	1.47e6	4.49e5	1.35e6	2.61e4
November	1.20e6	2.46e5	8.22e5	5.92e5
December	2.46e6	6.45e5	4.44e5	4.21e5
Annual	9.97e6	1.05e6	1.23e7	1.80e6

annual profit, respectively. Figures 5.9 and 5.10 display the resulting probability density functions for 2021 and 2022 price conditions, for two representative correlation coefficients $\rho = 0.3$ and $\rho = 0.7$ between investment cost and annual profit.

Tables 5.7 and 5.8 summarize key probabilistic metrics of the payback period, namely the mean μ_g, the standard deviation σ_g, and the probability that the investment is recovered within 15 years, which is half of the assumed

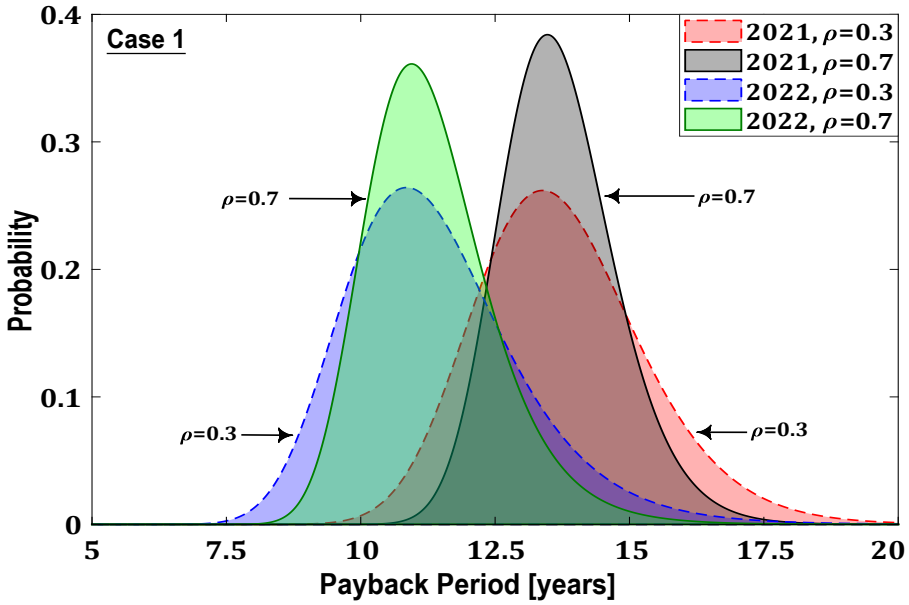

Figure 5.9: Probability density function of the payback period derived from 2021 market observations.

Table 5.7: Probabilistic metrics of the payback period based on 2021 market observations.

Descriptive Statistics	**Case 1**		**Case 5**	
	$\rho = 0.3$	$\rho = 0.7$	$\rho = 0.3$	$\rho = 0.7$
μ_g [years]	13.5564	13.5803	12.0422	12.0628
σ_g [years]	1.5275	1.0414	1.3349	0.9052
$\mathcal{P}(g \leq 15)$*	0.8277	0.9136	0.9866	0.9994

*$\mathcal{P}(g \leq 15) = \int_0^{15} f(g)\, dg$.

technical lifetime of the facility. This probability is given by

$$\mathcal{P}(g \leq 15) = \int_0^{15} f(g)\, dg.$$

Two main insights emerge from these results. First, the mean payback

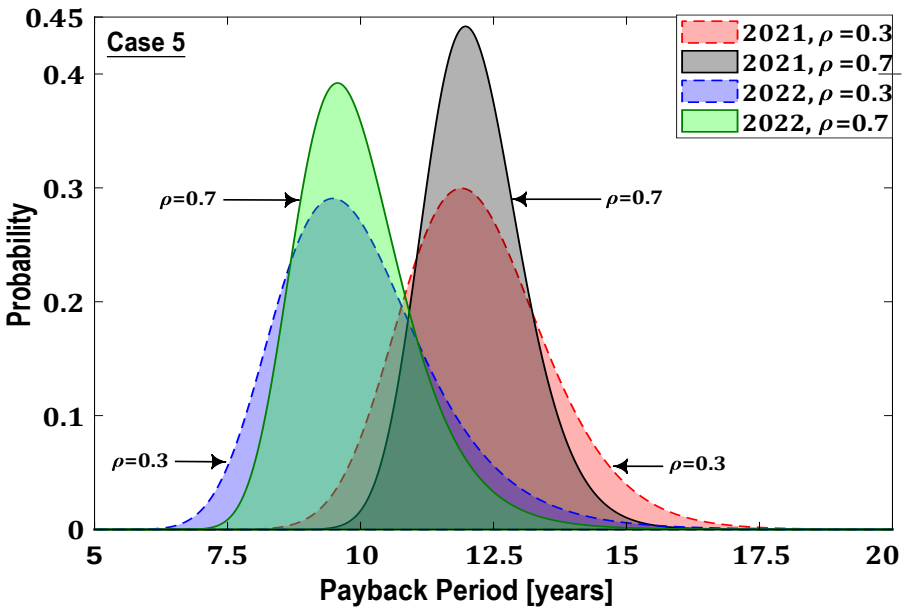

Figure 5.10: Probability density function of the payback period derived from 2022 market observations.

Table 5.8: Probabilistic metrics of the payback period based on 2022 market observations.

Descriptive Statistics	**Case 1**		**Case 5**	
	$\rho = 0.3$	$\rho = 0.7$	$\rho = 0.3$	$\rho = 0.7$
μ_g [years]	11.0983	11.1237	9.7185	9.7418
σ_g [years]	1.5167	1.1094	1.3788	1.0222
$\mathcal{P}(g \leq 15)$*	0.9950	0.9998	0.9994	1.0000

*$\mathcal{P}(g \leq 15) = \int_0^{15} f(g)\, dg$.

period based on 2022 price observations is at least two years shorter than the corresponding value for 2021 for both Case 1 and Case 5. This reflects the stronger arbitrage opportunities created by the high price levels and spreads in 2022, despite the challenging episodes in mid-2022. Second, a larger correlation coefficient ρ between investment cost and annual profit reduces the standard

deviation of the payback period, which leads to a narrower probability density function. This reduction in dispersion can be interpreted as higher predictability and lower uncertainty for investors when cost and profit move more coherently.

From a practical standpoint, the probability of achieving a payback period shorter than 15 years is above 80% for Case 1 and above 98% for Case 5 under 2021 price conditions, and it exceeds 99% for both cases under 2022 conditions. These results indicate that, under the considered assumptions, an LAES-LNG facility has a high likelihood of becoming profitable within half of its technical lifetime. Such conclusions cannot be drawn from deterministic payback calculations that ignore price uncertainty and its impact on annual profits. The probabilistic payback analysis therefore provides a more informative and transparent basis for evaluating LAES-LNG investments in future multi-energy markets.

5.6. Chapter Conclusion

This chapter has developed a day-ahead dispatch framework for an integrated LAES-LNG facility that couples an LNG regasification unit with an LAES and allows joint participation in the Iberian LNG and electricity markets. The dispatch problem has been formulated as a two-stage stochastic MILP that respects the sequential clearing of the two day-ahead markets and uses a reduced set of price scenarios for both commodities. By explicitly modeling the interaction between the LAES unit, the LNG storage, and the regasification process, the framework co-optimizes electricity arbitrage, LNG procurement, and the use of cold exergy within a single decision model.

The numerical case studies have shown that this integrated LAES-LNG configuration clearly outperforms two standalone LAES benchmarks. For the representative working day, the proposed facility achieves the highest expected profit, even after accounting for the cost of LNG purchases. The economically equivalent standalone LAES plant earns roughly one third of the profit of the LAES-LNG facility, while the highly efficient standalone LAES remains less profitable despite its favorable round-trip efficiency. The comparison of bidding and offering curves, as well as charging and discharging patterns, indicates that all facilities follow similar arbitrage logic, but the LAES-LNG plant can trade larger volumes at more favorable hours thanks to the additional thermal input from LNG. The sensitivity analysis of LNG loading and unloading capacities further highlights these parameters as critical design levers: higher rates increase

market interaction and improve profits, whereas lower rates constrain flexibility and reduce the facility's bottom line even when the overall traded volumes are comparable.

Beyond short-term operation, the chapter has assessed the investment attractiveness of the LAES-LNG facility through a probabilistic payback period analysis based on Hinkley's approach and real 2021–2022 Iberian price data. By combining statistical information on capital cost with the distributions of annual profits, the analysis derives probability density functions of the payback period for different correlation assumptions between cost and profit. The results show that the LAES-LNG facility can recover its investment within the assumed lifetime, whereas the standalone LAES plants do not under the same assumptions. The mean payback period obtained from 2022 market conditions is at least two years shorter than the one based on 2021 data, and the probability of recovering the investment within 15 years exceeds 80% for 2021 and is essentially equal to one for 2022. A higher correlation coefficient narrows the payback distribution, which reflects greater predictability and confidence in the investment outcome. These probabilistic indicators provide a richer and more informative picture than deterministic payback calculations used in earlier LAES studies.

Taken together, these findings suggest that coupling LAES with LNG regasification can transform LAES from a marginal storage option into a competitive candidate for large-scale deployment in multi-energy markets, provided that LNG handling capacities and market participation strategies are properly designed.

Chapter Publication

- **H. Khaloie** and F. Vallée, "Day-Ahead Dispatch of Liquid Air Energy Storage Coupled With LNG Regasification in Electricity and LNG Markets," *IEEE Transactions on Power Systems*, vol. 39, no. 3, pp. 5177–5190, May 2024.

CHAPTER 6

Strategic Look-Ahead Dispatch of Hybrid CAES-LAES

Chapters 4 and 5 have focused on market-based dispatch models for bulk storage that behave as price-taking (non-strategic) units in existing market structures. Chapter 4 develops a risk-aware, price-taking bidding framework for grid-scale lithium-ion batteries in day-ahead and intraday markets, and Chapter 5 introduces an integrated dispatch model for an LAES-LNG facility that coordinates electricity and LNG trading under uncertainty. This chapter advances the analysis to strategic, price-making behavior and studies a hybrid thermo-mechanical storage concept that combines CAES with LAES. This step closes the methodological loop of the thesis by linking coordinated techno-economic operation, strategic bidding in liberalized markets, and learning-assisted optimization within a single modeling framework.

The main contribution of this chapter is a *bi-level*, look-ahead strategic dispatch model for a hybrid CAES-LAES plant that participates as a price-making unit in the day-ahead electricity market. The upper-level problem represents the coordinated offer and internal scheduling decisions of the hybrid plant, while the lower-level problem captures market-clearing and price formation. The resulting *bi-level* problem is reformulated as a mixed-integer single-level model with equilibrium constraints and is equipped with a learning-assisted warm-start scheme that predicts high-quality initial values for binary variables.

The remainder of the chapter is organized as follows. Section 6.1 reviews the literature on CAES and LAES dispatch and bidding models. In Section 6.2, the hybrid CAES-LAES system architecture and modeling assumptions are presented, and the interaction between the CAES and LAES subsystems is clarified. Section 6.3 then develops the *bi-level* Stackelberg formulation of the

strategic look-ahead dispatch model together with its single-level reformulation. The learning-assisted optimization approach is detailed in Section 6.4. Section 6.5 reports the case study setup and numerical results. Finally, Section 6.6 concludes the chapter and provides practical recommendations for the design and operation of hybrid CAES-LAES facilities in future market environments.

6.1. Literature Review on CAES and LAES Dispatch Models

Advances in the domains of CAES and LAES have attracted increasing attention from both academia and industry, with a strong focus on techno-economic operation and market integration. A broad range of studies has examined their economic potential, considering both independent operation and coordinated use with other system components, in particular variable renewable generation. Within this context, several contributions have proposed bidding and scheduling models for CAES units in electricity markets. For instance, risk-aware participation strategies in the day-ahead market have been formulated based on information gap decision theory to handle price uncertainty, complemented by robust optimization and affine arithmetic techniques to represent non-standard CAES thermodynamic characteristics [195, 196, 197]. Building on these formulations, subsequent studies have integrated CAES with wind and photovoltaic resources and have employed adaptive and distributionally robust optimization to reduce conservatism and improve decision-making under multiple sources of uncertainty [198, 199].

Beyond CAES, numerous works have investigated LAES facilities from a market perspective. Early contributions have assessed the economic potential of LAES plants operating in arbitrage mode, and have shown that appropriate support schemes can justify the deployment of such emerging technologies [173]. Further analyses have examined the participation of LAES in real-time electricity markets, identifying operational strategies that exploit price volatility and system flexibility needs. The market dispatch of a typical LAES plant has also been studied using MILP models that explicitly capture thermodynamic constraints and operational limits [175, 176]. In a similar vein, the integration of a wind farm with a LAES facility has been analyzed in a Spanish case study, where an algorithmic dispatch scheme coordinates wind generation and cryogenic storage [178]. A detailed review of LAES technologies and LAES-LNG

integration, including the role of cryogenic tanks, cold and heat recovery, and coordinated participation in electricity and LNG markets, is already provided in Chapter 5; only the most relevant market-oriented aspects are recalled here to avoid repetition.

The limitations of standalone geologically unconstrained storage facilities, such as above-ground CAES and LAES, have motivated the design of hybrid CAES-LAES plants. Above-ground CAES offers relatively high round-trip efficiency but low energy density and higher storage costs, whereas LAES provides high-density storage in cryogenic tanks at the expense of lower efficiency. Hybrid concepts combine these technologies in a configuration that typically includes a high-capacity cryogenic tank for liquid air, an above-ground CAES unit with dedicated compression and expansion stages, and machinery that enables bi-directional conversion between liquid and compressed air. The objective is to obtain a scalable solution that merges the cost-effectiveness of LAES with the efficiency of above-ground CAES. Previous studies have examined such hybrid designs through parametric techno-economic analyses [35, 64, 65], but they rely on algorithmic or heuristic dispatch rules rather than fully formulated optimization models.

The existing literature reveals three gaps that motivate the present study. First, no optimization-based dispatch model explicitly coordinates internal energy transfers between the CAES and LAES subsystems while capturing their distinct operational states. Second, strategic storage formulations have not yet considered a hybrid CAES-LAES plant acting as a price-making agent with *look-ahead* offers in day-ahead electricity markets [67, 68, 69], which calls for a Stackelberg representation of the interaction with the market-clearing process. Third, *bi-level* models of strategic storage participation involve many integer variables in both bidding and market-clearing decisions, creating substantial computational burden; although warm-starting techniques for mixed-integer problems have been successfully applied in other power system contexts [72, 73, 74], they have not been used to initialize groups of binaries in a *bi-level* optimization. To address these gaps, this chapter develops a strategic look-ahead dispatch framework in which the hybrid CAES-LAES plant is modeled as a single price-making entity in a *bi-level* Stackelberg game, reformulated as a mixed-integer MPEC and solved with the aid of a learning-assisted warm-start approach for binary variables.

6.2. Hybrid CAES-LAES System Overview and Modeling Assumptions

Building on the research gaps identified in Section 6.1, this section introduces the hybrid CAES-LAES plant considered in this chapter and clarifies the main modeling assumptions that underpin its strategic look-ahead dispatch. The focus is on commercially mature thermo-mechanical storage configurations that are representative of existing and near-term deployments, while remaining compatible with the *bi-level* market framework developed in Section 6.3.

6.2.1 Hybrid CAES-LAES System Architecture

Figure 6.1 presents the schematic of the hybrid energy storage facility analyzed in this chapter, hereafter referred to as the hybrid CAES-LAES plant. The hybrid system comprises three primary components: a LAES unit, a CAES unit, and a dedicated set of machines that convert air between compressed and liquid states. It is worth mentioning that the cryogenic subsystem (LAES) operates based on liquid air technology without the incorporation of additional external heat sources [173].

In Figure 6.1, the top row represents the LAES unit and the bottom row represents the CAES unit. The two subsystems are coupled by intermediary machinery that enables bi-directional energy transfer between the cryogenic tank and the compressed air vessel. In the charging subsystems of both storage units, off-peak electricity from the grid drives the conversion of ambient air into either liquid air, stored in a cryogenic tank, or high-pressure air, stored in an above-ground pressure vessel. During discharge, the LAES unit pumps, evaporates, and expands the stored liquid air through several expansion stages to drive a turbine and supply electricity back to the grid. In parallel, the CAES subsystem co-fires the stored high-pressure air with natural gas fuel to generate high-rate electricity.

A key distinction between the CAES unit and a traditional gas turbine is that the CAES unit relies on pre-compressed air stored using off-peak electricity. In contrast, conventional gas turbines consume a substantial share of their fuel input, approximately two-thirds according to standard estimates, to compress ambient air during power generation. Although more advanced storage configurations could be considered, this chapter focuses on widely discussed and commercialized CAES and cryogenic plants [63, 200]. The primary objective

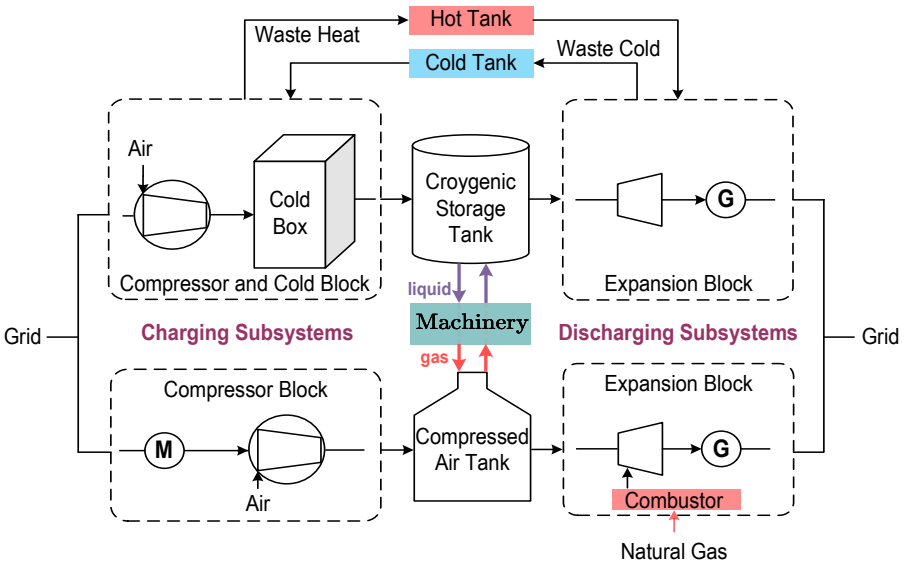

Figure 6.1: Schematic of the hybrid CAES-LAES plant.

is to evaluate the profitability of hybridizing these facilities and to identify a tractable yet representative operational formulation for their coupling. These plants are typically designed to provide daily-to-weekly storage services and to take advantage of short-term fluctuations in electricity prices.

6.2.2 Operational Modes and Internal Energy Transfer

The hybrid configuration relies on intermediate machinery positioned between the two storage tanks to enable bi-directional transfer and conversion between liquid air and compressed air. This additional degree of freedom allows the hybrid plant to overcome the limited volume of above-ground compressed air vessels and to better exploit periods of low electricity prices.

When the compressed air vessel approaches its maximum capacity during a low-price period, excess electricity can still be absorbed by converting compressed air into liquid air and storing it in the cryogenic tank. Conversely, the cryogenic tank can act as an extended storage reservoir for the CAES subsystem. Liquid air can be converted back into compressed air when required, which increases the effective energy capacity of the CAES subsystem and improves the ability of the hybrid plant to arbitrage across multiple days. In addition, the LAES unit retains the ability to operate independently. When liquid air

is available and market conditions are favorable, the cryogenic subsystem can generate electricity by evaporating and expanding the liquid air, even if the CAES subsystem does not charge.

This flexibility increases the value of the hybrid plant but also introduces operational complexity. Coordinated operation requires a careful alignment of the energy flows through the coupling machinery and the internal operating states of the two storage facilities. Each subsystem features distinct charging and discharging branches, and at a given time either the charging or the discharging branch can be active, not both. Simultaneous storage and release of energy within the same facility are therefore infeasible. Moreover, energy transfers between the tanks must respect the operating states of both origin and destination facilities. For example, transferring energy from the cryogenic tank to the compressed air vessel is allowed only if: (i) the cryogenic facility is not charging and can therefore release energy, and (ii) the CAES subsystem is in a charging state and able to receive additional compressed air. Analogous conditions apply to transfers from compressed air to liquid air.

These restrictions stem from shared infrastructure and technological limits in compressors, expanders, and pumps, and they have direct implications on feasible dispatch patterns [201]. The mathematical formulation in Section 6.3 incorporates these operational rules explicitly through binary variables and coupling constraints that govern the charging, discharging, and conversion modes of the hybrid CAES-LAES plant.

6.2.3 Look-Ahead Dispatch Perspective and Modeling Assumptions

From a market perspective, the hybrid CAES-LAES plant participates in the day-ahead electricity market as a strategic unit. The interaction between the plant and the market operator is cast as a Stackelberg game, where the storage operator acts as the leader and the day-ahead market operator is modeled as the follower [68]. The leader anticipates how its offering and bidding decisions will influence market-clearing outcomes and nodal prices, and selects an optimal schedule that maximizes profit over a look-ahead horizon. This representation contrasts with the single-level, price-taking models of Chapters 4 and 5, where storage follows exogenous prices, and it is consistent with the multi-level optimization framework introduced in Chapter 3.

Figure 6.2 summarizes this interaction. The upper-level problem represents

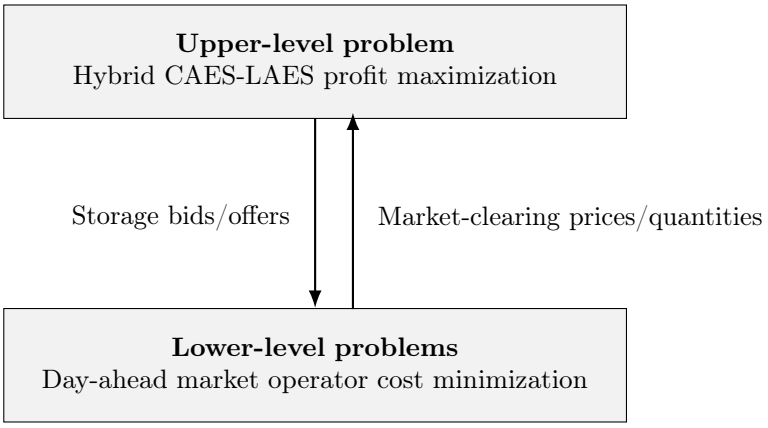

Figure 6.2: Bi-level Stackelberg representation of the hybrid CAES-LAES plant (leader) and the day-ahead market operator (follower).

the profit maximization of the hybrid CAES-LAES plant over a multi-day horizon. Its decisions include the energy quantities and prices that define the storage bids and offers submitted to the day-ahead market. For any given set of offers, the lower-level problem solves the day-ahead market clearing as a cost-minimization problem and returns the market-clearing prices and quantities at each node. Because the upper-level objective depends on these market outcomes, the resulting formulation is a mixed-integer MPEC. The detailed algebraic formulation of this *bi-level* model is provided in Section 6.3.

A critical modeling ingredient is the treatment of the state-of-charge at the boundaries of the dispatch window. In standard day-ahead formulations, storage facilities typically optimize their operation over a single trading day. When submitting offers/bids into a day-ahead auction, the operator focuses on arbitrage opportunities across the 24 hours of the upcoming day. Under this perspective, the facility usually faces a cyclicity constraint that requires the state-of-charge at the end of the dispatch window to match a given target, often identical to the initial level. This condition prevents systematic depletion or overfilling of the storage asset when the model is applied repeatedly on a day-by-day basis.

In contrast, a look-ahead formulation optimizes storage decisions over several consecutive days. The hybrid CAES-LAES plant then chooses its operation for the next day while internalizing the value of energy that can be shifted further into the future. In this setting, it is sufficient to restore the initial

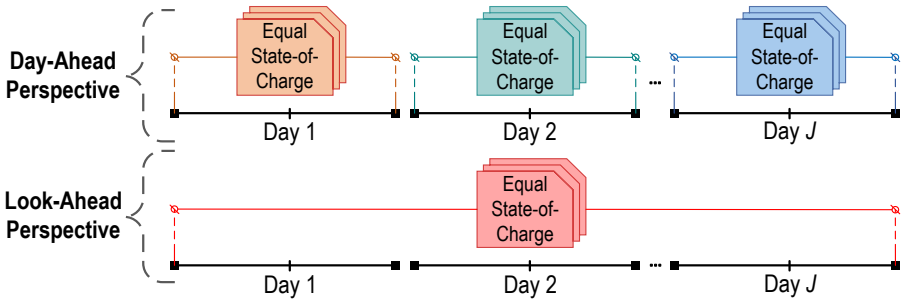

Figure 6.3: Day-ahead and look-ahead perspectives for energy storage dispatch.

state-of-charge at the end of the multi-day look-ahead window rather than at the end of each individual day. This relaxation allows the operator to exploit multi-day price patterns and the complementary roles of the compressed air and cryogenic tanks. Figure 6.3 illustrates the difference between the day-ahead and look-ahead perspectives from the viewpoint of storage operator.

The look-ahead window length is a modelling choice rather than a fixed market requirement. In practice, the storage operator selects this horizon by trading off (*i*) the ability to exploit multi-day price patterns and to coordinate the hybrid energy inventories, (*ii*) the loss of forecast accuracy as the lead time increases, and (*iii*) the resulting computational burden. To make this choice explicit, this chapter evaluates three representative look-ahead window lengths, ranging from the standard day-ahead horizon to a maximum horizon of six days, and quantifies how this selection affects dispatch decisions and market outcomes. In the numerical study of this chapter, the following modeling assumptions define the physical and market environment in which the hybrid CAES-LAES plant operates:

- The analysis accounts for three main sources of uncertainty, namely wind power variability, load fluctuations, and variations in generator offer prices. To represent these uncertainties in storage decisions, a scenario-based approach similar to [202] is employed. A deterministic model is solved across multiple realizations of the uncertain parameters, which yields solutions that are comparable to those obtained from static stochastic programming [203]. The scenarios are generated by independently sampling from a uniform symmetric deviation band centered around the point

forecasts associated with each lead day.[1]

- A maximum look-ahead horizon of six days is considered, and three representative window lengths within this range are evaluated. This choice enables a sensitivity analysis on the impact of horizon selection while keeping the resulting mixed-integer bi-level problem computationally tractable and limiting exposure to long-lead forecast uncertainty.
- A direct-current approximation is used to represent the transmission network, which enables a nodal pricing mechanism for all market participants [68, 69]. Market clearing is modeled as an economic dispatch problem rather than a full unit-commitment formulation [68, 69].
- The energy storage system develops its strategic behavior by anticipating the decisions of other market actors. Strategic pricing decisions of conventional generators and large consumers are not modeled explicitly and are considered beyond the scope of this thesis [68, 69].

These assumptions provide a consistent link between the hybrid CAES-LAES architecture of Section 6.2 and the strategic market environment considered in this chapter. On this basis, Section 6.3 develops the detailed *bi-level* formulation of the strategic look-ahead dispatch model, and Section 6.4 introduces the learning-assisted solution approach for the resulting mixed-integer MPEC.

6.3. Bi-Level Formulation of the Strategic Look-Ahead CAES-LAES Dispatch Model

This section presents the *bi-level* Stackelberg formulation that captures the strategic participation of the hybrid CAES-LAES plant in the day-ahead electricity market. In this leader-follower structure, the hybrid plant acts as the leader, while the day-ahead market operator is the follower, as discussed conceptually in Section 6.2.3. The upper-level problem represents the profit-maximizing look-ahead dispatch and market participation decisions of the hybrid plant, while the lower-level problem models the day-ahead market-clearing mechanism based on nodal pricing. The combination of the two levels yields a *bi-level* optimization

[1] The implications of replacing this fixed band with a lead-dependent, widening band are investigated in Appendix A.8.

problem, which is subsequently reformulated as a single-level mixed-integer MPEC. Throughout the formulation, the superscript α denotes the CAES subsystem and the superscript β denotes the cryogenic LAES subsystem. In the remainder of this section, Section 6.3.1 presents the upper-level optimization model, Section 6.3.2 details the lower-level market-clearing problem, and Section 6.3.3 derives the resulting single-level MPEC formulation.

6.3.1 Upper-Level Problem: Look-Ahead Storage Dispatch

The upper-level problem aims to maximize the profit of the hybrid CAES-LAES plant over the look-ahead window. The decision vector Ξ^{UL} includes the plant's offering and bidding decisions, the internal dispatch of the CAES and LAES subsystems, and the variables that describe the state-of-charge and coupling machinery. Formally, the set of upper-level decision variables Ξ^{UL}[2], which are valid for each storage facility f at time t on day j, is:

$$\Xi^{\mathrm{UL}} = \{p^{\alpha,x}_{j,f,t},\, p^{\alpha,y}_{j,f,t},\, p^{\beta,x}_{j,f,t},\, p^{\beta,y}_{j,f,t},\, \phi^{\gamma,x}_{j,f,t},\, \phi^{\gamma,y}_{j,f,t},\, \rho^{\gamma,x}_{j,f,t},\, \rho^{\gamma,y}_{j,f,t},\, q^{\alpha\to\beta}_{j,f,t},\, q^{\beta\to\alpha}_{j,f,t},\, s^{\alpha}_{j,f,t},\, s^{\beta}_{j,f,t},\, z^{\alpha}_{j,f,t},\, z^{\beta}_{j,f,t}\}.$$

For clarity, the formulation is organized into five groups: the objective function, market participation constraints, coupling machinery constraints, and the state-of-charge constraints of the CAES and LAES subsystems.

6.3.1.1 Objective Function

The objective function (6.1a) maximizes the profit of the hybrid CAES-LAES plant by aggregating the profits generated by each storage facility over the look-ahead window. The first terms in eqs. (6.1b) and (6.1c) represent the revenue of the CAES and LAES facilities from market arbitrage at bus b under a nodal pricing mechanism. The remaining negative terms in eqs. (6.1b) and (6.1c) account for the operational costs of these facilities during charging and discharging states, respectively. Since natural gas is used exclusively in the CAES system for co-firing high-pressure air, its fuel cost is reflected solely in

[2] All upper-level decision variables are introduced and defined at their first appearance in the mathematical formulation that follows.

the objective function of the CAES, eq. (6.1b).

$$\max_{\Xi^{\mathrm{UL}}} \underbrace{\mathcal{F}_1}_{\text{Profit}} = \underbrace{\mathcal{R}^1}_{\text{CAES}} + \underbrace{\mathcal{R}^2}_{\text{LAES}} \tag{6.1a}$$

$$\begin{aligned}\mathcal{R}^1 = \sum_{j\in\mathbb{J}}\sum_{f\in\mathbb{F}}\sum_{t\in\mathbb{T}}\Bigg[&\left(p^{\alpha,y}_{j,f,t} - p^{\alpha,x}_{j,f,t}\right)\lambda^{\mathrm{Elec}}_{j,b\in\Phi^{\mathrm{F}}_b,t} \\ &- p^{\alpha,y}_{j,f,t}\left(\Gamma^{\alpha}_{f}\lambda^{\mathrm{gas}} + C^{\alpha,y}_{f}\right) - p^{\alpha,x}_{j,f,t}C^{\alpha,x}_{f}\Bigg]\end{aligned} \tag{6.1b}$$

$$\begin{aligned}\mathcal{R}^2 = \sum_{j\in\mathbb{J}}\sum_{f\in\mathbb{F}}\sum_{t\in\mathbb{T}}\Bigg[&\left(p^{\beta,y}_{j,f,t} - p^{\beta,x}_{j,f,t}\right)\lambda^{\mathrm{Elec}}_{j,b\in\Phi^{\mathrm{F}}_b,t} \\ &- p^{\beta,y}_{j,f,t}C^{\beta,y}_{f} - p^{\beta,x}_{j,f,t}C^{\beta,x}_{f}\Bigg]\end{aligned} \tag{6.1c}$$

where $\mathcal{F}_1$ represents the total profit of the hybrid plant over the look-ahead horizon, and $\mathcal{R}^1$ and $\mathcal{R}^2$ denote the profit contributions of the CAES and LAES subsystems, respectively. The summations in (6.1b) and (6.1c) run over all days $j \in \mathbb{J}$, hybrid facilities $f \in \mathbb{F}$, and time intervals $t \in \mathbb{T}$. The decision variables $p^{\alpha,x}_{j,f,t}$ and $p^{\alpha,y}_{j,f,t}$ denote the charging and discharging power of the CAES unit, while $p^{\beta,x}_{j,f,t}$ and $p^{\beta,y}_{j,f,t}$ denote the corresponding charging and discharging power of the LAES unit. The parameter $\lambda^{\mathrm{Elec}}_{j,b\in\Phi^{\mathrm{F}}_b,t}$ represents the nodal electricity price at the bus b where the hybrid facility f is connected, with $b \in \Phi^{\mathrm{F}}_b$. The parameter Γ^{α}_{f} denotes the CAES heat rate, and λ^{gas} is the natural gas price. The coefficients $C^{\alpha,x}_{f}$ and $C^{\alpha,y}_{f}$ represent the variable operating costs of the CAES subsystem in charging and discharging states, respectively, while $C^{\beta,x}_{f}$ and $C^{\beta,y}_{f}$ represent the corresponding variable operating costs of the LAES subsystem. In the following, we introduce the operational and technical constraints associated with this upper-level optimization problem.

6.3.1.2 Market Participation Constraints

The hybrid plant participates in the day-ahead electricity market as a unified entity by submitting aggregated energy offers and bids[3] that combine both storage units. The market participation constraints in (6.1d)–(6.1l) link these unified offers and bids to the underlying CAES and LAES units while enforcing

[3]Offer and bid refer to selling and buying quantities, respectively [68, 69].

plant-level power rating and operating mode limits.

$$0 \leq \phi^{\gamma,x}_{j,f,t} \leq \overline{P}^{\alpha,x}_{f} z^{\alpha}_{j,f,t} + \overline{P}^{\beta,x}_{f} z^{\beta}_{j,f,t} \quad \forall\{j,f,t\} \tag{6.1d}$$

$$0 \leq \phi^{\gamma,y}_{j,f,t} \leq \overline{P}^{\alpha,y}(1 - z^{\alpha}_{j,f,t}) + \overline{P}^{\beta,y}_{f}(1 - z^{\beta}_{j,f,t}) \quad \forall\{j,f,t\} \tag{6.1e}$$

$$p^{\gamma,x}_{j,f,t} = p^{\alpha,x}_{j,f,t} + p^{\beta,x}_{j,f,t} \quad \forall\{j,f,t\} \tag{6.1f}$$

$$p^{\gamma,y}_{j,f,t} = p^{\alpha,y}_{j,f,t} + p^{\beta,y}_{j,f,t} \quad \forall\{j,f,t\} \tag{6.1g}$$

$$p^{\alpha,x}_{j,f,t} \leq \overline{P}^{\alpha,x}_{f} z^{\alpha}_{j,f,t} \quad \forall\{j,f,t\} \tag{6.1h}$$

$$p^{\beta,x}_{j,f,t} \leq \overline{P}^{\beta,x}_{f} z^{\beta}_{j,f,t} \quad \forall\{j,f,t\} \tag{6.1i}$$

$$p^{\alpha,y}_{j,f,t} \leq \overline{P}^{\alpha,y}_{f} \left(1 - z^{\alpha}_{j,f,t}\right) \quad \forall\{j,f,t\} \tag{6.1j}$$

$$p^{\beta,y}_{j,f,t} \leq \overline{P}^{\beta,y}_{f} \left(1 - z^{\beta}_{j,f,t}\right) \quad \forall\{j,f,t\} \tag{6.1k}$$

$$\rho^{\gamma,x}_{j,f,t}, \rho^{\gamma,y}_{j,f,t} \geq 0 \quad \forall\{j,f,t\} \tag{6.1l}$$

where the superscript γ denotes the aggregated hybrid plant participating in the market. The variables $\phi^{\gamma,x}_{j,f,t}$ and $\phi^{\gamma,y}_{j,f,t}$ represent the unified bid (charging) and offer (discharging) quantities submitted by the hybrid plant, and $\rho^{\gamma,x}_{j,f,t}$ and $\rho^{\gamma,y}_{j,f,t}$ denote the corresponding bid and offer prices. The variables $p^{\gamma,x}_{j,f,t}$ and $p^{\gamma,y}_{j,f,t}$ denote the market-cleared charging and discharging power of the hybrid plant, which are linked to the underlying subsystem powers $p^{\alpha,x}_{j,f,t}$, $p^{\alpha,y}_{j,f,t}$, $p^{\beta,x}_{j,f,t}$, and $p^{\beta,y}_{j,f,t}$ through (6.1f)–(6.1g). The binary variables $z^{\alpha}_{j,f,t}$ and $z^{\beta}_{j,f,t}$ indicate the charging mode of the CAES and LAES units (charging if $z = 1$) [204]. Constraints (6.1d) and (6.1e) impose plant-level power rating limits on the submitted bids and offers based on the subsystem ratings introduced in the objective function. Constraints (6.1h)–(6.1k) enforce the maximum power ratings at the subsystem level and prevent simultaneous charging and discharging [183]. Finally, (6.1l) ensures that the submitted offer and bid prices are non-negative [68].

6.3.1.3 Coupling Machinery Constraints

The coupling between the CAES and LAES subsystems is governed by a dedicated set of intermediary machines that perform bi-directional energy conversion between the compressed air vessel and the cryogenic tank. Constraints (6.1m) and (6.1n) define the maximum energy that can be transferred from the compressed air tank to the cryogenic tank, based on the machinery capacity $\overline{Q}^{\alpha\to\beta}_{f}$. To ensure feasible operation, (6.1m) imposes that the CAES facility is not

charging when it sends energy, while (6.1n) requires that the LAES facility is charging when it receives energy. Constraints (6.1o) and (6.1p) define the reverse transfer from the cryogenic tank to the compressed air tank and enforce the corresponding machinery capacity $\overline{Q}_f^{\beta\to\alpha}$ together with the required operating states of the two subsystems.

$$0 \le q_{j,f,t}^{\alpha\to\beta} \le \overline{Q}_f^{\alpha\to\beta}\left(1 - z_{j,f,t}^{\alpha}\right) \quad \forall\{j,f,t\} \tag{6.1m}$$

$$0 \le q_{j,f,t}^{\alpha\to\beta} \le \overline{Q}_f^{\alpha\to\beta} z_{j,f,t}^{\beta} \quad \forall\{j,f,t\} \tag{6.1n}$$

$$0 \le q_{j,f,t}^{\beta\to\alpha} \le \overline{Q}_f^{\beta\to\alpha}\left(1 - z_{j,f,t}^{\beta}\right) \quad \forall\{j,f,t\} \tag{6.1o}$$

$$0 \le q_{j,f,t}^{\beta\to\alpha} \le \overline{Q}_f^{\beta\to\alpha} z_{j,f,t}^{\alpha} \quad \forall\{j,f,t\} \tag{6.1p}$$

where $q_{j,f,t}^{\alpha\to\beta}$ and $q_{j,f,t}^{\beta\to\alpha}$ represent the energy transferred between the subsystems at day j, facility f, and time interval t, from compressed air to liquid air and from liquid air back to compressed air, respectively (in MWh). The parameters $\overline{Q}_f^{\alpha\to\beta}$ and $\overline{Q}_f^{\beta\to\alpha}$ denote the maximum transfer capacities of the coupling machinery in each direction for facility f, and they bound the admissible energy exchange in (6.1m)–(6.1p) given the operating modes already encoded in the binary variables $z_{j,f,t}^{\alpha}$ and $z_{j,f,t}^{\beta}$.

6.3.1.4 CAES State-of-Charge Constraints

The state-of-charge of the compressed air tank is expressed by (6.1q)–(6.1s), which implement the look-ahead framework and account for bi-directional energy transfer with the cryogenic tank. Constraint (6.1q) applies to the first period of the first day ($j = 1, t = 1$), (6.1r) applies to the first period of all subsequent days ($j > 1, t = 1$), and (6.1s) applies to all other periods ($t > 1$). Constraint (6.1t) enforces that the compressed air tank returns to its initial energy level at the end of the look-ahead window, and (6.1u) bounds the

state-of-charge within admissible limits.

$$s^{\alpha}_{j,f,t} = S^{\alpha}_{f,0} + p^{\alpha,x}_{j,f,t} + q^{\beta\to\alpha}_{j,f,t}\eta^{\beta\to\alpha}_{f} - p^{\alpha,y}_{j,f,t}\Upsilon^{\alpha}_{f} - q^{\alpha\to\beta}_{j,f,t} \quad \forall\{f\}, j = 1, t = 1 \tag{6.1q}$$

$$s^{\alpha}_{j,f,t} = s^{\alpha}_{j-1,f,t=\mathbb{T}} + p^{\alpha,x}_{j,f,t} + q^{\beta\to\alpha}_{j,f,t}\eta^{\beta\to\alpha}_{f} - p^{\alpha,y}_{j,f,t}\Upsilon^{\alpha}_{f} - q^{\alpha\to\beta}_{j,f,t} \quad \forall\{f\}, j > 1, t = 1 \tag{6.1r}$$

$$s^{\alpha}_{j,f,t} = s^{\alpha}_{j,f,t-1} + p^{\alpha,x}_{j,f,t} + q^{\beta\to\alpha}_{j,f,t}\eta^{\beta\to\alpha}_{f} - p^{\alpha,y}_{j,f,t}\Upsilon^{\alpha}_{f} - q^{\alpha\to\beta}_{j,f,t} \quad \forall\{j, f\}, \forall t > 1 \tag{6.1s}$$

$$s^{\alpha}_{j,f,t} = S^{\alpha}_{f,0} \quad \forall\{f\}, j = |\mathbb{J}|, t = |\mathbb{T}| \tag{6.1t}$$

$$\underline{S}^{\alpha}_{f} \leq s^{\alpha}_{j,f,t} \leq \overline{S}^{\alpha}_{f} \quad \forall\{j, f, t\} \tag{6.1u}$$

where $s^{\alpha}_{j,f,t}$ denotes the state-of-charge of the compressed air tank at day j, facility f, and time interval t. The parameter $S^{\alpha}_{f,0}$ represents the initial state-of-charge of that tank, while $\underline{S}^{\alpha}_{f}$ and $\overline{S}^{\alpha}_{f}$ denote its minimum and maximum admissible energy levels, respectively. The parameter Υ^{α}_{f} is the CAES energy ratio [$\mathrm{MWh_{in}/MWh_{out}}$], which links the discharged power to the corresponding energy withdrawal from the tank. Together, constraints (6.1q)–(6.1s) track the inter-temporal evolution of $s^{\alpha}_{j,f,t}$ over the look-ahead horizon, (6.1t) enforces a cyclic condition by requiring the final state-of-charge to match $S^{\alpha}_{f,0}$, and (6.1u) keeps the state-of-charge within the admissible operating band for all days and time intervals.

6.3.1.5 LAES State-of-Charge Constraints

The state-of-charge of the cryogenic tank is modeled by (6.1v)–(6.1x). Following [173], the round-trip efficiency of the LAES unit is distributed symmetrically between charging and discharging in the state-of-charge equations. Constraint (6.1y) requires the cryogenic tank to return to its initial level at the end of the look-ahead window, and (6.1z) enforces lower and upper bounds on the cryogenic state-of-charge.

$$s^{\beta}_{j,f,t} = S^{\beta}_{f,0} + p^{\beta,x}_{j,f,t}(\eta^{\beta,\mathrm{RTE}}_{f})^{\frac{1}{2}} + q^{\alpha\to\beta}_{j,f,t}\eta^{\alpha\to\beta}_{f} - p^{\beta,y}_{j,f,t}/(\eta^{\beta,\mathrm{RTE}}_{f})^{\frac{1}{2}} - q^{\beta\to\alpha}_{j,f,t}$$
$$\forall\{f\}, j = 1, t = 1 \tag{6.1v}$$
$$s^{\beta}_{j,f,t} = s^{\beta}_{j-1,f,t=|\mathbb{T}|} + p^{\beta,x}_{j,f,t}(\eta^{\beta,\mathrm{RTE}}_{f})^{\frac{1}{2}} + q^{\alpha\to\beta}_{j,f,t}\eta^{\alpha\to\beta}_{f} - p^{\beta,y}_{j,f,t}/(\eta^{\beta,\mathrm{RTE}}_{f})^{\frac{1}{2}}$$
$$- q^{\beta\to\alpha}_{j,f,t} \quad \forall\{f\}, j > 1, t = 1 \tag{6.1w}$$
$$s^{\beta}_{j,f,t} = s^{\beta}_{j,f,t-1} + p^{\beta,x}_{j,f,t}(\eta^{\beta,\mathrm{RTE}}_{f})^{\frac{1}{2}} + q^{\alpha\to\beta}_{j,f,t}\eta^{\alpha\to\beta}_{f} - p^{\beta,y}_{j,f,t}/(\eta^{\beta,\mathrm{RTE}}_{f})^{\frac{1}{2}}$$
$$- q^{\beta\to\alpha}_{j,f,t} \quad \forall\{f, j\}, \forall t > 1 \tag{6.1x}$$
$$s^{\beta}_{j,f,t} = S^{\beta}_{f,0} \quad \forall\{f\}, \forall j = |\mathbb{J}|, t = |\mathbb{T}| \tag{6.1y}$$
$$\underline{S}^{\beta}_{f} \le s^{\beta}_{j,f,t} \le \overline{S}^{\beta}_{f} \quad \forall\{j, f, t\} \tag{6.1z}$$

where $s^{\beta}_{j,f,t}$ denotes the state-of-charge of the cryogenic tank at day j, facility f, and time interval t. The parameter $S^{\beta}_{f,0}$ represents the initial cryogenic state-of-charge, while $\underline{S}^{\beta}_{f}$ and $\overline{S}^{\beta}_{f}$ are the minimum and maximum admissible energy levels of the tank. The parameter $\eta^{\beta,\mathrm{RTE}}_{f}$ is the round-trip efficiency of the LAES unit, which is applied symmetrically in (6.1v)–(6.1x) through the factor $(\eta^{\beta,\mathrm{RTE}}_{f})^{1/2}$ in charging and its reciprocal in discharging. The parameter $\eta^{\alpha\to\beta}_{f}$ denotes the efficiency of energy conversion from compressed air to liquid air in the coupling machinery. Together, (6.1v)–(6.1x) track the inter-temporal evolution of $s^{\beta}_{j,f,t}$ over the look-ahead horizon, (6.1y) imposes a cyclic end-of-horizon condition by matching the final and initial levels, and (6.1z) keeps the cryogenic state-of-charge within its admissible operating band. Taken together, (6.1a)–(6.1z) define the upper-level profit-maximization problem of the hybrid CAES-LAES plant over the multi-day look-ahead horizon.

6.3.2 Lower-Level Problem: Market-Clearing Mechanism

The lower-level problem models the day-ahead market-clearing process using a nodal pricing framework consistent with [68, 69]. It determines the dispatch of generators, wind plants, demands, and the hybrid CAES-LAES plant, as well as nodal prices and power flows, in response to all submitted offers and bids. The dual variables associated with equality and inequality constraints are indicated after a colon. The lower-level decision vector is denoted by Ξ^{LL}

[4], which collects all primal and dual variables of the market-clearing problem, valid for each time interval $t \in \mathbb{T}$ on each day $j \in \mathbb{J}$:

$$\Xi^{\mathrm{LL}} = \Big\{ p^{G}_{j,g,t},\, p^{W}_{j,w,t},\, p^{D}_{j,d,t},\, p^{\gamma,x}_{j,f,t},\, p^{\gamma,y}_{j,f,t},\, \theta_{j,b,t},\, \lambda^{\mathrm{Elec}}_{j,b,t},\, \mu,\, \xi,\, \delta \Big\}.$$

6.3.2.1 Objective Function

The objective function (6.2a) minimizes the total system cost and therefore maximizes social welfare. The first and second terms represent the offering and bidding costs of conventional generators and demands. The third term accounts for the costs associated with strategic storage offers and bids. Wind producers are assumed to have zero marginal cost and submit corresponding offers [68, 69].

$$\begin{aligned} \min_{\Xi^{\mathrm{LL}}} \; & \sum_{j\in\mathbb{J}} \sum_{g\in\mathbb{G}} \sum_{t\in\mathbb{T}} V^{G}_{j,g,t} p^{G}_{j,g,t} - \sum_{j\in\mathbb{J}} \sum_{d\in\mathbb{D}} \sum_{t\in\mathbb{T}} V^{D}_{j,d} p^{D}_{j,d,t} \\ & + \sum_{j\in\mathbb{J}} \sum_{f\in\mathbb{F}} \sum_{t\in\mathbb{T}} \Big[\rho^{\gamma,y}_{j,f,t} p^{\gamma,y}_{j,f,t} - \rho^{\gamma,x}_{j,f,t} p^{\gamma,x}_{j,f,t} \Big] \end{aligned} \tag{6.2a}$$

where $p^{G}_{j,g,t}$ denotes the cleared output of conventional generator g at day j and time interval t, and $V^{G}_{j,g,t}$ is the corresponding offer price. The variable $p^{D}_{j,d,t}$ denotes the cleared demand of consumer d, associated with the bid price $V^{D}_{j,d}$. The last summation in (6.2a) aggregates the contribution of strategic storage offers and bids through the market-interface prices and cleared quantities $\rho^{\gamma,x}_{j,f,t}$, $\rho^{\gamma,y}_{j,f,t}$, $p^{\gamma,x}_{j,f,t}$, and $p^{\gamma,y}_{j,f,t}$, as defined in the market participation constraints of the upper-level problem. The minimization is carried out over the set of lower-level decision variables Ξ^{LL}, which includes the cleared generation, demand, and storage quantities, while the corresponding lower-level constraints are introduced in the following sections.

6.3.2.2 Nodal Power Balance Constraint

Constraint (6.2b) enforces power balance at each node of the network under the direct-current approximation [68, 69]. The associated dual variables $\lambda^{\mathrm{Elec}}_{j,b,t}$

[4] All lower-level decision variables are introduced and defined at their first appearance in the mathematical formulation that follows.

correspond to the nodal electricity prices.

$$\sum_{d\in\Phi_b^{\mathrm{D}}} p^{D}_{j,d,t} + \sum_{b'\in\Phi_{b,b'}} \mathrm{Sus}_{b,b'}\left[\theta_{j,b,t} - \theta_{j,b',t}\right] = \sum_{g\in\Phi_b^{\mathrm{G}}} p^{G}_{j,g,t} + \sum_{w\in\Phi_b^{\mathrm{W}}} p^{W}_{j,w,t} + \sum_{f\in\Phi_b^{\mathrm{F}}} p^{\gamma,y}_{j,f,t} - p^{\gamma,x}_{j,f,t} : (\lambda^{\mathrm{Elec}}_{j,b,t}) \quad \forall\{j,b,t\} \tag{6.2b}$$

where Φ_b^{D}, Φ_b^{G}, Φ_b^{W}, and Φ_b^{F} denote the sets of demands, conventional generators, wind units, and hybrid storage facilities connected at bus b, respectively. The set $\Phi_{b,b'}$ contains the buses b' that are directly connected to bus b by a transmission line. The parameter $\mathrm{Sus}_{b,b'}$ represents the series susceptance of line (b,b'), and $\theta_{j,b,t}$ is the voltage angle at bus b (in radians). The dual variable $\lambda^{\mathrm{Elec}}_{j,b,t}$ is associated with the nodal power balance at bus b and time interval t.

6.3.2.3 Resource Dispatch Constraints

Constraints (6.2c) and (6.2d) limit the cleared offers from conventional generators and wind plants to their respective capacity and forecast levels. Constraint (6.2e) ensures that cleared demand bids do not exceed each consumer's peak-load forecast. Constraints (6.2f) and (6.2g) ensure that the cleared storage bids and offers remain within the values submitted by the hybrid CAES-LAES plant.

$$0 \le p^{G}_{j,g,t} \le \overline{P}^{G}_{g} : \quad (\underline{\mu}^{G}_{j,g,t}, \overline{\mu}^{G}_{j,g,t}) \quad \forall\{j,g,t\} \tag{6.2c}$$

$$0 \le p^{W}_{j,w,t} \le E^{W}_{j,w,t} : \ (\underline{\mu}^{W}_{j,w,t}, \overline{\mu}^{W}_{j,w,t}) \quad \forall\{j,w,t\} \tag{6.2d}$$

$$0 \le p^{D}_{j,d,t} \le \overline{E}^{D}_{j,d,t} : \ (\underline{\mu}^{D}_{j,d,t}, \overline{\mu}^{D}_{j,d,t}) \quad \forall\{j,d,t\} \tag{6.2e}$$

$$0 \le p^{\gamma,x}_{j,f,t} \le \phi^{\gamma,x}_{j,f,t} : \ (\underline{\mu}^{\gamma,x}_{j,f,t}, \overline{\mu}^{\gamma,x}_{j,f,t}) \quad \forall\{j,f,t\} \tag{6.2f}$$

$$0 \le p^{\gamma,y}_{j,f,t} \le \phi^{\gamma,y}_{j,f,t} : \quad (\underline{\mu}^{\gamma,y}_{j,f,t}, \overline{\mu}^{\gamma,y}_{j,f,t}) \quad \forall\{j,f,t\} \tag{6.2g}$$

where $\overline{P}^{G}_{g}$ denotes the installed capacity of conventional generator g (in MW), $E^{W}_{j,w,t}$ is the wind power forecast for plant w at day j and time interval t, and $\overline{E}^{D}_{j,d,t}$ is the peak-load forecast for demand d. The dual variables $(\underline{\mu}^{(\cdot)}_{j,\cdot,t}, \overline{\mu}^{(\cdot)}_{j,\cdot,t})$ are associated with the lower and upper bounds of the corresponding constraints and are later used in the derivation of the KKT conditions.

6.3.2.4 Power Flow Constraints

Constraint (6.2h) limits line flows to their thermal capacity, while (6.2i) selects the reference bus and (6.2j) bounds the phase-angle variables at all other buses.

$$-\overline{PL}_{b,b'} \leq \mathrm{Sus}_{b,b'}\left[\theta_{j,b,t} - \theta_{j,b',t}\right] \leq \overline{PL}_{b,b'} : (\underline{\xi}_{j,b,b',t}, \overline{\xi}_{j,b,b',t}) \quad \forall (b,b') \in \Phi_{b,b'}, \forall \{j,t\} \tag{6.2h}$$

$$\theta_{j,b,t} = 0 : \quad (\delta^{\mathrm{ref}}_{j,t}), \quad b = \{\mathrm{ref}\}, \forall \{j,t\} \tag{6.2i}$$

$$-\pi \leq \theta_{j,b,t} \leq \pi : (\underline{\delta}_{j,b,t}, \overline{\delta}_{j,b,t}) \quad \forall b \backslash \{\mathrm{ref}\}, \forall \{j,t\} \tag{6.2j}$$

where $\overline{PL}_{b,b'}$ denotes the thermal capacity of line (b,b'). The dual variables $\underline{\xi}_{j,b,b',t}$ and $\overline{\xi}_{j,b,b',t}$ are associated with the lower and upper line-flow limits in (6.2h). The constraint in (6.2i) fixes the voltage angle at the reference bus to zero, with $\delta^{\mathrm{ref}}_{j,t}$ as its dual variable, while (6.2j) bounds the voltage angles at all non-reference buses within $[-\pi, \pi]$, with $\underline{\delta}_{j,b,t}$ and $\overline{\delta}_{j,b,t}$ as the corresponding dual variables. Collectively, (6.2a)–(6.2j) define the lower-level market-clearing optimization problem.

6.3.3 Single-Level Reformulation and Computational Complexity

Section 6.3.1 and the lower-level market-clearing problem in Section 6.3.2 can be reformulated as a single-level MPEC by embedding the KKT conditions of the lower-level problem into the upper-level model. Since the lower-level problem is a linear and convex optimization problem, these KKT conditions are necessary and sufficient for optimality and provide an exact characterization of the market-clearing solution. The resulting single-level formulation couples the strategic decisions of the hybrid CAES-LAES plant with the equilibrium conditions of the day-ahead market.

The KKT system consists of stationarity constraints, which correspond to the first-order optimality conditions, and complementary slackness constraints, which link the primal and dual variables associated with the inequality constraints of the lower-level problem. In what follows, the stationarity conditions (6.3a)–(6.3g) and the complementary slackness conditions (6.3h)–(6.3u) are summarized. A step-by-step derivation of these expressions closely follows [205] and the structure of the lower-level problem (6.2).

6.3.3.1 Stationarity Constraints

The stationarity constraints (6.3a)–(6.3g) are obtained by differentiating the Lagrangian of the lower-level problem (6.2) with respect to its primal variables and setting the derivatives equal to zero. They express the marginal conditions that characterize optimal market-clearing decisions for generators, demands, wind units, storage, and network variables.

$$V^{G}_{j,g,t} - \lambda^{\text{Elec}}_{j,b\in\Phi^{\text{G}}_{g},t} + \overline{\mu}^{G}_{j,g,t} - \underline{\mu}^{G}_{j,g,t} = 0 \quad \forall\{j,g,t\} \tag{6.3a}$$

$$- \lambda^{\text{Elec}}_{j,b\in\Phi^{\text{W}}_{w},t} + \overline{\mu}^{W}_{j,w,t} - \underline{\mu}^{W}_{j,w,t} = 0 \quad \forall\{j,w,t\} \tag{6.3b}$$

$$- V^{D}_{j,d} + \lambda^{\text{Elec}}_{j,b\in\Phi^{\text{D}}_{d},t} + \overline{\mu}^{D}_{j,d,t} - \underline{\mu}^{D}_{j,d,t} = 0 \quad \forall\{j,d,t\} \tag{6.3c}$$

$$\rho^{\gamma,y}_{j,f,t} - \lambda^{\text{Elec}}_{j,b\in\Phi^{\text{F}}_{b},t} + \overline{\mu}^{\gamma,y}_{j,f,t} - \underline{\mu}^{\gamma,y}_{j,f,t} = 0 \quad \forall\{j,f,t\} \tag{6.3d}$$

$$\lambda^{\text{Elec}}_{j,b\in\Phi^{\text{F}}_{b},t} - \rho^{\gamma,x}_{j,f,t} + \overline{\mu}^{\gamma,x}_{j,f,t} - \underline{\mu}^{\gamma,x}_{j,f,t} = 0 \quad \forall\{j,f,t\} \tag{6.3e}$$

$$\sum_{b'\in\Phi_{b,b'}} \text{Sus}_{b,b'}\Big[\lambda^{\text{Elec}}_{j,b,t} - \lambda^{\text{Elec}}_{j,b',t} + \overline{\xi}_{j,b,b',t} - \overline{\xi}_{j,b',b,t} - \underline{\xi}_{j,b,b',t} + \underline{\xi}_{j,b',b,t}\Big] + \overline{\delta}_{j,b,t} - \underline{\delta}_{j,b,t} = 0 \quad \forall(b,b')\backslash\{\text{ref}\},\forall\{j,t\} \tag{6.3f}$$

$$\sum_{b'\in\Phi_{b,b'}} \text{Sus}_{b,b'}\Big[\lambda^{\text{Elec}}_{j,b,t} - \lambda^{\text{Elec}}_{j,b',t} + \overline{\xi}_{j,b,b',t} - \overline{\xi}_{j,b',b,t} - \underline{\xi}_{j,b,b',t} + \underline{\xi}_{j,b',b,t}\Big] + \delta^{\text{ref}}_{j,t} = 0 \quad \forall(b,b') = \{\text{ref}\}, \quad \forall\{j,t\} \tag{6.3g}$$

Constraints (6.3a)–(6.3e) state that, at optimum, the marginal offer or bid price of each generator, wind unit, demand, and storage decision is balanced by the corresponding nodal electricity price and the shadow prices of the capacity and bid limits. Constraints (6.3f) and (6.3g) correspond to stationarity with respect to the bus voltage angles. They link nodal prices, line shadow prices, and angle bounds through the susceptance matrix and the dual variables associated with power flow limits and angle constraints.

6.3.3.2 Complementary Slackness Constraints

The complementary slackness constraints (6.3h)–(6.3u) couple each lower-level inequality constraint with its associated dual variable. The notation $a \perp b$ indicates that $a \geq 0$, $b \geq 0$, and $a \cdot b = 0$, so that either the constraint is binding and the dual variable is positive, or the constraint is non-binding and the dual

variable is zero. This structure enforces the equilibrium relationship between primal feasibility and dual optimality in the market-clearing model.

$$0 \leq \underline{\mu}^{G}_{j,g,t} \perp p^{G}_{j,g,t} \geq 0 \quad \forall\{j,g,t\} \tag{6.3h}$$

$$0 \leq \overline{\mu}^{G}_{j,g,t} \perp \left(\overline{P}^{G}_{g} - p^{G}_{j,g,t}\right) \geq 0 \quad \forall\{j,g,t\} \tag{6.3i}$$

$$0 \leq \underline{\mu}^{W}_{j,w,t} \perp p^{W}_{j,w,t} \geq 0 \quad \forall\{j,w,t\} \tag{6.3j}$$

$$0 \leq \overline{\mu}^{W}_{j,w,t} \perp \left(E^{W}_{j,w,t} - p^{W}_{j,w,t}\right) \geq 0 \quad \forall\{j,w,t\} \tag{6.3k}$$

$$0 \leq \underline{\mu}^{D}_{j,d,t} \perp p^{D}_{j,d,t} \geq 0 \quad \forall\{j,d,t\} \tag{6.3l}$$

$$0 \leq \overline{\mu}^{D}_{j,d,t} \perp \left(\overline{E}^{D}_{j,d,t} - p^{D}_{j,d,t}\right) \geq 0 \quad \forall\{j,d,t\} \tag{6.3m}$$

$$0 \leq \underline{\mu}^{\gamma,y}_{j,f,t} \perp p^{\gamma,y}_{j,f,t} \geq 0 \quad \forall\{j,f,t\} \tag{6.3n}$$

$$0 \leq \overline{\mu}^{\gamma,y}_{j,f,t} \perp \left(\phi^{\gamma,y}_{j,f,t} - p^{\gamma,y}_{j,f,t}\right) \geq 0 \quad \forall\{j,f,t\} \tag{6.3o}$$

$$0 \leq \underline{\mu}^{\gamma,x}_{j,f,t} \perp p^{\gamma,x}_{j,f,t} \geq 0 \quad \forall\{j,f,t\} \tag{6.3p}$$

$$0 \leq \overline{\mu}^{\gamma,x}_{j,f,t} \perp \left(\phi^{\gamma,x}_{j,f,t} - p^{\gamma,x}_{j,f,t}\right) \geq 0 \quad \forall\{j,f,t\} \tag{6.3q}$$

$$0 \leq \underline{\xi}_{j,b,b',t} \perp \left(\mathrm{Sus}_{b,b'}\left[\theta_{j,b,t} - \theta_{j,b',t}\right] + \overline{PL}_{b,b'}\right) \geq 0 \quad \forall(b,b') \in \Phi_{b,b'}, \forall\{j,t\} \tag{6.3r}$$

$$0 \leq \overline{\xi}_{j,b,b',t} \perp \left(\overline{PL}_{b,b'} - \mathrm{Sus}_{b,b'}\left[\theta_{j,b,t} - \theta_{j,b',t}\right]\right) \geq 0 \quad \forall(b,b') \in \Phi_{b,b'}, \forall\{j,t\} \tag{6.3s}$$

$$0 \leq \underline{\delta}_{j,b,t} \perp \left(\theta_{j,b,t} + \pi\right) \geq 0 \quad \forall b \backslash \{\mathrm{ref}\}, \quad \forall\{j,t\} \tag{6.3t}$$

$$0 \leq \overline{\delta}_{j,b,t} \perp \left(\pi - \theta_{j,b,t}\right) \geq 0 \quad \forall b \backslash \{\mathrm{ref}\}, \quad \forall\{j,t\} \tag{6.3u}$$

Together, the stationarity conditions (6.3a)–(6.3g), the complementary slackness conditions (6.3h)–(6.3u), and the primal feasibility constraints of Section 6.3.2 (including power balance, resource limits, and network equations) form the complete KKT system of the lower-level market-clearing problem.

6.3.3.3 Resulting Single-Level MPEC and Linearization

Embedding the lower-level KKT conditions into the upper-level problem yields a single-level optimization model that maximizes the hybrid CAES-LAES profit (6.1a), subject to:

- the upper-level operational constraints (6.1b)–(6.1z),
- the lower-level equality constraints (6.2b) and (6.2i),
- the stationarity conditions (6.3a)–(6.3g), and

- the complementary slackness constraints (6.3h)–(6.3u).

The resulting MPEC is non-convex and contains two main sources of nonlinearity, which must be treated explicitly to obtain a tractable mixed-integer linear formulation.

(i) A first source of nonlinearity is the set of bilinear terms in (6.1b) and (6.1c), which involve the product of market-clearing prices and cleared storage bids and offers. Appendix A.6 describes how these terms are directly linearized following the approach in [69]. This linearization preserves the economic interpretation of the objective function while expressing all revenue components in affine form.

(ii) A second source of nonlinearity is the set of complementarity constraints (6.3h)-(6.3u), which are intrinsic to the KKT conditions. In power system optimization and operations research, big-M reformulations are a standard technique to linearize such constraints at the expense of introducing auxiliary binary variables [206]. Appendix A.7 presents the big-M linearization adopted in this chapter. The procedure used to select appropriate big-M values follows [68] and is designed to balance numerical stability and model tightness by avoiding unnecessarily conservative upper bounds.

After these linearization steps, the final formulation becomes a MILP that remains structurally complex due to the number of time periods, buses, market participants, and KKT-related binaries introduced by the big-M reformulation. Table 6.1 summarizes the nominal and effective decision-space dimensions of the single-level optimization model as a function of the main sets. The nominal space corresponds to the variable counts that would arise from a full nodal representation, while the effective space accounts for the actual number of lines and buses in the test system through the set $\Phi_{b,b'}$.

The scaling of the integer variable count with the number of time intervals, days, and network elements illustrates that the resulting MILP is computationally demanding, especially for long look-ahead horizons or large systems. This complexity motivates the learning-assisted warm-start procedures developed in Section 6.4, which aim to provide high-quality initial values for key binary variables and thereby improve the tractability of the strategic look-ahead dispatch problem.

Table 6.1: Breakdown of integer and continuous decision variables in the final single-level optimization model.

Nominal Space	**# Int.**	$2\lvert\mathbb{J}\rvert\lvert\mathbb{T}\rvert\big[\lvert\mathbb{G}\rvert+\lvert\mathbb{W}\rvert+\lvert\mathbb{D}\rvert+2\lvert\mathbb{F}\rvert+\lvert\mathbb{B}\rvert\big(\lvert\mathbb{B}\rvert+1\big)\big]$
	# Cont.	$\lvert\mathbb{J}\rvert\lvert\mathbb{T}\rvert\Big[3\lvert\mathbb{G}\rvert+3\lvert\mathbb{W}\rvert+3\lvert\mathbb{D}\rvert+18\lvert\mathbb{F}\rvert+2\big(\lvert\mathbb{B}\rvert^2+2\lvert\mathbb{B}\rvert\big)-1\Big]$
Effective Space	**# Int.**	$2\lvert\mathbb{J}\rvert\lvert\mathbb{T}\rvert\big[\lvert\mathbb{G}\rvert+\lvert\mathbb{W}\rvert+\lvert\mathbb{D}\rvert+2\lvert\mathbb{F}\rvert+\lvert\Phi_{b,b'}\rvert+\lvert\mathbb{B}\rvert\big]$
	# Cont.	$\lvert\mathbb{J}\rvert\lvert\mathbb{T}\rvert\Big[3\lvert\mathbb{G}\rvert+3\lvert\mathbb{W}\rvert+3\lvert\mathbb{D}\rvert+18\lvert\mathbb{F}\rvert+2\big(\lvert\Phi_{b,b'}\rvert+2\lvert\mathbb{B}\rvert\big)-1\Big]$

6.4. Learning-Assisted Solution Approach for the Mixed-Integer MPEC

The single-level formulation derived in Section 6.3.3 is linear in its algebraic structure but remains an NP[5]-hard MILP problem due to the large number of binary variables that it contains. As summarized in Table 6.1, both the nominal and effective decision spaces grow rapidly with the number of buses, generators, wind plants, demands, storage facilities, and with the length of the look-ahead horizon. For the IEEE 118-bus system [73] with one hybrid CAES-LAES plant and three wind sites over a six-day look-ahead horizon, the nominal binary space exceeds four million variables, while the effective binary space still contains more than 240,000 variables. This size makes a direct branch-and-bound search computationally demanding, even when using state-of-the-art mixed-integer solvers.

To improve tractability without altering the underlying MPEC formulation, this section develops a learning-assisted solution approach that provides informed initial values for the binary variables. The proposed framework treats the mixed-integer MPEC as the exact reference model and uses machine learning only to generate warm-starts, not to replace the optimization problem with an approximate surrogate. In this way, the solver remains free to adjust the binary variables as needed to recover optimality, while benefiting from a significant reduction in search effort.

[5]Non-deterministic Polynomial-time.

6.4.1 Structure of Binary Variables and Motivation

The final single-level model contains two main tiers of binary variables:

(i) Operational mode binaries. The variables $z^{\alpha}_{j,f,t}$ and $z^{\beta}_{j,f,t}$ indicate the operating mode of the CAES and LAES subsystems of each hybrid facility f at day j and time interval t. A value of one indicates a charging state. These binaries originate from the upper-level problem in Section 6.3.1 and carry over directly into the single-level MPEC.

(ii) Big-M binaries from complementarity conditions. The second tier consists of auxiliary binary variables introduced to linearize the complementarity constraints (6.3h)–(6.3u) through the big-M reformulation described in Appendix A.7. In the lower-level problem, a generic inequality constraint of the form $\wp(\varkappa) \geq 0$, associated with dual variable ℓ, appears in the KKT system as:

$$0 \leq \wp(\varkappa) \perp \ell \geq 0.$$

This complementarity relation is represented by a binary variable u and a big-M constant M through:

$$\wp(\varkappa) \leq Mu, \qquad \ell \leq M(1-u).$$

If $u = 1$, the optimum lies strictly inside the feasible region of $\wp(\varkappa) \geq 0$ and the constraint is *inactive*. In this case, small perturbations of the constraint boundary do not affect the optimal objective value. If $u = 0$, the optimum lies on the boundary and the constraint is *active*. In that case, shifting the boundary changes the optimal objective. The complete big-M reformulation applies this pattern to all complementarity conditions associated with generators, wind units, demands, storage limits, line flows, and voltage angles.

Together, the operational mode binaries and the big-M binaries form a high-dimensional binary vector at each time interval and for each day of the look-ahead horizon. The resulting search space is very large and highly structured. Patterns in demand, wind forecasts, and generator offers induce regularities in which constraints are active and which storage modes are optimal. The learning-assisted framework seeks to exploit these regularities. It predicts good candidate patterns for the binary variables as a function of observable system features. These predictions are then used to warm-start the solver, which

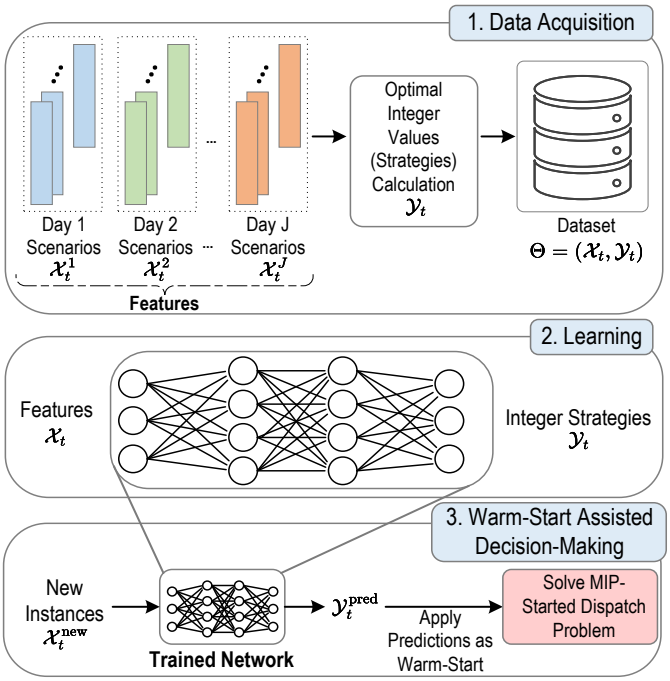

Figure 6.4: Overview of the learning-assisted optimization framework.

preserves the exact MPEC formulation and its optimality guarantees.

6.4.2 Three-Phase Learning-Assisted Framework

Figure 6.4 summarizes the proposed learning-assisted optimization framework. The process consists of three main phases: (*i*) offline data acquisition, (*ii*) training of a multi-label classifier, and (*iii*) warm-start assisted decision-making.

6.4.2.1 Phase I: Offline Data Acquisition

The first phase constructs a labeled data set that captures the relationship between system conditions and optimal binary decisions. For each hour t in the look-ahead horizon, a feature vector $\mathcal{X}_t$ is defined that contains the exogenous inputs relevant for market clearing and storage operation, such as:

- hourly demand forecasts at all buses;
- wind power forecasts at all wind sites;
- offer curves or marginal cost parameters of conventional generators.

Given a particular realization of $\mathcal{X}_t$, the exact single-level MPEC is solved offline to global optimality by allocating sufficient computational time. The resulting optimal binary vector for that hour is denoted by $\mathcal{Y}_t$, which includes both tiers of binary variables:

$$\mathcal{Y}_t = \left(z^{\alpha}_{j,f,t},\, z^{\beta}_{j,f,t},\, u^{(\cdot)}_{j,\cdot,t} \right).$$

Each sample therefore consists of an input–output pair

$$\Theta_t = (\mathcal{X}_t, \mathcal{Y}_t).$$

By varying demand profiles, wind conditions, and generator offers across many scenarios [136], a diverse collection of samples is generated. This data acquisition phase is carried out entirely offline and can be parallelized, since each scenario is independent. It concentrates the computational burden in a pre-processing stage and produces a data set that reflects the intrinsic mapping between market conditions and optimal binary decisions for the strategic hybrid plant.

6.4.2.2 Phase II: Multi-Label Neural Network Classifier

In the second phase, the collected samples are used to train a supervised learning model that approximates the mapping $\mathcal{X}_t \mapsto \mathcal{Y}_t$. The binary decision vector $\mathcal{Y}_t$ is high dimensional, since it includes all mode-selection binaries and all big-M binaries associated with the complementarity conditions. The learning task is therefore a multi-label classification problem.

A deep feedforward neural network is adopted as the classifier. This choice reflects its favorable scalability in high-dimensional output spaces, where alternative models such as support vector machines or decision trees tend to become less efficient or require problem-specific feature engineering. The network architecture follows a standard structure:

- an input layer that receives the feature vector $\mathcal{X}_t$;
- several fully connected hidden layers with rectified linear unit (ReLU) activation functions, arranged sequentially to capture non-linear interactions among features;
- an output layer with sigmoidal neurons, one neuron for each binary component of $\mathcal{Y}_t$.

The network is trained using a binary cross-entropy loss function, which is suitable for multi-label classification where each output neuron represents an independent Bernoulli variable. During training, the network learns to approximate the probability that each binary variable takes the value one, conditional on the given features. The learning phase results in a set of trained parameters that encode the empirical relationship between system conditions and optimal binary strategies in the considered set of scenarios.

The aim of this phase is not to propose an advanced deep-learning architecture, but rather to assess the practicality of a standard feedforward neural network in a *bi-level* setting with many integer variables. This assessment provides a reference point for future work that may consider more specialized architectures or hybrid learning–optimization schemes.

6.4.2.3 Phase III: Warm-Start Assisted Mixed-Integer Optimization

In the third phase, the trained neural network is integrated into the solution process of the strategic look-ahead dispatch problem. For a new, out-of-sample realization of the features $\mathcal{X}_t$ over the look-ahead window, the network is queried hour by hour. For each hour, it returns predicted probabilities for all binary variables. These probabilities are then converted into initial 0–1 values, for example through a thresholding rule that assigns one if the predicted probability exceeds a given threshold and zero otherwise.

The resulting binary vector is supplied to the mixed-integer solver as a warm-start solution for the full single-level MPEC. The solver is not constrained to accept the predicted binary pattern. It can branch away from this initial point if this leads to a better objective value or if feasibility requires a different combination of binaries.

In this framework, machine learning provides high-quality initial guesses for the two tiers of binary variables. The mixed-integer solver then refines these guesses and guarantees optimality with respect to the exact formulation defined in Sections 6.3 and 6.4 and Appendices A.6–A.7. Numerical results in Section 6.5 show that this learning-assisted warm-start can significantly reduce the computational time required to solve the strategic look-ahead dispatch problem, particularly in large systems and for longer look-ahead horizons, while preserving the economic interpretation and rigor of the underlying hybrid CAES-LAES model.

6.5. Case Study Design and Numerical Results

Building on the strategic look-ahead formulation and the learning-assisted solution framework developed in Sections 6.3 and 6.4, this section evaluates the performance of the hybrid CAES-LAES plant in a market environment. The analysis follows two main pathways. First, it investigates the profitability and market impacts of the hybrid CAES-LAES plant under different look-ahead horizons and price patterns. Second, it assesses the computational efficiency gains obtained by warm-starting the mixed-integer MPEC with the neural-network-based predictions described in Section 6.4.

6.5.1 Case Study Setup

The case study is designed to address two objectives:

- Assess the profitability of the hybrid CAES-LAES plant compared with standalone CAES and LAES facilities under different look-ahead window lengths, and
- Evaluate the computational benefits of the learning-assisted warm-start scheme for solving the single-level mixed-integer MPEC.

6.5.1.1 Test System and Data

A 6-bus illustrative test network, shown in Figure 6.5, is adopted as the main benchmark for the economic analysis of the hybrid CAES-LAES plant [68]. This compact system allows a transparent inspection of the plant's strategic behavior while preserving the essential features of nodal pricing and transmission constraints.

A 50 MW wind facility is connected at bus $b3$, and a single hybrid CAES-LAES plant is located at bus $b5$. The technical specifications of the hybrid plant, including power ratings, storage capacities, efficiencies, and operational cost parameters, are summarized in Table 6.2 [6]. Figure 6.5 also illustrates generator capacities, transmission-line ratings, and the per-unit reactances of all lines. Demand bids are set at 450 €/MWh in line with [68].

Wind production, load profiles, and hourly generator offer prices are derived

[6] Parameter values for charging and discharging power, storage capacities, heat rate, energy ratio, and round-trip efficiency are adopted from [57]; cryogenic tank sizing from [207]; the 10% minimum state-of-charge threshold from [63, 173]; coupling machinery efficiencies from [35]; and the USD–EUR exchange rate from [63].

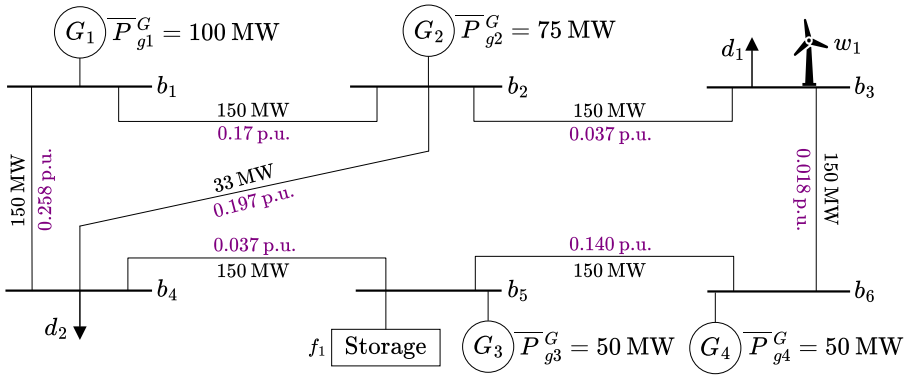

Figure 6.5: Illustrative 6-bus test network.

from Spanish market records. Two distinct historical periods are considered:

- First time frame: 7–12 December 2021, and
- Second time frame: 1–6 October 2021.

Figures 6.6 and 6.7 show the corresponding demand and wind power profiles. Demand is split equally between two loads, $d1$ and $d2$. Generator offer prices are not publicly disclosed for confidentiality reasons. Following [68, 69], generator offers are therefore assumed to vary within ±15% of the market-clearing prices of the corresponding period. Inverse optimization techniques for recovering offer curves from clearing prices exist [208] but are outside the scope of this chapter. The natural gas price is set to 107.98 €/MWh in the first time frame and to 92.94 €/MWh in the second time frame [209].

6.5.1.2 Look-Ahead Window Configurations

To examine the effect of the look-ahead horizon on strategic storage behavior and profitability, four cases are defined. All cases use the same six-day data sets, but differ in the length of the dispatch window internalized by the hybrid CAES-LAES plant:

- ***Cases 1, 2, and 3***: one-day, two-day, and three-day look-ahead windows, respectively;
- ***Case 4***: full six-day look-ahead window.

In the general formulation, the cyclic end-of-horizon conditions for the compressed air and cryogenic tanks are enforced through constraints (6.1t)

Table 6.2: Technical specifications of the hybrid CAES-LAES plant.

Parameter	**Value**	**Unit**	**Parameter**	**Value**	**Unit**
$C_f^{\alpha,x}$	2.5374	€/MWh	$C_f^{\alpha,y}$	2.5374	€/MWh
$C_f^{\beta,x}$	2.5374	€/MWh	$C_f^{\beta,y}$	2.5374	€/MWh
$\overline{Q}_f^{\alpha\to\beta}$	75	MWh	$\overline{Q}_f^{\beta\to\alpha}$	100	MWh
$\overline{P}_f^{\alpha,x}$	38	MW	$\overline{P}_f^{\alpha,y}$	50	MW
$\overline{P}_f^{\beta,x}$	60	MW	$\overline{P}_f^{\beta,y}$	32.9	MW
$S_{f,0}^{\alpha}$	175	MWh	$S_{f,0}^{\beta}$	100	MWh
$\overline{S_f^{\alpha}}$	250	MWh	$\underline{S_f^{\alpha}}$	25	MWh
$\overline{S_f^{\beta}}$	900	MWh	$\underline{S_f^{\beta}}$	90	MWh
Γ_f^{α}	1.144	$\frac{\text{MWh}_{\text{th}}}{\text{MWh}_{\text{out}}}$	Υ_f^{α}	0.692	$\frac{\text{MWh}_{\text{in}}}{\text{MWh}_{\text{out}}}$
$\eta_f^{\alpha\to\beta}$	73	%	$\eta_f^{\beta\to\alpha}$	96	%
$\eta_f^{\beta,\text{RTE}}$	55	%	-	-	-

and (6.1y), which require the final state-of-charge to return to the initial level $S_{f,0}^{\alpha}$ and $S_{f,0}^{\beta}$. In the present case study, these conditions are refined to match the length of each look-ahead window.

For Cases 1, 2, and 3, the modified cyclic conditions read:

$$s_{j,f,t}^{\alpha} = S_{f,0}^{\alpha}, \quad s_{j,f,t}^{\beta} = S_{f,0}^{\beta} \quad \forall\{f,j\}, t = 24 \tag{6.4}$$

$$s_{j,f,t}^{\alpha} = S_{f,0}^{\alpha}, \quad s_{j,f,t}^{\beta} = S_{f,0}^{\beta} \quad \forall f,\ \forall j \in \{2,4,6\},\ t = 24 \tag{6.5}$$

$$s_{j,f,t}^{\alpha} = S_{f,0}^{\alpha}, \quad s_{j,f,t}^{\beta} = S_{f,0}^{\beta} \quad \forall f,\ \forall j \in \{3,6\},\ t = 24 \tag{6.6}$$

For Case 4, the six-day look-ahead window restores the initial state-of-charge only at the end of the entire horizon:

$$s_{j,f,t}^{\alpha} = S_{f,0}^{\alpha}, \quad s_{j,f,t}^{\beta} = S_{f,0}^{\beta} \quad \forall f,\ \forall j = 6,\ t = 24 \tag{6.7}$$

These variations preserve the structure of the look-ahead formulation in Section 6.3, while enabling a consistent comparison of different dispatch hori-

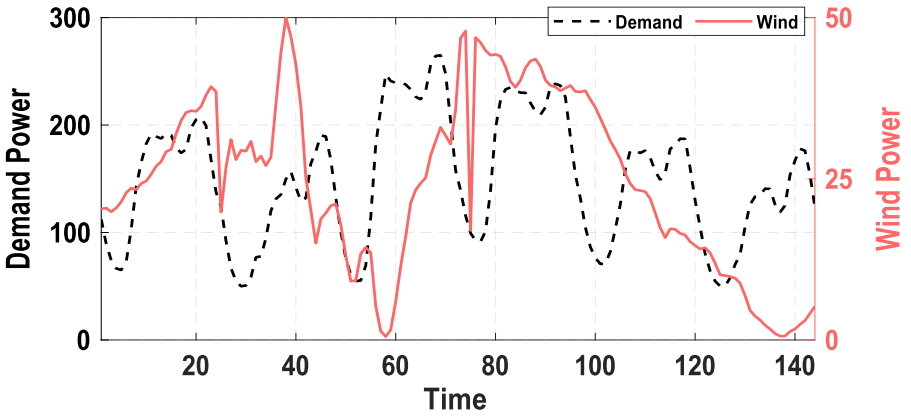

Figure 6.6: Demand and wind power profiles (MW) during the first time frame (7–12 December 2021).

zons.

6.5.1.3 Simulation Settings and Scenario Generation

The MILP formulation derived in Section 6.3.3 is implemented and solved with Gurobi. The optimality gap is set to zero in order to obtain exact benchmark solutions. All simulations are performed on a Windows laptop equipped with an 11^{th}-generation Intel Core i7 processor at 2.50 GHz and 16 GB of RAM.

To represent uncertainty in wind, load, and generator offer prices, ten equiprobable scenarios are generated. In each scenario, these quantities are independently perturbed by multiplicative factors drawn from a uniform distribution $\mathcal{U}(0.85, 1.15)$ around the nominal values of each lead day. The corresponding solutions approximate those of a static stochastic programming model [203]. Throughout this section, all reported results are scenario averages. For brevity, the term "average" is omitted in the presentation of results. The impact of replacing the fixed symmetric deviation band with a lead-dependent, widening band is investigated in Appendix A.8.

6.5.2 Profitability Analysis of the Hybrid CAES-LAES Plant

The profitability analysis compares hybrid CAES-LAES operation against a benchmark in which the CAES and LAES units are operated as standalone facilities with no internal energy transfer. Both configurations participate

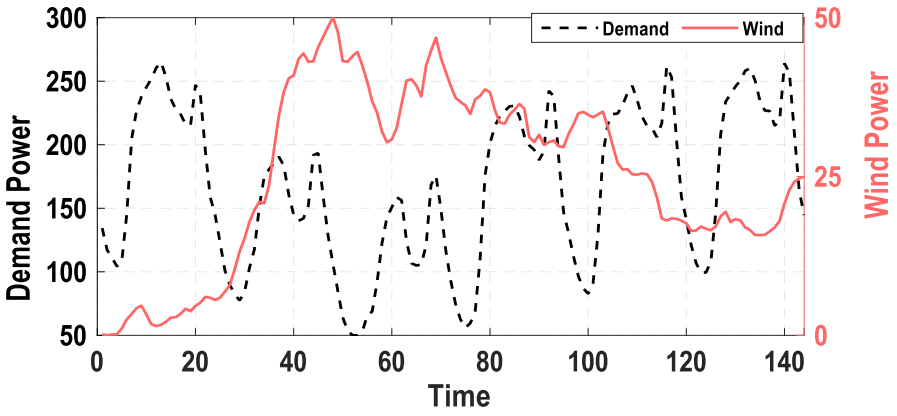

Figure 6.7: Demand and wind power profiles (MW) during the second time frame (1–6 October 2021).

Table 6.3: Profit and cleared offers/bids in standalone and hybrid CAES-CES systems across Cases 1 and 2—First time frame results (December 7-12, 2021).

System	**Case 1**			**Case 2**		
	Profit [€]	$\sum p^{\gamma,y}$ [MWh]	$\sum p^{\gamma,x}$ [MWh]	Profit [€]	$\sum p^{\gamma,y}$ [MWh]	$\sum p^{\gamma,x}$ [MWh]
Standalone Facilities	86,729	1,149	1,237	114,972	1,486	1,462
Hybrid Plant	93,518	1,306	1,407	118,003	1,606	1,558

strategically in the day-ahead market under the Stackelberg formulation of Section 6.3. The analysis covers the two time frames introduced above. To avoid repetition, the discussion focuses on the first period and then highlights the main differences observed in the second period.

6.5.2.1 First Time Frame: 7–12 December 2021

Tables 6.3 and 6.4 report the total profit and the cumulative cleared offers and bids of the standalone and hybrid configurations for Cases 1 to 4 in the first time frame. The hybrid technology consistently outperforms the standalone configuration for all look-ahead window lengths.

Table 6.4: Profit and cleared offers/bids in standalone and hybrid CAES-CES systems across Cases 3 and 4—First time frame results (December 7-12, 2021).

System	**Case 3**			**Case 4**		
	Profit [€]	$\sum p^{\gamma,y}$ [MWh]	$\sum p^{\gamma,x}$ [MWh]	Profit [€]	$\sum p^{\gamma,y}$ [MWh]	$\sum p^{\gamma,x}$ [MWh]
Standalone Facilities	146,324	1,552	1,765	164,946	1,704	1,879
Hybrid Plant	160,124	1,803	2,003	179,925	1,882	1,972

For a given configuration, extending the look-ahead horizon increases profit by enabling the plant to exploit multi-day price patterns. In Case 4, the hybrid plant gains an additional €14,979 relative to the standalone configuration, which corresponds to a profit uplift of 9.08%. When measured with respect to the daily look-ahead case (Case 1), the hybrid plant obtains 26.18%, 71.22%, and 92.39% higher profit in Cases 2, 3, and 4, respectively. These figures illustrate that carefully selecting the length of the dispatch window is a key design choice for strategic storage operators.

The mechanisms behind these profit gains can be understood by examining the market-clearing price trajectories and the daily profit breakdowns. Figure 6.8 shows the nodal prices at bus $b5$ in Case 4 over the six days. Since no line congestion occurs in this small system, prices remain uniform across buses. The alternation of high and low prices creates arbitrage opportunities that are more or less accessible depending on the length of the look-ahead horizon.

Figure 6.9 decomposes the hybrid plant's total profit into daily contributions for all four cases. In Case 1, the plant optimizes its operation on a day-by-day basis and must restore both storage tanks to their initial state-of-charge at the end of each day. This restriction limits the ability to move energy across days and leads to a relatively conservative use of storage.

In Case 2, the plant optimizes decisions over rolling two-day windows. By anticipating low prices on day 2, it can sell pre-existing energy during high-price hours of day 1, then recharge during low-price hours on day 2. The very low prices at the end of day 2 also create additional arbitrage opportunities. However, because the cyclicity condition is enforced every second day, the plant

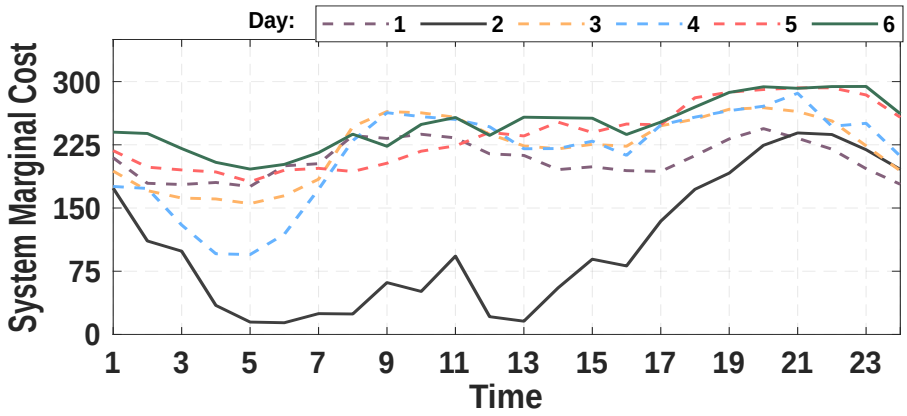

Figure 6.8: Market-clearing prices (€/MWh) in Case 4 (first time frame, 7–12 December 2021).

cannot fully exploit high-price episodes that occur beyond the two-day window.

Case 3 illustrates the benefit of further extending the horizon. With a three-day look-ahead, the plant anticipates the high prices on day 3 and strategically accumulates energy on day 2 to sell it on day 3, which results in a marked increase in cumulative profit. Case 4 then provides the most flexible setting in which the storage levels only need to return to their initial values at the end of day 6. The hybrid plant can then coordinate the use of the compressed air and cryogenic tanks over the entire period and align its charge-discharge pattern with the most favorable price cycles.

The strategic actions on day 6 in Case 4 are depicted in Figure 6.10, which shows the hybrid plant's hourly commitment and the corresponding market-clearing prices. Relative to Case 1, the plant discharges at a higher rate and sells at a lower price in the final hours, thereby increasing its market share. This behavior reduces the market-clearing price and illustrates how a strategic hybrid storage operator can influence market outcomes.

Table 6.5 details the impact of the look-ahead horizon on social welfare components. The table reports the expected profits of storage, conventional generators, and wind producers, along with consumers' expected surplus. The latter is defined as willingness-to-pay minus actual payment.

As the look-ahead horizon increases, the hybrid storage plant captures a larger share of the total supplier profit, mainly at the expense of conventional generators. At the same time, consumers benefit from lower prices, which

Figure 6.9: Daily net profit of the hybrid plant in Cases 1–4 (first time frame, 7–12 December 2021).

translate into higher surplus. The effect on wind producers is more nuanced and depends on the alignment between wind availability and periods in which the hybrid plant behaves strategically.

Finally, Figure 6.11 analyzes the sensitivity of profits to the sizes of the compressed air and cryogenic tanks in Case 4. Panel 6.11a focuses on the standalone configuration, while panel 6.11b reports the corresponding results for the hybrid plant.

For the standalone LAES facility, once the cryogenic tank exceeds approximately 800 MWh, further expansion brings only marginal increases in profit. The relatively low round-trip efficiency of the cryogenic subsystem limits the additional value of storing more energy. In contrast, increasing the CAES energy capacity enhances profitability in the standalone CAES system, due to its higher round-trip efficiency. In practice, however, above-ground high-pressure tanks are expensive, which may constrain this expansion.

In the hybrid configuration, increasing cryogenic storage capacity has a more pronounced effect on profitability than in the standalone LAES case. The profit trend in Figure 6.11b is generally upward with increasing cryogenic tank size, although not strictly monotonic. Beyond a certain threshold (for example, from 1,000 MWh to 1,100 MWh), the incremental gains become small. These observations point to the need for a dedicated sizing and siting study that optimizes tank capacities jointly with market participation decisions.

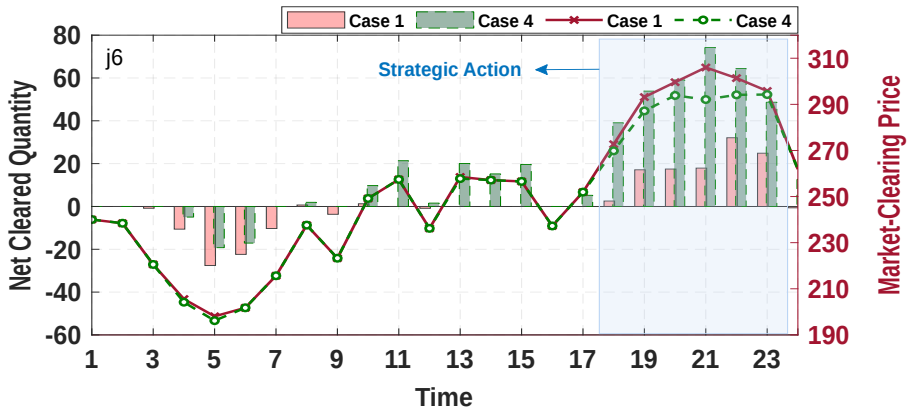

Figure 6.10: Hourly hybrid storage commitment (bars, MW) and market-clearing price (line, €/MWh) on day 6 (first time frame, 7–12 December 2021).

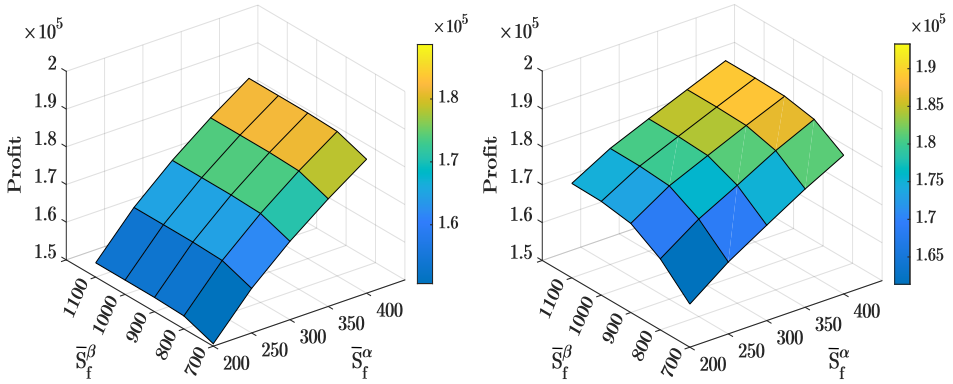

(a) Standalone facilities.

(b) Hybrid plant.

Figure 6.11: Profit sensitivity to cryogenic and compressed air tank sizes (MWh) in Case 4 (first time frame, 7–12 December 2021).

6.5.2.2 Second Time Frame: 1–6 October 2021

The second time frame, 1–6 October 2021, is used to verify the robustness of the previous findings under different demand and wind patterns. Figure 6.7 illustrates these profiles, which differ markedly from those of the December period. Figure 6.12 shows the market-clearing prices at bus $b5$ in Case 4. The presence of recurring price dips creates new arbitrage opportunities for the hybrid storage operator.

Table 6.5: Social welfare breakdown in Cases 1–4 (first time frame, 7–12 December 2021).

Case Study	**Expected Profit** [€]			**Expected Surplus** [€]
	$\sum_{\mathbb{H}}$ Storage	$\sum_{\mathbb{G}}$ Generator	$\sum_{\mathbb{W}}$ Wind	$\sum_{\mathbb{D}}$ Consumer
Case 1	93,518	252,419	680,224	4,914,322
Case 2	118,003	249,185	680,045	4,918,085
Case 3	160,124	247,813	681,406	4,919,603
Case 4	179,925	245,824	681,114	4,921,983

Table 6.6: Profitability assessment of standalone and hybrid CAES-LAES systems for 1–6 October 2021.

System	**Profit** [€]			
	Case 1	**Case 2**	**Case 3**	**Case 4**
Standalone Facilities	64,110	90,345	80,301	120,732
Hybrid Plant	65,491	98,076	81,339	130,031

Table 6.6 compares the profits of the standalone and hybrid configurations across Cases 1 to 4 for this second period. The hybrid CAES-LAES plant again outperforms the standalone configuration for all look-ahead windows. Increasing the dispatch horizon from one to six days raises the hybrid profit from €65,491 to €130,031 by exploiting price variability more effectively. Standalone facilities also benefit from longer horizons, with profit increasing from €64,110 to €120,732. The hybrid configuration, however, maintains a consistent advantage, which confirms the value of technological coupling.

Unlike in the December period, extending the look-ahead horizon does not always lead to strictly increasing profit. Moving from one to two days improves profitability, but extending to three days slightly reduces gains because the requirement to restore the initial storage levels at day 3 constrains the ability to benefit from later low-price hours. Extending the horizon further to six days

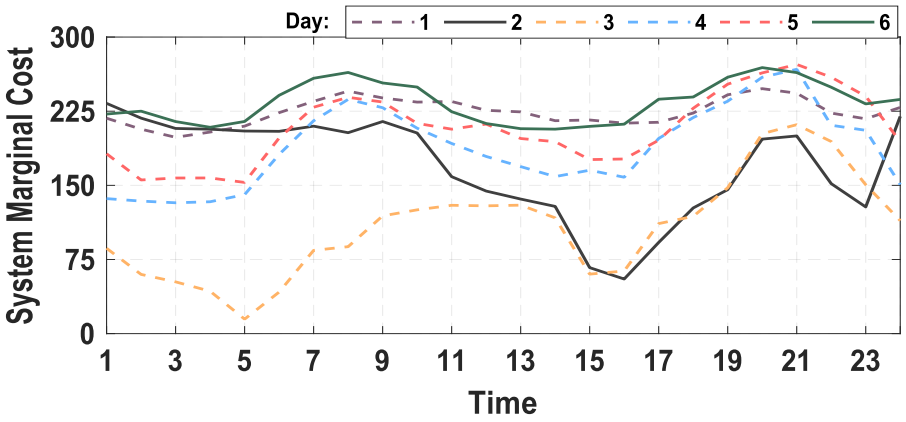

Figure 6.12: Market-clearing prices (€/MWh) in Case 4 during the second time frame (1–6 October 2021).

restores the positive trend and yields a substantial profit increase. These results reinforce the conclusion that an appropriate minimum look-ahead horizon must be selected in light of prevailing market conditions.

6.5.3 Computational Efficiency of the Learning-Assisted Model

The second part of this section quantifies the computational efficiency gains achieved by the learning-assisted framework proposed in Section 6.4. The focus is on the potential reduction in solution time and branch-and-cut iterations obtained by warm-starting large numbers of binary variables with a standard multi-label neural network classifier. All simulations in this part use data from the first time frame (7–12 December 2021).

6.5.3.1 Test Systems and Problem Dimensionality

Three network sizes are considered: the 6-bus system of Figure 6.5, the IEEE 24-bus test system, and the IEEE 118-bus test system. In each case, a single strategic hybrid CAES-LAES plant is installed at a representative bus, namely $b5$ in the 6-bus network, $b1$ in the 24-bus system, and $b15$ in the 118-bus system. The detailed network, generation, demand, and wind data for the IEEE 24-bus and 118-bus systems are reported in Appendices A.9 and A.10, respectively.

To reflect realistic system complexities, the sets of generators, demands, and wind plants are defined as follows:

Table 6.7: Comparison of integer and continuous decision variable counts across three test systems (six-day look-ahead).

Test Systems		**6-bus**	**24-bus**	**118-bus**
Nominal Space	**# Integers**	14,688	182,016	4,089,600
	# Continuous	19,296	195,120	4,147,920
Effective Space	**# Integers**	8,352	35,712	182,592
	# Continuous	12,960	48,816	240,912

- for the 6-bus network: $\{|\mathbb{G}|, |\mathbb{D}|, |\mathbb{W}|\} = \{4, 2, 1\}$,
- for the 24-bus network: $\{|\mathbb{G}|, |\mathbb{D}|, |\mathbb{W}|\} = \{12, 17, 1\}$,
- for the 118-bus network: $\{|\mathbb{G}|, |\mathbb{D}|, |\mathbb{W}|\} = \{54, 99, 3\}$.

For the 24-bus and 118-bus systems, the rated capacity of each wind farm is set to 100 MW. The feature vectors used by the neural network classifier therefore contain 7, 30, and 156 hourly features for the 6-bus, 24-bus, and 118-bus networks, respectively.

Table 6.7 summarizes the number of integer and continuous decision variables in the nominal and effective spaces of the six-day look-ahead formulation, following the definitions in Table 6.1. The effective space accounts for the actual number of transmission lines.

These figures confirm that the final mixed-integer problem is large even for moderate system sizes, and that the 118-bus case lies well within the range of challenging real-world market-clearing applications.

6.5.3.2 Data Generation and Neural Network Training

To explore a wide range of operating regimes, 19,440 samples are generated for each test system. For every sample, the components of the feature vector (demand forecasts, wind power forecasts, and generator offer prices) are independently scaled by factors drawn from a uniform distribution $\mathcal{U}(0.7, 1.3)$ around their nominal values. Demand forecasts are based on the nominal values reported in [210]. Wind forecasts are derived from data collected in Spain, Belgium, and France for the period 7–12 December 2021 [211] and are

Table 6.8: Hyperparameter tuning results for the neural network classifiers across test systems.

Test Systems	# Layers	# Units	Learning rate	Epochs	Batch Size
6-bus	5	452	3.047e-4	1,000	100
24-bus	4	433	4.585e-4	1,000	100
118-bus	4	510	2.511e-4	1,000	100

downscaled to represent 100 MW wind farms.[7]

Out of the 19,440 samples, 15,120 are used for training and the remaining samples are reserved for out-of-sample testing. For each sample, the full MILP formulation is solved offline with Gurobi and the resulting optimal binary vector is stored. These binaries correspond to both tiers of variables described in Section 6.4.1, that is, the operational mode binaries $z^{\alpha}_{j,f,t}$, $z^{\beta}_{j,f,t}$ and the big-M binaries associated with complementarity conditions.

For each test system, a single deep feedforward neural network classifier is trained to predict all binary variables simultaneously. The network architecture is tuned with Optuna [212] in PyTorch by varying:

- the number of hidden layers in the range $\{1, \ldots, 5\}$,
- the number of units per hidden layer in the range $\{4, \ldots, 512\}$,
- the learning rate in the interval $[10^{-5}, 10^{-1}]$.

During hyperparameter tuning, the number of epochs and the batch size are kept fixed. A total of 30 trials are performed, and the configuration with the highest classification accuracy on the validation set is selected. The resulting architectures are summarized in Table 6.8.

6.5.3.3 Classification Performance

Table 6.9 reports the out-of-sample classification metrics for the three test systems. The table lists the percentages of false negatives, false positives, true negatives, and true positives, along with the true negative rate, true positive rate, and overall accuracy. Here, an inactive binary is coded as 0 (negative) and an active binary is coded as 1 (positive).

[7]For the 24-bus network, only the wind data from Spain has been used.

Table 6.9: Out-of-sample classification metrics across test systems.

Test Systems	(%)						
	FN	**FP**	**TN**	**TP**	**TNR**	**TPR**	**Accuracy**
6-bus	0.78	0.67	19.82	78.73	96.23	99.15	98.55
24-bus	0.40	0.41	13.42	85.77	97.16	99.52	99.19
118-bus	0.58	0.60	12.77	86.05	95.64	99.30	98.82

Acronyms: FN: False Negative; FP: False Positive; TN: True Negative; TP: True Positive; TNR: True Negative Rate; TPR: True Positive Rate.

All classifiers achieve an accuracy above 98%, with both true negative and true positive rates above 95%. The fractions of false negatives and false positives remain below 1% in all systems. These values indicate that the neural networks can reliably distinguish between active and inactive binaries in the high-dimensional decision space induced by the mixed-integer MPEC.

6.5.3.4 Warm-Started Optimization and Efficiency Gains

The trained neural networks are then used to predict binary variables for new, out-of-sample feature vectors. For each time period and test system, the predicted probabilities are converted into 0-1 values through a thresholding rule and passed to Gurobi as a warm-start solution. The solver remains free to modify these values during branch-and-cut, so feasibility and global optimality with respect to the exact formulation are preserved.

The performance of the Warm-started Mixed-Integer Linear Programming (WMILP) is compared with that of the conventional MILP solved without warm-start [68, 69]. Table 6.10 summarizes the average solution times, the average number of iterations of the branch-and-cut algorithm, the percentage time savings, and the resulting out-of-sample profits for each test system.

The warm-started approach yields substantial reductions in both solution time and iteration count. Time savings reach up to 29.30% in the 24-bus system. The 118-bus system shows the largest absolute reduction in iterations but a more moderate time-saving rate, which reflects the dominant role of continuous variables and linear algebra operations in large-scale problems. In all cases, the out-of-sample profits obtained with MILP and WMILP are indistinguishable at the reported precision, which confirms that the warm-start strategy does

Table 6.10: Out-of-sample performance comparison between conventional MILP and WMILP.

Test Systems	**Solution time** (s)		**# of iterations** (average)		**Time saving** (%, average)	**Out-of-sample profit** (€, average)
	MILP	**WMILP**	**MILP**	**WMILP**		
6-bus	340	270	29,576	25,719	20.59	216,214
24-bus	546	386	51,989	42,640	29.30	244,382
118-bus	4,323	3,746	217,249	185,132	13.35	160,516

not compromise the quality of the optimal solution.

An additional observation is that the reduction in iterations correlates with the classification accuracy reported in Table 6.9. Systems with higher prediction accuracy tend to exhibit larger iteration reductions. This behavior is consistent with the interpretation of the neural network as a provider of high-quality initial patterns for the two tiers of binary variables, which in turn reduces the size of the effective search tree explored by the branch-and-cut algorithm.

Overall, the numerical results in this section show that the proposed hybrid CAES-LAES plant can significantly increase storage profitability and consumer surplus when operated with a suitably chosen look-ahead horizon. At the same time, the learning-assisted warm-start procedure provides a practical means of solving the resulting mixed-integer MPEC in large systems within reasonable computational times, while preserving the exactness and economic interpretability of the underlying strategic dispatch model.

6.6. Chapter Conclusion

This chapter developed a strategic dispatch framework for a hybrid CAES-LAES plant that participates in a day-ahead electricity market as a price-making agent. The model jointly coordinates the operation of the compressed air and cryogenic subsystems, including the bi-directional conversion machinery, and extends the dispatch problem to a multi-day look-ahead formulation. The resulting *bi-level* market-participation model, in which the hybrid plant acts as a leader and the market-clearing operator as a follower, was reformulated as

a single-level MILP using the KKT conditions of the lower-level problem. To address the large number of binary variables that arise in realistic systems, the chapter introduced a learning-assisted solution approach that uses a standard multi-label feedforward neural network to provide high-quality warm starts for the mixed-integer solver.

The numerical case studies, conducted on a 6-bus test system and extended to the IEEE 24-bus and 118-bus systems, yielded several key insights. First, the hybrid CAES-LAES configuration consistently outperforms the corresponding set of standalone CAES and LAES units in total profit, as it better exploits the complementarities between high-efficiency compressed air storage and high-density cryogenic storage. Second, the length of the dispatch window is a critical design parameter: in the studied setting, extending the horizon from one day to six days led to profit increases of up to about 90% relative to a purely day-ahead perspective and systematically improved consumers' expected surplus. Third, profit sensitivity analyses showed that increasing cryogenic storage capacity in the hybrid plant enhances profitability only up to a certain threshold, beyond which additional capacity brings negligible gains, which points to the need for carefully designed sizing studies. The robustness experiment with lead-dependent forecast-error bands in Appendix A.8 confirmed that these qualitative conclusions remain valid when forecast accuracy deteriorates with lead time. Finally, the learning-assisted warm-start strategy reduced the average solution time of the mixed-integer formulation by approximately 29.30% in the IEEE 24-bus system and 13.35% in the IEEE 118-bus system, without compromising optimality, which demonstrates its practical value for large-scale bi-level market models.

Chapter Publication

- **H. Khaloie**, A. Stankovski, B. Gjorgiev, G. Sansavini, and F. Vallée, "Hybrid Energy Storage Dispatch: A Bi-Level Look-Ahead Learning-Assisted Model," *IEEE Transactions on Energy Markets, Policy and Regulation*, vol. 3, no. 3, pp. 376–392, Sept. 2025.

CHAPTER 7

Conclusions and Perspectives

7.1. Summary

This thesis has introduced a set of optimization and learning-assisted models for the operation and market integration of bulk and long-duration energy storage technologies in liberalized electricity and multi-energy markets. It has combined detailed techno-economic representations of storage plants with stochastic programming, multi-level optimization, and data-driven warm-start strategies. The work has focused on three main classes of storage assets, namely grid-scale lithium-ion batteries, an integrated LAES-LNG configuration, and a hybrid CAES-LAES plant, and has examined both non-strategic and strategic market participation. Across these different settings, the thesis has sought to understand how storage operators can translate physical flexibility into stable and interpretable revenue streams under uncertainty.

Chapter 1 introduced the motivation and background of the thesis. It outlined the challenges that arose when variable renewable generation displaced conventional plants, highlighted the need for bulk and long-duration flexibility, and positioned storage as a central enabler of net-zero electricity systems. The chapter formulated the main research questions, targeted operational and market-integration aspects rather than pure investment planning, and explained how the subsequent chapters were connected.

Chapter 2 reviewed energy storage technologies and applications with emphasis on large-scale devices. It classified storage by power and energy ratings, response times, and discharge durations, and summarized the central roles storage played across system timescales. The chapter described the physical and economic characteristics of key technologies, including lithium-ion

batteries, compressed air, and liquid air energy storage, and explained how storage participated in wholesale electricity markets, thereby providing the physical and market context for the modeling work.

Chapter 3 developed the optimization and learning framework that supported the thesis. It introduced deterministic formulations for operational planning and extended them to scenario-based stochastic programming to capture uncertainty. The chapter presented multi-level optimization and optimality conditions, showed how these concepts led to MPEC in strategic market environments, and discussed the role of machine learning as a complement to optimization, forming the methodological toolbox used later.

Chapter 4 proposed a risk-aware bidding and dispatch framework for a grid-scale lithium-ion battery that participated in day-ahead and intraday electricity markets as a price-taking agent. It formulated a benchmark risk-neutral model that co-optimized charging and discharging decisions across the two market stages under technical constraints, and then introduced an extension with second-order SSD constraints to control the downside risk of revenues. Numerical studies evaluated how risk aversion and benchmark choice affected expected profit, revenue variability, and regret, and illustrated how non-strategic storage operators could embed explicit risk considerations into their bidding strategies.

Chapter 5 examined an integrated LAES-LNG configuration that coupled electricity and gas systems through a shared thermodynamic layout. It described the plant architecture, combining liquid air storage with liquefaction and regasification processes and cold exergy recovery, and formulated a two-stage stochastic dispatch model that co-optimized electricity generation and LNG regasification under uncertain electricity and LNG prices. To assess investment attractiveness, the chapter introduced a probabilistic payback period and showed how correlations between price uncertain revenue and plant investment costs influenced long-term economic feasibility.

Chapter 6 focused on the strategic look-ahead operation of a hybrid CAES-LAES plant in a network-constrained day-ahead electricity market. It described the main operating modes of the hybrid system and explained how the plant could exploit both compressed air and liquid air storage to provide long-duration flexibility. The chapter formulated a *bi-level* optimization model in which the hybrid plant acted as a strategic price-maker at the upper level, while the lower level cleared the day-ahead market under a direct-current approximation of power flows, and reformulated the problem as a mixed-integerMPEC.

To mitigate the computational burden, it proposed a learning-assisted solution strategy in which a feedforward neural network predicted promising integer patterns that warm-started the solver, and case studies on 6-bus, IEEE 24-bus, and IEEE 118-bus networks illustrated how hybridization and forecast horizon shaped the profitability and market impact of long-duration storage.

7.2. Conclusions

The main conclusions of this thesis relate to how bulk and long-duration storage can operate in liberalized markets under uncertainty and to how advanced optimization and learning techniques can support this operation. The models developed here show that it is possible to represent the economic behavior of storage assets in a unified framework that handles non-strategic and strategic participation, incorporates risk preferences, and captures sector-coupling effects. They also demonstrate that computational challenges, especially in *bi-level* and mixed-integer formulations, can be alleviated through informed use of machine learning without sacrificing solution quality.

For grid-scale lithium-ion batteries, the risk-aware bidding framework developed in this thesis highlights the importance of modeling revenue distributions rather than only expected values. The SSD formulation allows a storage operator to control downside risk in a transparent way by specifying acceptable dominance relations relative to a benchmark portfolio. Numerical results show that modest levels of risk aversion can substantially reduce regret and revenue volatility. The analysis also reveals that the choice of benchmark and the quality of the scenario set are crucial. Poorly chosen benchmarks or unrepresentative scenarios can lead to overly conservative strategies or misleading risk assessments. A key conclusion is that non-strategic batteries can improve their economic performance in uncertain markets by combining high-resolution inter-temporal models with risk measures that reflect investor preferences in an explicit and tractable manner.

The study of the integrated LAES-LNG configuration led to several specific conclusions about sector-coupled long-duration storage. The two-stage stochastic model showed that a coordinated operation of electricity generation, liquefaction, regasification, and cold exergy recovery allowed the plant to exploit temporal and cross-sector arbitrage opportunities that were not accessible for standalone LAES facilities. As a result, the integrated facility achieved higher expected operating profits and shorter payback periods than

reference configurations without sector-coupling. The probabilistic payback period metric proved particularly useful, since it summarized not only the central tendency of investment performance but also the likelihood of unfavorable outcomes, thereby offering a more informed view of economic feasibility than deterministic indicators. Finally, the case studies confirmed that both profitability and payback risk were strongly driven by LNG and electricity price volatility, emphasizing the need for carefully designed scenario sets and a robust evaluation of sector-coupled storage investments across a range of plausible market conditions.

The strategic hybrid CAES-LAES study provides insights into both long-duration storage behavior and the use of learning-assisted optimization in complex bi-level models. The results indicate that the length of the look-ahead horizon has a marked effect on optimal bidding strategies and on realized profits. Longer horizons allow the hybrid plant to exploit inter-temporal opportunities more fully, but they also increase model size and computational effort. Hybridization between compressed air and liquid air storage adds further flexibility by allowing the plant to exploit different efficiency profiles, charging pathways, and storage media, which can be particularly valuable under network congestion. From a methodological standpoint, the learning-assisted warm-start strategy emerges as an effective way to improve solver performance. By predicting promising patterns for integer variables, the neural network accelerates the search process and reduces solution times, especially in larger networks. The case studies confirm that this approach maintains near-optimal solution quality while enabling analyses that would otherwise be prohibitively expensive.

Across these three methodological studies, a unifying conclusion is that optimization-based models for bulk and long-duration storage must respect the interplay between technology, market design, and uncertainty. Risk-aware formulations can capture investor preferences and can support more stable revenue profiles. Sector-coupled technologies can quantify the added value of integrating storage with other infrastructures and can reveal conditions under which such integration is beneficial. Strategic *bi-level* formulations can represent the behavior of large storage units that influence market outcomes.

These conclusions also translate into practical recommendations for stakeholders who plan, operate, and regulate large-scale storage assets in liberalized electricity markets. For asset owners and system operators, a first implication is to select the market-participation model in line with the asset's expected

influence on market prices. When a storage plant is large relative to the relevant node or zone, price-taking dispatch may misrepresent both revenues and system impacts; in such cases, strategic formulations based on equilibrium constraints or MPEC provide a more appropriate decision-support tool than purely price-taking models. In addition, storage operators should treat the look-ahead horizon as a tunable operational design choice rather than a fixed modeling convention. In practice, the preferred horizon depends on the persistence of price signals, the accuracy of forecasts across lead days, and the operational flexibility of the technology. Operators can therefore rely on structured procedures to quantify the marginal value of extending the dispatch window and to identify a horizon that balances economic gains with forecast risk and computational tractability [213]. Finally, storage owners are typically able to retain detailed records of dispatch decisions and realized market outcomes; these data streams can support learning-assisted optimization workflows that warm-start commercial solvers from historical operation, thereby reducing computation time in large-scale implementations without additional data-collection requirements.

For policymakers, regulators, and market designers, the central implication is that the evaluation of long-duration storage should explicitly account for strategic behavior and forward-looking decision-making when such assets can affect price formation. Equilibrium-based tools, including MPEC formulations, offer a transparent means to assess how large storage resources reshape nodal prices, congestion rents, investment signals, and welfare distribution across market participants. These models are particularly valuable for stress-testing alternative market designs and regulatory measures before implementation and for quantifying system-level benefits of hybrid long-duration storage. In this context, targeted incentives or revenue-stabilization mechanisms may be justified to accelerate deployment when storage delivers measurable welfare gains that are not fully captured by private revenues [214]. More broadly, combining strategic equilibrium models with improved forecasting and learning-assisted optimization can provide a rigorous basis for planning, operating, and regulating next-generation storage portfolios in decarbonized power systems.

7.3. Prospects

The work presented in this thesis opens several paths for future research. One broad direction concerns richer representations of market products and more detailed market designs. The current models focus on energy markets and do

not explicitly include ancillary services, reserves, or capacity mechanisms, even though bulk and long-duration storage can provide such products. Extending the LAES-LNG model to co-optimize participation in energy and ancillary service markets, both in the electricity and gas domains, would provide a more complete picture of the plant's economic potential. Similarly, the strategic hybrid CAES-LAES framework could be expanded to include joint energy and reserve bidding, allowing a better understanding of how long-duration storage interacts with system balancing and security services.

A second direction relates to methodological enhancements of the strategic hybrid storage model and its solution techniques. The learning-assisted approach developed here relies on training data obtained from solving a KKT-based reformulation of the *bi-level* problem. This process becomes difficult for larger networks and longer horizons, since each additional feature combination requires solving a large mixed-integer program. Future work could investigate decomposition strategies, such as Benders-like methods or Lagrangian relaxations, to generate training data more efficiently. Alternative *bi-level* reformulations, for example duality-based approaches, may offer more compact representations that reduce the computational effort needed during dataset generation. Another important topic is the determination of economically meaningful look-ahead horizons in a price-making environment. While such models are available for price-taking batteries [213], extending them to strategic hybrid storage would require explicit consideration of network topology, rival strategies, demand uncertainty, and renewable generation patterns, as well as plant-specific thermodynamic behavior.

A third theme concerns richer representations of uncertainty and decision timing. The models in this thesis mainly adopt single-stage or two-stage formulations over limited horizons. Multi-stage stochastic programming would allow sequential decision processes in which storage operators update their actions as new information arrives. Such models could represent the interaction between forward, day-ahead, intraday, and real-time markets more accurately, especially for long-duration technologies that operate over multiple days or weeks. The challenge is to maintain computational tractability while introducing more refined risk measures, such as nested risk metrics or stage-wise dominance constraints. For the LAES-LNG case, multi-stage formulations could capture interactions between long-term fuel contracts, infrastructure utilization, and short-term dispatch decisions in a unified framework.

A fourth line of research involves deeper and more systematic integration

of machine learning into storage optimization. The feedforward neural network used here for warm-starting integer decisions is simple and effective, but it does not exploit temporal structures in the data and remains a black box from the perspective of the optimizer. Future work could test time series models, such as recurrent or long short-term memory networks, to forecast prices, loads, or binary on/off decisions under inter-temporal constraints, and to compare their performance with simpler architectures in terms of solution speed and robustness. It would also be valuable to study which features most strongly influence warm-start quality and how solver heuristics respond to different types of suggested integer configurations. Research on explainable machine learning and on tighter integration of forecasting modules within commercial solvers could help move warm-start strategies from empirical tools to more principled components of large-scale optimization workflows.

Finally, there is significant scope for more detailed techno-economic assessment and comparative analysis across storage technologies and market designs. The thesis has focused on operational optimization for given plant configurations and has used probabilistic payback periods as a first step toward investment evaluation. Future work could combine the developed operational models with detailed cost data and degradation representations to conduct comprehensive cost-benefit studies that compare standalone batteries, LAES, CAES, and integrated hybrids. Such studies could explore how technology improvements, policy changes, and different market rules influence the relative attractiveness of each option. They could also examine market environments in which operators relinquish some control over state-of-charge trajectories to system operators, as in designs where the market authority schedules storage within specified technical bounds. Linking these analyses to system-level planning models would provide insight into how portfolios of flexible assets, including bulk and long-duration storage, can support the long-term transition to net-zero energy systems.

Overall, the prospects outlined above show that the models and insights developed in this thesis are starting points rather than endpoints. They provide a structured foundation on which more detailed, more realistic, and more ambitious studies can build in order to understand and shape the role of large-scale storage in future energy systems.

APPENDIX A

Appendices

A.1. Perfect-Foresight Benchmark for Regret Evaluation

The ideal scenario-wise profits F_ω^{ideal} used in the regret metric of Section 4.4.1 are obtained from a perfect-foresight version of the battery bidding problem. In this setting, the operator is assumed to know the realization of day-ahead and intraday prices in advance and is allowed to adapt all decisions to each scenario ω. The resulting problem is a single-stage stochastic program, in which the only coupling across scenarios occurs in the objective function.

Let F_ω^{ideal} denote the maximum attainable profit in scenario ω. The perfect-information benchmark is then defined by

$$\max \sum_{\omega=1}^{\Omega} \pi_\omega F_\omega^{\text{ideal}}, \tag{A.1a}$$

$$\text{s.t. } F_\omega^{\text{ideal}} = \sum_{t=1}^{\mathcal{T}} \Bigg[\lambda_{t,\omega}^{\text{DA}} \big(P_{t,\omega}^{\text{DA,dis}} - P_{t,\omega}^{\text{DA,ch}}\big) + \lambda_{t,\omega}^{\text{ID}} \big(P_{t,\omega}^{\text{ID,dis}} - P_{t,\omega}^{\text{ID,ch}}\big) - \sum_{s=1}^{\mathcal{S}} \Phi_s \big(\xi_{s,t,\omega}^{\text{DA,dis}} + \xi_{s,t,\omega}^{\text{ID,dis}}\big) \Bigg] \qquad \forall \omega, \tag{A.1b}$$

where all operational variables carry the scenario index ω. The parameters $\lambda_{t,\omega}^{\text{DA}}$ and $\lambda_{t,\omega}^{\text{ID}}$ are the scenario-dependent day-ahead and intraday prices, while Φ_s is the degradation cost coefficient of segment s in the piecewise linear aging model, as in Section 4.2.2.

The operational constraints of the perfect-information problem are obtained by replicating the two-stage constraints (4.2)–(4.16) for each scenario and allowing all first-stage variables to depend on ω. More precisely:

- aggregated and segment-wise charge and discharge powers in both markets are indexed by (t, ω), that is,

$$P_t^{\mathrm{DA,dis}} \to P_{t,\omega}^{\mathrm{DA,dis}}, \quad P_t^{\mathrm{DA,ch}} \to P_{t,\omega}^{\mathrm{DA,ch}},$$

$$\xi_{s,t}^{\mathrm{DA,dis}} \to \xi_{s,t,\omega}^{\mathrm{DA,dis}}, \quad \xi_{s,t}^{\mathrm{DA,ch}} \to \xi_{s,t,\omega}^{\mathrm{DA,ch}},$$

  and similarly for the intraday quantities $P_{t,\omega}^{\mathrm{ID,dis}}$, $P_{t,\omega}^{\mathrm{ID,ch}}$, $\xi_{s,t,\omega}^{\mathrm{ID,dis}}$, and $\xi_{s,t,\omega}^{\mathrm{ID,ch}}$;

- the binary commitment variable becomes scenario-dependent, $\beta_t \to \beta_{t,\omega}$;

- the segment-wise and total state-of-charge variables, $\delta_{s,t,\omega}^{\mathrm{SoC}}$ and $\Delta_{t,\omega}^{\mathrm{SoC}}$, remain indexed by (s, t, ω) as in Section 4.2.2.

With these substitutions, each scenario ω has its own copy of the power limits, intraday adjustment limits, and state-of-charge dynamics, subject to the same technical parameters and bounds as in the original model. The resulting formulation yields $F_\omega^{\mathrm{ideal}}$ as the optimal value of (A.1b) for each scenario. These values are then used in the regret definition

$$\mathcal{G}_\omega(k_1) = F_\omega^{\mathrm{ideal}} - R_\omega(k_1),$$

introduced in Section 4.4.1, where $R_\omega(k_1)$ is the profit of the SSD-constrained two-stage strategy corresponding to a given benchmark k_1.

A.2. Robust Counterpart of the Battery Bidding Model

This appendix presents the robust counterpart of the battery bidding problem used in the comparative analysis of Section 4.5.3. The robust formulation captures bounded uncertainty in day-ahead and intraday prices by considering all realizations within symmetric intervals around nominal values and by limiting the number of periods in which prices can deviate from these nominal levels through robustness parameters.

Let $\bar{\lambda}_t^{\mathrm{DA}}$ and $\bar{\lambda}_t^{\mathrm{ID}}$ denote the nominal day-ahead and intraday prices, and let

$\hat{\lambda}^{\mathrm{DA}}$ and $\hat{\lambda}^{\mathrm{ID}}$ be the corresponding deviation bounds, so that prices are allowed to vary within $\pm 10\%$ of their nominal values. In the robust formulation, these bounded deviations are incorporated through a budget-of-uncertainty structure with parameters ϖ^{DA} and ϖ^{ID} that take values in $[0, \mathcal{T}]$ and limit the number of time periods that can experience worst-case deviations in each market.

Let $\mathrm{OF}^{\mathrm{det}}$ denote the deterministic objective function value obtained when all prices are fixed at their nominal values. In the notation of Chapter 4, this deterministic objective is

$$\mathrm{OF}^{\mathrm{det}} = \sum_{t=1}^{\mathcal{T}} \Bigg[\bar{\lambda}_t^{\mathrm{DA}} \big(P_t^{\mathrm{DA,dis}} - P_t^{\mathrm{DA,ch}}\big) + \bar{\lambda}_t^{\mathrm{ID}} \big(P_t^{\mathrm{ID,dis}} - P_t^{\mathrm{ID,ch}}\big) - \sum_{s=1}^{\mathcal{S}} \Phi_s \big(\xi_{s,t}^{\mathrm{DA,dis}} + \xi_{s,t}^{\mathrm{ID,dis}}\big) \Bigg]. \tag{A.2}$$

Under bounded price uncertainty, the robust counterpart of the profit-maximization problem can be cast as a max–min problem, where the battery operator chooses a bidding strategy that maximizes profit, while nature chooses a realization of prices within the uncertainty sets that minimizes it. Using duality theory, this max–min structure can be transformed into the following single-level optimization problem [215]:

$$\min \; -\mathrm{OF}^{\mathrm{det}} + \chi^1 \varpi^{\mathrm{DA}} + \chi^2 \varpi^{\mathrm{ID}} + \sum_{t=1}^{\mathcal{T}} \big(q_t^1 + q_t^2\big), \tag{A.3a}$$

subject to

$$q_t^1 + \chi^1 \geq \hat{\lambda}^{\mathrm{DA}} y_t^1 \qquad \forall t, \tag{A.3b}$$
$$q_t^2 + \chi^2 \geq \hat{\lambda}^{\mathrm{ID}} y_t^2 \qquad \forall t, \tag{A.3c}$$
$$q_t^1,\, q_t^2 \geq 0 \qquad \forall t, \tag{A.3d}$$
$$y_t^1,\, y_t^2 \geq 0 \qquad \forall t, \tag{A.3e}$$
$$\chi^1,\, \chi^2 \geq 0, \tag{A.3f}$$
$$P_t^{\mathrm{DA,dis}} - P_t^{\mathrm{DA,ch}} \leq y_t^1 \qquad \forall t, \tag{A.3g}$$
$$P_t^{\mathrm{ID,dis}} - P_t^{\mathrm{ID,ch}} \leq y_t^2 \qquad \forall t, \tag{A.3h}$$
$$\text{Deterministic counterparts of constraints (4.2)–(4.16).} \tag{A.3i}$$

In this formulation, q_t^1 and q_t^2 are non-negative dual variables associated

with the worst-case deviations of day-ahead and intraday prices in period t, and χ^1 and χ^2 are the dual variables associated with the robustness budgets ϖ^{DA} and ϖ^{ID}, respectively. The auxiliary variables y_t^1 and y_t^2 bound the net discharge revenues in each period and are introduced to linearize the robust counterpart of the max–min structure. Constraints (A.3b)–(A.3c) link the dual variables to the deviation bounds, while (A.3g)–(A.3h) connect the auxiliary variables to the net discharge decisions. The deterministic counterparts of constraints (4.2)–(4.16) in (A.3i) enforce the same technical limits and state-of-charge dynamics as in the risk-neutral model, evaluated at nominal prices and without scenario indices.

By varying the robustness parameters ϖ^{DA} and ϖ^{ID} between zero and $\mathcal{T}$, the decision-maker can explore the trade-off between protection against worst-case price deviations and expected profitability. These trade-offs are evaluated in Section 4.5.3 in terms of regret and out-of-sample performance, and the VIKOR method is used there to select a compromise robustness level.

A.3. Direct CO_2 intensity benchmark for the LAES-LNG discharge block

This appendix benchmarks the direct CO_2 emission intensity associated with the natural-gas-fired expansion block used during discharge of the LAES-LNG facility against a reference simple-cycle gas turbine. The calculation accounts for stack emissions from natural gas combustion only; upstream fuel-chain emissions and the carbon intensity of charging electricity are not included.

Let EF_{NG} denote the CO_2 emission factor of natural gas per unit of fuel energy. Following the U.S. environmental protection agency emission factor hub, $EF_{\mathrm{NG}} = 56.1$ $\mathrm{kgCO_2/MMBtu}$ (LHV basis) [216]. For a generation block with heat rate HR in $\mathrm{MMBtu/MWh_{out}}$, the direct emission intensity is

$$I_{\mathrm{CO_2}} = \mathrm{HR} \times EF_{\mathrm{NG}} \tag{A.4}$$

LAES-LNG discharge block: The discharge block of the LAES-LNG model operates at $\mathrm{HR_{LAES}} = 1.066$ $\mathrm{MWh_{th}/MWh_{out}}$. Using 1 $\mathrm{MWh_{th}} = 3.6$ MMBtu, this corresponds to:

$$\mathrm{HR_{LAES}} = 1.066 \times 3.6 = 3.8376 \ \mathrm{MMBtu/MWh_{out}} \tag{A.5}$$

and therefore

$$I_{\mathrm{CO_2}}^{\mathrm{LAES}} = 3.8376 \times 56.1 \approx 215.3 \ \mathrm{kgCO_2/MWh_{out}} \quad (\approx 215 \ \mathrm{gCO_2/kWh}) \quad \text{(A.6)}$$

Reference simple-cycle gas turbine: As a benchmark, the U.S. energy information administration reports an average operating heat rate of 10,999 Btu/kWh for gas-turbine units [217]. This is equivalent to $\mathrm{HR_{SCGT}} = 10.999$ MMBtu/$\mathrm{MWh_{out}}$, which yields

$$I_{\mathrm{CO_2}}^{\mathrm{SCGT}} = 10.999 \times 53.06 \approx 584 \ \mathrm{kgCO_2/MWh_{el}} \quad (\approx 584 \ \mathrm{gCO_2/kWh}) \quad \text{(A.7)}$$

Relative comparison: The direct CO_2 intensity of the LAES-LNG discharge block is lower by

$$\Delta = \left(1 - \frac{I_{\mathrm{CO_2}}^{\mathrm{LAES}}}{I_{\mathrm{CO_2}}^{\mathrm{SCGT}}}\right) \times 100 \approx 63.2\% \quad \text{(A.8)}$$

i.e., approximately 63% less direct CO_2 per unit of electricity produced than the reference simple-cycle gas turbine under the stated heat rate and emission factor assumptions.

A.4. Day-Ahead Dispatch Model for a standalone LAES Facility

To complement the LAES-LNG dispatch formulation developed in Section 5.3, this section presents the day-ahead dispatch model for a standalone LAES facility that participates only in the day-ahead electricity market. The formulation is adapted from [173] and is used throughout this thesis as a reference case to isolate the impact of LNG integration on operational decisions and profitability. The schematic layout of the standalone LAES plant is the one introduced in Chapter 2. The model uses the same notation and structure as the LAES-LNG formulation in Section 5.3, which facilitates a direct comparison between the two setups.

The day-ahead dispatch problem is written as a stochastic profit maximiza-

tion problem over a 24-hour horizon. The objective function is

$$\max_{\Xi^{\mathcal{H}\&\mathcal{N}},\Xi^{\mathcal{W}\&\mathcal{S}}} \ \mathbb{E}\,\mathcal{F}(y,\theta_d) = \sum_{t\in\mathcal{T}} \Bigg[\mathbb{E}_{\mathcal{H}\&\mathcal{N}} \Bigg[\underbrace{P^{\text{dis}}_{d,t} k_t \lambda^{\text{Elec}}_{d,t}}_{\mathcal{O}_2} \underbrace{- P^{\text{ch}}_{d,t} k_t \lambda^{\text{Elec}}_{d,t}}_{\mathcal{O}_3} - \underbrace{P^{\text{dis}}_{d,t} k_t \vartheta^{\text{dis}}}_{\mathcal{O}_4} - \underbrace{P^{\text{ch}}_{d,t} k_t \vartheta^{\text{ch}}}_{\mathcal{O}_5} \Bigg] \Bigg] \tag{A.9}$$

where $\mathcal{F}(y,\theta_d)$ denotes the profit of the standalone LAES facility, y is the vector of decision variables, and θ_d collects the electricity price scenarios. For each time period t, term $\mathcal{O}_2$ represents the revenue from selling electricity to the day-ahead market, while term $\mathcal{O}_3$ is the cost of buying electricity for charging and liquefying air. Terms $\mathcal{O}_4$ and $\mathcal{O}_5$ capture the variable operating costs during discharging and charging, respectively. These four terms correspond to $\mathcal{O}_2$ to $\mathcal{O}_5$ in the LAES-LNG objective (5.1), but without any LNG-related component in the first stage.

The objective function (A.9) is subject to power limits, energy balance constraints for the liquid air tank, and non-anticipativity and monotonicity conditions for the day-ahead offering and bidding curves.

Power limits and operating modes. The power traded by the LAES facility in the day-ahead electricity market must remain within the technical limits of the plant. The following constraints impose lower and upper bounds on discharge and charge power:

$$\underline{\mathcal{P}^{\text{dis}}} \alpha^{\text{dis}}_t \leq P^{\text{dis}}_{d,t} \leq \overline{\mathcal{P}^{\text{dis}}} \alpha^{\text{dis}}_t \quad \forall t, \forall d \tag{A.10}$$

$$\underline{\mathcal{P}^{\text{ch}}} \alpha^{\text{ch}}_t \leq P^{\text{ch}}_{d,t} \leq \overline{\mathcal{P}^{\text{ch}}} \alpha^{\text{ch}}_t \quad \forall t, \forall d \tag{A.11}$$

where $\underline{\mathcal{P}^{\text{dis}}}$ and $\overline{\mathcal{P}^{\text{dis}}}$ are the minimum and maximum discharge powers, and $\underline{\mathcal{P}^{\text{ch}}}$ and $\overline{\mathcal{P}^{\text{ch}}}$ are the corresponding charging limits. The binary variables α^{dis}_t and α^{ch}_t indicate whether the plant is in discharging or charging mode in period t. The LAES facility is not allowed to charge and discharge at the same time:

$$\alpha^{\text{dis}}_t + \alpha^{\text{ch}}_t \leq 1 \quad \forall t, \left\{ \alpha^{\text{dis}}_t, \alpha^{\text{ch}}_t \right\} \in \{0,1\} \tag{A.12}$$

Energy balance and inventory limits of the liquid air tank. The energy content of the liquid air tank evolves over time depending on the previous inventory, boil-off losses, and the net effect of charging and discharging. For the first time period and for the remaining periods, the inventory dynamics are modeled as:

$$q_{d,t}^{\mathrm{LAES}} = q_0^{\mathrm{LAES}} \left(1 - \frac{\mathcal{R}^{\mathrm{LAES}}}{24}\right) + P_{d,t}^{\mathrm{ch}} k_t \sqrt{\eta^{\mathrm{ETF}}} - \frac{P_{d,t}^{\mathrm{dis}} k_t}{\sqrt{\eta^{\mathrm{ETF}}}} \quad \forall t = 1, \forall d \tag{A.13}$$

$$q_{d,t}^{\mathrm{LAES}} = q_{d,t-1}^{\mathrm{LAES}} \left(1 - \frac{\mathcal{R}^{\mathrm{LAES}}}{24}\right) + P_{d,t}^{\mathrm{ch}} k_t \sqrt{\eta^{\mathrm{ETF}}} - \frac{P_{d,t}^{\mathrm{dis}} k_t}{\sqrt{\eta^{\mathrm{ETF}}}} \quad \forall t \geq 2, \forall d \tag{A.14}$$

where $q_{d,t}^{\mathrm{LAES}}$ is the liquid air inventory, q_0^{LAES} is the initial inventory level, $\mathcal{R}^{\mathrm{LAES}}$ is the hourly boil-off rate, and η^{ETF} is the round-trip efficiency of the LAES facility. The factor $\sqrt{\eta^{\mathrm{ETF}}}$ appears in both charging and discharging terms to represent the loss of energy between the two processes. To avoid end-of-horizon artifacts, the inventory is required to be cyclic:

$$q_{d,t}^{\mathrm{LAES}} = q_0^{\mathrm{LAES}} \quad \forall t = 24, \forall d \tag{A.15}$$

and must remain within the operational limits of the tank:

$$\underline{\mathcal{Q}^{\mathrm{LAES}}} \leq q_{d,t}^{\mathrm{LAES}} \leq \overline{\mathcal{Q}^{\mathrm{LAES}}} \quad \forall t, \forall d \tag{A.16}$$

where $\underline{\mathcal{Q}^{\mathrm{LAES}}}$ and $\overline{\mathcal{Q}^{\mathrm{LAES}}}$ denote the minimum and maximum allowable liquid air inventory.

Non-anticipativity and structure of offering and bidding curves. As in the LAES-LNG case, the standalone LAES facility participates in the day-ahead electricity market by submitting offering and bidding curves. The decision variables $P_{d,t}^{\mathrm{dis}}$ and $P_{d,t}^{\mathrm{ch}}$ therefore depend on electricity price scenarios d. Non-anticipativity requires that the facility cannot distinguish between scenarios that are identical from the perspective of day-ahead prices. When two scenarios d and d' yield the same price in period t, the offered and bid power levels must

coincide:

$$P^{\text{dis}}_{d,t} = P^{\text{dis}}_{d',t} \text{ if } \lambda^{\text{Elec}}_{d,t} = \lambda^{\text{Elec}}_{d',t} \quad \forall t, \forall d, d' \tag{A.17}$$

$$P^{\text{ch}}_{d,t} = P^{\text{ch}}_{d',t} \text{ if } \lambda^{\text{Elec}}_{d,t} = \lambda^{\text{Elec}}_{d',t} \quad \forall t, \forall d, d' \tag{A.18}$$

The market operator also enforces monotonicity properties for offering and bidding curves. Offers must be non-decreasing in price and bids must be non-increasing in price, which is modeled as

$$P^{\text{dis}}_{d,t} \geq P^{\text{dis}}_{d',t} \text{ if } \lambda^{\text{Elec}}_{d,t} \geq \lambda^{\text{Elec}}_{d',t} \quad \forall t, \forall d, d' \tag{A.19}$$

$$P^{\text{ch}}_{d,t} \leq P^{\text{ch}}_{d',t} \text{ if } \lambda^{\text{Elec}}_{d,t} \geq \lambda^{\text{Elec}}_{d',t} \quad \forall t, \forall d, d' \tag{A.20}$$

These constraints ensure that the facility submits economically rational supply and demand curves that conform to the market rules. The round-trip efficiency parameter $\sqrt{\eta^{\text{ETF}}}$ in (A.13) and (A.14) captures the net effect of conversion losses between charging and discharging in a compact way. Constraints (A.10) to (A.16) map directly to constraints (5.11) to (5.17) of the LAES-LNG model, and constraints (A.17) to (A.20) are analogous to the non-anticipativity and monotonicity constraints (5.20) to (5.23). The standalone LAES formulation in this section can therefore be viewed as a special case of the more general LAES-LNG model, with the LNG-related variables and constraints removed. This consistency facilitates the comparison of numerical results and supports the analysis of the incremental value of integrating LAES with LNG regasification.

A.5. Benchmark standalone LAES Configurations

This appendix documents the technical parameters of the two standalone LAES facilities that serve as benchmarks for the integrated LAES-LNG configuration analyzed in Chapter 5. These benchmark plants correspond to Case 2 and Case 3 in Section 5.5 and are used to quantify the incremental value of thermal integration with LNG regasification under identical market conditions.

Both benchmark facilities follow the same notation and modeling framework as the integrated plant. The parameters reported below include charging and discharging power limits, storage energy bounds, initial state of charge, daily

Table A.1: Technical specifications of the standalone LAES facility in Case 2.

Parameter	Value	Unit	Parameter	Value	Unit
$\overline{\mathcal{P}^{\text{dis}}}$	32.9	MW	$\mathcal{R}^{\text{LAES}}$	0.5	%/day
$\underline{\mathcal{P}^{\text{dis}}}$	0.987	MW	$\overline{\mathcal{Q}^{\text{LAES}}}$	480	MWh
$\overline{\mathcal{P}^{\text{ch}}}$	60	MW	$\underline{\mathcal{Q}^{\text{LAES}}}$	48	MWh
$\underline{\mathcal{P}^{\text{ch}}}$	48	MW	q_0^{LAES}	50	MWh
ϑ^{dis}	2.54	€/MWh	η^{RTE}	55	%
ϑ^{ch}	2.54	€/MWh	-	-	-

energy loss rate, round-trip efficiency, and variable operating costs. These quantities enter the mixed-integer day-ahead dispatch formulation presented in Appendix A.4 and allow a consistent comparison of short-term profitability across all case studies.

Case 2 represents a realistic standalone LAES facility that is economically equivalent to the LAES-LNG system in Case 1. Its energy capacity is set to 480 MWh, which matches the liquid air tank of the integrated plant, while the round-trip efficiency is limited to 55%. The charging and discharging power bounds, self-discharge rate, and variable operating costs reflect present-day technology and are chosen in line with [57]. The corresponding parameter values are summarized in Table A.1.

Case 3 represents an optimistic standalone LAES facility inspired by the high-performance configuration proposed in [173]. This plant features a round-trip efficiency of 70%, a reduced daily loss rate, and significantly lower variable operating costs for both charging and discharging. Its energy capacity is 247 MWh, with power limits tailored to the technology assumptions in [173]. These parameters provide a technology frontier against which the performance of the integrated LAES-LNG facility can be benchmarked. The detailed specification is given in Table A.2.

Table A.2: Technical specifications of the standalone LAES facility in Case 3.

Parameter	Value	Unit	Parameter	Value	Unit
$\overline{\mathcal{P}^{\text{dis}}}$	57	MW	$\mathcal{R}^{\text{LAES}}$	0.15	%/day
$\underline{\mathcal{P}^{\text{dis}}}$	1.71	MW	$\overline{\mathcal{Q}^{\text{LAES}}}$	247	MWh
$\overline{\mathcal{P}^{\text{ch}}}$	50	MW	$\underline{\mathcal{Q}^{\text{LAES}}}$	24.7	MWh
$\underline{\mathcal{P}^{\text{ch}}}$	40	MW	q_0^{LAES}	25	MWh
ϑ^{dis}	0.2259	€/MWh	η^{RTE}	70	%
ϑ^{ch}	0.1321	€/MWh	-	-	-

Together, Tables A.1 and A.2 provide the complete data required to reproduce the benchmark simulations discussed in Section 5.5 and to evaluate, in a transparent way, the incremental benefits of coupling LAES with LNG regasification in market-based operation.

A.6. Linearization Strategy for Bilinear Expressions in Equations (6.1b) and (6.1c)

This appendix complements Section 6.3.3 by detailing the linearization procedure used to remove the bilinear products between nodal electricity prices and storage dispatch decisions in the upper-level objective function. The bilinear terms appear in the revenue components of (6.1b) and (6.1c), where the charging and discharging powers of the CAES and LAES units are multiplied by the nodal electricity prices. To obtain a MILP formulation, these terms are re-expressed in linear form by exploiting the stationarity conditions of the lower-level KKT system and the strong duality property of the lower-level problem.

Step 1: Expressing Prices in Terms of Bids and Dual Variables

Starting from the stationarity conditions of the lower-level problem with respect to the cleared storage quantities, that is, constraints (6.3d) and (6.3e), the nodal electricity price at the bus where storage facility f is connected can be

written as

$$\lambda^{\text{Elec}}_{j,b\in\Phi^{\text{F}}_b,t} = \rho^{\gamma,y}_{j,f,t} + \overline{\mu}^{\gamma,y}_{j,f,t} - \underline{\mu}^{\gamma,y}_{j,f,t} \quad \forall\{j,f,t\} \tag{A.21}$$

$$\lambda^{\text{Elec}}_{j,b\in\Phi^{\text{F}}_b,t} = \rho^{\gamma,x}_{j,f,t} - \overline{\mu}^{\gamma,x}_{j,f,t} + \underline{\mu}^{\gamma,x}_{j,f,t} \quad \forall\{j,f,t\} \tag{A.22}$$

where $\rho^{\gamma,y}_{j,f,t}$ and $\rho^{\gamma,x}_{j,f,t}$ denote the offer and bid prices of the hybrid storage plant, and $\overline{\mu}^{\gamma,(\cdot)}_{j,f,t}$, $\underline{\mu}^{\gamma,(\cdot)}_{j,f,t}$ are the dual variables associated with the upper and lower bounds on the cleared storage quantities.

Step 2: Substituting Prices into the Storage Revenue

Using (A.21)–(A.22) together with the complementary slackness constraints (6.3n)–(6.3q), the revenue components $\mathcal{R}^1$ and $\mathcal{R}^2$ in (6.1b) and (6.1c) can be rewritten as:

$$\begin{aligned}\mathcal{R}^1 =& \sum_{j\in\mathbb{J}}\sum_{f\in\mathbb{F}}\sum_{t\in\mathbb{T}}\left(p^{\alpha,y}_{j,f,t} - p^{\alpha,x}_{j,f,t}\right)\lambda^{\text{Elec}}_{j,b\in\Phi^{\text{F}}_b,t} \\ =& \sum_{j\in\mathbb{J}}\sum_{f\in\mathbb{F}}\sum_{t\in\mathbb{T}} p^{\alpha,y}_{j,f,t}\left[\rho^{\gamma,y}_{j,f,t} + \overline{\mu}^{\gamma,y}_{j,f,t} - \underline{\mu}^{\gamma,y}_{j,f,t}\right] \sum_{j\in\mathbb{J}}\sum_{f\in\mathbb{F}}\sum_{t\in\mathbb{T}} p^{\alpha,x}_{j,f,t}\left[\rho^{\gamma,x}_{j,f,t} - \overline{\mu}^{\gamma,x}_{j,f,t} + \underline{\mu}^{\gamma,x}_{j,f,t}\right]\end{aligned} \tag{A.23}$$

$$\begin{aligned}\mathcal{R}^2 =& \sum_{j\in\mathbb{J}}\sum_{f\in\mathbb{F}}\sum_{t\in\mathbb{T}}\left(p^{\beta,y}_{j,f,t} - p^{\beta,x}_{j,f,t}\right)\lambda^{\text{Elec}}_{j,b\in\Phi^{\text{F}}_b,t} \\ =& \sum_{j\in\mathbb{J}}\sum_{f\in\mathbb{F}}\sum_{t\in\mathbb{T}}\Big[p^{\beta,y}_{j,f,t}\big(\rho^{\gamma,y}_{j,f,t} + \overline{\mu}^{\gamma,y}_{j,f,t} - \underline{\mu}^{\gamma,y}_{j,f,t}\big) - p^{\beta,x}_{j,f,t}\big(\rho^{\gamma,x}_{j,f,t} - \overline{\mu}^{\gamma,x}_{j,f,t} + \underline{\mu}^{\gamma,x}_{j,f,t}\big)\Big]\end{aligned} \tag{A.24}$$

Adding (A.23) and (A.24), grouping terms, and using the aggregation relations (6.1f)–(6.1g), that is,

$$p^{\gamma,y}_{j,f,t} = p^{\alpha,y}_{j,f,t} + p^{\beta,y}_{j,f,t}, \quad p^{\gamma,x}_{j,f,t} = p^{\alpha,x}_{j,f,t} + p^{\beta,x}_{j,f,t},$$

together with the complementary slackness conditions that eliminate products between primal and dual variables, the combined storage revenue can be written

as

$$\mathcal{R}^1 + \mathcal{R}^2 = \sum_{j\in\mathbb{J}} \sum_{f\in\mathbb{F}} \sum_{t\in\mathbb{T}} \left[p^{\gamma,y}_{j,f,t} \rho^{\gamma,y}_{j,f,t} + \phi^{\gamma,y}_{j,f,t} \overline{\mu}^{\gamma,y}_{j,f,t} - p^{\gamma,x}_{j,f,t} \rho^{\gamma,x}_{j,f,t} - \phi^{\gamma,x}_{j,f,t} \overline{\mu}^{\gamma,x}_{j,f,t} \right]. \tag{A.25}$$

Expression (A.25) is linear in the decision variables $p^{\gamma,x}$, $p^{\gamma,y}$, $\phi^{\gamma,x}$, $\phi^{\gamma,y}$, and the associated dual variables.

Step 3: Applying Strong Duality to the Lower-Level Problem

The lower-level market-clearing problem is a linear program. Therefore, the strong duality theorem applies and implies that, at optimality, the primal and dual objective values are equal. Applying strong duality to the lower-level objective function (6.2a) yields:

$$\begin{aligned}
&\sum_{j\in\mathbb{J}} \sum_{g\in\mathbb{G}} \sum_{t\in\mathbb{T}} V^G_{j,g,t} p^G_{j,g,t} - \sum_{j\in\mathbb{J}} \sum_{d\in\mathbb{D}} \sum_{t\in\mathbb{T}} V^D_{j,d} p^D_{j,d,t} + \sum_{j\in\mathbb{J}} \sum_{f\in\mathbb{F}} \sum_{t\in\mathbb{T}} \left(\rho^{\gamma,y}_{j,f,t} p^{\gamma,y}_{j,f,t} - \rho^{\gamma,x}_{j,f,t} p^{\gamma,x}_{j,f,t} \right) \\
&= - \sum_{j\in\mathbb{J}} \sum_{g\in\mathbb{G}} \sum_{t\in\mathbb{T}} \overline{\mu}^G_{j,g,t} \overline{P}^G_g - \sum_{j\in\mathbb{J}} \sum_{w\in\mathbb{W}} \sum_{t\in\mathbb{T}} \overline{\mu}^W_{j,w,t} E^W_{j,w,t} \\
&\quad - \sum_{j\in\mathbb{J}} \sum_{d\in\mathbb{D}} \sum_{t\in\mathbb{T}} \overline{\mu}^D_{j,d,t} \overline{E}^D_{j,d,t} - \sum_{j\in\mathbb{J}} \sum_{b\in\mathbb{B}\setminus\{\text{ref}\}} \sum_{t\in\mathbb{T}} \pi \left(\overline{\delta}_{j,b,t} + \underline{\delta}_{j,b,t} \right) \\
&\quad - \sum_{j\in\mathbb{J}} \sum_{f\in\mathbb{F}} \sum_{t\in\mathbb{T}} \left(\overline{\mu}^{\gamma,y}_{j,f,t} \phi^{\gamma,y}_{j,f,t} - \overline{\mu}^{\gamma,x}_{j,f,t} \phi^{\gamma,x}_{j,f,t} \right) \\
&\quad - \sum_{j\in\mathbb{J}} \sum_{(b,b')\in\Phi_{b,b'}} \sum_{t\in\mathbb{T}} \overline{PL}_{b,b'} \left(\overline{\xi}_{j,b,b',t} + \underline{\xi}_{j,b,b',t} \right).
\end{aligned} \tag{A.26}$$

Rearranging (A.26) and isolating the terms that involve the storage-related quantities yields:

$$\begin{aligned}
&\sum_{j\in\mathbb{J}}\sum_{f\in\mathbb{F}}\sum_{t\in\mathbb{T}}\Big[\overline{\mu}^{\gamma,y}_{j,f,t}\phi^{\gamma,y}_{j,f,t}+\overline{\mu}^{\gamma,x}_{j,f,t}\phi^{\gamma,x}_{j,f,t}+\rho^{\gamma,y}_{j,f,t}p^{\gamma,y}_{j,f,t}-\rho^{\gamma,x}_{j,f,t}p^{\gamma,x}_{j,f,t}\Big]\\
&=-\sum_{j\in\mathbb{J}}\sum_{g\in\mathbb{G}}\sum_{t\in\mathbb{T}}\big(V^{G}_{j,g,t}p^{G}_{j,g,t}+\overline{\mu}^{G}_{j,g,t}\overline{P}^{G}_{g}\big)+\sum_{j\in\mathbb{J}}\sum_{d\in\mathbb{D}}\sum_{t\in\mathbb{T}}\big(V^{D}_{j,d}p^{D}_{j,d,t}-\overline{\mu}^{D}_{j,d,t}\overline{E}^{D}_{j,d,t}\big)\\
&\quad-\sum_{j\in\mathbb{J}}\sum_{w\in\mathbb{W}}\sum_{t\in\mathbb{T}}\overline{\mu}^{W}_{j,w,t}E^{W}_{j,w,t}-\sum_{j\in\mathbb{J}}\sum_{(b,b')\in\Phi_{b,b'}}\sum_{t\in\mathbb{T}}\overline{PL}_{b,b'}\big(\overline{\xi}_{j,b,b',t}+\underline{\xi}_{j,b,b',t}\big)\\
&\quad-\sum_{j\in\mathbb{J}}\sum_{b\in\mathbb{B}\setminus\{\text{ref}\}}\sum_{t\in\mathbb{T}}\pi\big(\overline{\delta}_{j,b,t}+\underline{\delta}_{j,b,t}\big).
\end{aligned}\tag{A.27}$$

Step 4: Final Linear Expression for the Storage Contribution

Combining (A.25) with (A.27), and substituting into the upper-level objective function, leads to the following linear expression for $\mathcal{R}^1+\mathcal{R}^2$:

$$\begin{aligned}
\mathcal{R}^1+\mathcal{R}^2=&\sum_{j\in\mathbb{J}}\sum_{f\in\mathbb{F}}\sum_{t\in\mathbb{T}}\Big[-p^{\alpha,y}_{j,f,t}\big(\Gamma^{\alpha}_{f}\lambda^{\text{gas}}+C^{\alpha,y}_{f}\big)-p^{\alpha,x}_{j,f,t}C^{\alpha,x}_{f}\\
&\qquad\qquad-p^{\beta,y}_{j,f,t}C^{\beta,y}_{f}-p^{\beta,x}_{j,f,t}C^{\beta,x}_{f}\Big]\\
&-\sum_{j\in\mathbb{J}}\sum_{g\in\mathbb{G}}\sum_{t\in\mathbb{T}}\big(V^{G}_{j,g,t}p^{G}_{j,g,t}+\overline{\mu}^{G}_{j,g,t}\overline{P}^{G}_{g}\big)\\
&+\sum_{j\in\mathbb{J}}\sum_{d\in\mathbb{D}}\sum_{t\in\mathbb{T}}\big(V^{D}_{j,d}p^{D}_{j,d,t}-\overline{\mu}^{D}_{j,d,t}\overline{E}^{D}_{j,d,t}\big)\\
&-\sum_{j\in\mathbb{J}}\sum_{w\in\mathbb{W}}\sum_{t\in\mathbb{T}}\overline{\mu}^{W}_{j,w,t}E^{W}_{j,w,t}\\
&-\sum_{j\in\mathbb{J}}\sum_{(b,b')\in\Phi_{b,b'}}\sum_{t\in\mathbb{T}}\overline{PL}_{b,b'}\big(\overline{\xi}_{j,b,b',t}+\underline{\xi}_{j,b,b',t}\big)\\
&-\sum_{j\in\mathbb{J}}\sum_{b\in\mathbb{B}\setminus\{\text{ref}\}}\sum_{t\in\mathbb{T}}\pi\big(\overline{\delta}_{j,b,t}+\underline{\delta}_{j,b,t}\big).
\end{aligned}\tag{A.28}$$

Expression (A.28) is fully linear in the primal and dual variables of the single-level formulation. It replaces the original bilinear revenue terms in (6.1b) and (6.1c) and is used directly in the MILP model described in Section 6.3.3.

A.7. Linearization Strategy for Complementarity Constraints in Equations (6.3h)–(6.3u)

This appendix details the big-M linearization of the complementarity constraints associated with the lower-level KKT conditions in Section 6.3.3. The nonlinear relationships in (6.3h)–(6.3u) have the generic form

$$0 \leq a \perp b \geq 0,$$

which encodes the condition $a \geq 0$, $b \geq 0$, and $a \cdot b = 0$. In the final single-level MILP, each complementarity relation is represented by a set of linear constraints that use auxiliary binary variables and big-M parameters. The role of the auxiliary binaries is to select whether the primal inequality is binding or the associated dual variable is strictly positive, while the big-M constants enforce the corresponding bounds in a numerically stable manner.

Overview of the Big-M Reformulation

The nonlinear complementarity pairs are grouped according to the type of resource or network constraint they represent. Table A.3 summarizes the mapping from each pair of complementarity conditions in (6.3h)–(6.3u) to the linear constraints that replace them in the MILP model. For each group, $\check{M}^{(\cdot)}$ and $\hat{M}^{(\cdot)}$ denote resource-specific big-M values, while $\underline{u}_{(\cdot)}$ and $\overline{u}_{(\cdot)}$ are the auxiliary binary variables that encode the on/off status of the corresponding primal and dual variables.

Table A.3: Nonlinear complementarity constraints and their corresponding linearized counterparts.

Nonlinear constraints	**Linearized constraints**	**Nonlinear constraints**	**Linearized constraints**
(6.3h), (6.3i) $\longrightarrow$	(A.29a)–(A.29f)	(6.3j), (6.3k) $\longrightarrow$	(A.30a)–(A.30f)
(6.3l), (6.3m) $\longrightarrow$	(A.31a)–(A.31f)	(6.3n)–(6.3q) $\longrightarrow$	(A.32a)–(A.32k)
(6.3r), (6.3s) $\longrightarrow$	(A.33a)–(A.33g)	(6.3t), (6.3u) $\longrightarrow$	(A.34a)–(A.34g)

In the constraints that follow, each pair $(\check{M}^{(\cdot)}, \hat{M}^{(\cdot)})$ is selected according

to the magnitude of the corresponding primal and dual variables, following the guidelines in [68]. This selection avoids excessively loose bounds and contributes to a tighter and more numerically stable MILP formulation.

Generators, Wind Units, and Demands

The complementarity conditions for conventional generators in (6.3h)–(6.3i) are linearized as:

$$p^G_{j,g,t} \leq \check{M}^G \underline{u}^G_{j,g,t} \quad \forall\{j,g,t\} \tag{A.29a}$$
$$\underline{\mu}^G_{j,g,t} \leq \hat{M}^G (1 - \underline{u}^G_{j,g,t}) \quad \forall\{j,g,t\} \tag{A.29b}$$
$$\overline{P}^G_g - p^G_{j,g,t} \geq 0 \quad \forall\{j,g,t\} \tag{A.29c}$$
$$\overline{P}^G_g - p^G_{j,g,t} \leq \check{M}^G \overline{u}^G_{j,g,t} \quad \forall\{j,g,t\} \tag{A.29d}$$
$$\overline{\mu}^G_{j,g,t} \leq \hat{M}^G (1 - \overline{u}^G_{j,g,t}) \quad \forall\{j,g,t\} \tag{A.29e}$$
$$\underline{\mu}^G_{j,g,t},\ \overline{\mu}^G_{j,g,t} \geq 0 \quad \forall\{j,g,t\} \tag{A.29f}$$

where $\underline{u}^G_{j,g,t}$ and $\overline{u}^G_{j,g,t}$ are binary variables that indicate whether the lower or upper generator capacity constraint is potentially binding.

The complementarity conditions for wind units in (6.3j)–(6.3k) are treated analogously:

$$p^W_{j,w,t} \leq \check{M}^W \underline{u}^W_{j,w,t} \quad \forall\{j,w,t\} \tag{A.30a}$$
$$\underline{\mu}^W_{j,w,t} \leq \hat{M}^W (1 - \underline{u}^W_{j,w,t}) \quad \forall\{j,w,t\} \tag{A.30b}$$
$$E^W_{j,w,t} - p^W_{j,w,t} \geq 0 \quad \forall\{j,w,t\} \tag{A.30c}$$
$$E^W_{j,w,t} - p^W_{j,w,t} \leq \check{M}^W \overline{u}^W_{j,w,t} \quad \forall\{j,w,t\} \tag{A.30d}$$
$$\overline{\mu}^W_{j,w,t} \leq \hat{M}^W (1 - \overline{u}^W_{j,w,t}) \quad \forall\{j,w,t\} \tag{A.30e}$$
$$\underline{\mu}^W_{j,w,t},\ \overline{\mu}^W_{j,w,t} \geq 0 \quad \forall\{j,w,t\} \tag{A.30f}$$

The complementarity conditions for demands in (6.3l)–(6.3m) are linearized

as:

$$p^{D}_{j,d,t} \leq \check{M}^{D} \underline{u}^{D}_{j,d,t} \quad \forall\{j,d,t\} \tag{A.31a}$$
$$\underline{\mu}^{D}_{j,d,t} \leq \hat{M}^{D}(1 - \underline{u}^{D}_{j,d,t}) \quad \forall\{j,d,t\} \tag{A.31b}$$
$$\overline{E}^{D}_{j,d,t} - p^{D}_{j,d,t} \geq 0 \quad \forall\{j,d,t\} \tag{A.31c}$$
$$\overline{E}^{D}_{j,d,t} - p^{D}_{j,d,t} \leq \check{M}^{D} \overline{u}^{D}_{j,d,t} \quad \forall\{j,d,t\} \tag{A.31d}$$
$$\overline{\mu}^{D}_{j,d,t} \leq \hat{M}^{D}(1 - \overline{u}^{D}_{j,d,t}) \quad \forall\{j,d,t\} \tag{A.31e}$$
$$\underline{\mu}^{D}_{j,d,t},\ \overline{\mu}^{D}_{j,d,t} \geq 0 \quad \forall\{j,d,t\} \tag{A.31f}$$

Strategic Storage Participation

For the hybrid CAES-LAES plant, the complementarity relations (6.3n)–(6.3q) involve the cleared storage quantities and the limits defined by the submitted bids and offers. Their big-M linearization is given by:

$$p^{\gamma,y}_{j,f,t} \leq \check{M}^{\gamma,y} \underline{u}^{\gamma,y}_{j,f,t} \quad \forall\{j,f,t\} \tag{A.32a}$$
$$\underline{\mu}^{\gamma,y}_{j,f,t} \leq \hat{M}^{\gamma,y}(1 - \underline{u}^{\gamma,y}_{j,f,t}) \quad \forall\{j,f,t\} \tag{A.32b}$$
$$\phi^{\gamma,y}_{j,f,t} - p^{\gamma,y}_{j,f,t} \geq 0 \quad \forall\{j,f,t\} \tag{A.32c}$$
$$\phi^{\gamma,y}_{j,f,t} - p^{\gamma,y}_{j,f,t} \leq \check{M}^{\gamma,y} \overline{u}^{\gamma,y}_{j,f,t} \quad \forall\{j,f,t\} \tag{A.32d}$$
$$\overline{\mu}^{\gamma,y}_{j,f,t} \leq \hat{M}^{\gamma,y}(1 - \overline{u}^{\gamma,y}_{j,f,t}) \quad \forall\{j,f,t\} \tag{A.32e}$$
$$p^{\gamma,x}_{j,f,t} \leq \check{M}^{\gamma,x} \underline{u}^{\gamma,x}_{j,f,t} \quad \forall\{j,f,t\} \tag{A.32f}$$
$$\underline{\mu}^{\gamma,x}_{j,f,t} \leq \hat{M}^{\gamma,x}(1 - \underline{u}^{\gamma,x}_{j,f,t}) \quad \forall\{j,f,t\} \tag{A.32g}$$
$$\phi^{\gamma,x}_{j,f,t} - p^{\gamma,x}_{j,f,t} \geq 0 \quad \forall\{j,f,t\} \tag{A.32h}$$
$$\phi^{\gamma,x}_{j,f,t} - p^{\gamma,x}_{j,f,t} \leq \check{M}^{\gamma,x} \overline{u}^{\gamma,x}_{j,f,t} \quad \forall\{j,f,t\} \tag{A.32i}$$
$$\overline{\mu}^{\gamma,x}_{j,f,t} \leq \hat{M}^{\gamma,x}(1 - \overline{u}^{\gamma,x}_{j,f,t}) \quad \forall\{j,f,t\} \tag{A.32j}$$
$$\underline{\mu}^{\gamma,y}_{j,f,t},\ \overline{\mu}^{\gamma,y}_{j,f,t},\ \underline{\mu}^{\gamma,x}_{j,f,t},\ \overline{\mu}^{\gamma,x}_{j,f,t} \geq 0 \quad \forall\{j,f,t\} \tag{A.32k}$$

Transmission Line Flows

For each transmission line, the complementarity conditions (6.3r)–(6.3s) involve the line-flow limits and the corresponding dual variables. The big-M

reformulation is:

$$\text{Sus}_{b,b'}\left[\theta_{j,b,t} - \theta_{j,b',t}\right] + \overline{PL}_{b,b'} \geq 0 \quad \forall (b,b') \in \Phi_{b,b'}, \forall \{j,t\} \tag{A.33a}$$

$$\text{Sus}_{b,b'}\left[\theta_{j,b,t} - \theta_{j,b',t}\right] + \overline{PL}_{b,b'} \leq \check{M}^{\xi} \underline{u}^{\xi}_{j,b,b',t} \quad \forall (b,b') \in \Phi_{b,b'}, \forall \{j,t\} \tag{A.33b}$$

$$\underline{\xi}_{j,b,b',t} \leq \hat{M}^{\xi}(1 - \underline{u}^{\xi}_{j,b,b',t}) \quad \forall (b,b') \in \Phi_{b,b'}, \forall \{j,t\} \tag{A.33c}$$

$$\overline{PL}_{b,b'} - \text{Sus}_{b,b'}\left[\theta_{j,b,t} - \theta_{j,b',t}\right] \geq 0 \quad \forall (b,b') \in \Phi_{b,b'}, \forall \{j,t\} \tag{A.33d}$$

$$\overline{PL}_{b,b'} - \text{Sus}_{b,b'}\left[\theta_{j,b,t} - \theta_{j,b',t}\right] \leq \check{M}^{\xi} \overline{u}^{\xi}_{j,b,b',t} \quad \forall (b,b') \in \Phi_{b,b'}, \forall \{j,t\} \tag{A.33e}$$

$$\overline{\xi}_{j,b,b',t} \leq \hat{M}^{\xi}(1 - \overline{u}^{\xi}_{j,b,b',t}) \quad \forall (b,b') \in \Phi_{b,b'}, \forall \{j,t\} \tag{A.33f}$$

$$\underline{\xi}_{j,b,b',t},\ \overline{\xi}_{j,b,b',t} \geq 0 \quad \forall \{j,b,b',t\} \tag{A.33g}$$

Voltage Angle Bounds

Finally, the complementarity conditions (6.3t)–(6.3u) link the bounds on the voltage angles at non-reference buses to the dual variables $\underline{\delta}$ and $\overline{\delta}$. Their big-M linearization is

$$\theta_{j,b,t} + \pi \geq 0 \quad \forall b \backslash \{\text{ref}\}, \forall \{j,t\} \tag{A.34a}$$

$$\theta_{j,b,t} + \pi \leq \check{M}^{\delta} \underline{u}^{\delta}_{j,b,t} \quad \forall b \backslash \{\text{ref}\}, \forall \{j,t\} \tag{A.34b}$$

$$\underline{\delta}_{j,b,t} \leq \hat{M}^{\delta}(1 - \underline{u}^{\delta}_{j,b,t}) \quad \forall b \backslash \{\text{ref}\}, \forall \{j,t\} \tag{A.34c}$$

$$\pi - \theta_{j,b,t} \geq 0 \quad \forall b \backslash \{\text{ref}\}, \forall \{j,t\} \tag{A.34d}$$

$$\pi - \theta_{j,b,t} \leq \check{M}^{\delta} \overline{u}^{\delta}_{j,b,t} \quad \forall b \backslash \{\text{ref}\}, \forall \{j,t\} \tag{A.34e}$$

$$\overline{\delta}_{j,b,t} \leq \hat{M}^{\delta}(1 - \overline{u}^{\delta}_{j,b,t}) \quad \forall b \backslash \{\text{ref}\}, \forall \{j,t\} \tag{A.34f}$$

$$\underline{\delta}_{j,b,t},\ \overline{\delta}_{j,b,t} \geq 0 \quad \forall \{j,b,t\} \tag{A.34g}$$

Together, constraints (A.29a)–(A.34g) replace the complementarity conditions (6.3h)–(6.3u) in the single-level formulation. They generate the additional binary variables that contribute to the computational complexity of the final MILP, and they justify the learning-assisted warm-start procedures developed in Section 6.4 to improve the tractability of the strategic look-ahead dispatch model.

A.8. Economic Performance under Lead-Dependent Forecast Uncertainty

This appendix, which complements the analysis in Chapter 6, investigates how the economic performance of the proposed look-ahead framework changes when forecast uncertainty increases with lead time. The analysis complements the baseline results of Section 6.5, where a uniform deviation band of ±15% around nominal values was used for all lead days.

A.7.1 Motivation and Experimental Design

In practice, short-term forecasts are usually more accurate than medium-term forecasts. To capture this feature in a simple way, the six-day look-ahead simulation for 7–12 December 2021 is repeated with a linearly widening forecast-error envelope. The deviation band starts at ±10% on day 1 and increases by approximately four percentage points per day, reaching ±30% on day 6. Formally, the bounds for day $j \in \{1, \ldots, 6\}$ can be written as:

$$\pm\big(10 + 4\,(j-1)\big)\,\%,$$

which yields the sequence $\{\pm 10, \pm 14, \pm 18, \pm 22, \pm 26, \pm 30\}\,\%$.

The same six-day market data set, system model, and look-ahead formulation as in Section 6.5 are used. Scenario generation follows the baseline procedure, but the support of the uniform distribution is adapted to the lead-dependent band. For each lead day, wind production, load, and generator offer prices are independently perturbed around their nominal values within the corresponding band. The number of scenarios, solver settings, and all technical parameters are identical to those in the uniform ±15% benchmark. The MILPproblems are again solved with Gurobi at zero optimality gap, and the reported values are averages over the same set of equiprobable scenarios.

A.7.2 Impact on Profitability and Consumer Surplus

Table A.4 compares the main economic indicators obtained under the uniform and the lead-dependent error structures. For consistency with Section 6.5, the table reports: (i) the profits of the standalone and hybrid configurations under a six-day look-ahead horizon, (ii) the percentage advantage of the hybrid plant

over the standalone setup, (iii) the relative gain of six-day look-ahead over a purely day-ahead strategy for the hybrid plant, and (iv) the consumer surplus for Case 1 (day-ahead) and Case 4 (six-day look-ahead).

Table A.4: Economic outcomes under uniform and lead-dependent forecast error bands (7–12 December 2021).

Approach	**Uniform ±15 %**	**Lead-dependent**
Standalone facilities profit [€]	164,946	182,873
Hybrid plant profit [€]	179,925	196,532
Hybrid vs standalone advantage [%]	+9.08	+7.46
Look-ahead gain over day-ahead [%]	+92.40	+81.42
Consumer surplus (Case 1) [€]	4,914,322	4,879,287
Consumer surplus (Case 4) [€]	4,921,983	4,890,725

Several observations emerge from Table A.4. First, both configurations become more profitable under the lead-dependent band. The profit of the standalone facilities increases from €164,946 to €182,873, and the hybrid plant's profit rises from €179,925 to €196,532. This approximate 9% increase for the hybrid plant is consistent with the fact that a wider error band produces more pronounced variations around the expected trajectories. These variations create additional arbitrage opportunities, which the storage operator can exploit through inter-temporal shifting of energy.

Second, the relative advantage of the hybrid configuration over the standalone setup remains positive and sizeable, but it becomes slightly smaller. Under the uniform band, the hybrid plant earns 9.08% more profit than the standalone configuration. Under the lead-dependent band, this premium decreases to 7.46%. The hybrid plant still captures more value from price fluctuations, but the stronger volatility also allows the standalone units to improve their individual arbitrage performance.

Third, the benefit of extending the dispatch horizon from one day to six days remains substantial. For the hybrid plant, the relative gain of six-day look-ahead over day-ahead drops from 92.40% under the uniform band to 81.42% under the lead-dependent band. Even in the presence of stronger uncertainty at longer horizons, the strategic coordination of storage over multiple days continues to deliver large profit increases compared with a purely myopic operation.

Finally, consumer surplus slightly decreases when moving from the uni-

form to the lead-dependent band. For Case 1 (day-ahead), surplus falls from €4,914,322 to €4,879,287. For Case 4 (six-day look-ahead), it decreases from €4,921,983 to €4,890,725. This reduction suggests that the additional volatility induced by wider forecast bands leads to somewhat higher average consumer payments, even though the look-ahead strategy still improves surplus relative to day-ahead dispatch within each error structure.

The comparison in Table A.4 shows that introducing a simple lead-dependent representation of forecast uncertainty does not fundamentally alter the conclusions of Section 6.5. Both the standalone and hybrid configurations benefit from increased variability, but the hybrid plant remains more profitable across all cases. The economic value of extending the dispatch horizon from day-ahead to a six-day look-ahead horizon also remains high, even though the percentage gains decrease slightly when forecast accuracy deteriorates with lead time.

A.9. IEEE 24-Bus System Data

This appendix documents the data of the IEEE 24-bus system used in the comparative simulations of Chapter 6, and in particular in Section 6.5.3. The underlying network corresponds to the IEEE 24-bus reliability test system, adapted to host a hybrid CAES-LAES facility and a wind power plant. As illustrated in Fig. A.1, the strategic hybrid CAES-LAES unit is connected at bus 1, while a single 100 MW wind farm is located at bus 23. All line, generation, and demand data employed in the simulations are summarized in the following sections.

Transmission Line Data

The transmission network is represented by a set of lossless branches characterized by their series reactances and thermal capacity limits, and it is modeled with a direct current power flow formulation. Table A.5 lists all transmission lines, together with their series reactances (in p.u. on a 100 MVA base) and the corresponding maximum admissible active power flows $\overline{PL}$.

Generator Locations and Maximum Output

Conventional generating units are modeled with predetermined installed capacities. Table A.6 reports the bus index and the maximum active power limit $\overline{P}^G$ for each generator unit.

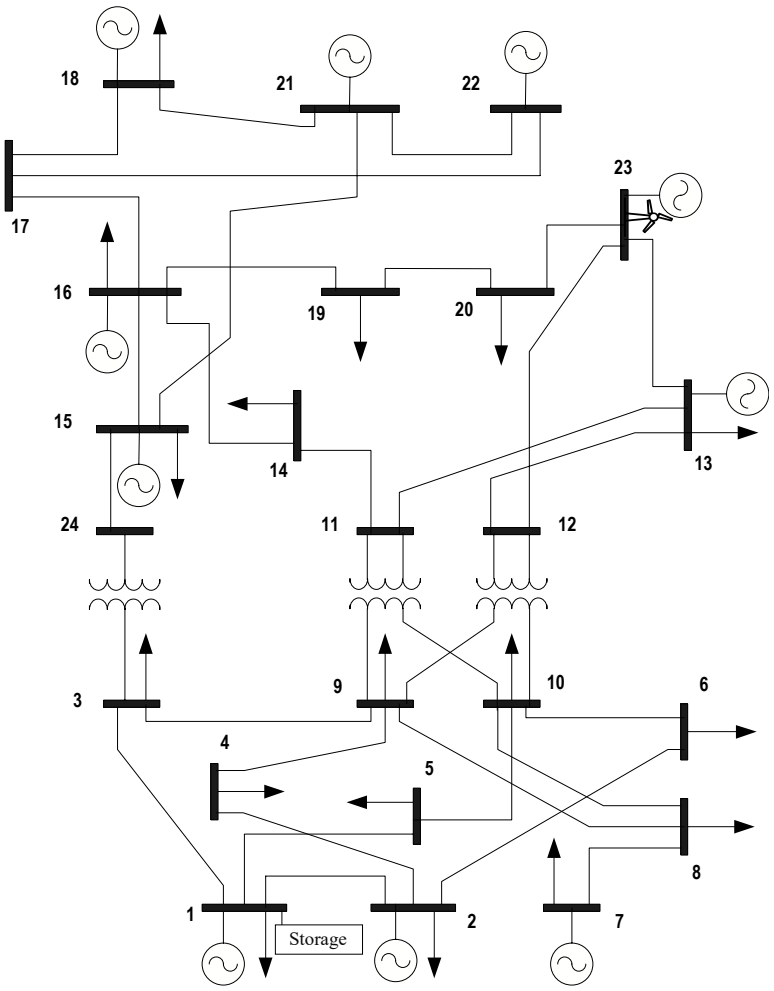

Figure A.1: Single-line diagram of the IEEE 24-bus system with the hybrid CAES-LAES facility at bus 1 and a wind farm at bus 23.

Demand Locations and Nominal Power

System load is modeled through aggregated demand blocks connected to specific buses. Table A.7 shows the nominal active power $\overline{E}^D$ of each demand block.

Additional Modeling Details

In the numerical experiments of Chapter 6, the following modeling choices are adopted for the IEEE 24-bus case:

Table A.5: IEEE 24-bus system: transmission line reactances and power capacities.

From	To	Reactance (p.u.)	$\overline{PL}$ (MW)	From	To	x (p.u.)	$\overline{PL}$ (MW)
1	2	0.0146	175	1	3	0.2253	175
1	5	0.0907	350	2	4	0.1356	175
2	6	0.2050	175	3	9	0.1271	175
3	24	0.0840	400	4	9	0.1110	175
5	10	0.0940	350	6	10	0.0642	175
7	8	0.0652	350	8	9	0.1762	175
8	10	0.1762	175	9	11	0.0840	400
9	12	0.0840	400	10	11	0.0840	400
10	12	0.0840	400	11	13	0.0488	500
11	14	0.0426	500	12	13	0.0488	500
12	23	0.0985	500	13	23	0.0884	500
14	16	0.0594	500	15	16	0.0172	500
15	21	0.0249	1000	15	24	0.0529	500
16	17	0.0263	500	16	19	0.0234	500
17	18	0.0143	500	17	22	0.1069	500
18	21	0.0132	1000	19	20	0.0203	1000
20	23	0.0112	1000	21	22	0.0692	500

Table A.6: IEEE 24-bus system: generator locations and maximum active power.

Gen	Bus	$\overline{P}^G$ (MW)
g1	1	152
g2	2	152
g3	7	350
g4	13	591
g5	15	60
g6	15	155
g7	16	155
g8	18	400
g9	21	400
g10	22	300
g11	23	310
g12	23	350

- Bus 13 is selected as the reference bus in the direct-current power flow representation;
- The strategic hybrid CAES-LAES facility is connected at bus 1, and the aggregated 100 MW wind farm is connected at bus 23, as depicted in Fig. A.1;
- For each time period, the demand at each bus is obtained by scaling the nominal value in Tables A.7 by a factor drawn from a continuous uniform distribution $U(0.7, 1.3)$, in order to represent temporal load variability around the nominal demand levels.

Table A.7: IEEE 24-bus system: demand locations and nominal active powers.

Load	Bus	$\overline{E}^D$ (MW)
d1	1	108
d2	2	97
d3	3	180
d4	4	74
d5	5	71
d6	6	136
d7	7	125
d8	8	171
d9	9	175
d10	10	195
d11	13	265
d12	14	194
d13	15	317
d14	16	100
d15	18	333
d16	19	181
d17	20	128

A.10. IEEE 118-Bus System Data

This appendix summarizes the data of the IEEE 118-bus system used in the numerical experiments of Chapter 6 and in Section 6.5.3. The IEEE 118-bus test system is here adapted to include a hybrid CAES-LAES facility and three geographically distributed wind farms. As indicated in Fig. A.2, the hybrid CAES-LAES unit is located at bus 15. Three 100 MW wind farms are connected at buses 12, 54, and 112, and are associated with wind production profiles from Spain, France, and Belgium, respectively [211]. The detailed line, generation, and demand data are reported in the following tables.

Transmission Line Data

The transmission network is represented by a set of lines characterized by their series reactances and thermal capacity limits. A direct current power flow model is used, with reactances expressed in p.u. on a 100 MVA base. Due to the size of the system, the data are presented in three compact tables. Tables A.8–A.10 list all branches with their series reactances and maximum active power flow limits $\overline{PL}$ [218].

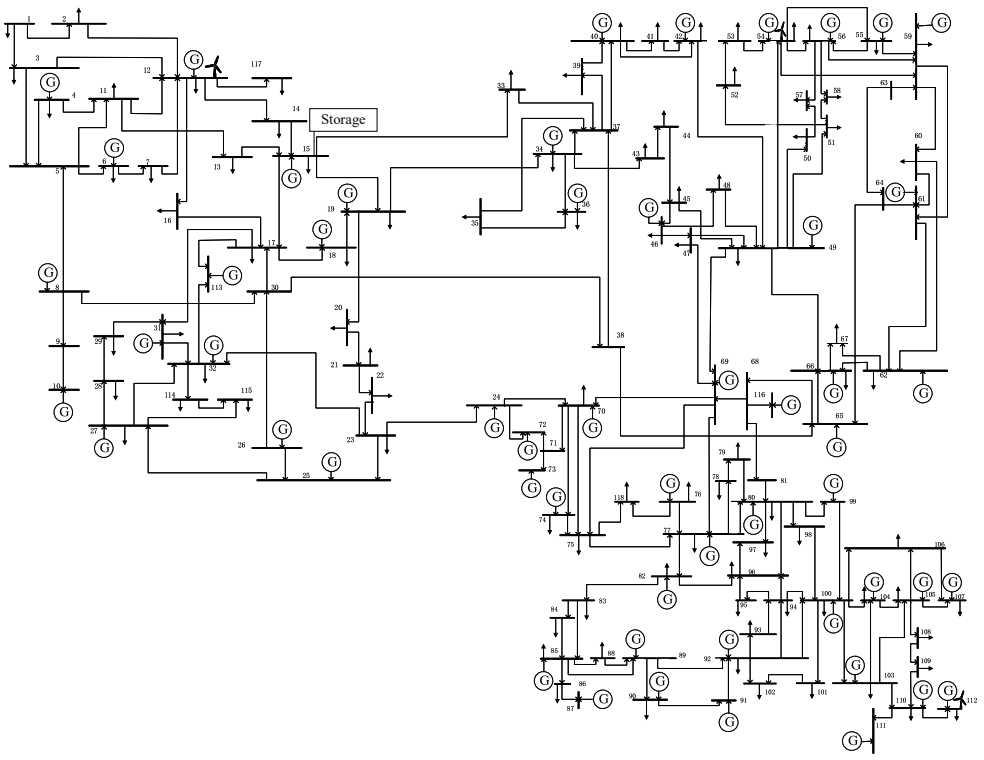

Figure A.2: Single-line diagram of the IEEE 118-bus system with the hybrid CAES-LAES facility at bus 15 and three wind farms at buses 12, 54, and 112.

Generator Locations and Maximum Output

Conventional generating units are characterized by given installed capacities. Table A.11 reports the bus index and the maximum active power limit $\overline{P}^G$ for each generator.

Table A.8: IEEE 118-bus system: transmission line reactances and capacities (part 1).

From	To	Reactance (p.u.)	$\overline{PL}$ (MW)	From	To	Reactance (p.u.)	$\overline{PL}$ (MW)
1	2	0.09990	600	1	3	0.04240	600
4	5	0.00798	1700	3	5	0.10800	600
5	6	0.05400	600	6	7	0.02080	600
8	9	0.03050	1700	8	5	0.02670	1700
9	10	0.03220	3500	4	11	0.06880	600
5	11	0.06820	600	11	12	0.01960	600
2	12	0.06160	600	3	12	0.16000	600
7	12	0.03400	600	11	13	0.07310	600
12	14	0.07070	600	13	15	0.24440	600
14	15	0.19500	600	12	16	0.08340	600
15	17	0.04370	1700	16	17	0.18010	600
17	18	0.05050	600	18	19	0.04930	600
19	20	0.11700	600	15	19	0.03940	600
20	21	0.08490	600	21	22	0.09700	600
22	23	0.15900	600	23	24	0.04920	600
23	25	0.08000	1700	26	25	0.03820	1700
25	27	0.16300	1700	27	28	0.08550	600
28	29	0.09430	600	30	17	0.03880	1700
8	30	0.05040	600	26	30	0.08600	1700
17	31	0.15630	600	29	31	0.03310	600
23	32	0.11530	600	31	32	0.09850	600
27	32	0.07550	600	15	33	0.12440	600
19	34	0.24700	600	35	36	0.01020	600
35	37	0.04970	600	33	37	0.14200	600
34	36	0.02680	600	34	37	0.00940	1700
38	37	0.03750	1700	37	39	0.10600	600
37	40	0.16800	600	30	38	0.05400	600
39	40	0.06050	600	40	41	0.04870	600
40	42	0.18300	600	41	42	0.13500	600
43	44	0.24540	600	34	43	0.16810	600

Table A.11: IEEE 118-bus system: generator locations and maximum active power.

Gen	Bus	$\overline{P}^G$ (MW)	Gen	Bus	$\overline{P}^G$ (MW)
g1	1	100.0	g2	4	100.0
g3	6	100.0	g4	8	100.0
g5	10	550.0	g6	12	185.0
g7	15	100.0	g8	18	100.0
g9	19	100.0	g10	24	100.0
g11	25	320.0	g12	26	414.0
g13	27	100.0	g14	31	107.0
g15	32	100.0	g16	34	100.0
g17	36	100.0	g18	40	100.0
g19	42	100.0	g20	46	119.0
g21	49	304.0	g22	54	148.0
g23	55	100.0	g24	56	100.0
g25	59	255.0	g26	61	260.0
g27	62	100.0	g28	65	491.0
g29	66	492.0	g30	69	805.2
g31	70	100.0	g32	72	100.0
g33	73	100.0	g34	74	100.0
g35	76	100.0	g36	77	100.0
g37	80	577.0	g38	85	100.0
g39	87	104.0	g40	89	707.0
g41	90	100.0	g42	91	100.0
g43	92	100.0	g44	99	100.0
g45	100	352.0	g46	103	140.0
g47	104	100.0	g48	105	100.0
g49	107	100.0	g50	110	100.0
g51	111	136.0	g52	112	100.0
g53	113	100.0	g54	116	100.0

Table A.9: IEEE 118-bus system: transmission line reactances and capacities (part 2).

From	To	Reactance (p.u.)	$\overline{PL}$ (MW)	From	To	Reactance (p.u.)	$\overline{PL}$ (MW)
44	45	0.09010	600	45	46	0.13560	600
46	47	0.12700	600	46	48	0.18900	600
47	49	0.06250	600	42	49	0.16150	1200
45	49	0.18600	600	48	49	0.05050	600
49	50	0.07520	600	49	51	0.13700	600
51	52	0.05880	600	52	53	0.16350	600
53	54	0.12200	600	49	54	0.14490	1200
54	55	0.07070	600	54	56	0.00955	600
55	56	0.01510	600	56	57	0.09660	600
50	57	0.13400	600	56	58	0.09660	600
51	58	0.07190	600	54	59	0.22930	600
56	59	0.12240	1200	55	59	0.21580	600
59	60	0.14500	600	59	61	0.15000	600
60	61	0.01350	1700	60	62	0.05610	600
61	62	0.03760	600	63	59	0.03860	1700
63	64	0.02000	1700	64	61	0.02680	1700
38	65	0.09860	1700	64	65	0.03020	1700
49	66	0.04595	3400	62	66	0.21800	600
62	67	0.11700	600	65	66	0.03700	1700
66	67	0.10150	600	65	68	0.01600	1700
47	69	0.27780	600	49	69	0.32400	600
68	69	0.03700	1700	69	70	0.12700	1700
24	70	0.41150	600	70	71	0.03550	600
24	72	0.19600	600	71	72	0.18000	600
71	73	0.04540	600	70	74	0.13230	600
70	75	0.14100	600	69	75	0.12200	1700
74	75	0.04060	600	76	77	0.14800	600
69	77	0.10100	600	75	77	0.19990	600
77	78	0.01240	600	78	79	0.02440	600
77	80	0.03317	3400	79	80	0.07040	600

Demand Locations and Nominal Power

System load is again represented through aggregated demand blocks connected to specific buses. Tables A.12 and A.13 summarize the nominal active power $\overline{E}^D$ of each demand block in the IEEE 118-bus system.

Table A.10: IEEE 118-bus system: transmission line reactances and capacity limits (part 3).

From	To	Reactance (p.u.)	$\overline{PL}$ (MW)	From	To	Reactance (p.u.)	$\overline{PL}$ (MW)
68	81	0.02020	1700	81	80	0.03700	1700
77	82	0.08530	700	82	83	0.03665	1700
83	84	0.13200	600	83	85	0.14800	600
84	85	0.06410	600	85	86	0.12300	3500
86	87	0.20740	3500	85	88	0.10200	1700
85	89	0.17300	600	88	89	0.07120	1700
89	90	0.06514	3400	90	91	0.08360	600
89	92	0.03827	3400	91	92	0.12720	600
92	93	0.08480	600	92	94	0.15800	600
93	94	0.07320	600	94	95	0.04340	600
80	96	0.18200	600	82	96	0.05300	600
94	96	0.08690	600	80	97	0.09340	600
80	98	0.10800	600	80	99	0.20600	700
92	100	0.29500	600	94	100	0.05800	600
95	96	0.05470	600	96	97	0.08850	600
98	100	0.17900	600	99	100	0.08130	600
100	101	0.12620	600	92	102	0.05590	600
101	102	0.11200	600	100	103	0.05250	1700
100	104	0.20400	600	103	104	0.15840	600
103	105	0.16250	600	100	106	0.22900	600
104	105	0.03780	600	105	106	0.05470	600
105	107	0.18300	600	105	108	0.07030	600
106	107	0.18300	600	108	109	0.02880	600
103	110	0.18130	600	109	110	0.07620	600
110	111	0.07550	600	110	112	0.06400	600
17	113	0.03010	600	32	113	0.20300	1700
32	114	0.06120	600	27	115	0.07410	600
114	115	0.01040	600	68	116	0.00405	1700
12	117	0.14000	600	75	118	0.04810	600
76	118	0.05440	600				

Table A.12: IEEE 118-bus system: demand blocks and nominal active powers (part 1).

Load	Bus	$\overline{E}^D$ (MW)	Load	Bus	$\overline{E}^D$ (MW)
d1	1	51	d2	2	20
d3	3	39	d4	4	39
d5	6	52	d6	7	19
d7	8	28	d8	11	70
d9	12	47	d10	13	34
d11	14	14	d12	15	90
d13	16	25	d14	17	11
d15	18	60	d16	19	45
d17	20	18	d18	21	14
d19	22	10	d20	23	7
d21	24	13	d22	27	71
d23	28	17	d24	29	24
d25	31	43	d26	32	59
d27	33	23	d28	34	59
d29	35	33	d30	36	31
d31	39	27	d32	40	66
d33	41	37	d34	42	96
d35	43	18	d36	44	16
d37	45	53	d38	46	28
d39	47	34	d40	48	20
d41	49	87	d42	50	17
d43	51	17	d44	52	18
d45	53	23	d46	54	113
d47	55	63	d48	56	84
d49	57	12	d50	58	12

Table A.13: IEEE 118-bus system: demand blocks and nominal active powers (part 2).

Load	Bus	$\overline{E}^D$ (MW)	Load	Bus	$\overline{E}^D$ (MW)
d51	59	277	d52	60	78
d53	62	77	d54	66	39
d55	67	28	d56	70	66
d57	72	12	d58	73	6
d59	74	68	d60	75	47
d61	76	68	d62	77	61
d63	78	71	d64	79	39
d65	80	130	d66	82	54
d67	83	20	d68	84	11
d69	85	24	d70	86	21
d71	88	48	d72	90	163
d73	91	10	d74	92	65
d75	93	12	d76	94	30
d77	95	42	d78	96	38
d79	97	15	d80	98	34
d81	99	42	d82	100	37
d83	101	22	d84	102	5
d85	103	23	d86	104	38
d87	105	31	d88	106	43
d89	107	50	d90	108	2
d91	109	8	d92	110	39
d93	112	68	d94	113	6
d95	114	8	d96	115	22
d97	116	184	d98	117	20
d99	118	33			

Additional Modeling Details

In both test systems, the following additional modeling assumptions are adopted:

- A single reference bus is selected for the direct current power flow equations (bus 13 of the IEEE 24-bus system and bus 69 of the IEEE 118-bus system serve as the reference buses);
- The hybrid CAES-LAES facility participates strategically from bus 1 in the IEEE 24-bus system and from bus 15 in the IEEE 118-bus system;
- At each time period, the demand at every bus is obtained by scaling the nominal active power in Tables A.7, A.12, and A.13 by a factor drawn from the continuous uniform distribution $\mathcal{U}(0.7, 1.3)$, which provides a simplified representation of load variability around the nominal demand levels.

List of Publications

The following publications document the research contributions that form the basis of this dissertation.

Journal Papers

- **H. Khaloie**, J. Faraji, F. Vallée, C. S. Lai, J.-F. Toubeau, and L. L. Lai, "Risk-Aware Battery Bidding With a Novel Benchmark Selection Under Second-Order Stochastic Dominance," *IEEE Transactions on Industry Applications*, vol. 59, no. 3, pp. 3009–3018, May–June 2023.

- **H. Khaloie** and F. Vallée, "Day-Ahead Dispatch of Liquid Air Energy Storage Coupled With LNG Regasification in Electricity and LNG Markets," *IEEE Transactions on Power Systems*, vol. 39, no. 3, pp. 5177–5190, May 2024.

- **H. Khaloie**, M. Dolányi, J.-F. Toubeau, and F. Vallée, "Review of Machine Learning Techniques for Optimal Power Flow," *Applied Energy*, vol. 388, p. 125637, 2025.

- **H. Khaloie**, A. Stankovski, B. Gjorgiev, G. Sansavini, and F. Vallée, "Hybrid Energy Storage Dispatch: A Bi-Level Look-Ahead Learning-Assisted Model," *IEEE Transactions on Energy Markets, Policy and Regulation*, vol. 3, no. 3, pp. 376–392, Sept. 2025.

The articles listed below were published during the PhD period. They address related topics, yet their material is not directly integrated into this dissertation.

Journal Papers

- **H. Khaloie**, J. -F. Toubeau, F. Vallée, C. S. Lai and L. L. Lai, "An Innovative Coalitional Trading Model for a Biomass Power Plant Paired With Green Energy Resources," *IEEE Transactions on Sustainable Energy*, vol. 13, no. 2, pp. 892-904, April 2022.

- H. Masrur, **H. Khaloie**, A. T. Al-Awami, S. El Ferik, and T. Senjyu, "Cost-aware modeling and operation of interconnected multi-energy microgrids considering environmental and resilience impact," *Applied Energy*, vol. 356, p. 122320, 2024.

Bibliography

[1] John ET Bistline. Roadmaps to net-zero emissions systems: emerging insights and modeling challenges. *Joule*, 5(10):2551–2563, 2021.

[2] Stephen Pye, Oliver Broad, Chris Bataille, Paul Brockway, Hannah E Daly, Richard Freeman, Ajay Gambhir, Oliver Geden, Fionn Rogan, S Sanghvi, et al. Modelling net-zero emissions energy systems requires a change in approach. *Climate Policy*, 21(2):222–231, 2021.

[3] Heleen L Van Soest, Michel GJ den Elzen, and Detlef P van Vuuren. Net-zero emission targets for major emitting countries consistent with the paris agreement. *Nature communications*, 12(1):2140, 2021.

[4] Virginia Murray and Kristie L Ebi. Ipcc special report on managing the risks of extreme events and disasters to advance climate change adaptation (srex), 2012.

[5] Hoesung Lee, Katherine Calvin, Dipak Dasgupta, Gerhard Krinner, Aditi Mukherji, Peter Thorne, Christopher Trisos, José Romero, Paulina Aldunce, Ko Barret, et al. Ipcc, 2023: Climate change 2023: Synthesis report, summary for policymakers. contribution of working groups i, ii and iii to the sixth assessment report of the intergovernmental panel on climate change [core writing team, h. lee and j. romero (eds.)]. ipcc, geneva, switzerland. 2023.

[6] United Nations Environment Programme. Emissions gap report 2024: No more hot air ... please! with a massive gap between rhetoric and reality, countries draft new climate commitments, 2024-10.

[7] Crippa M, Guizzardi D, Pagani F, Banja M, Muntean M, Schaaf E,

Monforti-Ferrario F, Becker WE, Quadrelli R, Risquez Martin A, Taghavi-Moharamli P, Köykkä J, Grassi G, Rossi S, Melo J, Oom D, Branco A, San-Miguel J, Manca G, Pisoni E, Vignati E, and Pekar F. Ghg emissions of all world countries. Technical Report KJ-01-24-010-EN-N (online),KJ-01-24-010-EN-C (print), Luxembourg (Luxembourg), 2024.

[8] Sam Fankhauser, Stephen M Smith, Myles Allen, Kaya Axelsson, Thomas Hale, Cameron Hepburn, J Michael Kendall, Radhika Khosla, Javier Lezaun, Eli Mitchell-Larson, et al. The meaning of net zero and how to get it right. *Nature climate change*, 12(1):15–21, 2022.

[9] Hannah Ritchie. Sector by sector: where do global greenhouse gas emissions come from? *Our World in Data*, 2020. https://ourworldindata.org/ghg-emissions-by-sector.

[10] Damian Carrington. Britain's net zero economy is booming, cbi says, Feb 2025.

[11] Gary Fuller. How cutting us air pollution could save 6,000 lives a year by 2030, Sep 2025.

[12] Chun Sing Lai and Malcolm D. McCulloch. Levelized cost of electricity for solar photovoltaic and electrical energy storage. *Applied Energy*, 190:191–203, 2017.

[13] Lucas Sens, Ulf Neuling, and Martin Kaltschmitt. Capital expenditure and levelized cost of electricity of photovoltaic plants and wind turbines–development by 2050. *Renewable Energy*, 185:525–537, 2022.

[14] Eero Vartiainen, Gaëtan Masson, Christian Breyer, David Moser, and Eduardo Román Medina. Impact of weighted average cost of capital, capital expenditure, and other parameters on future utility-scale pv levelised cost of electricity. *Progress in photovoltaics: research and applications*, 28(6):439–453, 2020.

[15] Renewables 2025 – Analysis IEA. Renewables 2025 – analysis - iea, Oct 2025.

[16] Peter D Lund, Juuso Lindgren, Jani Mikkola, and Jyri Salpakari. Review of energy system flexibility measures to enable high levels of variable

renewable electricity. *Renewable and sustainable energy reviews*, 45:785–807, 2015.

[17] Hendrik Kondziella and Thomas Bruckner. Flexibility requirements of renewable energy based electricity systems—a review of research results and methodologies. *Renewable and Sustainable Energy Reviews*, 53:10–22, 2016.

[18] Peter Palensky and Dietmar Dietrich. Demand side management: Demand response, intelligent energy systems, and smart loads. *IEEE transactions on industrial informatics*, 7(3):381–388, 2011.

[19] Nestor A Sepulveda, Jesse D Jenkins, Fernando J De Sisternes, and Richard K Lester. The role of firm low-carbon electricity resources in deep decarbonization of power generation. *Joule*, 2(11):2403–2420, 2018.

[20] Behnam Zakeri and Sanna Syri. Electrical energy storage systems: A comparative life cycle cost analysis. *Renew. Sustain. Energy Rev*, 42(2015):569–596, 2015.

[21] Xing Luo, Jihong Wang, Mark Dooner, and Jonathan Clarke. Overview of current development in electrical energy storage technologies and the application potential in power system operation. *Applied energy*, 137:511–536, 2015.

[22] Jacqueline A Dowling, Katherine Z Rinaldi, Tyler H Ruggles, Steven J Davis, Mengyao Yuan, Fan Tong, Nathan S Lewis, and Ken Caldeira. Role of long-duration energy storage in variable renewable electricity systems. *Joule*, 4(9):1907–1928, 2020.

[23] Oliver Schmidt, Adam Hawkes, Ajay Gambhir, and Iain Staffell. The future cost of electrical energy storage based on experience rates. *Nature Energy*, 2(8):1–8, 2017.

[24] Bloomberg new energy outlook 2019: The future of the energy sector - power technology. `https://www.power-technology.com/news/bloomberg-new-energy-outlook-2019-2/`.

[25] Bnef evo report 2020 | bloombergnef | bloomberg finance lp. `https://about.bnef.com/electric-vehicle-outlook-2020/`.

[26] Global wind and solar costs to fall even faster, while coal fades even in china and india | bloombergnef. https://about.bnef.com/blog/global-wind-solar-costs-fall-even-faster-coal-fades-even-china-india/.

[27] | bloombergnef. https://about.bnef.com/blog/energy-storage-investments-boom-battery-costs-halve-next-decade/.

[28] Francisco Díaz-González, Andreas Sumper, Oriol Gomis-Bellmunt, and Roberto Villafáfila-Robles. A review of energy storage technologies for wind power applications. *Renewable and sustainable energy reviews*, 16(4):2154–2171, 2012.

[29] Paul Denholm, Erik Ela, Brendan Kirby, and Michael Milligan. The role of energy storage with renewable electricity generation. Technical Report NREL/TP-6A2-47187, National Renewable Energy Laboratory (NREL), Golden, CO, 2010.

[30] Bulk and transmission energy storage: Technology and projects, 2020 update. https://www.epri.com/research/products/000000003002019016,.

[31] Janina C Ketterer. The impact of wind power generation on the electricity price in germany. *Energy economics*, 44:270–280, 2014.

[32] U.s. grid energy storage factsheet | center for sustainable systems. https://css.umich.edu/publications/factsheets/energy/us-grid-energy-storage-factsheet,.

[33] Vermont liquid air energy storage system, us. https://www.power-technology.com/marketdata/vermont-liquid-air-energy-storage-system-us/.

[34] Andrea Vecchi, Yongliang Li, Yulong Ding, Pierluigi Mancarella, and Adriano Sciacovelli. Liquid air energy storage (laes): A review on technology state-of-the-art, integration pathways and future perspectives. *Advances in Applied Energy*, 3:100047, 2021.

[35] Bharath Kantharaj, Seamus Garvey, and Andrew Pimm. Thermodynamic analysis of a hybrid energy storage system based on compressed air and

liquid air. *Sustainable energy technologies and assessments*, 11:159–164, 2015.

[36] Andreas Coester, Marjan W Hofkes, and Elissaios Papyrakis. Economic analysis of batteries: Impact on security of electricity supply and renewable energy expansion in germany. *Applied energy*, 275:115364, 2020.

[37] Martin Ebner, Federica Marone, Marco Stampanoni, and Vanessa Wood. Visualization and quantification of electrochemical and mechanical degradation in li ion batteries. *Science*, 342(6159):716–720, 2013.

[38] Maxwell Woody, Maryam Arbabzadeh, Geoffrey M Lewis, Gregory A Keoleian, and Anna Stefanopoulou. Strategies to limit degradation and maximize li-ion battery service lifetime-critical review and guidance for stakeholders. *Journal of Energy Storage*, 28:101231, 2020.

[39] Xuebing Han, Languang Lu, Yuejiu Zheng, Xuning Feng, Zhe Li, Jianqiu Li, and Minggao Ouyang. A review on the key issues of the lithium ion battery degradation among the whole life cycle. *ETransportation*, 1:100005, 2019.

[40] Emil Namor, Fabrizio Sossan, Rachid Cherkaoui, and Mario Paolone. Control of battery storage systems for the simultaneous provision of multiple services. *IEEE Transactions on Smart Grid*, 10(3):2799–2808, 2018.

[41] Zhiwei Xu, Zechun Hu, Yonghua Song, and Jianhui Wang. Risk-averse optimal bidding strategy for demand-side resource aggregators in day-ahead electricity markets under uncertainty. *IEEE Transactions on Smart Grid*, 8(1):96–105, 2017.

[42] Matea Vidan, Fabio D'Andreagiovanni, and Hrvoje Pandžić. Individual thermal generator and battery storage bidding strategies based on robust optimization. *IEEE Access*, 9:66829–66838, 2021.

[43] Ali Hajebrahimi, Innocent Kamwa, Morad Mohamed Abdelmageed Abdelaziz, and Ali Moeini. Scenario-wise distributionally robust optimization for collaborative intermittent resources and electric vehicle aggregator bidding strategy. *IEEE Transactions on Power Systems*, 35(5):3706–3718, 2020.

[44] Farhad Samadi Gazijahani and Javad Salehi. Igdt-based complementarity approach for dealing with strategic decision making of price-maker vpp considering demand flexibility. *IEEE Transactions on Industrial Informatics*, 16(4):2212–2220, 2019.

[45] Mohamed Kareem AlAshery, Dongliang Xiao, and Wei Qiao. Second-order stochastic dominance constraints for risk management of a wind power producer's optimal bidding strategy. *IEEE Transactions on Sustainable Energy*, 11(3):1404–1413, 2019.

[46] Matteo Malavasi, Sergio Ortobelli Lozza, and Stefan Trück. Second order of stochastic dominance efficiency vs mean variance efficiency. *European Journal of Operational Research*, 290(3):1192–1206, 2021.

[47] Fatemeh Fathi, Azar Sheikhzeinoddin, and Rezvan Talebnejad. Environmental and economic risk management of seed maize production in iran. *Journal of cleaner production*, 258:120772, 2020.

[48] He Qing, Wang Lijian, Zhou Qian, Lu Chang, Du Dongmei, and Liu Wenyi. Thermodynamic analysis and optimization of liquefied air energy storage system. *Energy*, 173:162–173, 2019.

[49] Xiaodong Peng, Xiaohui She, Chuan Li, Yimo Luo, Tongtong Zhang, Yongliang Li, and Yulong Ding. Liquid air energy storage flexibly coupled with lng regasification for improving air liquefaction. *Applied energy*, 250:1190–1201, 2019.

[50] Ting Liang, Tongtong Zhang, Xipeng Lin, Tafone Alessio, Mathieu Legrand, Xiufen He, Harriet Kildahl, Chang Lu, Haisheng Chen, Alessandro Romagnoli, et al. Liquid air energy storage technology: a comprehensive review of research, development and deployment. *Progress in Energy*, 5(1):012002, 2023.

[51] Farshad Kalavani, Behnam Mohammadi-Ivatloo, and Kazem Zare. Optimal stochastic scheduling of cryogenic energy storage with wind power in the presence of a demand response program. *Renewable Energy*, 130:268–280, 2019.

[52] Jinwoo Park, Seungsik Cho, Meng Qi, Wonjun Noh, Inkyu Lee, and Il Moon. Liquid air energy storage coupled with liquefied natural gas

cold energy: focus on efficiency, energy capacity, and flexibility. *Energy*, 216:119308, 2021.

[53] Marco Antonelli, Stefano Barsali, Umberto Desideri, Romano Giglioli, Fabrizio Paganucci, and Gianluca Pasini. Liquid air energy storage: Potential and challenges of hybrid power plants. *Applied energy*, 194:522–529, 2017.

[54] Tugberk Hakan Cetin, Mehmet Kanoglu, and Neslihan Yanikomer. Cryogenic energy storage powered by geothermal energy. *Geothermics*, 77:34–40, 2019.

[55] Mohammad Hossein Nabat, M Soltani, Amir Reza Razmi, Jatin Nathwani, and MB Dusseault. Investigation of a green energy storage system based on liquid air energy storage (laes) and high-temperature concentrated solar power (csp): Energy, exergy, economic, and environmental (4e) assessments, along with a case study for san diego, us. *Sustainable Cities and Society*, 75:103305, 2021.

[56] Pau Farres-Antunez, Haobai Xue, and Alexander J White. Thermodynamic analysis and optimisation of a combined liquid air and pumped thermal energy storage cycle. *Journal of Energy Storage*, 18:90–102, 2018.

[57] Juwon Kim, Yeelyong Noh, and Daejun Chang. Storage system for distributed-energy generation using liquid air combined with liquefied natural gas. *Applied energy*, 212:1417–1432, 2018.

[58] Boda Li, Ying Chen, Wei Wei, Yunhe Hou, and Shengwei Mei. Enhancing resilience of emergency heat and power supply via deployment of lng tube trailers: A mean-risk optimization approach. *Applied Energy*, 318:119204, 2022.

[59] Boda Li, Ying Chen, Wei Wei, Zhaojian Wang, and Shengwei Mei. Online coordination of lng tube trailer dispatch and resilience restoration of integrated power-gas distribution systems. *IEEE Transactions on Smart Grid*, 13(3):1938–1951, 2022.

[60] Ian M Trotter, Marília Fernandes Maciel Gomes, Marcelo José Braga, Bjørn Brochmann, and Ole Nikolai Lie. Optimal lng (liquefied natural gas) regasification scheduling for import terminals with storage. *Energy*, 105:80–88, 2016.

[61] Wenqi Wu, Yunpeng Xiao, Xiuli Wang, Jianxue Wang, and Xifan Wang. Operating strategy of lng terminal in interdependent electricity and natural gas markets. *IEEE Transactions on Energy Markets, Policy and Regulation*, 2023.

[62] Marcus King, Anjali Jain, Rohit Bhakar, Jyotirmay Mathur, and Jihong Wang. Overview of current compressed air energy storage projects and analysis of the potential underground storage capacity in india and the uk. *Renewable and Sustainable Energy Reviews*, 139:110705, 2021.

[63] Hooman Khaloie and François Vallée. Day-ahead dispatch of liquid air energy storage coupled with lng regasification in electricity and lng markets. *IEEE Transactions on Power Systems*, 39(3):5177–5190, 2023.

[64] Andrew J Pimm, Seamus D Garvey, and Bharath Kantharaj. Economic analysis of a hybrid energy storage system based on liquid air and compressed air. *Journal of energy storage*, 4:24–35, 2015.

[65] Bharath Kantharaj, Seamus Garvey, and Andrew Pimm. Compressed air energy storage with liquid air capacity extension. *Applied energy*, 157:152–164, 2015.

[66] Subholagno Mitra, Anil C Mahato, Abhijit Nag, and Dharmendra Kumar. Various methodologies to improve the energy efficiency of a compressed air energy storage system. *Energy Storage*, 4(5):e315, 2022.

[67] Shubhrajit Bhattacharjee, Ramteen Sioshansi, and Hamidreza Zareipour. Comparing participation models in electricity markets for hybrid energy-storage resources. *IEEE Transactions on Power Systems*, pages 1–11, 2024.

[68] Ehsan Nasrolahpour, Jalal Kazempour, Hamidreza Zareipour, and William D. Rosehart. Impacts of ramping inflexibility of conventional generators on strategic operation of energy storage facilities. *IEEE Transactions on Smart Grid*, 9(2):1334–1344, 2018.

[69] Yishen Wang, Yury Dvorkin, Ricardo Fernández-Blanco, Bolun Xu, Ting Qiu, and Daniel S. Kirschen. Look-ahead bidding strategy for energy storage. *IEEE Transactions on Sustainable Energy*, 8(3):1106–1117, 2017.

[70] Roohallah Khatami, Konstantinos Oikonomou, and Masood Parvania. Look-ahead optimal participation of compressed air energy storage in day-ahead and real-time markets. *IEEE Transactions on Sustainable Energy*, 11(2):682–692, 2020.

[71] Yi Huang, Dan Gordon, and Paul Scott. Receding horizon dispatch of multi-period look-ahead market for energy storage integration. *Applied Energy*, 352:121856, 2023.

[72] Álinson S Xavier, Feng Qiu, and Shabbir Ahmed. Learning to solve large-scale security-constrained unit commitment problems. *INFORMS Journal on Computing*, 33(2):739–756, 2021.

[73] Kyri Baker. Learning warm-start points for ac optimal power flow. In *2019 IEEE 29th International Workshop on Machine Learning for Signal Processing (MLSP)*, pages 1–6, 2019.

[74] Asunción Jiménez-Cordero, Juan Miguel Morales, and Salvador Pineda. Warm-starting constraint generation for mixed-integer optimization: A machine learning approach. *Knowledge-Based Systems*, 253:109570, 2022.

[75] Philippe Artzner, Freddy Delbaen, Jean-Marc Eber, and David Heath. Coherent measures of risk. *Mathematical finance*, 9(3):203–228, 1999.

[76] Panos Kouvelis and Gang Yu. *Robust discrete optimization and its applications*, volume 14. Springer Science & Business Media, 2013.

[77] Peter Taylor, Ronan Bolton, Dave Stone, Xiao-Ping Zhang, Chris Martin, and Paul Upham. Pathways for energy storage in the uk. *Report for the centre for low carbon futures, York*, 2012.

[78] C Opathella, Ayman Elkasrawy, Amr A Mohamed, and B Venkatesh. Optimal scheduling of merchant-owned energy storage systems with multiple ancillary services. *IEEE Open Access Journal of Power and Energy*, 7:31–40, 2019.

[79] Raymond H Byrne, Tu A Nguyen, David A Copp, Babu R Chalamala, and Imre Gyuk. Energy management and optimization methods for grid energy storage systems. *IEEE Access*, 6:13231–13260, 2017.

[80] Haisheng Chen, Thang Ngoc Cong, Wei Yang, Chunqing Tan, Yongliang

Li, and Yulong Ding. Progress in electrical energy storage system: A critical review. *Progress in natural science*, 19(3):291–312, 2009.

[81] Yalsin Gogus. *Energy storage systems-Volume I.* EOLSS Publications, 2009.

[82] Abraham Alem Kebede, Theodoros Kalogiannis, Joeri Van Mierlo, and Maitane Berecibar. A comprehensive review of stationary energy storage devices for large scale renewable energy sources grid integration. *Renewable and Sustainable Energy Reviews*, 159:112213, 2022.

[83] Mukrimin Sevket Guney and Yalcin Tepe. Classification and assessment of energy storage systems. *Renewable and Sustainable Energy Reviews*, 75:1187–1197, 2017.

[84] Léonard Wagner. Overview of energy storage technologies. In *Future Energy*, pages 613–631. Elsevier, 2014.

[85] Christopher K Dyer. Fuel cells for portable applications. *Journal of Power Sources*, 106(1-2):31–34, 2002.

[86] Gilles Flamant, Daniel Gauthier, Hadrien Benoit, Jean-Louis Sans, Roger Garcia, Benjamin Boissière, Renaud Ansart, and Mehrdji Hemati. Dense suspension of solid particles as a new heat transfer fluid for concentrated solar thermal plants: On-sun proof of concept. *Chemical engineering science*, 102:567–576, 2013.

[87] Xiudong Wei, Zhenwu Lu, Zhifeng Wang, Weixing Yu, Hongxing Zhang, and Zhihao Yao. A new method for the design of the heliostat field layout for solar tower power plant. *Renewable Energy*, 35(9):1970–1975, 2010.

[88] Wolf-Dieter Steinmann. Thermo-mechanical concepts for bulk energy storage. *Renewable and Sustainable Energy Reviews*, 75:205–219, 2017.

[89] Rachel Carnegie, Douglas Gotham, David Nderitu, and Paul V Preckel. Utility scale energy storage systems. *State Utility Forecasting Group. Purdue University*, 1:27, 2013.

[90] Ahmed F Zobaa. *Energy Storage: Technologies and Applications.* BoD–Books on Demand, 2013.

[91] Andreas V Olympios, Joshua D McTigue, Pau Farres-Antunez, Alessio Tafone, Alessandro Romagnoli, Yongliang Li, Yulong Ding, Wolf-Dieter Steinmann, Liang Wang, Haisheng Chen, et al. Progress and prospects of thermo-mechanical energy storage—a critical review. *Progress in Energy*, 3(2):022001, 2021.

[92] Xing Luo, Jihong Wang, Jacek D Wojcik, Jianguo Wang, Decai Li, Mihai Draganescu, Yaowang Li, and Shihong Miao. Review of voltage and frequency grid code specifications for electrical energy storage applications. *Energies*, 11(5):1070, 2018.

[93] Micah S Ziegler and Jessika E Trancik. Re-examining rates of lithium-ion battery technology improvement and cost decline. *Energy & Environmental Science*, 14(4):1635–1651, 2021.

[94] Holger C Hesse, Michael Schimpe, Daniel Kucevic, and Andreas Jossen. Lithium-ion battery storage for the grid—a review of stationary battery storage system design tailored for applications in modern power grids. *Energies*, 10(12):2107, 2017.

[95] Jens Vetter, Petr Novák, Markus Robert Wagner, Claudia Veit, K-C Möller, JO Besenhard, Martin Winter, Margret Wohlfahrt-Mehrens, Christoph Vogler, and Abderrezak Hammouche. Ageing mechanisms in lithium-ion batteries. *Journal of power sources*, 147(1-2):269–281, 2005.

[96] Namgil Paik. KEPCO's energy storage system projects for frequency regulation. Presentation slides, CAREC Knowledge Sharing Program on ICT for Energy (Seoul, 17–20 April 2017). `https://www.carecprogram.org/uploads/07-KEPCO%E2%80%99s-Energy-Storage-System-Projects-for-Frequency-Regulation.pdf`, April 2017. Accessed: 2026-01-05.

[97] Jennifer B Dunn, Linda Gaines, John Sullivan, and Michael Q Wang. Impact of recycling on cradle-to-gate energy consumption and greenhouse gas emissions of automotive lithium-ion batteries. *Environmental science & technology*, 46(22):12704–12710, 2012.

[98] Global EV Outlook 2023 – Analysis IEA. Global ev outlook 2023 – analysis - iea, Apr 2023.

[99] Osama Tasneem, Hamza Tasneem, and Xiaojun Xian. Lithium-ion battery technologies for grid-scale renewable energy storage. *Next Research*, page 100297, 2025.

[100] Stuart Nelmes. Liquid air energy storage (LAES). Presentation slides (Highview Enterprises Ltd.), HIES2017 (University of Warwick). `https://warwick.ac.uk/fac/sci/eng/research/grouplist/electricalpower/images/newsnevents/hies2017/presentations/hies2017_highview.pdf`, 2017. Accessed: 2026-01-05.

[101] EM Smith. Storage of electrical energy using supercritical liquid air. *Proceedings of the Institution of Mechanical Engineers*, 191(1):289–298, 1977.

[102] Kenji Kishimoto, K Hasegawa, and TJMJG Asano. Development of generator of liquid air storage energy system. *Mitsubishi Juko Giho*, 35:60–63, 1998.

[103] Plants | highview power. `https://highviewpower.com/plants/`.

[104] Highview power developing 2 gwh of liquid air long duration energy storage projects in spain | highview power. `https://highviewpower.com/news_announcement/highview-power-developing-2-gwh-of-liquid-air-long-duration-energy-storage-projects-in-spain/`.

[105] Chile's 50-mw/600-mwh laes project wins approval. `https://renewablesnow.com/news/chiles-50-mw600-mwh-laes-project-wins-approval-796804/`.

[106] Marcus Budt, Daniel Wolf, Roland Span, and Jinyue Yan. A review on compressed air energy storage: Basic principles, past milestones and recent developments. *Applied energy*, 170:250–268, 2016.

[107] Laijun Chen, Tianwen Zheng, Shengwei Mei, Xiaodai Xue, Binhui Liu, and Qiang Lu. Review and prospect of compressed air energy storage system. *Journal of Modern Power Systems and Clean Energy*, 4(4):529–541, 2016.

[108] Samir Succar and Robert H. Williams. Compressed air energy storage: Theory, resources, and applications for wind power. Technical report,

Princeton Environmental Institute, Princeton University, April 2008. Dated: 2008-04-08. Accessed: 2026-01-05.

[109] Chaobin Guo, Lehua Pan, Keni Zhang, Curtis M Oldenburg, Cai Li, and Yi Li. Comparison of compressed air energy storage process in aquifers and caverns based on the huntorf caes plant. *Applied Energy*, 181:342–356, 2016.

[110] Fritz Crotogino, Klaus-Uwe Mohmeyer, and Roland Scharf. Huntorf caes: More than 20 years of successful operation. *Orlando, Florida, USA*, 2001.

[111] Heidar Jafarizadeh, M Soltani, and Jatin Nathwani. Assessment of the huntorf compressed air energy storage plant performance under enhanced modifications. *Energy Conversion and Management*, 209:112662, 2020.

[112] DR Hounslow, W Grindley, RM Loughlin, and J Daly. The development of a combustion system for a 110 mw caes plant. 1998.

[113] S. Sucar Succar, Robert Howard Williams, Angela Cavallo, Charles Kanakam Christopher, Paul Denholm Nrel, David C. Denkenberger, Aleksandra Kalinowski, Michael McGill, Robert H. Socolow, and IAN R. Vann. Compressed air energy storage : Theory , resources , and applications for wind power 8. 2008.

[114] Y Nikravesh, K Muralidharan, and G Frantziskonis. Techno-economic assessment and design optimization of compressed air energy storage using filament wound carbon fiber reinforced plastic pressure vessels. *Journal of Energy Storage*, 40:102754, 2021.

[115] Trading products | epex spot. https://www.epexspot.com/en/tradingproducts.

[116] Jean-François Toubeau, Thuy-Hai Nguyen, Hooman Khaloie, Yi Wang, and François Vallée. Forecast-driven stochastic scheduling of a virtual power plant in energy and reserve markets. *IEEE Systems Journal*, 16(4):5212–5223, 2022.

[117] Juan Arteaga and Hamidreza Zareipour. A price-maker/price-taker model for the operation of battery storage systems in electricity markets. *IEEE Transactions on Smart Grid*, 10(6):6912–6920, 2019.

[118] Stephen Boyd and Lieven Vandenberghe. *Convex optimization*. Cambridge university press, 2004.

[119] Mokhtar S Bazaraa, Hanif D Sherali, and Chitharanjan M Shetty. *Nonlinear programming: theory and algorithms*. John wiley & sons, 2006.

[120] Allen J Wood, Bruce F Wollenberg, and Gerald B Sheblé. *Power generation, operation, and control*. John wiley & sons, 2013.

[121] Juan M Morales, Antonio J Conejo, Henrik Madsen, Pierre Pinson, and Marco Zugno. *Integrating renewables in electricity markets: operational problems*, volume 205. Springer Science & Business Media, 2013.

[122] Haoran Zhao, Qiuwei Wu, Shuju Hu, Honghua Xu, and Claus Nygaard Rasmussen. Review of energy storage system for wind power integration support. *Applied energy*, 137:545–553, 2015.

[123] Dimitris Bertsimas and John N Tsitsiklis. *Introduction to linear optimization*, volume 6. Athena scientific Belmont, MA, 1997.

[124] Antonio J Conejo, Miguel Carrión, Juan M Morales, et al. *Decision making under uncertainty in electricity markets*, volume 1. Springer, 2010.

[125] John R Birge and Francois Louveaux. *Introduction to stochastic programming*. Springer, 1997.

[126] Alexander Shapiro, Darinka Dentcheva, and Andrzej Ruszczynski. *Lectures on stochastic programming: modeling and theory*. SIAM, 2021.

[127] Hooman Khaloie, Amir Abdollahi, Miadreza Shafie-khah, Amjad Anvari-Moghaddam, Sayyad Nojavan, Pierluigi Siano, and João P.S. Catalão. Coordinated wind-thermal-energy storage offering strategy in energy and spinning reserve markets using a multi-stage model. *Applied Energy*, 259:114168, 2020.

[128] Hooman Khaloie, Amir Abdollahi, Miadreza Shafie-Khah, Pierluigi Siano, Sayyad Nojavan, Amjad Anvari-Moghaddam, and João P.S. Catalão. Co-optimized bidding strategy of an integrated wind-thermal-photovoltaic system in deregulated electricity market under uncertainties. *Journal of Cleaner Production*, 242:118434, 2020.

[129] Stephan Dempe. *Foundations of bilevel programming*. Springer, 2002.

[130] Jonathan F Bard. *Practical bilevel optimization: algorithms and applications*, volume 30. Springer Science & Business Media, 2013.

[131] Steven A Gabriel, Antonio J Conejo, J David Fuller, Benjamin F Hobbs, and Carlos Ruiz. *Complementarity modeling in energy markets*, volume 180. Springer Science & Business Media, 2012.

[132] Carlos Ruiz, Antonio J Conejo, J David Fuller, Steven A Gabriel, and Benjamin F Hobbs. A tutorial review of complementarity models for decision-making in energy markets. *EURO Journal on Decision Processes*, 2(1):91–120, 2014.

[133] Zhi-Quan Luo, Jong-Shi Pang, and Daniel Ralph. *Mathematical programs with equilibrium constraints*. Cambridge University Press, 1996.

[134] Jiri Outrata, Michal Kocvara, and Jochem Zowe. *Nonsmooth approach to optimization problems with equilibrium constraints: theory, applications and numerical results*, volume 28. Springer Science & Business Media, 2013.

[135] D P Bertsekas. Nonlinear programming. *Journal of the Operational Research Society*, 48(3):334–334, 1997.

[136] Hooman Khaloie, Mihaly Dolanyi, Jean-Francois Toubeau, and François Vallée. Review of machine learning techniques for optimal power flow. *Applied Energy*, 388:125637, 2025.

[137] Pádraig Cunningham, Matthieu Cord, and Sarah Jane Delany. Supervised learning. In *Machine learning techniques for multimedia: case studies on organization and retrieval*, pages 21–49. Springer, 2008.

[138] Trevor Hastie, Robert Tibshirani, Jerome Friedman, Trevor Hastie, Robert Tibshirani, and Jerome Friedman. Unsupervised learning. *The elements of statistical learning: Data mining, inference, and prediction*, pages 485–585, 2009.

[139] Richard S Sutton and Andrew G Barto. *Reinforcement learning: An introduction*. MIT press, 2018.

[140] Ian Goodfellow, Jean Pouget-Abadie, Mehdi Mirza, Bing Xu, David Warde-Farley, Sherjil Ozair, Aaron Courville, and Yoshua Bengio. Gener-

ative adversarial nets. *Advances in neural information processing systems*, 27, 2014.

[141] James Kotary, Ferdinando Fioretto, Pascal Van Hentenryck, and Bryan Wilder. End-to-end constrained optimization learning: A survey. *arXiv preprint arXiv:2103.16378*, 2021.

[142] Feng Xia, Ke Sun, Shuo Yu, Abdul Aziz, Liangtian Wan, Shirui Pan, and Huan Liu. Graph learning: A survey. *IEEE Transactions on Artificial Intelligence*, 2(2):109–127, 2021.

[143] Constance Crozier and Kyri Baker. Data-driven probabilistic constraint elimination for accelerated optimal power flow. In *2022 IEEE Power & Energy Society General Meeting (PESGM)*, pages 1–5. IEEE, 2022.

[144] Hooman Khaloie, Andrej Stankovski, Blazhe Gjorgiev, Giovanni Sansavini, and François Vallée. Hybrid energy storage dispatch: A bi-level look-ahead learning-assisted model. *IEEE Transactions on Energy Markets, Policy and Regulation*, 3(3):376–392, 2025.

[145] Sihan Zeng, Alyssa Kody, Youngdae Kim, Kibaek Kim, and Daniel K. Molzahn. A reinforcement learning approach to parameter selection for distributed optimal power flow. *Electric Power Systems Research*, 212:108546, 2022.

[146] David Biagioni, Peter Graf, Xiangyu Zhang, Ahmed S Zamzam, Kyri Baker, and Jennifer King. Learning-accelerated admm for distributed dc optimal power flow. *IEEE Control Systems Letters*, 6:1–6, 2020.

[147] Bolun Xu, Jinye Zhao, Tongxin Zheng, Eugene Litvinov, and Daniel S Kirschen. Factoring the cycle aging cost of batteries participating in electricity markets. *IEEE Transactions on Power Systems*, 33(2):2248–2259, 2017.

[148] Nitin Padmanabhan, Mohamed Ahmed, and Kankar Bhattacharya. Battery energy storage systems in energy and reserve markets. *IEEE Transactions on Power Systems*, 35(1):215–226, 2019.

[149] Guannan He, Qixin Chen, Chongqing Kang, Pierre Pinson, and Qing Xia. Optimal bidding strategy of battery storage in power markets considering

performance-based regulation and battery cycle life. *IEEE Transactions on Smart Grid*, 7(5):2359–2367, 2015.

[150] Elian Pusceddu, Behnam Zakeri, and Giorgio Castagneto Gissey. Synergies between energy arbitrage and fast frequency response for battery energy storage systems. *Applied Energy*, 283:116274, 2021.

[151] Yi Dong, Zhen Dong, Tianqiao Zhao, and Zhengtao Ding. A strategic day-ahead bidding strategy and operation for battery energy storage system by reinforcement learning. *Electric power systems research*, 196:107229, 2021.

[152] Konstantinos Steriotis, Karlo Šepetanc, Konstantinos Smpoukis, Nikolaos Efthymiopoulos, Prodrommos Makris, Emmanouel Varvarigos, and Hrvoje Pandžić. Stacked revenues maximization of distributed battery storage units via emerging flexibility markets. *IEEE Transactions on Sustainable Energy*, 13(1):464–478, 2021.

[153] Danman Wu, Tengyun Qi, Wei Wei, Jianping Liu, Laijun Chen, and Shengwei Mei. An efficient decomposition method for bilevel energy storage arbitrage problem. *CSEE Journal of Power and Energy Systems*, 8(2):652–658, 2022.

[154] Xuan Wu, Jenny Zhao, and Antonio J Conejo. Optimal battery sizing for frequency regulation and energy arbitrage. *IEEE Transactions on Power Delivery*, 37(3):2016–2023, 2021.

[155] Xichen Fang, Hongye Guo, Xian Zhang, Xuanyuan Wang, and Qixin Chen. An efficient and incentive-compatible market design for energy storage participation. *Applied Energy*, 311:118731, 2022.

[156] Hooman Khaloie, Amjad Anvari-Moghaddam, Javier Contreras, Jean-François Toubeau, Pierluigi Siano, and François Vallée. Offering and bidding for a wind producer paired with battery and caes units considering battery degradation. *International Journal of Electrical Power & Energy Systems*, 136:107685, 2022.

[157] Anupam A Thatte, Le Xie, Daniel E Viassolo, and Sunita Singh. Risk measure based robust bidding strategy for arbitrage using a wind farm and energy storage. *IEEE Transactions on Smart Grid*, 4(4):2191–2199, 2013.

[158] Hooman Khaloie, Amjad Anvari-Moghaddam, Nikos Hatziargyriou, and Javier Contreras. Risk-constrained self-scheduling of a hybrid power plant considering interval-based intraday demand response exchange market prices. *Journal of Cleaner Production*, 282:125344, 2021.

[159] Jianxiao Wang, Haiwang Zhong, Wenyuan Tang, Ram Rajagopal, Qing Xia, Chongqing Kang, and Yi Wang. Optimal bidding strategy for microgrids in joint energy and ancillary service markets considering flexible ramping products. *Applied Energy*, 205:294–303, 2017.

[160] Xuejiao Han and Gabriela Hug. A distributionally robust bidding strategy for a wind-storage aggregator. *Electric power systems research*, 189:106745, 2020.

[161] Amirhossein Khazali, Navid Rezaei, Wencong Su, and Mohsen Kalantar. Risk-aware bilevel optimal offering strategy of a joint wind/storage unit based on information gap decision theory. *IEEE Systems Journal*, 15(2):1939–1949, 2021.

[162] Seyyed Ahmad Hosseini, Jean-François Toubeau, Zacharie De Grève, Yi Wang, Nima Amjady, and François Vallée. Data-driven multi-resolution probabilistic energy and reserve bidding of wind power. *IEEE Transactions on Power Systems*, 38(1):85–99, 2022.

[163] Hooman Khaloie, Jean-François Toubeau, François Vallée, Chun Sing Lai, and Loi Lei Lai. An innovative coalitional trading model for a biomass power plant paired with green energy resources. *IEEE Transactions on Sustainable Energy*, 13(2):892–904, 2021.

[164] Jamal Faraji, Abbas Ketabi, Hamed Hashemi-Dezaki, Miadreza Shafie-Khah, and Joao PS Catalao. Optimal day-ahead self-scheduling and operation of prosumer microgrids using hybrid machine learning-based weather and load forecasting. *IEEE Access*, 8:157284–157305, 2020.

[165] Edward Anderson, Huifu Xu, and Dali Zhang. Confidence levels for cvar risk measures and minimax limits. *Optimization online*, 2014.

[166] Hooman Khaloie, François Vallée, Chun Sing Lai, Jean-François Toubeau, and Nikos D Hatziargyriou. Day-ahead and intraday dispatch of an integrated biomass-concentrated solar system: A multi-objective risk-

controlling approach. *IEEE Transactions on Power Systems*, 37(1):701–714, 2021.

[167] Serafim Opricovic and Gwo-Hshiung Tzeng. Extended vikor method in comparison with outranking methods. *European journal of operational research*, 178(2):514–529, 2007.

[168] Mohammad Kazem Sayadi, Majeed Heydari, and Kamran Shahanaghi. Extension of vikor method for decision making problem with interval numbers. *Applied mathematical modelling*, 33(5):2257–2262, 2009.

[169] Ozan Erdinc. Economic impacts of small-scale own generating and storage units, and electric vehicles under different demand response strategies for smart households. *Applied Energy*, 126:142–150, 2014.

[170] Esios red eléctrica. `https://www.esios.ree.es/es`, 2025.

[171] Scenario reduction and tree construction (scenred). `https://www.gams.com/51/docs/T_LIBINCLUDE_SCENRED.html`, 2025.

[172] Gams - cutting edge modeling. `https://www.gams.com/`, 2025.

[173] Hadi Khani and Mohammad R Dadash Zadeh. Real-time optimal dispatch and economic viability of cryogenic energy storage exploiting arbitrage opportunities in an electricity market. *IEEE Transactions on Smart Grid*, 6(1):391–401, 2014.

[174] Chunping Xie, Yan Hong, Yulong Ding, Yongliang Li, and Jonathan Radcliffe. An economic feasibility assessment of decoupled energy storage in the uk: With liquid air energy storage as a case study. *Applied Energy*, 225:244–257, 2018.

[175] Boqiang Lin, Wei Wu, Mengqi Bai, Chunping Xie, and Jonathan Radcliffe. Liquid air energy storage: Price arbitrage operations and sizing optimization in the gb real-time electricity market. *Energy Economics*, 78:647–655, 2019.

[176] Andrea Vecchi, James Naughton, Yongliang Li, Pierluigi Mancarella, and Adriano Sciacovelli. Multi-mode operation of a liquid air energy storage (laes) plant providing energy arbitrage and reserve services–analysis of optimal scheduling and sizing through milp modelling with integrated thermodynamic performance. *Energy*, 200:117500, 2020.

[177] Andrea Vecchi, Yongliang Li, Pierluigi Mancarella, and Adriano Sciacovelli. Integrated techno-economic assessment of liquid air energy storage (laes) under off-design conditions: Links between provision of market services and thermodynamic performance. *Applied Energy*, 262:114589, 2020.

[178] Mathieu Legrand, Raúl Labajo-Hurtado, Luis Miguel Rodríguez-Antón, and Yolanda Doce. Price arbitrage optimization of a photovoltaic power plant with liquid air energy storage. implementation to the spanish case. *Energy*, 239:121957, 2022.

[179] Qi Zhang, Ignacio E Grossmann, Clara F Heuberger, Arul Sundaramoorthy, and Jose M Pinto. Air separation with cryogenic energy storage: optimal scheduling considering electric energy and reserve markets. *AIChE Journal*, 61(5):1547–1558, 2015.

[180] Fulin Kong, Yuxin Liu, Minghai Shen, Lige Tong, Shaowu Yin, Li Wang, and Yulong Ding. A novel economic scheduling of multi-product deterministic demand for co-production air separation system with liquid air energy storage. *Renewable Energy*, 209:533–545, 2023.

[181] Huajie Ding, Pierre Pinson, Zechun Hu, and Yonghua Song. Optimal offering and operating strategies for wind-storage systems with linear decision rules. *IEEE Transactions on Power Systems*, 31(6):4755–4764, 2016.

[182] F.J. Nogales, J. Contreras, A.J. Conejo, and R. Espinola. Forecasting next-day electricity prices by time series models. *IEEE Transactions on Power Systems*, 17(2):342–348, 2002.

[183] Hooman Khaloie, Mojgan Mollahassani-Pour, and Amjad Anvari-Moghaddam. Optimal behavior of a hybrid power producer in day-ahead and intraday markets: A bi-objective cvar-based approach. *IEEE Transactions on Sustainable Energy*, 12(2):931–943, 2020.

[184] Bodie Zvi, Kane Alex, and Marcus J Alan. Investments. 2024.

[185] Alex Cukierman. The effects of uncertainty on investment under risk neutrality with endogenous information. *Journal of political economy*, 88(3):462–475, 1980.

[186] Morris H DeGroot. Probability and statistics. 1986.

[187] David V Hinkley. On the ratio of two correlated normal random variables. *Biometrika*, 56(3):635–639, 1969.

[188] Jerald F Lawless. *Statistical models and methods for lifetime data*. John Wiley & Sons, 2011.

[189] Us dollar to euro history: 2021. `https://www.exchangerates.org.uk/USD-EUR-spot-exchange-rates-history-2021.html`, 2021.

[190] X Wang M Economides. Liquefied natural gas (lng). *Advanced Natural Gas Engineering (Gulf Publishing Company, 2009)*.

[191] Higher calorific values of common fuels: Reference data. https://www.engineeringtoolbox.com/fuels-higher-calorific-values-d$_1$69.*html*, 2023.

[192] Arrigo Battistelli. Boil off gas handling on lng fuelled vessels with high pressure gas injected engines. 2014.

[193] Geoffrey Rothwell. Cost contingency as the standard deviation of the cost estimate. *COST ENGINEERING-ANN ARBOR THEN MORGANTOWN-*, 47(7):22, 2005.

[194] Raji Atia and Noboru Yamada. Sizing and analysis of renewable energy and battery systems in residential microgrids. *IEEE Transactions on Smart Grid*, 7(3):1204–1213, 2016.

[195] Soroush Shafiee, Hamidreza Zareipour, Andrew M Knight, Nima Amjady, and Behnam Mohammadi-Ivatloo. Risk-constrained bidding and offering strategy for a merchant compressed air energy storage plant. *IEEE Transactions on Power Systems*, 32(2):946–957, 2016.

[196] Matheus F Zambroni de Souza, Claudio A Cañizares, and Kankar Bhattacharya. Self-scheduling models of a caes facility under uncertainties. *IEEE Transactions on Power Systems*, 36(4):3607–3617, 2021.

[197] Matheus F Zambroni de Souza, Claudio A Cañizares, Kankar Bhattacharya, and Alvaro Lorca. Affine policies and principal components analysis for self-scheduling in caes facilities. *IEEE Transactions on Power Systems*, 38(3):2261–2274, 2022.

[198] Ahmad Attarha, Nima Amjady, Shahab Dehghan, and Behdad Vatani. Adaptive robust self-scheduling for a wind producer with compressed air energy storage. *IEEE Transactions on Sustainable Energy*, 9(4):1659–1671, 2018.

[199] Amirhossein Dolatabadi, Hussein Abdeltawab, and Yasser Abdel-Rady I Mohamed. Deep reinforcement learning-based self-scheduling strategy for a caes-pv system using accurate sky images-based forecasting. *IEEE Transactions on Power Systems*, 38(2):1608–1618, 2022.

[200] IEA. Prospects for large-scale energy storage in decarbonised power grids, 2009. Licence: CC BY 4.0.

[201] S Succar. Compressed air energy storage: Theory, resources and applications for wind power. *Princeton Environmental Institute (PEI), Princeton University*, 2008.

[202] Hantao Cui, Fangxing Li, Xin Fang, Hao Chen, and Honggang Wang. Bilevel arbitrage potential evaluation for grid-scale energy storage considering wind power and lmp smoothing effect. *IEEE Transactions on Sustainable Energy*, 9(2):707–718, 2018.

[203] András Prékopa. *Stochastic programming*, volume 324. Springer Science & Business Media, 2013.

[204] Hooman Khaloie, Jamal Faraji, François Vallée, Chun Sing Lai, Jean-François Toubeau, and Loi Lei Lai. Risk-aware battery bidding with a novel benchmark selection under second-order stochastic dominance. *IEEE Transactions on Industry Applications*, 59(3):3009–3018, 2023.

[205] José Manuel Arroyo. Bilevel programming applied to power system vulnerability analysis under multiple contingencies. *IET generation, transmission & distribution*, 4(2):178–190, 2010.

[206] José Fortuny-Amat and Bruce McCarl. A representation and economic interpretation of a two-level programming problem. *Journal of the operational Research Society*, 32(9):783–792, 1981.

[207] Giuseppe Leo Guizzi, Michele Manno, Ludovica Maria Tolomei, and Ruggero Maria Vitali. Thermodynamic analysis of a liquid air energy storage system. *Energy*, 93:1639–1647, 2015.

[208] Carlos Ruiz, Antonio J Conejo, and Dimitris J Bertsimas. Revealing rival marginal offer prices via inverse optimization. *IEEE Transactions on Power Systems*, 28(3):3056–3064, 2013.

[209] Mibgas - iberian gas market. `https://www.mibgas.es/en`, 2025.

[210] Ray Daniel Zimmerman, Carlos Edmundo Murillo-Sánchez, and Robert John Thomas. Matpower: Steady-state operations, planning, and analysis tools for power systems research and education. *IEEE Transactions on Power Systems*, 26(1):12–19, 2011.

[211] Entso-e transparency platform. Accessed on March 10, 2025.

[212] Takuya Akiba, Shotaro Sano, Toshihiko Yanase, Takeru Ohta, and Masanori Koyama. Optuna: A next-generation hyperparameter optimization framework. In *Proceedings of the 25th ACM SIGKDD International Conference on Knowledge Discovery and Data Mining*, 2019.

[213] Eléa Prat, Richard M. Lusby, Juan Miguel Morales, Salvador Pineda, and Pierre Pinson. How long is long enough? finite-horizon approximation of energy storage scheduling problems, 2024.

[214] Ramteen Sioshansi. When energy storage reduces social welfare. *Energy Economics*, 41:106–116, 2014.

[215] Dimitris Bertsimas and Melvyn Sim. The price of robustness. *Operations research*, 52(1):35–53, 2004.

[216] U.S. Environmental Protection Agency. Emission factors for greenhouse gas inventories, 2025. Table 1: Natural gas CO_2 emission factor, 53.06 kg CO_2/MMBtu (HHV basis).

[217] U.S. Energy Information Administration. Electric power annual: Heat rate, by prime mover and energy source, 2024. Natural gas gas-turbine average heat rate reported as 10,999 Btu/kWh.

[218] Ivonne Peña, Carlo Brancucci Martinez-Anido, and Bri-Mathias Hodge. An extended ieee 118-bus test system with high renewable penetration. *IEEE Transactions on Power Systems*, 33(1):281–289, 2018.

Energy Storage Integration in Market-Based Energy Systems: Advanced Technologies and Decision-Making Models